RUHR-UNIVERSITÄT BOCHUM

RUB

Modeling of growth and fiber reorientation in soft biological tissues

Anna Zahn

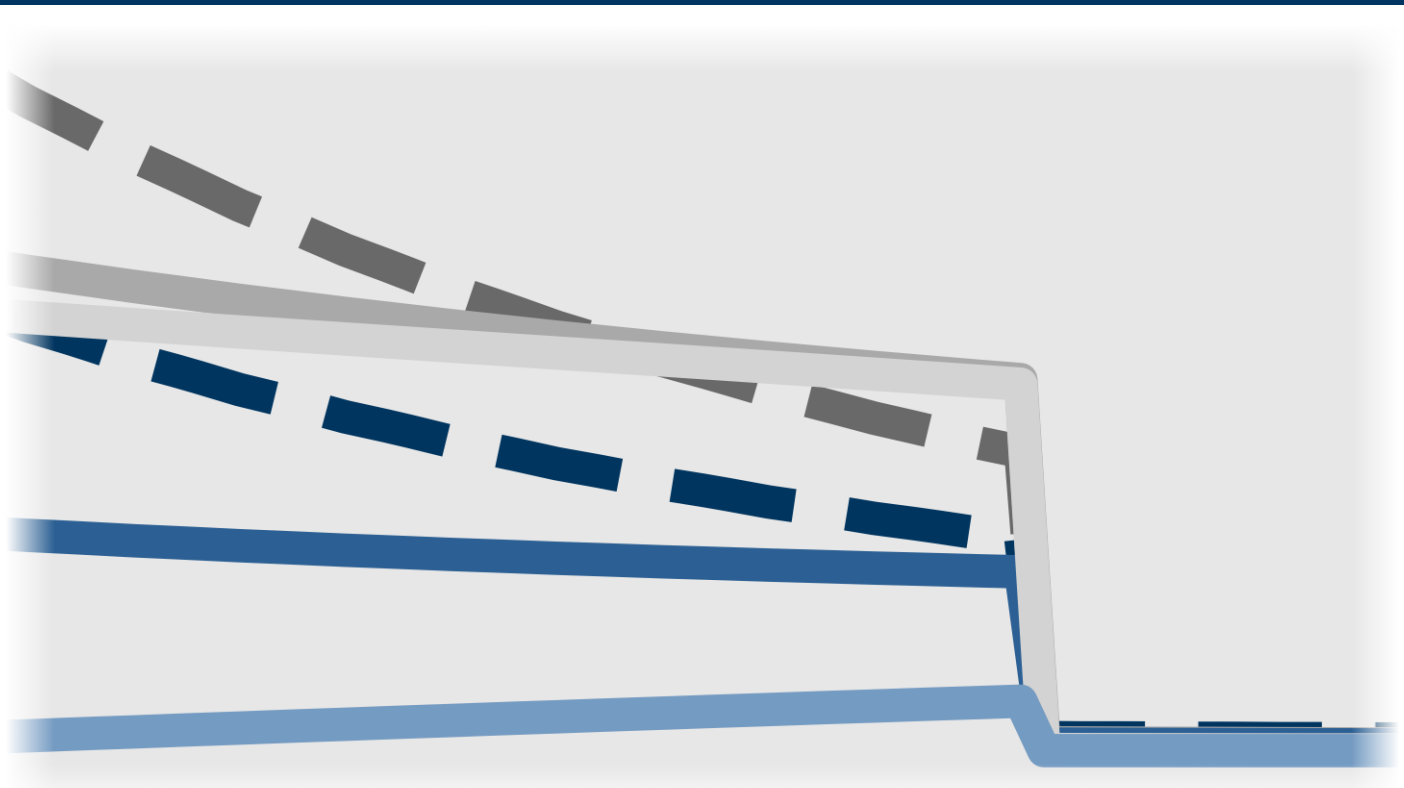

Modeling of growth and fiber reorientation in soft biological tissues

Zur Erlangung des Grades
Doktor-Ingenieurin
an der Fakultät für Bau- und Umweltingenieurwissenschaften
der Ruhr-Universität Bochum
genehmigte Dissertation

von

Anna Zahn

Einreichung der Dissertation: 14.12.2020
Tag der mündlichen Prüfung: 19.05.2021

Erstgutachter: Prof. Dr.-Ing. habil. Daniel Balzani
Zweitgutachter: Prof. Dr.-Ing. habil. Jörg Schröder

Mitteilungen aus dem Institut für Mechanik
Nr. 186

Publisher:

Institute for Mechanics
Ruhr-University Bochum
D-44780 Bochum

Prof. Dr.-Ing. habil. Daniel Balzani
Chair for Continuum Mechanics

Herausgeber:

Institut für Mechanik
Ruhr-Universität Bochum
44780 Bochum

Prof. Dr.-Ing. habil. Daniel Balzani
Lehrstuhl für Kontinuumsmechanik

ISBN 978-3-935892-64-3

Vorwort

An dieser Stelle möchte ich mich bei allen, die auf die eine oder andere Weise dazu beigetragen haben, dass die vorliegende Arbeit entstehen, sich über Höhen und Tiefen hinweg stetig fortentwickeln und schließlich zum Abschluss gebracht werden konnte, aufs herzlichste bedanken.

Dresden, im August 2021 Anna Zahn

Abstract

In this work, a framework for the combined simulation of anisotropic growth and fiber reorientation in soft biological tissues with application to arterial walls with two families of collagen fibers is presented and implemented in a nonlinear finite element setting. It is thought to enable the approximation of residual stresses and fiber orientations in patient-specific arterial wall simulations based on mechanically founded assumptions on the underlying adaptation processes, which are assumed to be stress-driven. In accordance with their suitability to carry tensile loads, the collagen fibers are supposed to be arranged symmetrically with respect to the directions of the tensile principal stresses. Growth is modeled by a multiplicative decomposition of the deformation gradient, where the growth tensor itself is decomposed into up to three parts associated to the directions of the principal stresses. Due to the possibility to combine different basic forms of growth and different stress-based driving force functions for the three directions, a large number of hypothetical growth mechanisms is included in the general framework. For their comparison and evaluation, a method based on a mechano-biologically motivated objective function and idealized, rotationally symmetric arterial segments is developed. The comparative study points out that purely radial growth can hardly be justified from a mechanical point of view and confirms that growth in arterial walls should be assumed to be anisotropic. Apart from numerical examples on growth and fiber reorientation in idealized arterial segments with restriction to standard constitutive equations, a patient-specific artery is considered and the extensibility to enhanced material models is shown by inclusion of the active material response.

Zusammenfassung

In der vorliegenden Arbeit wird ein Modell für die kombinierte Simulation anisotropen Wachstums und sich umorientierender Fasern in biologischen Weichgeweben vorgestellt, das auf Arterienwände mit zwei Kollagenfaserfamilien angewandt wird. Das Modell wird im Rahmen der nicht-linearen Finite-Elemente-Methode umgesetzt und soll auf Basis mechanisch fundierter Annahmen über die zugrundeliegenden, als spannungsgesteuert vorausgesetzten Adaptionsvorgänge die Approximierung von Eigenspannungen und Faserorientierungen in numerischen Simulationen patientenspezifischer Arterien ermöglichen. Dazu wird angenommen, dass sich Kollagenfasern entsprechend ihrer Fähigkeit, Zugspannungen aufzunehmen, bevorzugt symmetrisch bezüglich der Hauptzugspannungsrichtungen anordnen. Wachstum wird anhand einer multiplikativen Zerlegung des Deformationsgradienten beschrieben, wobei der Wachstumstensor selbst in bis zu drei Anteile zerlegt wird, die den Hauptspannungsrichtungen zugeordnet sind. Aufgrund der Möglichkeit, unterschiedliche Grundformen des Wachstums und verschiedene, das Wachstum steuernde Spannungsmaße zu kombinieren, ist eine Vielzahl hypothetischer Wachstumsmechanismen im allgemeinen Modell enthalten. Für deren Vergleich und Bewertung wird eine Methode entwickelt, die auf einer mechanisch-biologisch motivierten Zielfunktion und der Nutzung wenig rechenintensiver, rotationssymmetrischer Arteriensegmente basiert. Es wird deutlich, dass reines Radialwachstum aus mechanischer Sicht kaum gerechtfertigt werden kann und dass Wachstum in Arterien als anisotrop angesehen werden sollte. Neben numerischen Beispielen zu Wachstum und sich umorientierenden Fasern in idealisierten Arterien mit einem üblichen Materialmodell wird eine patientenspezifische Arterie untersucht und am Beispiel des aktiven Beitrags glatter Muskelzellen die Erweiterbarkeit des Modells auf komplexere Materialmodelle gezeigt.

Contents

1 Introduction

Nowadays, use of computational simulation techniques in the medical context can no longer be dismissed as unrealizable wishful thinking. Increasing computing power and a focus of biomechanical research on problems with clinical relevance pave the way towards a virtual patient, based on which treatment and therapeutic options can be evaluated and optimized before they are put into practice on the real patient. By such patient-specific numerical simulations, the probability of complications as for example defective implantation can be reduced in advance. Due to the complexity of the human body and its functioning, reliable predictions continue to be a great challenge, but simulations can also help to improve fundamental understanding. This work deals with computational simulation of soft biological tissues with a focus on arterial walls. In the context of cardiovascular diseases, such simulations might help one day to predict the probability of rupture in atherosclerotic arteries or aneurysms, to optimize treatment methods like stenting or balloon angioplasty or even to examine the effectiveness of drugs. As a prerequisite, the complex material behavior of arterial tissues in health and disease, with all its biological, chemical, mechanical and possible further aspects, has to be understood and to be implemented in numerical models. This work should be considered as an attempt to contribute to this understanding from a mechanical point of view.

An important aspect of the mechanical behavior of arterial walls is the existence of residual stresses, which significantly affect the distribution of load-induced stresses and can therefore not be neglected in numerical simulations. Residual stresses are self-equilibrating stresses which are present in the absence of any external load. Reducing stress peaks and gradients in the arterial wall under in vivo loading conditions, they have a beneficial effect on the load-bearing behavior. Many approaches for the incorporation of residual stresses in numerical simulations make use of this observation by estimating the unknown stresses based on the assumption of uniform strain or stress distributions over the wall thickness in the physiological state, which can be traced back to the uniform circumferential strain hypothesis by Takamizawa & Hayashi (1987). For example, to name a few of the publications of the last decade, Polzer, Bursa, et al. (2013) proposed to simulate the emergence of residual stresses by applying a linearly distributed, isotropic growth deformation with a volume increase at the inner and a volume decrease at the outer surface of the vessel. This induces compressive residual stresses in the inner and tensile residual stresses in the outer part of the wall. The amount of growth and resorption is determined such that the gradient of von Mises or hydrostatic stress over the wall thickness is minimized and the wall thickness remains constant. With this generalization of the uniform stress hypothesis to a stress which does not contain directional information, an eased application to arbitrary arterial geometries deviating from idealized tubes is enabled. Actually, the applicability to patient-specific arteries is being deemed more and more important and emphasized by many researchers. It is also ensured in the approaches by Schröder & Brinkhues (2014) and Schröder & von Hoegen (2016), where the residual stress is computed based on the deviation of a local stress measure to its sectorial volume average. For that purpose, each separate layer of the

artery is divided circumferentially and axially into sectors, such that potential irregularities along the circumference and the vessel length automatically find their way into the height of the residual stresses. If residual stresses are identified by means of such engineering approaches, it is in general necessary to perform several iterative steps until the final solution, which indeed minimizes the considered strain or stress gradient, is found. This is avoided in the approach by Joldes, Noble, et al. (2018), which as a non-iterative, non-invasive post-processing method for computed stress distributions focuses on computational inexpensiveness and suitability for clinical application. On the basis of standard clinical data, i. e. CT angiography and blood pressure measurements, an estimation for the distribution of the maximum principal stress in the arterial wall under the influence of residual stresses is obtained in a one step calculation. Since the numerical values of residual stresses and stress components apart from the maximum principal stress can not be provided, the method is restricted to applications where the peak wall stress in a given physiological situation is matter of interest, for example the estimation of the probability of rupture in abdominal aortic aneurysms.

A second class of approaches incorporates residual stresses by means of the reverse simulation of residual deformations. The existence of residual stresses in arteries can be visualized by cutting load-free arterial rings in radial direction. Due to a release of residual stresses, which ends up in a new self-equilibrated state, the rings spring open. As frequently done, for example by Holzapfel, Gasser & Ogden (2000) or Balzani, Schröder & Gross (2007), the effect of circumferential residual stresses can be included by defining the opened state of the artery as stress-free reference configuration, which has to be closed to a tube by an initial bending deformation before applying the external loads. Whereas Holzapfel, Gasser & Ogden consider idealized arterial geometries, for which this initial step can be solved analytically, the numerical realization of the closing procedure proposed by Balzani, Schröder & Gross allows for the investigation of arbitrary arterial geometries. Nonetheless, it is generally accepted by now that a single opening angle is not enough to characterize the entire residual stress state of an artery. Apart from depending on various factors like position in the arterial tree, species, age, gender and state of health, the opening angle is highly layer-specific. Furthermore, not only the circumferential, but also the axial direction should be taken into account when analyzing residual deformations: when being excised from the body, arterial segments usually contract in axial direction. As observed for the opening angle in circumferential direction, also the deformations of axial strips differ in the three arterial layers (Holzapfel, Sommer, Auer, et al., 2007). The residual stress state in arterial walls should thus rather be considered as a fully three-dimensional property. On the basis of the experimental data gathered by Holzapfel, Sommer, Auer, et al. (2007), a mathematical model for the inclusion of three-dimensional, layer-specific residual stresses in the analysis of arteries which are idealized as circular cylindrical tubes is provided by Holzapfel & Ogden (2010). For each layer, an individual bending and stretching deformation from the configuration assumed as stress-free to a closed cylindrical tube is formulated mathematically. Restricting their analysis to an incompressible, isotropic constitutive material model, Holzapfel & Ogden are able to indicate explicit expressions for the radial, circumferential and axial stress components. An extension to an advanced anisotropic material model by Holzapfel, Niestrawska, et al. (2015) was presented by Sigaeva, Sommer, et al. (2019). For the transition from idealized to patient-specific geometries, the method proposed by Urevc, Brumen, et al. (2015) and Urevc, Halilovič, et al. (2016) could be applied. Using an analogy to thermomechanics, they map residual stresses from an idealized circular tube to a patient-specific artery by applying appropriate thermal loads to the in vivo configuration. In their original approach, they quantify the residual stresses in the idealized

arterial segment with the help of a single opening angle which is determined by adopting the uniform strain hypothesis, but use of experimental data such as those of Holzapfel, Sommer, Auer, et al. (2007) would also be possible.
Two other exemplary methods, which enable the analysis of patient-specific geometries but can not be assigned to the aforementioned groups of models, are proposed by Ahamed, Dorfmann & Ogden (2016) and Ares, Blanco, et al. (2017). Ahamed, Dorfmann & Ogden introduced an invariant-based, anisotropic constitutive formulation, where a dependency of the strain energy function on a residual stress tensor is postulated. Assuming a quadratic distribution of the radial residual stress and zero axial residual stresses, they obtain an equation for the circumferential residual stresses, which involves a single parameter defining the stress magnitude. Being consistent with the residual stresses obtained from a simple opening angle method, these residual stresses are not able to represent the complexity of real residual stress states. To achieve this, a more general ansatz for the residual stress tensor would be required. In the variational formulation by Ares, Blanco, et al., the residual deformations and the associated residual stresses in arterial walls are estimated based on medical full displacement field measurements at known blood pressures. An approximation of the residual stress state is obtained by minimization of a cost functional, which represents the mechanical imbalance due to lack of knowledge on the residual stresses.

Taking residual stresses as a given, neither approaches which focus on the (purely technical) smoothing of strain or stress gradients nor methods based on the reverse simulation of opening angle or related experiments do say something about their genesis. It is a widely accepted assumption that the existence of residual stresses in soft biological tissues is causally related to growth and remodeling processes, which are initialized whenever deviations from the physiological state persist for more than a few days. By addition or removal of mass (growth) and/or the adaptation of material properties and structure (remodeling), biological tissues are able to restore former strain or stress levels. This implies the genesis of residual stresses. As an alternative to the approaches mentioned above, residual stresses can thus be taken into account in numerical simulations of arterial walls by considering them as a result of arterial growth and remodeling. Although the exact mechanisms of both processes are far from understood, it is assumed that growth and remodeling are substantially controlled by mechanical stimuli. For that reason, a multitude of publications with biomechanical background gave attention to the topic within the last decades. For an overview on the scientific progress, the chronological sequence of overview articles by Ambrosi, Ateshian, et al. (2011), Menzel & Kuhl (2012), Kuhl (2014), Cyron & Humphrey (2017) and Ambrosi, Ben Amar, et al. (2019) is recommended. Mainly two conceptually different methods developed over time for the computational modeling of growth. The first one relies on a multiplicative decomposition of the deformation gradient, and the second one makes use of the theory of constrained mixtures introduced by Humphrey & Rajagopal (2002).
By decomposing the deformation gradient into a growth part and an elastic part, Rodriguez, Hoger & McCulloch laid the foundations for the first concept in 1994. Essentially, they introduced a virtual intermediate state at which each material point is assumed to have grown without constraints imposed by neighboring points. When reassembling all material points as prescribed by the elastic part of the deformation, residual stresses evolve. The challenge of this approach is the definition of the growth part of the deformation on the basis of hypotheses on the source, the amount and the spatial characteristics of growth. Typically, the growth tensor is formulated as a function of one or more scalar variables associated to the amount of

growth, which in this work will be denoted as growth factors. In the following, some of the many publications in this context, amongst others those which were important for the development of this work, are highlighted. Taber & Humphrey (2001) formulated a solution for a thick-walled, pressurized and axially extended tube, where the growth tensor is chosen such that specified homeostatic values of the circumferential stress and the flow-induced shear stress are obtained. Already in 2002, more general forms for the growth tensor were proposed by Lubarda & Hoger, who considered isotropic, but also transversely isotropic and orthotropic growth, and by Imatani & Maugin, whose growth tensor includes a preferred direction which can adapt to changes of the stress state. Lubarda & Hoger (2002) introduced equations for the stress-driven evolution of the growth factors, which are still applied in similar form to date. As already done by Imatani & Maugin (2002), the evolution of growth is thereby often assumed to be driven by the Mandel stress instead of the 2$^{\text{nd}}$ Piola-Kirchhoff stress used by Lubarda & Hoger. With their algorithmic framework for the treatment of multiplicative growth within a finite element setting, Himpel, Kuhl, et al. (2005) and Kuhl, Maas, et al. (2007) took a step back towards a simplified form of the growth tensor, which describes isotropic growth by means of a single growth factor. Introducing the latter as internal variable, they solved the evolution equation at the integration point level by applying an implicit Euler backward scheme and computed the resulting extra part of the incremental tangent modulus. In order to simulate strain-driven ventricular dilation and stress-driven wall thickening in the heart, Göktepe, Abilez & Kuhl (2010) extended this framework to anisotropic growth. Their growth tensor is motivated micro-mechanically and includes three decoupled growth factors, which are associated to the in-plane muscle fiber orientation, its in-plane normal vector and the out-of-plane normal vector of the wall. Similarly, Sáez, Peña, et al. (2014) focused on wall thickening in a hypertensive human carotid artery as a result of strain- or stress-driven growth in radial direction. In such approaches, a local cylindrical coordinate system is required at each material point for the definition of the anisotropy directions of the growth tensor. Especially in irregular patient-specific geometries, it might be difficult to identify the radial, circumferential and axial directions at each point. Apart from that, it seems plausible that the anisotropy of growth at a certain point rather depends on the local mechanical field quantities than on the orientation in a notional coordinate system. That idea is the starting point for the generalized growth tensor proposed in this work and in preceding articles (Zahn & Balzani, 2017, 2018a). Assuming that growth in arterial walls is stress-driven, the anisotropy of the growth tensor is defined based on the local principal stress state. In the past few years, this thought has also been adopted by other authors working on anisotropic multiplicative growth. In the approach by Liu, Zhang, et al. (2019), a link between the principal directions of the Cauchy stress tensor and growth in the two directions perpendicular to the considered principal stress is presumed for the simulation of growth in an idealized two-layered aorta. However, by exclusion of axial growth and by neglecting the radial stress, this idea is not consistently realized. In a general local formulation, a special treatment of individual directions should rather be avoided to ensure the applicability in more general boundary value problems with differing signs and differing order of the principal stresses. Otherwise, the formulation is again not independent of structural information. The anisotropic growth model recently developed by Soleimani, Muthyala, et al. (2020) has still not been applied to arteries, but it meets this demand: without single exceptions, growth is assumed to evolve in the directions of the principal Cauchy stresses as long as those stresses do not exceed a certain compressive level. The amount of growth in the three directions is thereby distributed according to the ratio of the principal stresses. In contrast to all multiplicative growth models mentioned so far, the model by Soleimani, Muthyala, et al.

also includes a dependence on the concentration of nutrients, which is introduced as additional primary variable and described by a diffusion equation. Notwithstanding that growth is assumed to be driven mechanically to a large extent, the availability of nutrients is an indispensable basic requirement. Nevertheless, biochemical factors are not taken into account in this work.
Since the focus of this work is on multiplicative growth, the following paragraph is thought to just give a short overview on history and potential of constrained mixture models for growth and remodeling in soft biological tissues. For a better insight, a look at the introductions of the cited articles might be valuable. In constrained mixture models, each volume element is considered as a mixture of tissue constituents like elastin, collagen and smooth muscle cells, which are allowed to have different stress-free configurations, deposition times and turnover rates, but share the same displacement (Humphrey & Rajagopal, 2002). These frame conditions provide numerous opportunities to analyze the effect of single constituents and their evolving properties, orientations and volume fractions on the overall tissue behavior. This enables the formulation and verification of diverse hypotheses on growth and remodeling in arterial walls (Valentín & Holzapfel, 2012). For example, Zeinali-Davarani, Sheidaei & Baek (2011) investigated the effect of different forms of elastin degradation on the formation of an abdominal aortic aneurysm. In other approaches, not only solid constituents, but also the tissue's interstitial fluid is taken into consideration, such that the tissue consists of a constrained mixture of solid constituents forming a porous, permeable matrix and an unconstrained mixture of fluids flowing through (see e. g. Ateshian & Ricken, 2010). Due to the requirement of tracking past configurations over time, (constrained) mixture models are mathematically and computationally complex and their application has first been limited to membrane models or other simplified cases, which did not allow for the simulation of three-dimensional volumetric growth. A generalization of the theory to 3D finite element formulations has for example been proposed by Valentín, Humphrey & Holzapfel (2013), but, as reported by Braeu, Seitz, et al. (2017), such attempts have been restricted to isotropic growth. The development of homogenized constrained mixture models, where a homogenization over time is applied and only a single time-independent reference configuration is involved, enabled an extension to anisotropic growth by combination of the concept of mixture theory with a decomposition of the deformation gradient (Cyron, Aydin & Humphrey, 2016; Braeu, Seitz, et al., 2017). Another possibility for the simplification of a general constrained mixture model with respect to its mathematical treatment has recently been demonstrated by Latorre & Humphrey (2018). By replacing the evolution equations by an equivalent set of pre-integrated, time-independent equations, the long-term result of growth and remodeling in response to a persistent external load can directly be computed.

Whereas remodeling in its general meaning of an adaptation of material properties and composition is an inherent part of constrained mixture models, it is not included in models for volumetric, multiplicative growth following the concept of Rodriguez, Hoger & McCulloch (1994). Here, it depends on the constitutive equations to which extent remodeling can be taken into account. The highly nonlinear, anisotropic mechanical behavior of arterial tissues is usually described by material models which at least include the contributions of an isotropic ground substance and of two embedded families of load-bearing collagen fibers, whose orientation is indicated by vectors. Within the limits of such a material formulation, remodeling can be incorporated by means of a reorientation of the fiber vectors in response to the external loads. It is a well accepted assumption that the arrangement of the fibers is a result of continuous mechano-biological optimization processes, but as for growth, there is no general consent on the involved mechanisms. For materials with two or more, in general non-perpendicular fiber

orientations, it is often assumed that the fibers are arranged symmetrically in between the directions of (positive) principal strains or stresses. The components of the fiber vectors in the coordinate system spanned by the principal directions are thereby computed based on the ratio of the principal values. Strain-driven approaches in this context have for instance been pursued by Driessen, Wilson, et al. (2004), Driessen, Cox, et al. (2008) or Creane, Maher, et al. (2011), whereas Hariton, deBotton, et al. (2007a, 2007b), Olsson & Klarbring (2008) or Fausten, Balzani & Schröder (2016) preferred stresses. Some of the authors compared strain- to stress-driven fiber remodeling and detected that the results in general are similar, but, as expected, in detail differ due to the nonlinearity of the stress-strain relationship. Driessen, Wilson, et al. (2004) analyzed the effects of varying pressure load and axial strain in axisymmetric two-layered arteries with reorienting fibers. For the update of the fiber vectors, they defined a simple scalar evolution equation based on the angle between the existing and the target fiber orientation vectors. Driessen, Cox, et al. (2008) extended this approach to a material law with fibers that are dispersed around a main direction and applied it to an idealized artery and an aortic valve. With their application of a strain-based fiber reorientation algorithm to patient-specific carotid bifurcations, Creane, Maher, et al. showed that even the fiber patterns observed in complex geometrical regions can qualitatively be predicted if a dispersion of the fibers and its variability depending on the ratio of the principal strains are included. In the stress-based approach by Hariton, deBotton, et al. (2007a), which was applied to the model of a human carotid bifurcation (Hariton, deBotton, et al., 2007b), the final fiber distribution is computed iteratively in repeated simulations of the boundary value problem. In order to increase efficiency and stability of this approach, Fausten, Balzani & Schröder (2016) proposed an enhanced algorithmic scheme, where the iterative update of the fiber vectors happens in the loaded state and where the principal stresses are averaged over all Gauß points in a finite element. Olsson & Klarbring (2008) developed a model for combined growth and fiber reorientation, which is specialized to rotationally symmetric geometries and aims at a normalization of the circumferential and axial stresses towards predefined homeostatic values. With respect to the preferred angle between the fiber vectors and the circumferential direction, they adopted the hypothesis used by Hariton, deBotton, et al. (2007a) and described the reorientation by an evolution equation.

The framework for combined growth and fiber reorientation presented in this work has been developed with the aim to enable the approximation of residual stresses and collagen fiber distributions in numerical simulations of arterial walls based on mechanically founded assumptions on the underlying adaptation mechanisms. In Chapter 2, relevant aspects of the mechanical behavior of arterial walls and experimental observations on the regulation of strain or stress levels by means of growth and remodeling processes are summarized. It becomes apparent that growth in arteries should be considered as a complex multiaxial phenomenon, where interdependencies of conflicting regulative processes might be involved. The Chapters 3 and 4 provide the basis for a continuum mechanical description of growth by multiplicative decomposition of the deformation gradient and for the implementation of the proposed model in a finite element framework. Based thereon, a generalized framework for the phenomenological consideration of anisotropic, stress-driven growth is introduced in Chapter 5. By decomposition of the growth tensor into up to three parts, which are associated to the directions of the principal stresses and can adopt different basic forms, a large number of hypothetical growth mechanisms can be realized. For example, growth perpendicular to tensile principal stresses or growth in the direction of the compressive principal stress, which both could be motivated on the basis of

mechanical argumentation and/or experimental observations, are included in the general form of the growth tensor. In order to obtain a general local formulation, which should in principle not only be applicable to arteries idealized as cylindrical tubes, but also to arbitrarily shaped geometries, use of any kind of structural information, i. e. a dependence of the growth tensor on the axes of the cylindrical coordinate system, is avoided.
The redistribution of stresses in numerical simulations of soft biological tissues is strongly dependent on the arrangement of the reinforcing collagen fibers, which are the main load-bearing constituent. It is thus essential for the simulation of any stress-driven process to ensure a sufficiently realistic approximation of the fiber orientations. Apart from depending on the radial position within the vessel, the main orientation of collagen fibers in arterial walls can adapt over time if required. A model for the reorientation of the fibers in response to changes of the local stress state, which is the subject of Chapter 6, can capture these effects. In Chapter 7, numerical examples on the effects of different forms of growth and fiber reorientation on the stress state in idealized arterial segments are presented. For the assessment of different growth mechanisms with respect to their mechano-biological relevance, a method for the comparison of model variants on the basis of an objective function and optimized parameter sets is developed and applied. In this context, use of a special finite element for rotationally symmetric problems, which has only one spatial degree of freedom, significantly increases the efficiency of each single simulation. After the detailed analysis of the proposed framework on the basis of such idealized geometries, Chapter 8 gives an outlook to its application in patient-specific arteries and underlines its combinability with enhanced material models using the example of smooth muscle activity. In Chapter 9, the work and its main results are summarized and final conclusions are drawn.

2 Mechanical behavior of arterial walls

The aim of this chapter is to give a general overview on function and structure of arteries and on the fundamental characteristics of their mechanical behavior. This will provide the background knowledge required for the comprehension of the subsequent chapters. First, structure and material composition of arteries will be described from a mechanical point of view. Based thereon, essential mechanical properties of arterial walls will be explained. Apart from strong nonlinearity, anisotropy and quasi-incompressibility, the existence of residual stresses is an important point which has to be considered in enhanced numerical models of soft biological tissues. Residual stresses are directly connected with the adaptation of arteries to their mechanobiological environment. For this reason, some relevant aspects of arterial adaptation will finally be discussed.

2.1 Structure of the arterial wall

The arterial system consists of an enormous number of vessels with unique structural and functional properties. Its general function is the transport of blood away from the heart within two subsystems: the pulmonic and the systemic subsystem. In the smaller pulmonic subsystem, oxygen-poor blood is transported in low-pressure vessels from the heart to the lungs. The larger systemic subsystem, which requires a higher pressure, is responsible for the distribution of oxygenated, nutrient-rich blood from the heart to the rest of the body. The main vessel of the systemic subsystem, with a diameter of about 2.5 cm and a mean wall thickness of 2 mm in humans (Burton, 1954), is the aorta. It forms the trunk of the arterial tree, starting from which the arterial system branches into smaller and smaller arteries, arterioles and capillaries, finally arriving at diameters of about 8 µm (Burton, 1954). Along this tree, the microstructure of the arterial wall varies for reasons inherent to the system, but beyond that it also depends on age, animal species, local adaptations and diseases. Notwithstanding those differences, arteries can be categorized into elastic arteries, which have a relatively large diameter and are situated close to the heart, and muscular arteries located further at the periphery of the arterial system. By change of the arterial lumen, both types of arteries are involved in the regulation of the blood flow, but the relevant mechanisms differ. Muscular arteries, which have a higher content of smooth muscle cells, have the ability to actively adapt their diameter under the influence of neurohumoral stimulation (Levy & Tedgui, 1999, p. 8), for example in order to direct the blood to regions with increased need or to keep it away from regions with vascular injuries (Humphrey, 2002, p. 260). In elastic arteries, distention and contraction arise as a time-delayed, passive elastic reaction to the contraction of the heart, which causes pressure changes within the range of systolic and diastolic blood pressure (Humphrey, 2002, pp. 259–260). As the active arterial response will not be taken into consideration in this work, the focus will be set on elastic arteries.

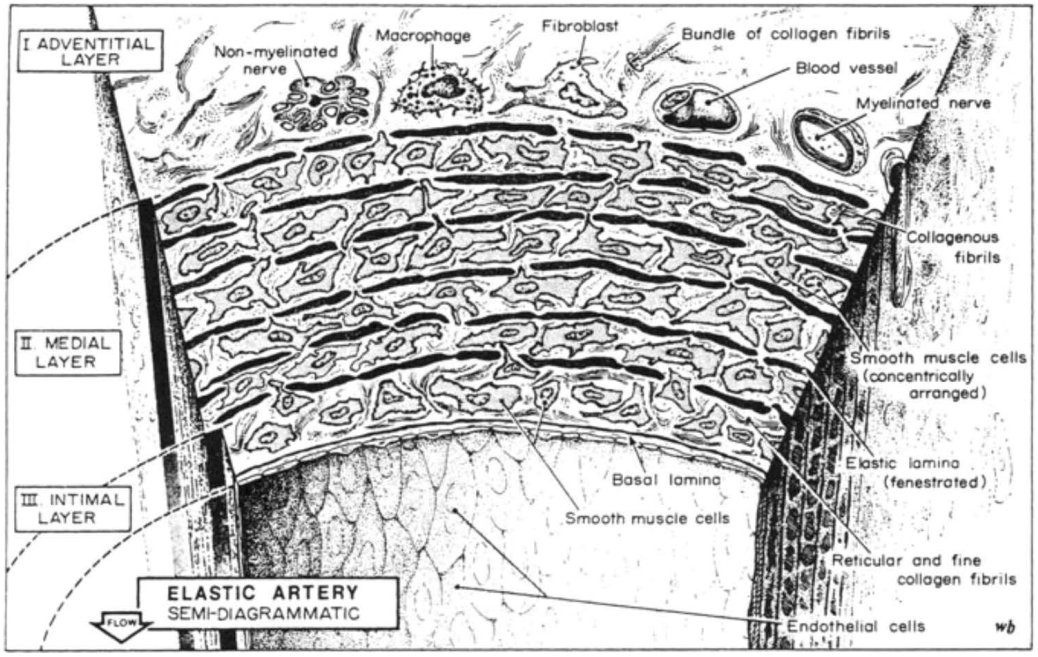

Figure 2.1: Arterial walls consist of three specific regions which are separated by elastin lamellae and can be distinguished by their constituents. The schematic illustration of a typical elastic artery shown here is adopted from Rhodin (2014).

Common to all types of arteries is that they are composed of three distinguishable, concentric cylindrical layers, which are, beginning from the inside of the vessel, denoted as intima, media and adventitia. A schematic illustration of the wall structure of a healthy elastic artery is shown in Fig. 2.1. The main constituents and characteristics of the individual layers will be described in the following paragraphs.

Intima. The innermost layer of the arterial wall is similar in most elastic and muscular arteries and consists of a single layer of endothelial cells attached to a thin basal lamina. This collagen-dominated lamina provides some structural support to the wall but primarily serves as adherent meshwork enabling the growth of the endothelial cells (Humphrey, 2002, p. 255), which themselves are mechanically negligible (Burton, 1954). Covering all surfaces in contact with the blood, the endothelium forms a smooth and continuous layer of flat polygonal cells that are elongated in the direction of the blood flow. It enables the movement of substances, ions and metabolites from the lumen into the vessel wall. Within two to three years, the endothelium is completely renewed by replication of the endothelial cells.
In many cases, especially in young and healthy individuals, endothelium and basal lamina are directly applied to the internal elastic lamina, which marks the begin of the medial layer. At specific locations, for example in the aorta, an additional subendothelial layer, predominantly built of smooth muscle cells, elastic and collagen fibers and proteoglycans may exist. Furthermore, the intima is known to thicken and stiffen with increasing age, a process which is accompanied by the deposition of atherosclerotic plaque. With such age-induced and pathological changes, the contribution of the intima might become mechanically significant (Holzapfel, Gasser & Ogden, 2000).

Media. A fenestrated sheet of elastin, the internal elastic lamina, separates the intima from the media, which is formed by smooth muscle cells embedded in an extracellular matrix composed of collagen and elastin fibers. The external boundary of the media is likewise marked by the external elastic lamina. The fenestration in those laminae allows for the radial transport of metabolites. In elastic arteries, the media consists of multiple well-defined fiber-reinforced layers bordered by further fenestrated elastic laminae. Each layer including the adjacent lamina is seen as structural and functional unit of uniform thickness of 12–17 µm regardless of artery and animal species (Wolinsky & Glagov, 1967; Clark & Glagov, 1985; Levy & Tedgui, 1999). The number of lamellar units is roughly proportional to the radius of the vessel and thus decreases towards the periphery with decreasing vessel size. There are 40–60 such units in a human aorta depending on age, but only eight in a rat aorta (Levy & Tedgui, 1999). Smooth muscles and fibrous extracellular matrix in the medial layers form a complex, organized network with a helical orientation relative to the vessel axis. The slope of this helix is rather small, such that the fibrous material is almost oriented in circumferential direction. Due to this structure, the media is endowed with high strength and resilience and can therefore be seen as the mechanically most significant layer in healthy arteries (Holzapfel, Gasser & Ogden, 2000). According to Wolinsky & Glagov (1967), collagen and elastin sum up to about 60 % of the dry weight of the media in adult mammals, whereby the ratio between both depends on the specific artery. About 90 % of total arterial collagen is assembled into cylindrical-shaped fibrils with diameters of 10–500 nm, which can be combined into fibers of 0.1–100 µm thickness and finally into fiber bundles. Collagen organized in such a manner is one of the central load bearing components contributing almost the entire passive resistance to circumferential and axial loading. In contrast to that, elastin fibers are responsible for storing the majority of elastic energy and provide high flexibility and resilience of the arterial wall at low loads (Robertson & Watton, 2013).

Adventitia. The adventitia mainly consists of fibroblasts, i. e. collagen producing cells, in a collagenous extracellular matrix with admixed elastin. It contains nerves and – if the media has more than 29 lamellar units – the vasa vasorum, a network of small blood vessels required for the supply of the wall if the supply from the intimal surface through the arterial layers is not sufficient (Humphrey, 2002). The thickness of the adventitia amounts to about 10 % of the entire wall thickness in elastic, and 50 % in muscular arteries, but its outer limit is often difficult to define since it merges with the perivascular connective tissue (Levy & Tedgui, 1999; Humphrey, 2002). As in the media, the collagen fibers are arranged in helical structures, but in the adventitia they tend to be oriented in axial and not in circumferential direction. However, their orientation varies across the wall thickness and along the vasculature between those two limits (Robertson & Watton, 2013). In the unloaded state and at low internal pressure, the collagen fibers are undulated and do not significantly contribute to the strength of the arterial wall. The stiffness of the adventitia becomes prominent at higher pressures, when the fibers reach their straightened length. Then, the adventitia protects the vessel against overdistension and rupture (Holzapfel, Gasser & Ogden, 2000; Humphrey, 2002).

Apart from cells and extracellular matrix, soft biological tissues contain a high amount of liquids. According to Humphrey (2002, p. 268), a large portion adding up to 70–80 % of the wet weight of the arterial wall is water. As well as the organized arrangement of the solid constituents, this aspect of the material composition has a major effect on the mechanical behavior of arterial walls, which is the subject of the following section.

2.2 Basic mechanical properties

The survey of the structure of the arterial wall in Sec. 2.1 points out that the individual wall components are not arranged randomly but with specific orientations, which can be assumed to be structurally and mechanically well-founded. It can be hypothesized from this structure that the mechanical behavior of arterial walls is relatively complex, and indeed experiments confirm that media and adventitia, the mechanically relevant layers, behave nonlinearly and different in axial and circumferential direction (see e. g. Maltzahn, Warriyar & Keitzer, 1984; Shadwick, 1999; Holzapfel, Sommer, Gasser, et al., 2005). This anisotropy, illustrated exemplarily in Fig. 2.2 for the media of human coronary arteries, can be attributed to the orientation of the collagen fibers, which are the main load-bearing constituent. With fibers oriented primarily around the circumferential direction, the media shows an increased stiffness and thus higher stresses in circumferential than in axial direction. The strong nonlinearity of the material response can be attributed to the fact that collagen fibers have a crimped and wavy nature in the load-free state (Robertson & Watton, 2013) and do not become activated till a certain value of stretch is reached in the depicted uniaxial tension tests.

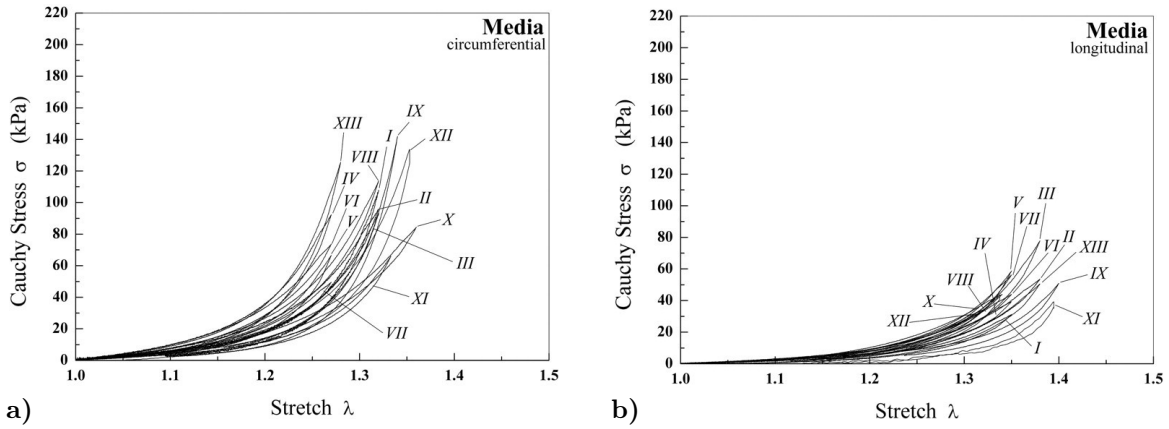

Figure 2.2: Soft biological tissues are characterized by large deformations and a highly nonlinear, anisotropic material behavior. This is attested by the shown graphs, which originate from Holzapfel, Sommer, Gasser, et al. (2005, Fig. 3) and illustrate the results of uniaxial tension tests carried out on media samples of 13 undiseased human coronary arteries in **a)** circumferential and **b)** longitudinal (i. e. axial) direction. The stretch λ is computed as ratio of deformed and initial length.

As adumbrated by the curves in Fig. 2.2, which have different loading and unloading paths, arterial tissues do not behave fully elastically. Humphrey (2002, pp. 280 ff.) reports that their passive response is characterized by hysteresis under cyclic loading, relaxation under constant strain and creeping under constant loads, which suggests use of viscoelastic constitutive equations. However, after preconditioning in several load cycles, the material response turns out to be virtually repeatable. Due to their exposure to cyclic hemodynamic loads, the behavior of arteries in physiological situations can therefore be regarded as pseudoelastic (Humphrey, 2002, 2008).

Another reasonable assumption for many loading conditions, including isothermal conditions and near-physiological loads, is the assumption of incompressibility (Humphrey, 2002, pp. 268–269).

Because of the high content of water, arterial walls reveal a nearly volume conserving behavior as already stated by Carew, Vaishnav & Patel (1968). More recently, the incompressibility assumption has however been called into question, for example by Yosibash, Manor, et al. (2014)/Yossef, Farajian, et al. (2017), who detected relative volume changes of 2–6 % in the physiological pressure range for porcine common carotid, saphenous and femoral arteries. A revision of the incompressibility assumption is also postulated by Nolan & McGarry (2016), who report a Poisson's ratio of 0.44 for the ground matrix of ovine aortic tissues.

The mechanical behavior of arterial walls is substantially controlled by the existence of residual stresses. Already in 1960, Bergel had reported that arteries shorten if they are excised from the body and unroll themselves if they are split open longitudinally, and concluded that even if unloaded, arteries are not free of stress. Beginning with the work of Fung et al. and Vaishnav et al. since 1983, residual stresses in blood vessels have been examined at a progressive rate, for example by Chuong & Fung (1986), Vaishnav & Vossoughi (1987), Takamizawa & Hayashi (1987), Fung & Liu (1989) or Fung (1991). The observation that arterial rings bend up after a radial cut implies that compressive circumferential stresses are present in the inner, and tensile circumferential stresses in the outer part of the wall. The hypothesis of compressive stresses near the lumen is supported by the observation that the internal elastic lamina is more wavy in the intact load-free than in the physiological and cut configurations (Humphrey, 2002, p. 271). Actually, Humphrey suspects that the constituents made of elastin have a dominating role in this context since collagen fibers are highly undulated in the load-free state throughout the entire vessel and can thus not contain tensile residual stresses as occurring in the outer part of the wall. Of course, residual stresses affect the mechanical behavior and the distribution of the load-induced stresses over the wall thickness. The common assumption that the reference configuration, which as highlighted in Chapter 3 is essential for the definition of stress and strain, is stress-free, can thus not be applied to arterial walls. In order to quantify the amount of residual stresses, the opening angle was introduced. The illustration by Fung & Liu (1989) given in Fig. 2.3 c) shows that already in the past, the opening angle was known to depend on many factors: in addition to the longitudinal position within the artery and the

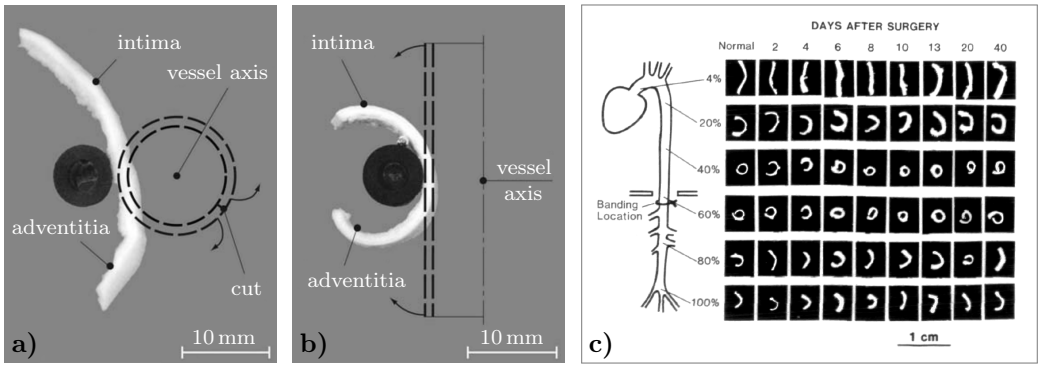

Figure 2.3: As confirmed by the deformations of **a)** a circumferential strip and **b)** an axial strip excised from a human aorta, both figures formally adapted from Holzapfel, Sommer, Auer, et al. (2007, Fig. 7), residual stresses in arteries are three-dimensional. The deformation of **c)** radially sliced rings of rat aortas, adapted from Fung & Liu (1989, Fig. 2), shows that they additionally depend on the position in the body and on the blood pressure, which has artificially been increased in a surgery by banding the abdominal aorta with a metal clip.

trend of the blood pressure, also species, age, gender, smooth muscle activity and other diseases apart from hypertension, for example diabetes and atherosclerosis, are significant according to Matsumoto & Hayashi (1996a) and Humphrey (2002, p. 277). By now, further findings confirm that the suitability of the opening angle for a quantification of residual stresses is limited. Though one radial cut, regardless of its position, has been observed by the group of Fung to be enough to release most of the residual stress (Humphrey, 2002, p. 274), later experiments revealed that this indeed only holds for cuts in radial direction. Since 1993 the opening angle is known to be layer-specific, which means that an arterial ring without layer-wise separation, i. e. circumferential cuts, is by no means stress-free (Matsumoto & Hayashi, 1996a; Humphrey, 2002). Holzapfel, Sommer, Auer, et al. (2007) impressively point out that residual stresses have to be regarded as a fully three-dimensional property of arterial tissues. Just as circumferential strips, also axial strips deform considerably due to the inherent residual stresses as exemplarily shown in Fig. 2.3 a) and b) for non-separated strips from a human aorta. A separation of the individual layers reveals that those deformations are layer-specific as well.

In the in vivo state, most arteries are significantly stretched in axial direction. For rat, canine and porcine aortas, values between 20 % and 60 %, strongly varying with the position in the aortic tree, have been reported according to Humphrey (2002, p. 287), for example by Han & Fung (1995). For this reason, a longitudinal contraction of arteries excised from the body is observed. As suggested by the experiments of Holzapfel, Sommer, Auer, et al. (2007), this contraction can only be seen as an average reaction to the excision just as the opening angle of the non-separated artery can only represent an average measure of residual stresses in circumferential direction. Considering the axial in vivo stretch together with the large extension in circumferential direction due to normal systolic and diastolic blood pressures of 120 mmHg and 80 mmHg, the deformations in arteries are clearly large even without consideration of movements as for example bending of the extremities or pathological conditions like hypertension or during clinical treatment. It is therefore essential to apply the theory of finite deformations for the numerical analysis of arterial walls.

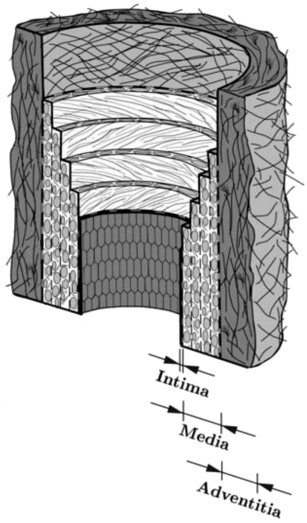

Intima:
- mechanically negligible in healthy arteries
- thickens and stiffens with progressing age and atherosclerosis

Media:
- high strength and resilience due to well-defined layers reinforced by collagen and elastin fibers
- mechanically most significant layer in healthy arteries

Adventitia:
- increased stiffness at high pressures when collagen fibers are straightened
- limits acute overdistension

Figure 2.4: Relevance of the arterial layers in healthy, elastic arteries for the passive mechanical response. The schematic illustration of the arterial wall is extracted from Holzapfel, Gasser & Ogden (2000, Fig. 1).

In this work, an existing orthotropic material model for soft biological tissues by Balzani, Neff, et al. (2006) will be employed for the fundamental relation between stress and strain. Building thereon, arterial adaptation processes introduced in the subsequent section will be examined based on a phenomenological description of growth and fiber reorientation. For a motivation of the underlying material model, the relevant information regarding the mechanical relevance of the individual arterial layers is summarized in Fig. 2.4. If only physiological or nearly physiological conditions in healthy arteries are considered, a hyperelastic formulation in the framework of large strains is a reasonable choice. With restriction to a phenomenological description of the passive material behavior, the anisotropy can be incorporated by idealizing the arterial layers as isotropic ground materials with embedded, reinforcing fibers representing the collagenous constituents. In order to capture the helical arrangement of the fibers, at least two fiber families with opposite orientation, symmetrically arranged with respect to the circumferential direction, have to be taken into account. According to Schriefl, Zeindlinger, et al. (2012), it is not even necessary to include more than two fiber families. Nonetheless, the simplest implementation of this assumption disregards the fact that fibers usually are dispersed around a main orientation. As for example listed by Holzapfel, Niestrawska, et al. (2015), many material models accounting for fiber dispersion have already been proposed, for instance by use of generalized structural tensors as explained by Ogden (2017). An extension of the model by Balzani, Neff, et al. (2006) towards a more realistic description is thus conceivable. Details on this model, amongst others on the satisfaction of the incompressibility condition, are given in Sec. 7.1. The incorporation of residual stresses, which is indispensable for a qualitatively realistic simulation of the material behavior of arterial tissues, is directly linked to the main concern of this work, the modeling of growth and fiber reorientation. Indeed, residual stresses can be seen as a result of continuous adaptation of the living tissue to its mechanobiological environment, triggered by the aim of keeping up optimal functionality.

2.3 Arterial adaptation

Beginning with its formation in the embryo over normal development and aging up to disease and injury, the vasculature is subject to many different changes. During normal maintenance in mature tissues, referred to as homeostasis, all constituents are slowly replaced in a regular, balanced manner without changes of overall mass, tissue composition or mechanical properties. Thereby, the turnover rates of the individual constituents are different: about 0.02 % of endothelial cells and 0.06 % of smooth muscle cells are replaced per day, collagen has a half-life in the order of weeks to months and the half-life of elastin is comparable to the lifespan of the organism (Langille, 1993; Humphrey, 2002, p. 499), which means that the capacity of repairing elastin components is limited (Robertson & Watton, 2013). Persistent deviations from the homeostatic state can lead to markedly increasing turnover rates and result in a significant modification of mass, composition and properties of the arterial wall. For example, collagen can be produced within 10 to 20 minutes in the case of disease or injury and also elastin, which in general is mainly synthesized around time of birth, may be produced or degraded much faster in pathological than in physiological situations (Humphrey, 2002, pp. 514–515). The tissue adaptation which takes place in response to altered environmental conditions can be classified into two different processes: growth and remodeling. In the context of this work, the term “growth” is used for the addition of new material equal to the material which is

already present, that is to say without changes in composition or density. For sure, growth is not in general restricted to volumetric, i. e. density preserving increase in mass, but for soft biological tissues this restriction is often used (e. g. by Rodriguez, Hoger & McCulloch, 1994; Himpel, Kuhl, et al., 2005, and in other publications mentioned by them) and is self-evident if growth is assumed not to change the tissue properties. A decrease in mass at the same conditions is referred to as negative growth or atrophy. "Remodeling" in contrast is meant to describe processes that change the internal structure of the tissue by reorganization of the existing constituents. Such adaptations are thus associated to changes of the material properties. Within the context of the phenomenological material model by Balzani, Neff, et al. (2006), remodeling is incorporated by allowing the collagen fibers to reorient. A dependency of the material parameters on the mechanical situation, as proposed by Rachev, Stergiopulos & Meister (1998) for arteries subjected to hypertension, will indeed not be considered. To establish the connection between adaptation and residual stresses, the notion of incompatible growth needs to be explained. Briefly, when modeling growth in the framework of continuum mechanics, each tissue constituent is allowed to grow independently, such that the continuity of the entire structure would be lost if there were no internal forces restoring compatibility. As these forces exist independent on external loads, they give rise to residual stresses, which means that residual stresses can automatically be taken into account if suitable growth processes are modeled. Details on incompatible growth are given by Skalak, Zargaryan, et al. (1996), and also Humphrey (2002, pp. 507 f.) treats this subject in a comprehensible way.

Growth and remodeling are thought to be fundamentally controlled by mechanical stimuli. They occur whenever functional changes, that is deviations from the homeostatic state, for example altered blood pressure or flow, persist for more than a few days. Such changes may occur in phases which require adjustment of the vascular supply, for example during pregnancy, when muscle tissues adapt to intensified exercise or disuse, or during pathologic disorders (Langille, 1993). Many studies deal with the question of how stresses or strains are connected with changes of structure and function of single cells, matrix constituents or entire blood vessels. In the following paragraphs, some important results, mostly as reported by Humphrey (2002) and Matsumoto & Hayashi (1996a), are summarized. Additional information on the mechanobiology of cells can be found in the review article published by Wang & Thampatty (2006).

Adaptation of cells and fibers to changes in stress or strain. In vitro studies on endothelial cells show that the level of shear stresses applied to the cells is linked to the extent of their elongation in the direction of flow. Moreover, the shear stress affects the production of molecules by endothelial cells: an increase in shear stress leads to upregulation of vasodilators and downregulation of vasoconstrictors. This is consistent with the in vivo observation that arteries dilate if blood flow is increased and constrict if flow is reduced (Humphrey, 2002, pp. 524 f.). As examined by Langille (1993) on the basis of denuded rabbit carotid arteries, an intact endothelium, which gets lost at shear stresses larger than 40 Pa (Humphrey, 2002, p. 524), can even be assumed to be the prerequisite for these adaptations. If subjected to 10–20 % of cyclic uniaxial stretch, endothelial cells increase their rate of replication and elongate in the direction orthogonal to the direction of stretch (Humphrey, 2002, p. 528). Assuming that in blood vessels with physiological conditions, the circumferential stretch is higher than the axial stretch, this is in line with the observed orientation of the endothelial cells in the direction of blood flow.

Smooth muscle cells are known to have two phenotypes which usually depend on the age of the organism. During vascular development, smooth muscle cells synthesize proteins constituting the extracellular matrix. In mature arteries however, they are contractile and regulate the blood pressure, but in case of damage or disease, they are able to revert back to the synthetic phenotype (Humphrey, 2002, p. 373). If smooth muscle cells are cultured for a few days at a non-physiological pressure of 10 mmHg, they return to the synthetic phenotype, if cultured at 80 mmHg they remain contractile (Humphrey, 2002, p. 538). The experiments performed by Leung, Glagov & Mathews (1976) on smooth muscle cells, apparently of synthetic phenotype, suggest a direct relationship between mechanical forces and the production rate of connective tissue components. The researchers isolated smooth muscle cells from the media of a rabbit aorta and cultured them on elastin membranes, which were either kept stationary, subjected to cyclic stretches of 10 % or agitated without stretching. Cyclic stretching led to a two- to fourfold increase in synthesis of collagen and other matrix components. As indicated by Humphrey (2002), the effect of stress or strain on smooth muscle cells has been shown in many further studies, but the results are not always consistent, which might partly be due to use of cells from different vessels in different species of different age, analyzed in different experiments with nonuniform realization and evaluation. The existence of an anyhow response of cells to stress or strain however is undeniable and has also been observed for fibroblasts, which are the primary producers of extracellular matrix in the adventitia of mature arteries (Humphrey, 2002, p. 537).
The ability to react to mechanical stimuli has also been confirmed for fibers within soft connective tissues. In different studies, for example by Tower, Neidert & Tranquillo (2002) or Wang, Brewster & Gleason Jr. (2013), uncrimping and subsequent reorientation of collagen fibers are examined. Recently, Krasny, Morin, et al. (2017) performed uniaxial tension tests on circumferential, axial and diagonal strips from rabbit carotid arteries and found out that regardless of the initial orientation, collagen fibers in the adventitia reorient towards the direction of the load. This behavior is in contrast to the less distinctive reorientation of adventitial elastin and medial collagen and elastin fibers, which can virtually be predicted based on the deformed geometry of the specimens.

Adaptation to changes in blood flow. By now, the hypothesis of a two-step mechanism of arterial adaptation to changes in blood flow, as elaborated by Rodbard (1975), is commonly accepted. In a first step, an immediate physiological adjustment of the vascular caliber by vasodilation or vasoconstriction takes place. A dilation in response to increased flow occurs within seconds to minutes, whereas the constriction of vessels subjected to reduced blood flow is much slower and can take several hours as reported by Langille (1993) for sheep carotid arteries. If the changes in blood flow persist, the arterial wall starts to adjust anatomically, amongst other by restructuring of the media (Langille, 1993). The experimental findings suggest that the adaptation mechanisms aim at the restoration of a constant wall shear stress of about 1.5 Pa in large arteries (Kamiya & Togawa, 1980; Langille, 1993; Humphrey, 2002, pp. 552–553) and are mediated by the endothelium, which detects flow-induced deviations from this value. Indeed, acute vascular response is only observed if the endothelium is intact (Langille, 1993; Humphrey, 2002, p. 552) and thus able to send control signals to the smooth muscle cells. Structural changes due to persistently altered blood flow do not only manifest themselves by changes in diameter, but also by changes in the vessel length or rather the in vivo prestretch (Humphrey, 2002, pp. 558–559). This emphasizes the multiaxial character of growth and remodeling and the associated residual stresses.

Adaptation to changes in blood pressure. A detailed review of the mechanical response of the arterial wall to hypertension, with special reference to the rat thoracic aorta, is presented by Matsumoto & Hayashi (1996a), and also the textbook by Humphrey on cardiovascular solid mechanics is a valuable reference in which the author provides additional information on side aspects as for instance different methods for the artificial elevation of blood pressure in animal experiments (Humphrey, 2002, pp. 367–373). The most evident arterial reaction to an elevated blood pressure is an increase of the wall thickness, primarily caused by thickening of the media. Several studies, for example by Wolinsky (1970) or Matsumoto & Hayashi (1996a) showed that the number of lamellar units in the media thereby remains unchanged, see Fig. 2.5. The longitudinal sections through the aortic wall given in that figure furthermore imply that the increase in thickness of the medial layers especially occurs near the inner surface of the wall, where the effect of the elevated pressure on the mechanical fields is more pronounced. This is in agreement with the assumption that the wall of hypertensive arteries thickens in order to counteract an increase of the circumferential stress or even to maintain it at a constant level (Matsumoto & Hayashi, 1996a; Humphrey, 2002, p. 540). The rat experiments by Matsumoto & Hayashi suggest that only the outer but not the inner diameter of the vessel correlates with the in vivo blood pressure, such that the arterial lumen, which is supposed to correlate with flow rate and shear stress, remains constant in case of pressure changes.

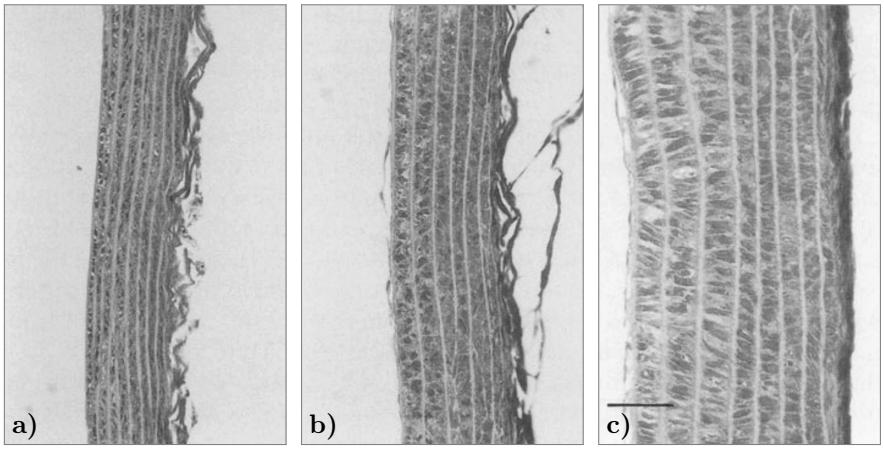

Figure 2.5: Longitudinal sections through the aortic wall in **a)** a normotensive rat with a systolic blood pressure of $p_{\text{sys}} = 145\,\text{mmHg}$, **b)** a hypertensive rat with $p_{\text{sys}} = 200\,\text{mmHg}$ and **c)** a severely hypertensive rat with $p_{\text{sys}} = 240\,\text{mmHg}$. The figure is taken from Matsumoto & Hayashi (1996a, p. 102), who indicate that the enlargement scale is the same in each part of the figure.[1] It is perceptible that hypertension is accompanied by increased thickness of the medial layers, especially towards the intima, which points to the left.

With respect to the structural changes, Humphrey indicates that the observations are diverse and partly contradictory. Thickening of the arterial wall seems to be primarily caused by hypertrophy, i. e. increase in size of the smooth muscle cells, but also the absolute amounts of collagen and elastin increase as e. g. shown by Ooshima, Fuller, et al. (1974) and Nissen, Cardinale & Udenfriend (1978) for collagen production in hypertensive rat aortas. Whereas

[1] With comparison to the indicated primary source Matsumoto & Hayashi (1996b), which though just contains smaller cutouts of the figure, this statement should be questioned. There, the thickness ratios of the aortic walls exposed to hypertension to those with normal blood pressure are less pronounced.

some researchers report a more or less constant percentage of wall constituents, others observed a decreasing fraction of collagen due to a disproportionate increase in smooth muscle content. Several publications reveal that also the adventitia thickens (Humphrey, 2002, p. 376). Again it has to be stated that a comparison of different species, arteries and experimental setups, for example concerning the duration of the induced hypertension or the age at which it is induced, make it difficult to compare different findings. Moreover, arterial adaptation to hypertension is a time-dependent process: wall thickening happens very rapid, but there are also chronic changes acting on a slower time scale. Matsumoto & Hayashi (1996a) point out that the elastic modulus, which at hypertension temporarily increases due to the nonlinearity of the material behavior, is restored to its normotensive value within 16 weeks. As a consequence of the associated nonuniform growth and remodeling processes, the observed opening angle changes over time as already documented by Fung & Liu (1989) and shown in Fig. 2.3 c). Changes in blood pressure can thus be supposed to always have an effect on the residual stress state.

Another fact pointing out that it is far from clear why exactly arteries adapting to non-physiological conditions behave as it is observed, is the unexpected behavior in response to hypertension stated for the axial direction. Whereas stresses and strains in circumferential direction seem to be gradually restored to their physiological values, axial in vivo stress and strain in hypertensive arteries are significantly lower than in normal conditions (Wolinsky, 1970; Matsumoto & Hayashi, 1996b; Humphrey, Eberth, et al., 2009). According to Matsumoto & Hayashi (1996a, pp. 101 f.), this could have different reasons. On the one hand, pure radial growth, leading to an increase of the wall thickness without any effect on the axial direction, might not be realistic as amongst others speculated by Langille (1993). An enlargement of the medial smooth muscle cells, which are mainly oriented in circumferential direction, likely involves volume increases in both, the radial and the axial direction, such that axial stress and strain are reduced by a non-visible elongation of the vessel, which is still subjected to the same boundary conditions. On the other hand, the reduced in vivo stretch could imply that restoration of increased stresses or strains has priority over restoration of stresses or strains which have fallen below the homeostatic level. In particular, a decreased axial in vivo stretch might be less serious than an increased circumferential stress. Indeed, as summarized in the following paragraph, there are studies which confirm differences in the reaction to reduced and increased axial stretches.

Adaptation to changes in axial stretch. If deviations from the physiological axial in vivo stretch occur, the ability of the tissue to adapt seems to depend on the sign of these deviations. As shown by Jackson, Gotlieb & Langille (2002), an increased axial stretch in rabbit carotid arteries is regulated within just a few days by compensating tissue growth and remodeling, whereas a reduced axial stretch does not lead to a normalization. In contrast, those arteries even became tortuous although 30 % of axial strain were left. The adapting arteries did not exclusively grow in axial direction, but also showed an increase in wall thickness and circumference, which can not be justified by reduced blood pressure and flow since both remained unchanged in the experiments. It can thus be suspected that normalization of elevated axial stretch is favored over maintenance of the homeostatic wall shear and circumferential stress, provided that those stresses do not increase. Based on the results by Jackson, Gotlieb & Langille (2002) and also confirmed by the experiments of Han, Ku & Vito (2003) and Humphrey, Eberth, et al. (2009), the compensating growth and remodeling processes in response to elevated axial stretch can be assumed to be much faster than those provoked by increased blood flow or pressure.

The adaptation is characterized by significant increase of the replication rates of endothelial and smooth muscle cells and by increased production of elastin and collagen. Since they are also observed in the absence of an endothelium, Jackson, Gotlieb & Langille suppose that those processes are controlled by the smooth muscle cells.

Adaptation during aging. Apart from adaptations due to disease or injury, normal gradual changes in mass and structure are known to occur during aging. The formation of new blood vessels in the embryo and other remodeling processes before maturation are thereby explicitly excluded and not accounted for in this work because the circumstances at this time of development are completely different (Langille, 1993; Humphrey, 2002, p. 554). As summarized by Humphrey (2002, pp. 578 f.), the intima tends to thicken and become more fibrotic with age. In the media, which also thickens, an increasing amount of collagen is deposited and elastin is gradually degraded. For the adventitia, Humphrey indicates that the changes are less specific. Altogether, age-related growth and remodeling result in reduced distensibility, increased stiffness and a rising thickness to radius ratio. For example, Langille (1993) mentions that the abdominal aorta of adults gradually increases in diameter by 40–50 %. At the same time, a significant age-correlated decrease in axial prestretch is observed (Horny, Adamek, et al., 2012).

In summary, all these observations indicate that unidirectional growth, which might be suited to normalize single strain or stress components deviating from their homeostatic values, seems not to be possible in arteries. Instead, growth has to be considered as a multiaxial process involving the radial, circumferential and axial directions. However, there seem to be connections between the following functional changes, mechanical quantities and geometric vessel properties: Altered blood flow mainly affects wall shear stress, which is regulated by an adaptation of the arterial lumen. Changes in blood pressure are associated to changes in circumferential stress and strain, which can be normalized by adaptation of the wall thickness. Axial in vivo prestretch, which is related to the axial stress, can be regulated by an adaptation of the vessel length. Of course, there are interdependencies which might prevent the restoration of the homeostatic state for each particular strain or stress. In these cases, restoration of those strains/stresses which exceed their homeostatic values might be assumed to have priority, even if it happens at the expense of a reduction of other strains/stresses below their homeostatic values. Adaptation in arteries can thus really be considered as an optimization problem, the aims of which are still unknown to a large extent.

3 Continuum mechanical foundations

The basic concept for the description and analysis of all physical phenomena studied in this work is the framework of continuum mechanics. Within this framework, it is assumed that all quantities of interest, such as displacements or stresses, can be described by continuous functions if the length scale of the body of investigation is considerably larger than the length scale of its microstructure. This separation of scales allows to average locally heterogeneous material properties into homogeneous fields, such that no detailed modeling of composition, behavior and properties of the microstructural components is required in order to still obtain an adequate approximation of the macroscopic material behavior. With diameters in the order of micrometers, collagen fibers are considerably smaller than the wall thickness of elastic arteries, which is in the order of millimeters. For the analysis of stresses within the arterial wall, the ratio of micro- and macroscopic length scales is thus smaller than 0.01. Below this well-tried experience value, the continuum approach is applicable (Humphrey, 2002, p. 68).
In this chapter, the fundamentals of continuum mechanics are summarized, primarily based on the relevant parts in the textbooks by Wriggers (2008), Humphrey (2002), Holzapfel (2000) and Altenbach (2012). For the extension of the basic equations to solids with a growing mass, the research papers by Himpel, Kuhl, et al. (2005) and Kuhl, Maas, et al. (2007) have been used as main reference.

3.1 Kinematics

Basis of all continuum mechanical considerations are the kinematics, a branch of mechanics which addresses the geometrical description of the motion and deformation of bodies by means of the variables time and position. After the introduction of basic kinematic equations, their extensions necessary within the framework of multiplicative growth will be explained.

3.1.1 Basics of kinematics

For the description of the motion and deformation of a continuum, the physical body $\mathcal{B} \subset \mathbb{R}^3$ is considered as a set of continuously distributed material points in the Euclidian space $\mathbb{R}^3$. In its reference configuration at $t = t_0$ prior to deformation, the position of a material point within body $\mathcal{B}$ is defined by a position vector $\boldsymbol{X}$, see Fig. 3.1. This configuration is also referred to as material or Lagrangian configuration. The transformation of the body to its deformed state at a particular point in time $t \in \mathbb{R}^+$ is described by a one-to-one, i. e. invertible mapping $\boldsymbol{\varphi}(\boldsymbol{X}, t) : \mathcal{B} \to \mathcal{S}$, which maps each material point $\boldsymbol{X} \in \mathcal{B}$ to its counterpart $\boldsymbol{x} \in \mathcal{S}$ in the

actual configuration $\mathcal{S} \subset \mathbb{R}^3$, also denoted as spatial or Eulerian configuration. The location of material point $\boldsymbol{X}$ at a fixed time t is thus given by

$$\boldsymbol{x} = \boldsymbol{\varphi}(\boldsymbol{X}, t) = \boldsymbol{\varphi}_t(\boldsymbol{X}) \tag{3.1}$$

and the displacement vector associated to that point is

$$\boldsymbol{u}(\boldsymbol{X}, t) = \boldsymbol{x} - \boldsymbol{X} \tag{3.2}$$

as illustrated in Fig. 3.1. Here, the referential or Lagrangian approach is adopted which means that the continuum mechanical fields are considered as functions of the material points $\boldsymbol{X}$ in the reference configuration. In contrast, especially useful in fluid mechanics, the spatial or Eulerian approach formulates mechanical fields as functions of the actual coordinates $\boldsymbol{x}$. For many quantities which exist in both configurations, capital Roman letters, e. g. $\boldsymbol{X}$, V, will be used for the reference configuration and small Roman letters, e. g. $\boldsymbol{x}$, v, for the actual configuration.

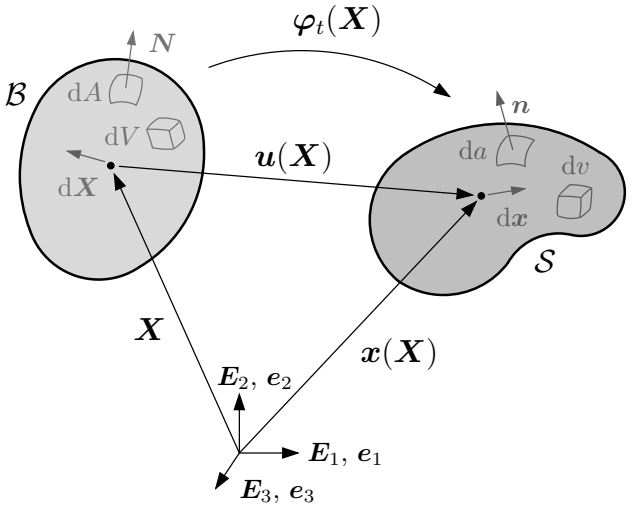

Figure 3.1: Illustration of a physical body in its undeformed reference configuration $\mathcal{B}$, where the position of a material point is given by vector $\boldsymbol{X}$, and in the deformed, actual configuration $\mathcal{S}$ with position vector $\boldsymbol{x}$. Infinitesimal line, area and volume elements are displayed in gray. When using orthonormal Cartesian basis vectors $\boldsymbol{E}_i/\boldsymbol{e}_i$, the reference and actual coordinate systems can be chosen to coincide.

The relation between two infinitesimal line elements $\mathrm{d}\boldsymbol{x}$ and $\mathrm{d}\boldsymbol{X}$ in the actual and reference configuration can be described as a linear transformation by a second-order tensor $\boldsymbol{F}$ as

$$\mathrm{d}\boldsymbol{x} = \boldsymbol{F}\,\mathrm{d}\boldsymbol{X}, \tag{3.3}$$

where $\boldsymbol{x}$ is a function of $\boldsymbol{X}$. Due to this functional dependence, the chain rule expression

$$\mathrm{d}\boldsymbol{x} = \frac{\partial \boldsymbol{x}}{\partial \boldsymbol{X}}\,\mathrm{d}\boldsymbol{X} \tag{3.4}$$

must hold and the second-order tensor $\boldsymbol{F}$ can be identified as

$$\boldsymbol{F} = \frac{\partial \boldsymbol{x}}{\partial \boldsymbol{X}} = \mathrm{Grad}[\boldsymbol{x}] = \mathrm{Grad}[\boldsymbol{\varphi}(\boldsymbol{X}, t)], \tag{3.5}$$

or alternatively, by using Eq. 3.2, be expressed as

$$\boldsymbol{F} = \mathrm{Grad}[\boldsymbol{u} + \boldsymbol{X}] = \mathrm{Grad}[\boldsymbol{u}] + \boldsymbol{I}. \tag{3.6}$$

This tensor $\boldsymbol{F}$, denoted as deformation gradient, is a fundamental measure for the description of deformations and one of the most important continuum mechanical quantities. It does not only define the transformation of line elements, but also of the normal vectors $\mathrm{d}\boldsymbol{A} = \boldsymbol{N}\,\mathrm{d}A$ to area elements and of volume elements $\mathrm{d}V$, whose counterparts $\mathrm{d}\boldsymbol{a} = \boldsymbol{n}\,\mathrm{d}a$ and $\mathrm{d}v$ in the actual configuration are given by

$$\mathrm{d}\boldsymbol{a} = \mathrm{cof}[\boldsymbol{F}]\,\mathrm{d}\boldsymbol{A} = \det[\boldsymbol{F}]\,\boldsymbol{F}^{-\mathrm{T}}\,\mathrm{d}\boldsymbol{A} \qquad \text{and} \qquad \mathrm{d}v = \det[\boldsymbol{F}]\,\mathrm{d}V, \tag{3.7}$$

see Fig. 3.1 for an illustration. The compatibility condition $\nabla \times \boldsymbol{F} = \boldsymbol{0}$, which guarantees that the deforming body remains continuous, i. e. free of holes or overlaps, is automatically fulfilled due to the fact that $\boldsymbol{F}$ is defined as the gradient of a vector field (Slaughter, 2002, pp. 71, 110 f.). In order to ensure the invertibility of the mappings in Eq. 3.1 and Eq. 3.3, the existence of the inverse of the deformation gradient

$$\boldsymbol{F}^{-1} = \frac{\partial \boldsymbol{X}}{\partial \boldsymbol{x}} = \mathrm{grad}[\boldsymbol{X}] \tag{3.8}$$

has to be guaranteed. The determinant of $\boldsymbol{F}$, also referred to as Jacobian J, has thus to be non-zero. Moreover, this determinant must be positive in order to avoid negative actual volume elements $\mathrm{d}v$ in Eq. 3.7, i. e.

$$J := \det[\boldsymbol{F}] > 0. \tag{3.9}$$

For the introduction of a strain measure, the difference of the squared lengths of an infinitesimal line element in reference and actual configuration is considered. With $\mathrm{d}\boldsymbol{x} \cdot \mathrm{d}\boldsymbol{x} = \boldsymbol{F}\,\mathrm{d}\boldsymbol{X} \cdot \boldsymbol{F}\,\mathrm{d}\boldsymbol{X} = \mathrm{d}\boldsymbol{X} \cdot \boldsymbol{F}^{\mathrm{T}}\boldsymbol{F}\,\mathrm{d}\boldsymbol{X}$, the relation

$$\mathrm{d}\boldsymbol{x} \cdot \mathrm{d}\boldsymbol{x} - \mathrm{d}\boldsymbol{X} \cdot \mathrm{d}\boldsymbol{X} = \mathrm{d}\boldsymbol{X} \cdot \left(\boldsymbol{F}^{\mathrm{T}}\boldsymbol{F} - \boldsymbol{I}\right) \mathrm{d}\boldsymbol{X} \tag{3.10}$$

is obtained, which shows that the right Cauchy-Green tensor

$$\boldsymbol{C} := \boldsymbol{F}^{\mathrm{T}}\boldsymbol{F} \tag{3.11}$$

is a convenient measure for changes in deformation. The deformation gradient itself includes rigid body motions in addition to the "real" deformation in the sense of extension, compression or shear. A unique right polar decomposition $\boldsymbol{F} = \boldsymbol{R}\boldsymbol{U}$ into an orthogonal rotation tensor $\boldsymbol{R}$ with $\boldsymbol{R}^{-1} = \boldsymbol{R}^{\mathrm{T}}$ and a positive definite, symmetric stretch tensor $\boldsymbol{U}$ with $\boldsymbol{U}^{\mathrm{T}} = \boldsymbol{U}$ allows to separate both parts. From

$$\boldsymbol{C} = \boldsymbol{F}^{\mathrm{T}}\boldsymbol{F} = (\boldsymbol{R}\boldsymbol{U})^{\mathrm{T}}\,\boldsymbol{R}\boldsymbol{U} = \boldsymbol{U}^{\mathrm{T}}\boldsymbol{R}^{\mathrm{T}}\boldsymbol{R}\boldsymbol{U} = \boldsymbol{U}^2 \tag{3.12}$$

it becomes obvious that also $\boldsymbol{C}$ is a symmetric tensor which does not contain any rigid body motions.

For the formulation of fundamental mechanical laws, time derivatives of the kinematic quantities have to be considered. Assuming that the time derivative $\mathrm{d}\dot{\boldsymbol{x}}$ of an infinitesimal line element $\mathrm{d}\boldsymbol{x}$ in the actual configuration is related to the line element itself through the relation

$$\mathrm{d}\dot{\boldsymbol{x}} = \boldsymbol{l}\,\mathrm{d}\boldsymbol{x} \tag{3.13}$$

with a second-order tensor $\boldsymbol{l}$, the identity

$$\boldsymbol{l} = \frac{\partial \dot{\boldsymbol{x}}}{\partial \boldsymbol{x}} = \operatorname{grad}[\dot{\boldsymbol{x}}] \tag{3.14}$$

is obtained in analogy to Eq. 3.3–3.5. Describing the local changes of the velocity $\dot{\boldsymbol{x}} = \partial \boldsymbol{x}/\partial t$ at a material point in the spatial configuration, this tensor is referred to as spatial velocity gradient. Its relation to the time derivative of the deformation gradient is given by

$$\dot{\boldsymbol{F}} = \frac{\partial}{\partial t}\left(\frac{\partial \boldsymbol{x}}{\partial \boldsymbol{X}}\right) = \frac{\partial}{\partial \boldsymbol{X}}\left(\frac{\partial \boldsymbol{x}}{\partial t}\right) = \frac{\partial \dot{\boldsymbol{x}}}{\partial \boldsymbol{X}} = \frac{\partial \dot{\boldsymbol{x}}}{\partial \boldsymbol{x}}\frac{\partial \boldsymbol{x}}{\partial \boldsymbol{X}} = \boldsymbol{l}\boldsymbol{F}, \tag{3.15}$$

and thus the spatial velocity gradient $\boldsymbol{l}$ can also be expressed as

$$\boldsymbol{l} = \dot{\boldsymbol{F}}\boldsymbol{F}^{-1}. \tag{3.16}$$

The time derivative of the Jacobian can then be derived as

$$\dot{J} = \frac{\partial \det[\boldsymbol{F}]}{\partial t} = \frac{\partial \det[\boldsymbol{F}]}{\partial \boldsymbol{F}} \cdot \frac{\partial \boldsymbol{F}}{\partial t} = J\boldsymbol{F}^{-\mathrm{T}} \cdot \dot{\boldsymbol{F}} = J \operatorname{tr}[\boldsymbol{F}^{-\mathrm{T}}\dot{\boldsymbol{F}}^{\mathrm{T}}] = J \operatorname{tr}[\boldsymbol{l}] = J \operatorname{div}[\dot{\boldsymbol{x}}] \tag{3.17}$$

and using this relation, the time derivatives

$$\mathrm{d}\dot{\boldsymbol{a}} = \operatorname{div}[\dot{\boldsymbol{x}}]\,\mathrm{d}\boldsymbol{a} - \boldsymbol{l}^{\mathrm{T}}\mathrm{d}\boldsymbol{a} \qquad \text{and} \qquad \mathrm{d}\dot{v} = \operatorname{div}[\dot{\boldsymbol{x}}]\,\mathrm{d}v \tag{3.18}$$

of the terms given in Eq. 3.7 are obtained. During the derivation of $\mathrm{d}\boldsymbol{a}$, the expression $\dot{\boldsymbol{F}}^{-\mathrm{T}} = -\boldsymbol{F}^{-\mathrm{T}}\dot{\boldsymbol{F}}^{\mathrm{T}}\boldsymbol{F}^{-\mathrm{T}}$ obtained from $\frac{\partial}{\partial t}\left(\boldsymbol{F}^{-\mathrm{T}}\boldsymbol{F}^{\mathrm{T}}\right) = \boldsymbol{0}$ has to be inserted.

Since this work aims at describing the deformations of growing continua, the following extension of the basic kinematic equations is required.

3.1.2 Kinematics of multiplicative growth

Considering the overall deformation as the sequence of a growth deformation and a remaining elastic deformation, growth can be taken into account by a multiplicative decomposition of the deformation gradient as initially proposed in this context by Rodriguez, Hoger & McCulloch (1994) and later used by Lubarda & Hoger (2002) and Himpel, Kuhl, et al. (2005) among others. As illustrated in Fig. 3.2, the decomposition

$$\boldsymbol{F} = \boldsymbol{F}_{\mathrm{e}}\boldsymbol{F}_{\mathrm{g}} \tag{3.19}$$

comes along with the introduction of an intermediate configuration $\mathcal{B}_{\mathrm{i}} \subset \mathbb{R}^3$. This fictive intermediate state represents a new stress-free state which is related to the stress-free reference state $\mathcal{B}$ through a growth tensor $\boldsymbol{F}_{\mathrm{g}}$ describing the growth process. Each material point is allowed to grow independently of its neighboring points, such that in general, holes or overlaps might occur in the intermediate configuration. Since the growth tensor $\boldsymbol{F}_{\mathrm{g}}$ is thus not associated to a continuous displacement field, it does not fulfill the compatibility condition $\nabla \times \boldsymbol{F}_{\mathrm{g}} = \boldsymbol{0}$. In order to ensure the continuity of the body in the actual configuration $\mathcal{S}$ and the compatibility of the overall deformation gradient $\boldsymbol{F}$, an elastic deformation $\boldsymbol{F}_{\mathrm{e}} = \boldsymbol{F}\boldsymbol{F}_{\mathrm{g}}^{-1}$ connecting the intermediate

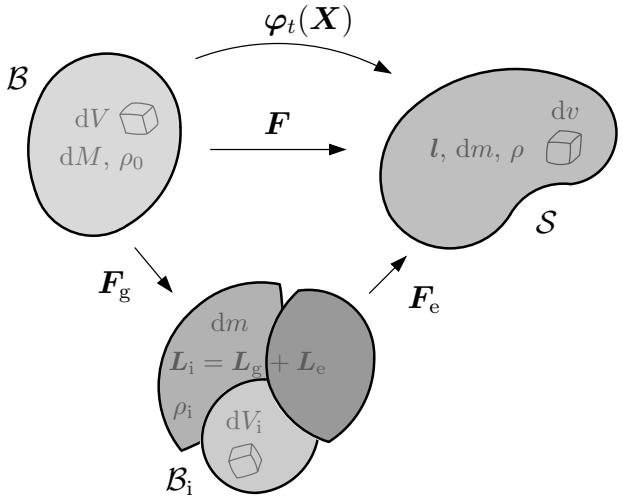

Figure 3.2: Multiplicative decomposition of the deformation gradient $\boldsymbol{F}$ in a growth part $\boldsymbol{F}_\mathrm{g}$ and a remaining elastic part $\boldsymbol{F}_\mathrm{e}$. The configuration $\mathcal{B}_\mathrm{i}$ equals a fictive intermediate state at which each material point has grown without generation of stresses.

and the actual configuration might be required. As done in Eq. 3.9 for the overall deformation gradient, the Jacobians

$$J_\mathrm{g} := \det[\boldsymbol{F}_\mathrm{g}] > 0 \qquad \text{and} \qquad J_\mathrm{e} := \det[\boldsymbol{F}_\mathrm{e}] > 0 \tag{3.20}$$

with $J = J_\mathrm{g} J_\mathrm{e}$ are defined. With these definitions, the overall volume change J of a volume element $\mathrm{d}V$ deforming into $\mathrm{d}v = J\,\mathrm{d}V$, cf. Eq. 3.7, can clearly be split into a part J_g related to growth and a part J_e related to the remaining elastic deformation, i. e.

$$\mathrm{d}V_\mathrm{i} = J_\mathrm{g}\,\mathrm{d}V \qquad \text{and} \qquad \mathrm{d}v = J_\mathrm{e}\,\mathrm{d}V_\mathrm{i}, \tag{3.21}$$

where $\mathrm{d}V_\mathrm{i}$ is the volume element in the intermediate configuration $\mathcal{B}_\mathrm{i}$. Since only this latter part of the deformation is assumed to generate stresses, a corresponding deformation measure

$$\boldsymbol{C}_\mathrm{e} = \boldsymbol{F}_\mathrm{e}^\mathrm{T}\boldsymbol{F}_\mathrm{e} = \left(\boldsymbol{F}\boldsymbol{F}_\mathrm{g}^{-1}\right)^\mathrm{T}\boldsymbol{F}\boldsymbol{F}_\mathrm{g}^{-1} = \boldsymbol{F}_\mathrm{g}^{-\mathrm{T}}\boldsymbol{F}^\mathrm{T}\boldsymbol{F}\boldsymbol{F}_\mathrm{g}^{-1} = \boldsymbol{F}_\mathrm{g}^{-\mathrm{T}}\boldsymbol{C}\boldsymbol{F}_\mathrm{g}^{-1} \tag{3.22}$$

is defined. Due to its definition in analogy to the right Cauchy-Green tensor given in Eq. 3.11, $\boldsymbol{C}_\mathrm{e}$ is also symmetric and does not contain rigid body rotations.

The spatial velocity gradient from Eq. 3.16 can be pulled back to the intermediate configuration using the operation

$$\boldsymbol{L}_\mathrm{i} = \boldsymbol{F}_\mathrm{e}^{-1}\boldsymbol{l}\boldsymbol{F}_\mathrm{e} = \boldsymbol{F}_\mathrm{e}^{-1}\dot{\boldsymbol{F}}\boldsymbol{F}^{-1}\boldsymbol{F}_\mathrm{e} = \boldsymbol{F}_\mathrm{e}^{-1}\dot{\boldsymbol{F}}\boldsymbol{F}_\mathrm{g}^{-1}, \tag{3.23}$$

where the time derivative of the deformation gradient can be expressed as

$$\dot{\boldsymbol{F}} = \frac{\partial(\boldsymbol{F}_\mathrm{e}\boldsymbol{F}_\mathrm{g})}{\partial t} = \boldsymbol{F}_\mathrm{e}\dot{\boldsymbol{F}}_\mathrm{g} + \dot{\boldsymbol{F}}_\mathrm{e}\boldsymbol{F}_\mathrm{g}. \tag{3.24}$$

Inserting this expression in Eq. 3.23, the velocity gradient in the intermediate configuration can be formulated as

$$\boldsymbol{L}_\mathrm{i} = \dot{\boldsymbol{F}}_\mathrm{g}\boldsymbol{F}_\mathrm{g}^{-1} + \boldsymbol{F}_\mathrm{e}^{-1}\dot{\boldsymbol{F}}_\mathrm{e} =: \boldsymbol{L}_\mathrm{g} + \boldsymbol{L}_\mathrm{e} \tag{3.25}$$

with two additive parts defined as

$$\boldsymbol{L}_\mathrm{g} \coloneqq \dot{\boldsymbol{F}}_\mathrm{g}\boldsymbol{F}_\mathrm{g}^{-1} \qquad \text{and} \qquad \boldsymbol{L}_\mathrm{e} \coloneqq \boldsymbol{F}_\mathrm{e}^{-1}\dot{\boldsymbol{F}}_\mathrm{e}, \tag{3.26}$$

see Himpel, Kuhl, et al. (2005). Due to their structure which is similar to the definition of the spatial velocity gradient $\boldsymbol{l}$, these tensors are referred to as growth velocity gradient and as elastic velocity gradient. With the help of these velocity gradients, the derivatives

$$\dot{J}_\mathrm{g} = J_\mathrm{g}\boldsymbol{F}_\mathrm{g}^{-\mathrm{T}} \cdot \dot{\boldsymbol{F}}_\mathrm{g} = J_\mathrm{g}\dot{\boldsymbol{F}}_\mathrm{g} \cdot \boldsymbol{F}_\mathrm{g}^{-\mathrm{T}} = J_\mathrm{g}\,\mathrm{tr}[\dot{\boldsymbol{F}}_\mathrm{g}\boldsymbol{F}_\mathrm{g}^{-1}] = J_\mathrm{g}\,\mathrm{tr}[\boldsymbol{L}_\mathrm{g}], \tag{3.27a}$$

$$\dot{J}_\mathrm{e} = J_\mathrm{e}\boldsymbol{F}_\mathrm{e}^{-\mathrm{T}} \cdot \dot{\boldsymbol{F}}_\mathrm{e} = J_\mathrm{e}\,\mathrm{tr}[\boldsymbol{F}_\mathrm{e}^{-1}\dot{\boldsymbol{F}}_\mathrm{e}] = J_\mathrm{e}\,\mathrm{tr}[\boldsymbol{L}_\mathrm{e}] \tag{3.27b}$$

can be formulated in analogy to $\dot{J} = J\,\mathrm{tr}[\boldsymbol{l}]$ deduced in Eq. 3.17.

3.2 Stress vectors and tensors

As a consequence of the definition of different configurations with different sizes of the infinitesimal area elements, some considerations concerning the definition of stresses are required. Finally, the true stresses within the deformed continuum are matter of interest, which are naturally defined as force per unit area in the actual configuration. In the cross section of a deformed body, a stress vector $\boldsymbol{t}$ can be defined as

$$\boldsymbol{t} = \frac{\mathrm{d}\boldsymbol{f}}{\mathrm{d}a}, \tag{3.28}$$

where $\mathrm{d}\boldsymbol{f}$ is the force vector acting on the infinitesimal area element $\mathrm{d}a$ in the actual configuration, see Fig. 3.3 for an illustration. This force vector can be disassembled into a normal component in the direction of unit normal vector $\boldsymbol{n}$ and two perpendicular shear components within the cutting plane. However, one single stress vector is not sufficient to characterize the full stress state at a material point, which consists of three normal and six shear stresses. Therefore, the Cauchy stress tensor $\boldsymbol{\sigma}$ is introduced, in which all stress components at a material point are enclosed. The stress vector associated to an arbitrary cutting plane can then be computed from $\boldsymbol{\sigma}$ by means of the Cauchy theorem

$$\boldsymbol{t} = \boldsymbol{\sigma}\boldsymbol{n}, \tag{3.29}$$

where $\boldsymbol{n}$ is the unit normal vector of the cutting plane. The components of the Cauchy stress tensor are the real stresses acting in the body, which means that they are associated to the real cross section in the actual configuration. Due to the balance of angular momentum, see Sec. 3.3.3, the Cauchy stress tensor is symmetric, i. e. $\boldsymbol{\sigma}^\mathrm{T} = \boldsymbol{\sigma}$.
For the definition of a stress tensor relating the forces to the reference configuration, a stress vector $\boldsymbol{T}$ can be introduced in the same manner as

$$\boldsymbol{T} = \frac{\mathrm{d}\boldsymbol{f}}{\mathrm{d}A} \tag{3.30}$$

as shown in Fig. 3.3. Since the incremental force vector $\mathrm{d}\boldsymbol{f}$ is the same in both configurations, the equation

$$\boldsymbol{T}\,\mathrm{d}A \overset{!}{=} \boldsymbol{t}\,\mathrm{d}a = \boldsymbol{\sigma}\boldsymbol{n}\,\mathrm{d}a \tag{3.31}$$

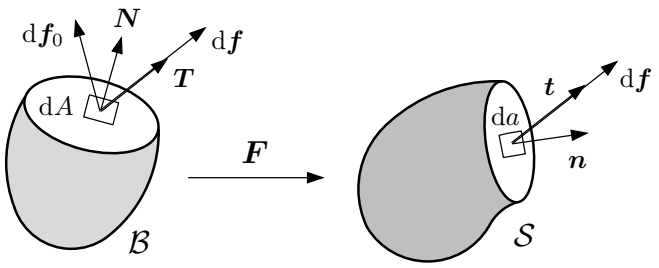

Figure 3.3: Stress vectors $\boldsymbol{T} = \frac{\mathrm{d}\boldsymbol{f}}{\mathrm{d}A}$ and $\boldsymbol{t} = \frac{\mathrm{d}\boldsymbol{f}}{\mathrm{d}a}$ in reference and actual configuration.

must be satisfied, where $\boldsymbol{n}\,\mathrm{d}a = J\boldsymbol{F}^{-\mathrm{T}}\boldsymbol{N}\mathrm{d}A$ holds due to Eq. 3.7. Inserting this yields

$$\boldsymbol{T} = J\boldsymbol{\sigma}\boldsymbol{F}^{-\mathrm{T}}\boldsymbol{N} = \boldsymbol{P}\boldsymbol{N} \qquad \text{with} \qquad \boldsymbol{P} := J\boldsymbol{\sigma}\boldsymbol{F}^{-\mathrm{T}}, \tag{3.32}$$

where $\boldsymbol{P}$ is denoted as 1st Piola-Kirchhoff or nominal stress tensor. The 1st Piola-Kirchhoff stress tensor is unsymmetric, which might sometimes be disadvantageous, and has a mixed basis with the first basis vector in the actual and the second one in the reference configuration. With

$$\boldsymbol{S} := \boldsymbol{F}^{-1}\boldsymbol{P}, \tag{3.33}$$

a tensor with two basis vectors in the reference configuration is obtained. It is denoted as 2nd Piola-Kirchhoff stress tensor and is related to the Cauchy stress through $\boldsymbol{\sigma} = {}^1\!/_J\,\boldsymbol{F}\boldsymbol{S}\boldsymbol{F}^{\mathrm{T}}$. In a geometrical sense, $\boldsymbol{S}$ can be explained with the help of a "pseudo" stress vector consisting of a pullback of the force vector to the reference configuration, i. e. $\mathrm{d}\boldsymbol{f}_0 = \boldsymbol{F}^{-1}\,\mathrm{d}\boldsymbol{f}$, which is referred to the area element $\mathrm{d}A$. In contrast to $\boldsymbol{\sigma}$ and $\boldsymbol{P}$, $\boldsymbol{S}$ can thus not be interpreted as a stress based on physical argumentation, it has rather to be understood as a helpful mathematic quantity. Like the Cauchy stress tensor, the 2nd Piola-Kirchhoff stress tensor is symmetric due to the balance of angular momentum.

3.3 Balance equations and entropy inequality

The balance equations constitute a set of fundamental laws of continuum mechanics, which are natural laws and have thus to be satisfied at every time and whichever material is considered. They describe the correlation between certain physical quantities characterizing the state of the continuum body and external effects. The balanced quantities are mass, linear and angular momentum as well as energy of the body. A growing continuum is an open system where the amount of mass is not fixed. Changes of those state variables are thus caused by generation or reduction of mass and by external forces.
Another fundamental law complementing the balance equations is the second law of thermodynamics, which states that entropy can never decrease.

3.3.1 Balance of mass

The mass of a continuum body which occupies a particular volume is defined by its mass density. In the reference configuration $\mathcal{B}$, an infinitesimal mass element

$$\mathrm{d}M = \rho_0\,\mathrm{d}V \tag{3.34}$$

is obtained as the product of the infinitesimal volume element $\mathrm{d}V$ and the reference mass density ρ_0. This density does not need to be constant over the body and thus depends on the material point $\boldsymbol{X}$, but it is not time-dependent. In the actual configuration $\mathcal{S}$ however, where mass and volume are allowed to change over time, the actual mass density ρ, which defines the infinitesimal mass element

$$\mathrm{d}m = \rho \, \mathrm{d}v, \tag{3.35}$$

depends on location and time. The same holds for the mass density ρ_i, which is defined in the intermediate configuration $\mathcal{B}_\mathrm{i}$. The infinitesimal mass element $\mathrm{d}M_\mathrm{i}$ in this configuration is given by

$$\mathrm{d}M_\mathrm{i} = \rho_\mathrm{i} \, \mathrm{d}V_\mathrm{i} \equiv \mathrm{d}m, \tag{3.36}$$

and since growth is assumed to take place during the transformation from the reference to the intermediate configuration but not afterwards, it equals the final mass element $\mathrm{d}m$. In order to track the evolution of the final mass with respect to the reference configuration, an additional mass density

$$\bar{\rho}_0 = \frac{\mathrm{d}m}{\mathrm{d}V} \equiv J \, \frac{\mathrm{d}m}{\mathrm{d}v} = J \, \rho \equiv J_\mathrm{g} \, \frac{\mathrm{d}m}{\mathrm{d}V_\mathrm{i}} = J_\mathrm{g} \rho_\mathrm{i} \tag{3.37}$$

is defined. With $\mathcal{R}_0$ denoting a mass source per time and per unit volume in the reference configuration, the actual mass element can be expressed as the sum of the reference mass element $\mathrm{d}M$ and the gain within the time interval $[t_0, t_1]$ according to

$$\mathrm{d}m = \mathrm{d}M + \int_{t_0}^{t_1} \mathcal{R}_0 \, \mathrm{d}t \, \mathrm{d}V, \tag{3.38}$$

see Himpel, Kuhl, et al. (2005). Replacing $\mathrm{d}m$ by $\bar{\rho}_0 \, \mathrm{d}V$ from Eq. 3.37 and $\mathrm{d}M$ by $\rho_0 \, \mathrm{d}V$ from Eq. 3.34, this equation can be reformulated as

$$\bar{\rho}_0 = \rho_0 + \int_{t_0}^{t_1} \mathcal{R}_0 \, \mathrm{d}t. \tag{3.39}$$

Differentiation with respect to time yields the local form of balance of mass in the reference configuration, namely

$$\dot{\bar{\rho}}_0 = \mathcal{R}_0, \tag{3.40}$$

which has to be fulfilled at each material point for all times. Inserting $\bar{\rho}_0 = J \, \rho$ from Eq. 3.37 and using Eq. 3.17, the balance of mass in the actual configuration

$$\dot{\rho} + \rho \, \mathrm{tr}[\boldsymbol{l}] = \frac{\mathcal{R}_0}{J} \tag{3.41}$$

is obtained. Analogously, Eq. 3.40 can be transformed to the intermediate configuration. With $\bar{\rho}_0 = J_\mathrm{g} \, \rho_\mathrm{i}$ from Eq. 3.37 and with Eq. 3.27a, the local form of balance of mass in the intermediate configuration reads

$$\dot{\rho}_\mathrm{i} + \rho_\mathrm{i} \, \mathrm{tr}[\boldsymbol{L}_\mathrm{g}] = \frac{\mathcal{R}_0}{J_\mathrm{g}}. \tag{3.42}$$

From this result, further information on the mass source $\mathcal{R}_0$ can be extracted. If density changes during growth are excluded, which means that an increase of mass is exclusively caused by

an increase of volume, the mass density in the intermediate configuration equals ρ_0 and does therefore not depend on time. Then, with $\rho_\mathrm{i} = \rho_0 = \text{const.}$, Eq. 3.42 turns into

$$\mathcal{R}_0 = J_\mathrm{g}\, \rho_0\, \mathrm{tr}[\boldsymbol{L}_\mathrm{g}] = \bar{\rho}_0\, \mathrm{tr}[\boldsymbol{L}_\mathrm{g}], \tag{3.43}$$

from which the mass source can directly be identified if the growth tensor $\boldsymbol{F}_\mathrm{g}$ and its time derivative $\dot{\boldsymbol{F}}_\mathrm{g}$ are known.

3.3.2 Balance of linear momentum

The balance of linear momentum requires that the time derivative $\dot{\boldsymbol{L}}$ of the total linear momentum must balance all forces $\boldsymbol{f}$ that act on the body, thus $\dot{\boldsymbol{L}} = \boldsymbol{f}$. The linear momentum $\boldsymbol{L}$ is thereby defined as mass times velocity integrated over all material points and its time derivative is given by

$$\dot{\boldsymbol{L}} = \frac{\partial}{\partial t} \int_\mathcal{S} \rho\, \dot{\boldsymbol{x}}\, \mathrm{d}v, \tag{3.44}$$

whereas the vector of all acting forces reads

$$\boldsymbol{f} = \int_\mathcal{S} \rho\, \boldsymbol{b}\, \mathrm{d}v + \int_{\partial\mathcal{S}} \boldsymbol{t}\, \mathrm{d}a + \int_\mathcal{S} \frac{\mathcal{R}_0}{J}\, \dot{\boldsymbol{x}}\, \mathrm{d}v. \tag{3.45}$$

Therein, $\boldsymbol{b}$ denotes the volume acceleration and $\boldsymbol{t}$ the traction vector acting on the surface $\partial\mathcal{S}$ of the body. The last term, with $\mathcal{R}_0/J$ denoting the mass source per time and unit volume in the actual configuration, is included to account for the effect of additionally added mass, see e. g. Lubarda & Hoger (2002). All integrals are formally evaluated over the actual configuration of the body, where the external forces act, but they can be replaced by integrals over the reference configuration using $\mathrm{d}v = J\,\mathrm{d}V$. Since $\mathrm{d}V$ does not vary with time, this allows to change the order of time differentiation and integration in Eq. 3.44, which can then be reformulated as

$$\begin{aligned} \dot{\boldsymbol{L}} &= \frac{\partial}{\partial t} \int_\mathcal{B} \rho\, \dot{\boldsymbol{x}}\, J\, \mathrm{d}V = \int_\mathcal{B} \frac{\partial}{\partial t} \left(\rho\, \dot{\boldsymbol{x}}\, J\right) \mathrm{d}V = \int_\mathcal{B} \left(\dot{\rho}\, \dot{\boldsymbol{x}}\, J + \rho\, \ddot{\boldsymbol{x}}\, J + \rho\, \dot{\boldsymbol{x}}\, \dot{J}\right) \mathrm{d}V \\ &= \int_\mathcal{B} \left(\dot{\rho} + \rho\, \mathrm{tr}[\boldsymbol{l}]\right) \dot{\boldsymbol{x}}\, J\, \mathrm{d}V + \int_\mathcal{B} \rho\, \ddot{\boldsymbol{x}}\, J\, \mathrm{d}V = \int_\mathcal{B} \mathcal{R}_0\, \dot{\boldsymbol{x}}\, \mathrm{d}V + \int_\mathcal{B} \bar{\rho}_0\, \ddot{\boldsymbol{x}}\, \mathrm{d}V. \end{aligned} \tag{3.46}$$

In the second line, Eq. 3.17 as well as the balance of mass from Eq. 3.41 and the density transformation from Eq. 3.37 have been inserted. With Eq. 3.29 and making use of Gauß' divergence theorem $\int_{\partial\mathcal{S}} \boldsymbol{\sigma}\boldsymbol{n}\, \mathrm{d}a = \int_\mathcal{S} \mathrm{div}[\boldsymbol{\sigma}]\, \mathrm{d}v$, the vector of all acting forces can be expressed as

$$\begin{aligned} \boldsymbol{f} &= \int_\mathcal{S} \rho\, \boldsymbol{b}\, \mathrm{d}v + \int_\mathcal{S} \mathrm{div}[\boldsymbol{\sigma}]\, \mathrm{d}v + \int_\mathcal{S} \frac{\mathcal{R}_0}{J}\, \dot{\boldsymbol{x}}\, \mathrm{d}v \\ &= \int_\mathcal{B} \rho\, \boldsymbol{b}\, J\, \mathrm{d}V + \int_\mathcal{B} \mathrm{div}[\boldsymbol{\sigma}] J\, \mathrm{d}V + \int_\mathcal{B} \mathcal{R}_0\, \dot{\boldsymbol{x}}\, \mathrm{d}V \\ &= \int_\mathcal{B} \bar{\rho}_0\, \boldsymbol{b}\, \mathrm{d}V + \int_\mathcal{B} \mathrm{Div}[\boldsymbol{P}]\, \mathrm{d}V + \int_\mathcal{B} \mathcal{R}_0\, \dot{\boldsymbol{x}}\, \mathrm{d}V, \end{aligned} \tag{3.47}$$

where the equivalence $\mathrm{Div}[\boldsymbol{P}] = J\,\mathrm{div}[\boldsymbol{\sigma}]$ has been used (cf. HOLZAPFEL, 2000, p. 146). Setting $\dot{\boldsymbol{L}} = \boldsymbol{f}$, the balance of linear momentum turns out to be

$$\int_{\mathcal{B}} \bar{\rho}_0\, \ddot{\boldsymbol{x}}\, \mathrm{d}V = \int_{\mathcal{B}} \bar{\rho}_0\, \boldsymbol{b}\, \mathrm{d}V + \int_{\mathcal{B}} \mathrm{Div}[\boldsymbol{P}]\, \mathrm{d}V, \tag{3.48}$$

which does not involve additional terms associated to growth. Omitting the integration over $\mathcal{B}$ results in the local form of the balance of linear momentum

$$\bar{\rho}_0\, \ddot{\boldsymbol{x}} = \bar{\rho}_0\, \boldsymbol{b} + \mathrm{Div}[\boldsymbol{P}], \tag{3.49}$$

which is formulated with respect to the reference configuration.

3.3.3 Balance of angular momentum

In an analogous manner as for linear momentum and forces, the balance of angular momentum requires that the time derivative $\dot{\boldsymbol{J}}$ of the total moment of momentum balances the sum of all moments $\boldsymbol{m}$ acting on the body. Defining the moments with reference to the origin of the coordinate system, the time derivative of the angular momentum is given by

$$\dot{\boldsymbol{J}} = \frac{\partial}{\partial t} \int_{\mathcal{S}} \boldsymbol{x} \times \rho\, \dot{\boldsymbol{x}}\, \mathrm{d}v \tag{3.50}$$

and the vector of applied moments is

$$\boldsymbol{m} = \int_{\mathcal{S}} \boldsymbol{x} \times \rho\, \boldsymbol{b}\, \mathrm{d}v + \int_{\partial\mathcal{S}} \boldsymbol{x} \times \boldsymbol{t}\, \mathrm{d}a + \int_{\mathcal{S}} \boldsymbol{x} \times \frac{\mathcal{R}_0}{J}\, \dot{\boldsymbol{x}}\, \mathrm{d}v. \tag{3.51}$$

Again, when evaluating the integrals in the reference configuration, the order of time differentiation and integration can be switched, such that Eq. 3.50 together with Eq. 3.17, Eq. 3.41 and $\rho\, J = \bar{\rho}_0$ from Eq. 3.37 yields

$$\begin{aligned} \dot{\boldsymbol{J}} &= \int_{\mathcal{B}} \frac{\partial}{\partial t} \left(\boldsymbol{x} \times \rho\, \dot{\boldsymbol{x}}\, J\right) \mathrm{d}V = \int_{\mathcal{B}} \left(\boldsymbol{x} \times \dot{\rho}\, \dot{\boldsymbol{x}}\, J + \boldsymbol{x} \times \rho\, \ddot{\boldsymbol{x}}\, J + \boldsymbol{x} \times \rho\, \dot{\boldsymbol{x}}\, \dot{J}\right) \mathrm{d}V \\ &= \int_{\mathcal{B}} \left(\boldsymbol{x} \times \mathcal{R}_0\, \dot{\boldsymbol{x}} + \boldsymbol{x} \times \bar{\rho}_0\, \ddot{\boldsymbol{x}}\right) \mathrm{d}V. \end{aligned} \tag{3.52}$$

The vector $\boldsymbol{m}$ can be simplified with Eq. 3.29 and a modification of the divergence theorem specified in Eq. A.16 of Appendix A. This leads to

$$\boldsymbol{m} = \int_{\mathcal{B}} \left(\boldsymbol{x} \times \bar{\rho}_0\, \boldsymbol{b} + \boldsymbol{x} \times J\, \mathrm{div}[\boldsymbol{\sigma}] + \boldsymbol{\epsilon} : J\, \boldsymbol{\sigma}^{\mathrm{T}} + \boldsymbol{x} \times \mathcal{R}_0\, \dot{\boldsymbol{x}}\right) \mathrm{d}V, \tag{3.53}$$

where $\boldsymbol{\epsilon}$ denotes the 3^{rd} order permutation tensor, see Eq. A.2. Evaluation of the condition $\dot{\boldsymbol{J}} = \boldsymbol{m}$ then leads to the identity

$$\int_{\mathcal{B}} \boldsymbol{x} \times \bar{\rho}_0\, \ddot{\boldsymbol{x}}\, \mathrm{d}V = \int_{\mathcal{B}} \left(\boldsymbol{x} \times \bar{\rho}_0\, \boldsymbol{b} + \boldsymbol{x} \times J\, \mathrm{div}[\boldsymbol{\sigma}] + \boldsymbol{\epsilon} : J\, \boldsymbol{\sigma}^{\mathrm{T}}\right) \mathrm{d}V, \tag{3.54}$$

which, due to $J\,\mathrm{div}[\boldsymbol{\sigma}] = \mathrm{Div}[\boldsymbol{P}]$ and the balance of linear momentum in Eq. 3.49, finally appears as

$$\mathbf{0} = \int_{\mathcal{B}} \boldsymbol{\epsilon} : J\,\boldsymbol{\sigma}^{\mathrm{T}}\,\mathrm{d}V. \tag{3.55}$$

This equation can only be fulfilled if the expression $J\,\boldsymbol{\sigma}^{\mathrm{T}}$ is symmetric. Insertion of $\boldsymbol{\sigma} = {}^{1}\!/_{J}\,\boldsymbol{F}\boldsymbol{S}\boldsymbol{F}^{\mathrm{T}}$ reveals that this is equivalent to symmetry of $\boldsymbol{S}$, which means that the balance of angular momentum finally demands the symmetries

$$\boldsymbol{\sigma}^{\mathrm{T}} = \boldsymbol{\sigma} \qquad \text{and} \qquad \boldsymbol{S}^{\mathrm{T}} = \boldsymbol{S} \tag{3.56}$$

of the Cauchy and the 2$^{\mathrm{nd}}$ Piola-Kirchhoff stress tensor.

3.3.4 Balance of energy (first law of thermodynamics)

The balance of energy claims that the change of internal and kinetic energy must equal the rate of work done on the continuum body in terms of mechanical and thermal external loads and by addition of mass. Expressed by a formula, the balance of energy reads as $\dot{\mathcal{E}} + \dot{\mathcal{K}} = \mathcal{P} + \mathcal{Q} + \mathcal{G}$, where the individual terms are specified as follows. The internal energy $\mathcal{E}$ is given by the integral

$$\mathcal{E} = \int_{\mathcal{S}} \rho\, e\,\mathrm{d}v \;\equiv\; \int_{\mathcal{B}} \bar{\rho}_0\, e\,\mathrm{d}V \tag{3.57}$$

over the specific internal energy e, which is a thermodynamic state variable defined per unit reference mass. Integrating over the reference configuration, the order of time differentiation and integration can be inverted, such that $\dot{\mathcal{E}}$ can be computed with Eq. 3.40 to be

$$\dot{\mathcal{E}} = \int_{\mathcal{B}} \left(\mathcal{R}_0\, e + \bar{\rho}_0\, \dot{e}\right)\,\mathrm{d}V. \tag{3.58}$$

The kinetic energy $\mathcal{K}$ is defined as

$$\mathcal{K} = \int_{\mathcal{S}} \tfrac{1}{2}\,\rho\,\dot{\boldsymbol{x}}\cdot\dot{\boldsymbol{x}}\,\mathrm{d}v \;\equiv\; \int_{\mathcal{B}} \tfrac{1}{2}\,\bar{\rho}_0\,\dot{\boldsymbol{x}}\cdot\dot{\boldsymbol{x}}\,\mathrm{d}V, \tag{3.59}$$

where time differentiation yields

$$\dot{\mathcal{K}} = \int_{\mathcal{B}} \frac{\partial}{\partial t}\left(\tfrac{1}{2}\,\bar{\rho}_0\,\dot{\boldsymbol{x}}\cdot\dot{\boldsymbol{x}}\right)\mathrm{d}V = \int_{\mathcal{B}} \left(\tfrac{1}{2}\,\mathcal{R}_0\,\dot{\boldsymbol{x}}\cdot\dot{\boldsymbol{x}} + \bar{\rho}_0\,\ddot{\boldsymbol{x}}\cdot\dot{\boldsymbol{x}}\right)\mathrm{d}V \tag{3.60}$$

with the same argumentation as for $\dot{\mathcal{E}}$. Volume and surface forces are doing external mechanical work on the body. The time rate of this work, i. e. the external mechanical power, is given by

$$\mathcal{P} = \int_{\mathcal{S}} \rho\,\boldsymbol{b}\cdot\dot{\boldsymbol{x}}\,\mathrm{d}v + \int_{\partial\mathcal{S}} \boldsymbol{t}\cdot\dot{\boldsymbol{x}}\,\mathrm{d}a, \tag{3.61}$$

where Eq. 3.29 and use of index notation allow to write the integrand of the second term as $\boldsymbol{t}\cdot\dot{\boldsymbol{x}} = \boldsymbol{\sigma}\boldsymbol{n}\cdot\dot{\boldsymbol{x}} = \boldsymbol{\sigma}^{\mathrm{T}}\dot{\boldsymbol{x}}\cdot\boldsymbol{n}$. Replacing the integral over the actual configuration by an integral

over the reference configuration and using $\rho\, J = \bar{\rho}_0$ from Eq. 3.37 as well as Eq. 3.7 and Eq. 3.32 results in

$$\begin{aligned}\mathcal{P} &= \int_{\mathcal{B}} \bar{\rho}_0\, \boldsymbol{b} \cdot \dot{\boldsymbol{x}}\, \mathrm{d}V + \int_{\partial\mathcal{B}} \boldsymbol{\sigma}^{\mathrm{T}} \dot{\boldsymbol{x}} \cdot J\, \boldsymbol{F}^{-\mathrm{T}} \boldsymbol{N}\, \mathrm{d}A \\ &= \int_{\mathcal{B}} \bar{\rho}_0\, \boldsymbol{b} \cdot \dot{\boldsymbol{x}}\, \mathrm{d}V + \int_{\partial\mathcal{B}} \boldsymbol{F}\boldsymbol{P}^{\mathrm{T}} \dot{\boldsymbol{x}} \cdot \boldsymbol{F}^{-\mathrm{T}} \boldsymbol{N} \mathrm{d}A \\ &= \int_{\mathcal{B}} \bar{\rho}_0\, \boldsymbol{b} \cdot \dot{\boldsymbol{x}}\, \mathrm{d}V + \int_{\partial\mathcal{B}} \boldsymbol{P}^{\mathrm{T}} \dot{\boldsymbol{x}} \cdot \boldsymbol{N}\, \mathrm{d}A.\end{aligned} \tag{3.62}$$

In this form, the surface integral of the second term can be converted to a volume integral with the aid of Gauß' divergence theorem $\int_{\partial\mathcal{B}} \boldsymbol{a} \cdot \boldsymbol{N}\, \mathrm{d}A = \int_{\mathcal{B}} \mathrm{Div}[\boldsymbol{a}]\, \mathrm{d}V$, i. e.

$$\int_{\partial\mathcal{B}} \boldsymbol{P}^{\mathrm{T}} \dot{\boldsymbol{x}} \cdot \boldsymbol{N}\, \mathrm{d}A = \int_{\mathcal{B}} \mathrm{Div}[\boldsymbol{P}^{\mathrm{T}} \dot{\boldsymbol{x}}]\, \mathrm{d}V. \tag{3.63}$$

The divergence of $\boldsymbol{P}^{\mathrm{T}} \dot{\boldsymbol{x}}$ with respect to the reference coordinates X_i is computed in index notation as

$$\frac{\partial P_{ki}\, \dot{x}_k}{\partial X_i} = P_{ki,i}\, \dot{x}_k + P_{ki}\, \frac{\partial x_{k,i}}{\partial t} = P_{ki,i}\, \dot{x}_k + P_{ki}\, \dot{F}_{ki}, \tag{3.64}$$

which is equivalent to $\mathrm{Div}[\boldsymbol{P}] \cdot \dot{\boldsymbol{x}} + \boldsymbol{P} : \dot{\boldsymbol{F}}$. The rate of external mechanical work can thus finally be expressed as

$$\mathcal{P} = \int_{\mathcal{B}} \bar{\rho}_0\, \boldsymbol{b} \cdot \dot{\boldsymbol{x}}\, \mathrm{d}V + \int_{\mathcal{B}} (\mathrm{Div}[\boldsymbol{P}] \cdot \dot{\boldsymbol{x}} + \boldsymbol{P} : \dot{\boldsymbol{F}})\, \mathrm{d}V. \tag{3.65}$$

If heat is transferred between the body and its surroundings, thermal work is done. The rate of this work is given by

$$\mathcal{Q} = \int_{\mathcal{S}} \rho\, r_0\, \mathrm{d}v - \int_{\partial\mathcal{S}} \boldsymbol{q} \cdot \boldsymbol{n}\, \mathrm{d}a, \tag{3.66}$$

where r_0 denotes a heat source per time and unit reference mass and $\boldsymbol{q}$ is a inward heat flux per time entering the body across a unit surface element in the current configuration. Since the unit normal vector $\boldsymbol{n}$ points in the opposite direction, a negative sign arises. With Eq. 3.7 leading to

$$\boldsymbol{q} \cdot \boldsymbol{n}\, \mathrm{d}a = \boldsymbol{q} \cdot J\, \boldsymbol{F}^{-\mathrm{T}} \boldsymbol{N}\, \mathrm{d}A = J\, \boldsymbol{F}^{-1} \boldsymbol{q} \cdot \boldsymbol{N}\, \mathrm{d}A \qquad \text{with} \qquad J\, \boldsymbol{F}^{-1} \boldsymbol{q} =: \boldsymbol{q}_0, \tag{3.67}$$

integration over the reference configuration and the divergence theorem can again be applied to reformulate the rate of thermal work as

$$\mathcal{Q} = \int_{\mathcal{B}} \bar{\rho}_0\, r_0\, \mathrm{d}V - \int_{\mathcal{B}} \mathrm{Div}[\boldsymbol{q}_0]\, \mathrm{d}V. \tag{3.68}$$

The term denoted by $\mathcal{G}$ is added following Lubarda & Hoger (2002) in order to take the rate of kinetic and internal energy associated with the additional mass into account. It reads

$$\mathcal{G} = \int_{\mathcal{S}} \frac{\mathcal{R}_0}{J} \left(\tfrac{1}{2}\, \dot{\boldsymbol{x}} \cdot \dot{\boldsymbol{x}} + e\right) \mathrm{d}v \equiv \int_{\mathcal{B}} \mathcal{R}_0 \left(\tfrac{1}{2}\, \dot{\boldsymbol{x}} \cdot \dot{\boldsymbol{x}} + e\right) \mathrm{d}V. \tag{3.69}$$

Inserting the balance of linear momentum from Eq. 3.49, $\dot{\mathcal{E}} + \dot{\mathcal{K}} = \mathcal{P} + \mathcal{Q} + \mathcal{G}$ finally leads to the local form of the balance of energy

$$\bar{\rho}_0 \, \dot{e} = \boldsymbol{P} : \dot{\boldsymbol{F}} - \mathrm{Div}[\boldsymbol{q}_0] + \bar{\rho}_0 \, r_0. \tag{3.70}$$

Due to the consideration of thermal in addition to mechanical energy, this balance equation equals a fundamental axiom of thermodynamics, which is also known as first law of thermodynamics. For later reference, the alternative representation

$$\bar{\rho}_0 \, \dot{e} = \tfrac{1}{2} \, \boldsymbol{S} : \dot{\boldsymbol{C}} - \mathrm{Div}[\boldsymbol{q}_0] + \bar{\rho}_0 \, r_0 \tag{3.71}$$

is introduced, where the substitution $\boldsymbol{P} : \dot{\boldsymbol{F}} = \boldsymbol{S} : \boldsymbol{F}^{\mathrm{T}} \dot{\boldsymbol{F}} = \boldsymbol{S} : \mathrm{sym}[\boldsymbol{F}^{\mathrm{T}} \dot{\boldsymbol{F}}] = \frac{1}{2} \, \boldsymbol{S} : \dot{\boldsymbol{C}}$ has been performed, which is possible due to the symmetry of $\boldsymbol{S}$.

3.3.5 Entropy inequality (second law of thermodynamics)

The first law of thermodynamics states that for all processes with exchange of mechanical or thermal energy, the sum of energy remains constant. It does however not restrict the direction of energy transfer. Nonetheless, it is observable that heat always flows from warmer to colder regions or that mechanical energy can generate heat, but not contrariwise unless external energy is supplied. In order to ensure that a physical process is consistent with this observation, the second law of thermodynamics has to be satisfied. This law states that the total production of entropy per time, as a whole denoted as Γ, is never negative. Formulated in terms of the Clausius-Duhem inequality, this means that

$$\Gamma = \frac{\partial}{\partial t} \int_{\mathcal{S}} \rho \, \eta_0 \, \mathrm{d}v - \tilde{\mathcal{Q}} \geq 0 \tag{3.72}$$

must hold, where η_0 is the specific entropy, defined by unit reference mass. According to that, the time derivative of the inherent entropy of a body does not need to equal the rate of entropy input $\tilde{\mathcal{Q}}$ as in previous balance equations, but their difference is claimed to be non-negative. The rate of entropy input $\tilde{\mathcal{Q}}$ is defined as

$$\tilde{\mathcal{Q}} = \int_{\mathcal{S}} \frac{\rho \, r_0}{\theta} \, \mathrm{d}v - \int_{\partial\mathcal{S}} \frac{1}{\theta} \, \boldsymbol{q} \cdot \boldsymbol{n} \, \mathrm{d}a + \int_{\mathcal{S}} \frac{\mathcal{R}_0}{J} \, \eta_0 \, \mathrm{d}v + \int_{\mathcal{S}} \rho \, \mathcal{S}_0 \, \mathrm{d}v, \tag{3.73}$$

where the first two terms are inner entropy sources and entropy fluxes across the surface, which are assumed to be related via the absolute temperature $\theta > 0$ in Kelvin to the heat source r_0 and the heat flux $\boldsymbol{q}$, respectively. The third term is associated to the entropy production by addition of new material and the fourth one is an additional entropy source, which is included following Himpel, Kuhl, et al. (2005) and Himpel (2007) to take further non-mechanical, irreversible processes related to growth and remodeling into account. Reformulation of Eq. 3.72 by integrating over the reference configuration and using Eq. 3.17, Eq. 3.37 and the balance of mass from Eq. 3.41 as well as Eq. 3.67 and the divergence theorem leads to the local form

$$\bar{\rho}_0 \, \dot{\eta}_0 - \frac{\bar{\rho}_0 \, r_0}{\theta} + \mathrm{Div}\left[\frac{\boldsymbol{q}_0}{\theta}\right] - \bar{\rho}_0 \, \mathcal{S}_0 \geq 0. \tag{3.74}$$

The divergence term can be evaluated according to

$$\mathrm{Div}\left[\frac{\boldsymbol{q}_0}{\theta}\right] = \frac{1}{\theta}\,\mathrm{Div}[\boldsymbol{q}_0] + \boldsymbol{q}_0 \cdot \mathrm{Grad}\left[\frac{1}{\theta}\right] = \frac{1}{\theta}\,\mathrm{Div}[\boldsymbol{q}_0] - \frac{1}{\theta^2}\,\boldsymbol{q}_0 \cdot \mathrm{Grad}[\theta] \tag{3.75}$$

and the local balance of energy from Eq. 3.71 provides an expression for $\mathrm{Div}[\boldsymbol{q}_0]$. Inserting both into Eq. 3.74 yields

$$\bar{\rho}_0\,(\theta\,\dot{\eta}_0 - \dot{e}) + \tfrac{1}{2}\,\boldsymbol{S} : \dot{\boldsymbol{C}} - \frac{1}{\theta}\,\boldsymbol{q}_0 \cdot \mathrm{Grad}[\theta] - \theta\,\bar{\rho}_0\,\mathcal{S}_0 \geq 0. \tag{3.76}$$

Now, the existence of a scalar-valued free Helmholtz energy $\bar{\psi} := e - \theta\,\eta_0$, defined per unit reference mass, is postulated. An alternative representation of the local form of the entropy inequality is then obtained as

$$\mathcal{D} := -\bar{\rho}_0\left(\dot{\bar{\psi}} + \dot{\theta}\,\eta_0\right) + \tfrac{1}{2}\,\boldsymbol{S} : \dot{\boldsymbol{C}} - \frac{1}{\theta}\,\boldsymbol{q}_0 \cdot \mathrm{Grad}[\theta] - \theta\,\bar{\rho}_0\,\mathcal{S}_0 \geq 0 \tag{3.77}$$

with $\mathcal{D}$ denoting the internal dissipation. For isothermal processes with $\dot{\theta} = 0$ and $\boldsymbol{q}_0 = \boldsymbol{0}$, the entropy inequality reduces to

$$\mathcal{D} := \tfrac{1}{2}\,\boldsymbol{S} : \dot{\boldsymbol{C}} - \bar{\rho}_0\,\dot{\bar{\psi}} - \theta\,\bar{\rho}_0\,\mathcal{S}_0 \geq 0. \tag{3.78}$$

Assuming that the free energy $\bar{\psi}$ is a function of the right Cauchy-Green tensor $\boldsymbol{C}$, a set of n_a scalar variables a_i and a set of $n_{\boldsymbol{B}}$ tensor-valued variables $\boldsymbol{B}_i$, i. e. $\bar{\psi} = \bar{\psi}(\boldsymbol{C}, a_i, \boldsymbol{B}_i)$, its time derivative is given by

$$\dot{\bar{\psi}} = \frac{\partial \bar{\psi}}{\partial \boldsymbol{C}} : \dot{\boldsymbol{C}} + \sum_{i=1}^{n_a} \frac{\partial \bar{\psi}}{\partial a_i}\,\dot{a}_i + \sum_{i=1}^{n_{\boldsymbol{B}}} \frac{\partial \bar{\psi}}{\partial \boldsymbol{B}_i} : \dot{\boldsymbol{B}}_i. \tag{3.79}$$

Inserting this derivative into Eq. 3.78 results in

$$\left[\tfrac{1}{2}\,\boldsymbol{S} - \bar{\rho}_0\,\frac{\partial \bar{\psi}}{\partial \boldsymbol{C}}\right] : \dot{\boldsymbol{C}} - \bar{\rho}_0\left[\sum_i \frac{\partial \bar{\psi}}{\partial a_i}\,\dot{a}_i + \sum_j \frac{\partial \bar{\psi}}{\partial \boldsymbol{B}_j} : \dot{\boldsymbol{B}}_j + \theta\,\mathcal{S}_0\right] \geq 0, \tag{3.80}$$

where the second bracket term might be zero in particular situations. In order to satisfy the entropy inequality for any arbitrary process, where aside from that $\dot{\boldsymbol{C}}$ might be negative, the standard argument of rational continuum mechanics is to require the first bracket term to be zero. From this condition, the constraint

$$\boldsymbol{S} = 2\,\bar{\rho}_0\,\frac{\partial \bar{\psi}}{\partial \boldsymbol{C}} \tag{3.81}$$

for the construction of constitutive equations for the stresses is obtained. For the formulation of a free energy function that is able to describe well the desired material behavior and leads to theoretically proper constitutive equations, further guidance is provided by fundamental mechanical principles of material modeling and by basic considerations on the treatment of material symmetries.

3.4 Confinements for the construction of constitutive equations

A material that postulates the existence of a scalar-valued Helmholtz free energy function $\bar{\psi}$ is denoted as hyperelastic material. Within the theory of finite hyperelasticity, a wide range of physical phenomena can be described as for instance presented by Truesdell & Noll (1965/1992) or Holzapfel (2000). In spite of the constraint in Eq. 3.81, which simplifies the determination of the stress tensor and holds for all hyperelastic materials, the development of constitutive equations remains a challenging task. Further restrictions can be deduced from fundamental principles of material modeling and from material symmetries. In the following, only principles that are immediately relevant for the constitutive equations used in this work are mentioned. More principles and details are amongst others given by Truesdell & Noll (1965/1992) or Altenbach (2012, pp. 218–221).

Principle of physical consistency. Constitutive equations are not allowed to contradict the balance equations and, in order to be also thermodynamically consistent, have to fulfill the entropy inequality.

Principle of causality. Following the principle of cause and effect, motion and temperature are usually chosen as independent variables in thermomechanical continua. Other state variables like stresses, heat fluxes, energy and entropy can be identified from those primary variables and are therefore denoted as dependent variables. In this work, isothermal conditions are presumed and thus only motion remains as independent variable.

Principle of determinism. The actual values of the thermomechanical state variables at one material point of the continuum are determined by the actual load and by the history of the independent state variables at all material points, but do not depend on future values.

Principle of local action. The dependency of the state variables of one material point on all material points can be concretized by the principle of local action, which states that long-distance effects can be neglected and only material points in the direct neighborhood have to be taken into account. In consequence, there is no need of including higher-order spatial derivatives and it is thus sufficient to include the deformation gradient and, if thermal effects are considered, the temperature as well as its gradient.

Principle of material frame indifference. The behavior of a material is required to be independent on the observer and is therefore not allowed to be affected by rigid body rotations applied to the actual configuration. With $\boldsymbol{Q} \in \mathrm{SO}(3)$ denoting an orthogonal tensor from the special orthogonal group SO(3) of all rotations, i. e. $\boldsymbol{Q}^{-1} = \boldsymbol{Q}^{\mathrm{T}}$ and $\det[\boldsymbol{Q}] = 1$, a rotated position vector $\boldsymbol{x}^{+}$ is related to the position vector $\boldsymbol{x} = \boldsymbol{F}\boldsymbol{X}$ through $\boldsymbol{x}^{+} = \boldsymbol{Q}\boldsymbol{x} = \boldsymbol{Q}\boldsymbol{F}\boldsymbol{X}$. For the rotation of a second-order tensor $\boldsymbol{A}$, the relation $\boldsymbol{A}^{+} = \boldsymbol{Q}\boldsymbol{A}\boldsymbol{Q}^{\mathrm{T}}$ can be shown if $\boldsymbol{A}^{+}$ is represented as the dyadic product of two rotated vectors.
Assuming that both observers viewing the actual position vector as $\boldsymbol{x}$ and $\boldsymbol{x}^{+}$ refer to the same reference configuration, the identity $\boldsymbol{X}^{+} = \boldsymbol{X}$ holds and the deformation gradient relating $\boldsymbol{X}^{+}$ to $\boldsymbol{x}^{+}$ can be identified as $\boldsymbol{F}^{+} = \boldsymbol{Q}\boldsymbol{F} \neq \boldsymbol{Q}\boldsymbol{F}\boldsymbol{Q}^{\mathrm{T}}$. Thus, the deformation gradient is not a frame-indifferent tensor and a formulation of constitutive relations based on a free energy function $\bar{\psi}(\boldsymbol{F})$ would involve further action in order to assure the frame indifference of the stress tensor. In

contrast to $\boldsymbol{F}$, the Cauchy-Green tensor with $\boldsymbol{C}^+ = \boldsymbol{F}^{+\mathrm{T}}\boldsymbol{F}^+ = \boldsymbol{F}^{\mathrm{T}}\boldsymbol{Q}^{\mathrm{T}}\boldsymbol{Q}\boldsymbol{F} = \boldsymbol{F}^{\mathrm{T}}\boldsymbol{F} = \boldsymbol{C}$ proves to be even entirely independent on the observer.
With reference to Fig. 3.4 it can be stated that the same holds for the tensor $\boldsymbol{C}_{\mathrm{e}}$. If the free energy function is thus formulated as a function of $\boldsymbol{C}$ or $\boldsymbol{C}_{\mathrm{e}}$, material frame indifference is automatically ensured. Since growth is not assumed to generate stresses, which means that the intermediate configuration $\mathcal{B}_{\mathrm{i}}$ is per definition stress-free, the elastic part of the deformation has to be considered as input variable. For this reason, the functional dependence $\bar{\psi} = \bar{\psi}(\boldsymbol{C}_{\mathrm{e}})$ is presumed.

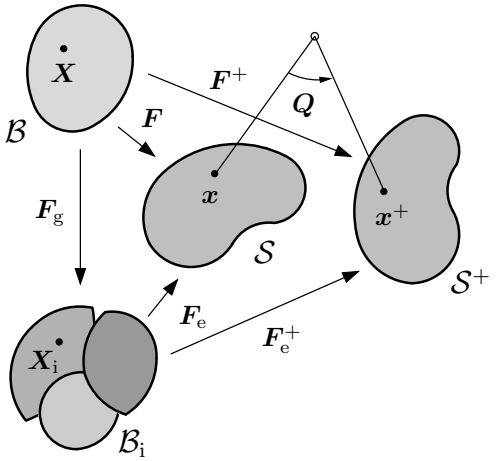

Figure 3.4: Application of a rigid body rotation to the actual configuration shows that neither $\boldsymbol{F}$ nor $\boldsymbol{F}_{\mathrm{e}}$ with their counterparts $\boldsymbol{F}^+ = \boldsymbol{Q}\boldsymbol{F}$ and $\boldsymbol{F}_{\mathrm{e}}^+ = \boldsymbol{Q}\boldsymbol{F}_{\mathrm{e}}$ are frame-indifferent tensors. The deformation tensors $\boldsymbol{C}$ and $\boldsymbol{C}_{\mathrm{e}}$ however do not at all depend on the frame of reference.

Modeling of material symmetries in the framework of invariant formulation. Further restrictions on the dependence of the free energy function $\bar{\psi}$ on the deformation tensor $\boldsymbol{C}_{\mathrm{e}}$ are imposed by special symmetries of the material behavior, which are characterized by the symmetry group $\mathcal{G}$ of the considered material. The symmetry group contains all rotations $\boldsymbol{Q}$ of the reference configuration that do not affect the material response. If for example an isotropic material behavior is postulated, not any rigid body rotation $\boldsymbol{Q} \in \mathrm{SO}(3)$ applied to the reference configuration is allowed to have an effect on the constitutive response and thus the symmetry group of such a material is $\mathcal{G}^{\mathrm{iso}} = \mathrm{SO}(3)$.

In the framework of multiplicative growth, only the elastic part $\boldsymbol{F}_{\mathrm{e}}$ of the deformation is assumed to generate stresses, which means that the rotation has to be applied to both stress-free configurations $\mathcal{B}$ and $\mathcal{B}_{\mathrm{i}}$ in order to investigate its effect on the material response. This issue is illustrated in Fig. 3.5, where the reference and the intermediate configuration are rotated by the same orthogonal tensor $\boldsymbol{Q}$ such that the rotated position vectors are given by $\boldsymbol{X}^* = \boldsymbol{Q}\boldsymbol{X}$ and $\boldsymbol{X}_{\mathrm{i}}^* = \boldsymbol{Q}\boldsymbol{X}_{\mathrm{i}}$. To identify the deformation gradient $\boldsymbol{F}^*$ and its elastic part $\boldsymbol{F}_{\mathrm{e}}^*$, the position vector $\boldsymbol{X}$ in $\boldsymbol{x} = \boldsymbol{F}\boldsymbol{X}$ has to be replaced by alternative expressions involving $\boldsymbol{X}^*$ and $\boldsymbol{X}_{\mathrm{i}}^*$. With $\boldsymbol{X} = \boldsymbol{Q}^{\mathrm{T}}\boldsymbol{X}^*$ and $\boldsymbol{X}_{\mathrm{i}}^* = \boldsymbol{Q}\boldsymbol{X}_{\mathrm{i}} = \boldsymbol{Q}\boldsymbol{F}_{\mathrm{g}}\boldsymbol{X}$ solved for $\boldsymbol{X}$, the wanted tensors can be found from

$$\boldsymbol{x} = \boldsymbol{F}\boldsymbol{X} = \boldsymbol{F}\boldsymbol{Q}^{\mathrm{T}}\boldsymbol{X}^* = \boldsymbol{F}^*\boldsymbol{X}^* \qquad \Rightarrow \quad \boldsymbol{F}^* = \boldsymbol{F}\boldsymbol{Q}^{\mathrm{T}}, \tag{3.82}$$

$$\boldsymbol{x} = \boldsymbol{F}\boldsymbol{X} = \boldsymbol{F}\boldsymbol{F}_{\mathrm{g}}^{-1}\boldsymbol{Q}^{\mathrm{T}}\boldsymbol{X}_{\mathrm{i}}^* = \boldsymbol{F}_{\mathrm{e}}\boldsymbol{Q}^{\mathrm{T}}\boldsymbol{X}_{\mathrm{i}}^* = \boldsymbol{F}_{\mathrm{e}}^*\boldsymbol{X}_{\mathrm{i}}^* \qquad \Rightarrow \quad \boldsymbol{F}_{\mathrm{e}}^* = \boldsymbol{F}_{\mathrm{e}}\boldsymbol{Q}^{\mathrm{T}}. \tag{3.83}$$

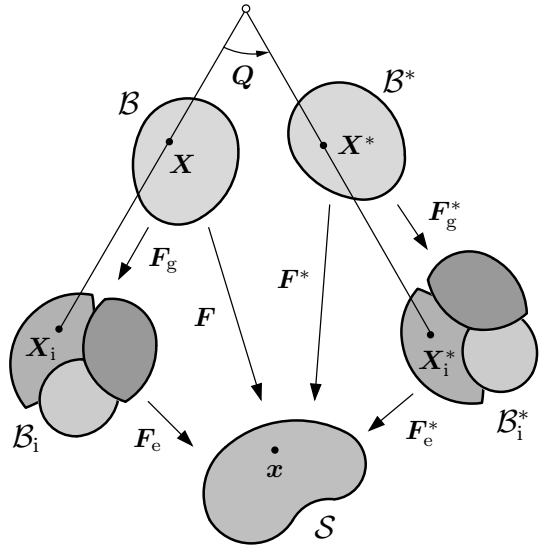

Figure 3.5: Application of a rigid body rotation to the stress-free configurations leads to the deformation gradients $\boldsymbol{F}^* = \boldsymbol{F}\boldsymbol{Q}^\mathrm{T}$ and $\boldsymbol{F}_\mathrm{e}^* = \boldsymbol{F}_\mathrm{e}\boldsymbol{Q}^\mathrm{T}$ and thus to the deformation tensors $\boldsymbol{C}^* = \boldsymbol{Q}\boldsymbol{C}\boldsymbol{Q}^\mathrm{T}$ and $\boldsymbol{C}_\mathrm{e}^* = \boldsymbol{Q}\boldsymbol{C}_\mathrm{e}\boldsymbol{Q}^\mathrm{T}$. The material response must not be affected if $\boldsymbol{Q} \in \mathcal{G}$. For isotropic materials with $\mathcal{G}^\mathrm{iso} = \mathrm{SO}(3)$, this is ensured if the constitutive equations are formulated in terms of coordinate-invariant measures of $\boldsymbol{C}$ or $\boldsymbol{C}_\mathrm{e}$.

The associated deformation tensors are obtained as $\boldsymbol{C}^* = \boldsymbol{F}^{*\mathrm{T}}\boldsymbol{F}^* = \boldsymbol{Q}\boldsymbol{C}\boldsymbol{Q}^\mathrm{T}$ and $\boldsymbol{C}_\mathrm{e}^* = \boldsymbol{Q}\boldsymbol{C}_\mathrm{e}\boldsymbol{Q}^\mathrm{T}$ and are therefore given by conventional rotation of $\boldsymbol{C}$ and $\boldsymbol{C}_\mathrm{e}$. Consequently, measures of the deformation tensors which are invariant with respect to all rotations $\boldsymbol{Q} \in \mathcal{G}$ have to be chosen in order to guarantee the material symmetries asked for by the symmetry group $\mathcal{G}$, which means to fulfill

$$\bar{\psi}(\boldsymbol{C}_\mathrm{e}) = \bar{\psi}(\boldsymbol{Q}\boldsymbol{C}_\mathrm{e}\boldsymbol{Q}^\mathrm{T}) \quad \forall \quad \boldsymbol{Q} \in \mathcal{G} \tag{3.84}$$

for energy functions formulated in terms of $\boldsymbol{C}_\mathrm{e}$. For isotropic materials with $\mathcal{G}^\mathrm{iso} = \mathrm{SO}(3)$, only arguments which are completely independent on the coordinate system are thus acceptable. According to the representation theorem for invariants, which is for example proved by Truesdell & Noll (1965/1992), isotropic materials can hence be described by a free energy function $\bar{\psi}(\boldsymbol{C}_\mathrm{e}) = \bar{\psi}(I_1, I_2, I_3)$ formulated in terms of the principal invariants

$$I_1 := \mathrm{tr}[\boldsymbol{C}_\mathrm{e}], \qquad I_2 := \tfrac{1}{2}\left(I_1^2 - \mathrm{tr}[\boldsymbol{C}_\mathrm{e}^2]\right) = \mathrm{tr}[\mathrm{cof}\,\boldsymbol{C}_\mathrm{e}], \qquad I_3 := \det[\boldsymbol{C}_\mathrm{e}] \tag{3.85}$$

of the deformation tensor $\boldsymbol{C}_\mathrm{e}$. These three invariants constitute an integrity basis of $\boldsymbol{C}_\mathrm{e}$ with respect to the symmetry group $\mathcal{G}^\mathrm{iso}$, which means that they are sufficient to express any further invariant of $\boldsymbol{C}_\mathrm{e}$ subjected to rotations $\boldsymbol{Q} \in \mathcal{G}^\mathrm{iso}$, see e. g. Betten & Helisch (1992). Alternatively, the invariants

$$J_1 := \mathrm{tr}[\boldsymbol{C}_\mathrm{e}], \qquad J_2 := \mathrm{tr}[\boldsymbol{C}_\mathrm{e}^2], \qquad J_3 := \mathrm{tr}[\boldsymbol{C}_\mathrm{e}^3] \tag{3.86}$$

could be used, which are related to the previous ones by

$$J_1 = I_1, \qquad J_2 = I_1^2 - 2\,I_2, \qquad J_3 = I_1^3 - 3\,I_1\,I_2 + 3\,I_3. \tag{3.87}$$

Considering as an example the invariants

$$J_1^* = \mathrm{tr}[\boldsymbol{C}_\mathrm{e}^*] = \boldsymbol{Q}\boldsymbol{C}_\mathrm{e}\boldsymbol{Q}^\mathrm{T} : \boldsymbol{I} = \boldsymbol{Q}^\mathrm{T}\boldsymbol{Q} : \boldsymbol{C}_\mathrm{e} = J_1, \tag{3.88}$$

$$J_2^* = \mathrm{tr}[\boldsymbol{C}_\mathrm{e}^{*2}] = \boldsymbol{Q}\boldsymbol{C}_\mathrm{e}\boldsymbol{Q}^\mathrm{T}\boldsymbol{Q}\boldsymbol{C}_\mathrm{e}\boldsymbol{Q}^\mathrm{T} : \boldsymbol{I} = \boldsymbol{Q}\boldsymbol{C}_\mathrm{e}^2\boldsymbol{Q}^\mathrm{T} : \boldsymbol{I} = \boldsymbol{Q}^\mathrm{T}\boldsymbol{Q} : \boldsymbol{C}_\mathrm{e}^2 = J_2, \tag{3.89}$$

$$\vdots$$

$$J_n^* = \mathrm{tr}[\boldsymbol{C}_\mathrm{e}^{*n}] = \boldsymbol{Q}\boldsymbol{C}_\mathrm{e}^n\boldsymbol{Q}^\mathrm{T} : \boldsymbol{I} = \boldsymbol{Q}^\mathrm{T}\boldsymbol{Q} : \boldsymbol{C}_\mathrm{e}^n = J_n, \tag{3.90}$$

it can be stated that they are indeed independent on each rotation of the stress-free configuration. For the construction of constitutive equations for soft biological tissues, another type of symmetry is of crucial importance, namely the one of a material with embedded fibers. If an isotropic material is reinforced with fibers uniformly aligned in one specific direction, its stiffness in that direction will increase. Since the behavior in the transverse plane of the preferred direction will remain isotropic, such a material is said to behave transversely isotropically. The symmetry group $\mathcal{G}^\mathrm{ti} = \{\boldsymbol{Q} \in \mathrm{SO}(3) \,|\, \boldsymbol{Q}\boldsymbol{A} = \pm\boldsymbol{A}\}$ of a transversely isotropic material thus consists of all rotations about a preferred direction, which is defined in the reference configuration by a unit vector $\boldsymbol{A}$ with $|\boldsymbol{A}| = 1$. Due to growth, the constitute equation has to be formulated based on the intermediate configuration and therefore the preferred direction in this configuration, i. e.

$$\boldsymbol{A}_\mathrm{i} = \frac{\boldsymbol{F}_\mathrm{g}\boldsymbol{A}}{|\boldsymbol{F}_\mathrm{g}\boldsymbol{A}|} \qquad \text{with} \qquad |\boldsymbol{A}_\mathrm{i}| = 1 \tag{3.91}$$

has to be considered. However, only information on the orientation but not the sign of those vectors is relevant for the constitutive equation. For this reason, a sign-independent, quadratic form of the preferred direction is defined as

$$\boldsymbol{M}_\mathrm{i} := \boldsymbol{A}_\mathrm{i} \otimes \boldsymbol{A}_\mathrm{i} = (-\boldsymbol{A}_\mathrm{i}) \otimes (-\boldsymbol{A}_\mathrm{i}) \qquad \text{with} \qquad \mathrm{tr}[\boldsymbol{M}_\mathrm{i}] = |\boldsymbol{A}_\mathrm{i}|^2 = 1 \tag{3.92}$$

and referred to as structural tensor since it contains the relevant information on the material's structure. The structural tensors defined in the intermediate and in the reference configuration are related through

$$\boldsymbol{M}_\mathrm{i} = \frac{\boldsymbol{F}_\mathrm{g}\boldsymbol{M}\boldsymbol{F}_\mathrm{g}^\mathrm{T}}{|\boldsymbol{F}_\mathrm{g}\boldsymbol{A}|^2} = \frac{\boldsymbol{F}_\mathrm{g}\boldsymbol{M}\boldsymbol{F}_\mathrm{g}^\mathrm{T}}{(\boldsymbol{F}_\mathrm{g}\boldsymbol{M}) : \boldsymbol{F}_\mathrm{g}} \qquad \text{with} \qquad \boldsymbol{M} := \boldsymbol{A} \otimes \boldsymbol{A}. \tag{3.93}$$

The free energy function $\bar{\psi}$ of a growing transversely isotropic material is now supposed to be a function of $\boldsymbol{C}_\mathrm{e}$ and $\boldsymbol{M}_\mathrm{i}$, which is claimed to be independent on a rotation $\boldsymbol{Q} \in \mathcal{G}^\mathrm{ti}$ of the intermediate configuration. With $\boldsymbol{A}_\mathrm{i}^* = \boldsymbol{Q}\boldsymbol{A}_\mathrm{i}$ and $\boldsymbol{M}_\mathrm{i}^* = \boldsymbol{Q}\boldsymbol{A}_\mathrm{i} \otimes \boldsymbol{Q}\boldsymbol{A}_\mathrm{i} = \boldsymbol{Q}\boldsymbol{A}_\mathrm{i} \otimes \boldsymbol{A}_\mathrm{i}\boldsymbol{Q}^\mathrm{T} = \boldsymbol{Q}\boldsymbol{M}_\mathrm{i}\boldsymbol{Q}^\mathrm{T}$, the requirement imposed by material symmetry gets

$$\bar{\psi}(\boldsymbol{C}_\mathrm{e}, \boldsymbol{M}_\mathrm{i}) = \bar{\psi}(\boldsymbol{Q}\boldsymbol{C}_\mathrm{e}\boldsymbol{Q}^\mathrm{T}, \boldsymbol{Q}\boldsymbol{M}_\mathrm{i}\boldsymbol{Q}^\mathrm{T}) \quad \forall \quad \boldsymbol{Q} \in \mathcal{G}^\mathrm{ti}, \tag{3.94}$$

and, by comparison with Eq. 3.84 and the subsequent explanations, it can be stated that this requirement is even met for all rotations $\boldsymbol{Q} \in \mathrm{SO}(3)$ if coordinate-invariant measures of $\boldsymbol{C}_\mathrm{e}$ and $\boldsymbol{M}_\mathrm{i}$ are used. To obtain an integrity basis for these two symmetric second-order tensors, further invariants have to be included in addition to those given in Eq. 3.85 or Eq. 3.86, see for example Spencer & Rivlin (1958) or Truesdell & Noll (1965/1992). On the one hand, three independent invariants of $\boldsymbol{M}_\mathrm{i}$ are formally required. Practically, they are obsolete because they are equal to 1 or 0 due to the property $|\boldsymbol{A}_\mathrm{i}| = 1$. On the other hand, the mixed invariants

$$J_4 = \mathrm{tr}[\boldsymbol{C}_\mathrm{e}\boldsymbol{M}_\mathrm{i}], \qquad J_5 = \mathrm{tr}[\boldsymbol{C}_\mathrm{e}^2\boldsymbol{M}_\mathrm{i}], \qquad J_6 = \mathrm{tr}[\boldsymbol{C}_\mathrm{e}\boldsymbol{M}_\mathrm{i}^2], \qquad J_7 = \mathrm{tr}[\boldsymbol{C}_\mathrm{e}^2\boldsymbol{M}_\mathrm{i}^2] \tag{3.95}$$

of $\boldsymbol{C}_\mathrm{e}$ and $\boldsymbol{M}_\mathrm{i}$ have to be added. Again due to $|\boldsymbol{A}_\mathrm{i}| = 1$, the identities $J_6 = J_4$ and $J_7 = J_5$ hold, such that the Helmholtz energy for a transversely isotropic material can be formulated in terms of $\bar{\psi}(\boldsymbol{C}_\mathrm{e}, \boldsymbol{M}_\mathrm{i}) = \bar{\psi}(I_1, I_2, I_3, J_4, J_5)$. Since the structural tensor $\boldsymbol{M}_\mathrm{i}$ is defined in the intermediate configuration and thus not affected by a change of the observer, the principle of material frame difference is still satisfied.

Based on the principles and considerations above, the functional form of the free energy function $\bar{\psi}$ can be specified. In order to fulfill the principle of material frame indifference a priori, it is formulated in terms of the elastic part $\boldsymbol{C}_\mathrm{e}$ of the Cauchy-Green tensor. Assuming that the orthotropic behavior of arterial tissues can be idealized by the superposition of one isotropic and several transversely isotropic contributions, which might be related to an isotropic ground matrix and a number n_f of embedded fiber families, the free energy function additionally has to depend on a set of structural tensors $\boldsymbol{M}_\mathrm{i}^{(a)}$ with $a \in [1, \ldots, n_\mathrm{f}]$. If the interaction between the fiber families is assumed to be negligible, no mixed invariants of their structural tensors have to be included and the restrictions imposed by the material symmetries can be satisfied by formulating $\bar{\psi}$ as a function of the isotropic invariants I_1, I_2 and I_3 and the transversely isotropic invariants $J_4^{(a)}$ and $J_5^{(a)}$ for each fiber family. Since the Helmholtz free energy $\bar{\psi}$ first introduced in Eq. 3.77 is defined per unit reference mass, it is furthermore assumed to depend on the density $\bar{\rho}_0$ as proposed by Himpel, Kuhl, et al. (2005). Finally, the free energy function is thus supposed to have the structure

$$\bar{\psi} = \bar{\psi}(\bar{\rho}_0, \boldsymbol{C}_\mathrm{e}, \boldsymbol{M}_\mathrm{i}^{(a)}) = \bar{\psi}(\bar{\rho}_0, I_1, I_2, I_3, J_4^{(a)}, J_5^{(a)}) \qquad \text{for} \qquad a \in [1, \ldots, n_\mathrm{f}] \tag{3.96}$$

with the principal invariants I_1, I_2 and I_3 given in Eq. 3.85 and the mixed invariants $J_4^{(a)}$ and $J_5^{(a)}$ given in Eq. 3.95.

3.5 Evaluation of the entropy inequality

Following the demands imposed by the material behavior of arterial tissues and the principles of material modeling, the free Helmholtz energy $\bar{\psi}$ is assumed to be a function of the deformation tensor $\boldsymbol{C}_\mathrm{e}$, a set of n_f structural tensors $\boldsymbol{M}_\mathrm{i}^{(a)}$ and the density $\bar{\rho}_0$ relating the grown mass, which equals the actual mass, to the reference volume. With

$$\bar{\psi} = \bar{\psi}(\bar{\rho}_0, \boldsymbol{C}_\mathrm{e}, \boldsymbol{M}_\mathrm{i}^{(a)}) = \bar{\psi}(\bar{\rho}_0, \boldsymbol{C}, \boldsymbol{F}_\mathrm{g}, \boldsymbol{M}^{(a)}), \tag{3.97}$$

see Eq. 3.22 and Eq. 3.93, the Clausius-Duhem inequality from Eq. 3.80 can be specified with the balance of mass from Eq. 3.40 as

$$\left[\tfrac{1}{2}\,\boldsymbol{S} - \bar{\rho}_0\,\frac{\partial \bar{\psi}}{\partial \boldsymbol{C}}\right] : \dot{\boldsymbol{C}} - \bar{\rho}_0 \left[\frac{\partial \bar{\psi}}{\partial \boldsymbol{F}_\mathrm{g}} : \dot{\boldsymbol{F}}_\mathrm{g} + \sum_{a=1}^{n_\mathrm{f}} \frac{\partial \bar{\psi}}{\partial \boldsymbol{M}^{(a)}} : \dot{\boldsymbol{M}}^{(a)} + \frac{\partial \bar{\psi}}{\partial \bar{\rho}_0}\,\mathcal{R}_0 + \theta\,\mathcal{S}_0\right] \geq 0, \tag{3.98}$$

which, as already stated, leads to the equation $\boldsymbol{S} = 2\,\bar{\rho}_0\,\partial\bar{\psi}/\partial\boldsymbol{C}$ for the stresses. Since stresses are assumed to result only from the elastic part of the deformation, a functional dependency

on $\boldsymbol{C}_\mathrm{e}$ is rather desired than on $\boldsymbol{C}$. This can be achieved by reformulating the derivative of $\bar{\psi}$ with respect to $\boldsymbol{C}$ according to

$$\frac{\partial \bar{\psi}}{\partial \boldsymbol{C}} = \frac{\partial \bar{\psi}}{\partial \boldsymbol{C}_\mathrm{e}} : \frac{\partial \boldsymbol{C}_\mathrm{e}}{\partial \boldsymbol{C}} = \frac{\partial \bar{\psi}}{\partial \boldsymbol{C}_\mathrm{e}} : \left(\boldsymbol{F}_\mathrm{g}^{-\mathrm{T}} \boxtimes \boldsymbol{F}_\mathrm{g}^{-\mathrm{T}}\right) = \boldsymbol{F}_\mathrm{g}^{-1} \frac{\partial \bar{\psi}}{\partial \boldsymbol{C}_\mathrm{e}} \boldsymbol{F}_\mathrm{g}^{-\mathrm{T}}, \tag{3.99}$$

where the elastic part of the deformation defined in Eq. 3.22 has been expressed as $\boldsymbol{C}_\mathrm{e} = \boldsymbol{F}_\mathrm{g}^{-\mathrm{T}} \boldsymbol{C} \boldsymbol{F}_\mathrm{g}^{-1} = \left(\boldsymbol{F}_\mathrm{g}^{-\mathrm{T}} \boxtimes \boldsymbol{F}_\mathrm{g}^{-\mathrm{T}}\right) : \boldsymbol{C}$ with the help of the calculation rule mentioned in Eq. A.5 of Appendix A. Defining the 2nd Piola-Kirchhoff stress in the intermediate configuration as

$$\boldsymbol{S}_\mathrm{e} := 2\, \bar{\rho}_0 \frac{\partial \bar{\psi}}{\partial \boldsymbol{C}_\mathrm{e}} \tag{3.100}$$

in analogy to Eq. 3.81, the pullback operation $\boldsymbol{S} = \boldsymbol{F}_\mathrm{g}^{-1} \boldsymbol{S}_\mathrm{e} \boldsymbol{F}_\mathrm{g}^{-\mathrm{T}}$ can be recognized from Eq. 3.99. Moreover, it can be concluded, that a strain energy function $\psi = \bar{\rho}_0\, \bar{\psi}$ defined per unit reference volume can be used for the computation of the stresses, which is due to the isothermal conditions (Humphrey, 2002, p. 92). Then, the equations

$$\boldsymbol{S} = 2 \frac{\partial \psi}{\partial \boldsymbol{C}} \qquad \text{and} \qquad \boldsymbol{S}_\mathrm{e} = 2 \frac{\partial \psi}{\partial \boldsymbol{C}_\mathrm{e}} \tag{3.101}$$

hold true. From Eq. 3.98, the reduced dissipation inequality

$$\mathcal{D}_\mathrm{red} = -\bar{\rho}_0 \frac{\partial \bar{\psi}}{\partial \boldsymbol{F}_\mathrm{g}} : \dot{\boldsymbol{F}}_\mathrm{g} - \bar{\rho}_0 \sum_{a=1}^{n_\mathrm{f}} \frac{\partial \bar{\psi}}{\partial \boldsymbol{M}^{(a)}} : \dot{\boldsymbol{M}}^{(a)} - \bar{\rho}_0 \frac{\partial \bar{\psi}}{\partial \bar{\rho}_0} \mathcal{R}_0 - \theta\, \bar{\rho}_0\, \mathcal{S}_0 \geq 0 \tag{3.102}$$

is obtained. Using the symmetry of $\boldsymbol{C}_\mathrm{e}$ stated in Sec. 3.1.2, which also implies symmetry of $\partial \bar{\psi} / \partial \boldsymbol{C}_\mathrm{e}$, and the derivatives provided in Eq. A.21 and Eq. A.19, the derivative

$$\frac{\partial \bar{\psi}}{\partial \boldsymbol{F}_\mathrm{g}} = \frac{\partial \bar{\psi}}{\partial \boldsymbol{C}_\mathrm{e}} : \frac{\partial \boldsymbol{C}_\mathrm{e}}{\partial \boldsymbol{F}_\mathrm{g}} = \frac{\partial \bar{\psi}}{\partial \boldsymbol{C}_\mathrm{e}} : \frac{\partial \left(\boldsymbol{F}_\mathrm{g}^{-\mathrm{T}} \boldsymbol{C} \boldsymbol{F}_\mathrm{g}^{-1}\right)}{\partial \boldsymbol{F}_\mathrm{g}} = -2\, \boldsymbol{C}_\mathrm{e} \frac{\partial \bar{\psi}}{\partial \boldsymbol{C}_\mathrm{e}} \boldsymbol{F}_\mathrm{g}^{-\mathrm{T}} \tag{3.103}$$

can be derived in index notation. Inserting this in Eq. 3.102 and using the relation $\left(\boldsymbol{C}_\mathrm{e} \boldsymbol{S}_\mathrm{e} \boldsymbol{F}_\mathrm{g}^{-\mathrm{T}}\right) : \dot{\boldsymbol{F}}_\mathrm{g} = \left(\boldsymbol{C}_\mathrm{e} \boldsymbol{S}_\mathrm{e} \boldsymbol{F}_\mathrm{g}^{-\mathrm{T}}\right) : (\boldsymbol{L}_\mathrm{g} \boldsymbol{F}_\mathrm{g}) = (\boldsymbol{C}_\mathrm{e} \boldsymbol{S}_\mathrm{e}) : \boldsymbol{L}_\mathrm{g}$, the inequality reads

$$\mathcal{D}_\mathrm{red} = (\boldsymbol{C}_\mathrm{e} \boldsymbol{S}_\mathrm{e}) : \boldsymbol{L}_\mathrm{g} - \bar{\rho}_0 \sum_{a=1}^{n_\mathrm{f}} \frac{\partial \bar{\psi}}{\partial \boldsymbol{M}^{(a)}} : \dot{\boldsymbol{M}}^{(a)} - \bar{\rho}_0 \frac{\partial \bar{\psi}}{\partial \bar{\rho}_0} \mathcal{R}_0 - \theta\, \bar{\rho}_0\, \mathcal{S}_0 \geq 0. \tag{3.104}$$

In order to replace the Helmholtz free energy function $\bar{\psi}$ defined per unit reference mass by the strain energy function $\psi = \bar{\rho}_0\, \bar{\psi}$ defined per unit reference volume, the remaining derivatives of $\bar{\psi}$ are computed as follows. For $\partial \bar{\psi} / \partial \boldsymbol{M}^{(a)}$, the expression

$$\frac{\partial \bar{\psi}}{\partial \boldsymbol{M}^{(a)}} = \frac{\partial \left(\bar{\rho}_0^{-1}\, \psi\right)}{\partial \boldsymbol{M}^{(a)}} = \frac{1}{\bar{\rho}_0} \frac{\partial \psi}{\partial \boldsymbol{M}^{(a)}} + \psi \frac{\partial \bar{\rho}_0^{-1}}{\partial \boldsymbol{F}_\mathrm{g}} : \frac{\partial \boldsymbol{F}_\mathrm{g}}{\partial \boldsymbol{M}^{(a)}} = \frac{1}{\bar{\rho}_0} \frac{\partial \psi}{\partial \boldsymbol{M}^{(a)}} - \frac{\psi}{\bar{\rho}_0} \boldsymbol{F}_\mathrm{g}^{-\mathrm{T}} : \frac{\partial \boldsymbol{F}_\mathrm{g}}{\partial \boldsymbol{M}^{(a)}} \tag{3.105}$$

is obtained, where $\partial \bar{\rho}_0^{-1} / \partial \boldsymbol{F}_\mathrm{g}$ has been computed with $\bar{\rho}_0 = J_\mathrm{g}\, \rho_\mathrm{i}$ from Eq. 3.37 and $\partial J_\mathrm{g} / \partial \boldsymbol{F}_\mathrm{g} = J_\mathrm{g}\, \boldsymbol{F}_\mathrm{g}^{-\mathrm{T}}$ according to

$$\frac{\partial \bar{\rho}_0^{-1}}{\partial \boldsymbol{F}_\mathrm{g}} = \frac{1}{\rho_\mathrm{i}} \frac{\partial J_\mathrm{g}^{-1}}{\partial \boldsymbol{F}_\mathrm{g}} = -\frac{1}{\rho_\mathrm{i}\, J_\mathrm{g}^2} \frac{\partial J_\mathrm{g}}{\partial \boldsymbol{F}_\mathrm{g}} = -\frac{1}{\rho_\mathrm{i}\, J_\mathrm{g}} \boldsymbol{F}_\mathrm{g}^{-\mathrm{T}} = -\frac{1}{\bar{\rho}_0} \boldsymbol{F}_\mathrm{g}^{-\mathrm{T}}. \tag{3.106}$$

Furthermore,

$$\frac{\partial \bar{\psi}}{\partial \bar{\rho}_0} = \frac{\partial \left(\bar{\rho}_0^{-1} \, \psi \right)}{\partial \bar{\rho}_0} = -\frac{\psi}{\bar{\rho}_0^2} \tag{3.107}$$

holds and the mass source $\mathcal{R}_0 = \bar{\rho}_0 \, \mathrm{tr}[\boldsymbol{L}_\mathrm{g}]$ is given by Eq. 3.43 for the assumption of pure mass growth with a constant density $\rho_\mathrm{i} = \rho_0$. Inserting all these terms in Eq. 3.104, the final form of the entropy inequality is

$$\mathcal{D}_\mathrm{red} = (\boldsymbol{C}_\mathrm{e} \boldsymbol{S}_\mathrm{e}) : \boldsymbol{L}_\mathrm{g} + \sum_{a=1}^{n_\mathrm{f}} \left(\psi \, \boldsymbol{F}_\mathrm{g}^{-\mathrm{T}} : \frac{\partial \boldsymbol{F}_\mathrm{g}}{\partial \boldsymbol{M}^{(a)}} - \frac{\partial \psi}{\partial \boldsymbol{M}^{(a)}} \right) : \dot{\boldsymbol{M}}^{(a)} + \psi \, \mathrm{tr}[\boldsymbol{L}_\mathrm{g}] - \theta \, \bar{\rho}_0 \, \mathcal{S}_0 \geq 0, \tag{3.108}$$

which can be solved for the additional entropy source $\mathcal{S}_0$.

4 Finite element method

With the balance equations specified in the previous chapter, a set of equations is available which in principle permits to compute the deformed state of a body charged by external loads. The balance of mass defines the relation between the mass densities or volumes in the reference and in the deformed state. From the balance of angular momentum, the precondition of symmetric stress tensors can be derived and the balance of energy leads, together with the entropy inequality, to a constraint for the constitutive equations which relate strains and stresses. The balance of linear momentum, $\bar{\rho}_0 \, \ddot{\boldsymbol{x}} = \bar{\rho}_0 \, \boldsymbol{b} + \mathrm{Div}[\boldsymbol{P}]$ as formula, brings everything together as it implicitly constitutes the connection between actual position $\boldsymbol{x}$ and stress. However, this equation represents a complex system of nonlinear partial differential equations due to the vectorial quantities, the twofold time derivative of $\boldsymbol{x}$ and the expression $\mathrm{Div}[\boldsymbol{P}]$, which involves a twofold derivative with respect to $\boldsymbol{x}$ and nonlinearity in $\boldsymbol{x}$. It has to be satisfied at each material point with its particular boundary conditions. The solution of this complex problem can in general not be achieved analytically. A standard numerical and thus approximate method for the solution of systems of differential equations is the finite element method. It subdivides the whole domain in individual subdomains, the elements, and thereby reduces the continuous problem to a finite number of discrete problems. The finite element method evolved simultaneously with the appearance of digital computers, which enabled the solution of high numbers of discrete problems and whose increasing power makes rise the complexity of methods and solved problems up to the present. In this chapter, the concepts of classical finite element method relevant for the numerical investigations of this work are summarized. Within those limits, only a small part of the whole powerful method, which has numerous enhancements, is covered. For information beyond that, extensive treatises on finite element method are available, for example by Zienkiewicz & Taylor (2000a and 2000b) and Wriggers (2008).

4.1 Basic principles of finite element method

Three basic steps are required to solve the balance of linear momentum by means of the finite element method. First, the original equation is replaced by a weak formulation, which transforms the vectorial into a scalar equation. Since this equation is still nonlinear in the solution variable and can in general not be solved analytically, numerical treatment involving linearization is pursued. In a final step, the linearized equation, which has to hold at each material point of the body, is discretized in order to reduce the infinite number of unknowns in the continuous problem to a finite number of unknowns at predefined nodal points, between which an interpolation is presumed. In this work, the standard displacement formulation is considered, where the nodal displacements are introduced as only unknowns. If not noted otherwise, the three-dimensional case with three degrees of freedom per node is described. Common vectors as $\boldsymbol{X}$ and $\boldsymbol{u}$ then have three components according to the three spatial dimensions. This will no longer apply in Sec. 4.2, where special finite elements for axisymmetric problems are discussed.

4.1.1 Weak form of the balance of linear momentum

As stated in Eq. 3.49, the local form of the balance of linear momentum requires that the set of differential equations

$$\mathrm{Div}[\boldsymbol{P}] + \bar{\rho}_0 \left(\boldsymbol{b} - \ddot{\boldsymbol{x}}\right) = \boldsymbol{0} \tag{4.1}$$

with $\boldsymbol{P} = \boldsymbol{F}\boldsymbol{S}$ and $\boldsymbol{S} = 2\,\partial\psi/\partial\boldsymbol{C}$ is fulfilled at each material point of the considered body. Together with the boundary conditions

$$\boldsymbol{u} = \bar{\boldsymbol{u}} \quad \text{on} \quad \partial\mathcal{B}_{\boldsymbol{u}} \qquad \text{and} \qquad \boldsymbol{T} = \boldsymbol{P}\boldsymbol{N} = \bar{\boldsymbol{T}} \quad \text{on} \quad \partial\mathcal{B}_{\boldsymbol{\sigma}} \tag{4.2}$$

for the displacements $\boldsymbol{u}$ and the stress vectors $\boldsymbol{T}$, prescribed on the respective surface areas $\partial\mathcal{B}_{\boldsymbol{u}}$ and $\partial\mathcal{B}_{\boldsymbol{\sigma}}$ of the body, this problem is referred to as strong form of the balance of linear momentum. In general, no closed analytical solution for the displacements $\boldsymbol{u}$ is available, such that approximating numerical methods like the finite element method have to be used. The finite element method rests upon a weak formulation of the above problem, which seeks to satisfy the momentum balance on average over the whole domain. To this end, Eq. 4.1 is multiplied by a weighting or test function $\delta\boldsymbol{u} = \{\delta\boldsymbol{u} | \delta\boldsymbol{u} = \boldsymbol{0} \text{ on } \partial\mathcal{B}_{\boldsymbol{u}}\}$ and integrated over the entire body, which leads to the scalar-valued equation

$$\int_{\mathcal{B}} \left(\mathrm{Div}[\boldsymbol{P}] + \bar{\rho}_0 \left(\boldsymbol{b} - \ddot{\boldsymbol{x}}\right)\right) \cdot \delta\boldsymbol{u}\,\mathrm{d}V = 0. \tag{4.3}$$

The test function $\delta\boldsymbol{u}$ is arbitrary. For this reason, it can also be interpreted as the difference between a displacement field $\tilde{\boldsymbol{u}}$ characterizing a virtual configuration in the direct neighborhood of the current configuration and the real displacement field $\boldsymbol{u}$, i. e. $\delta\boldsymbol{u} = \tilde{\boldsymbol{u}} - \boldsymbol{u}$ (cf. Holzapfel, 2000, pp. 372 f.). Denoting thus an arbitrary and infinitesimal, virtual change of $\boldsymbol{u}$, $\delta\boldsymbol{u}$ is then also referred to as variation of $\boldsymbol{u}$ or as virtual displacement field, which is independent on the real displacement $\boldsymbol{u}$. With $\mathrm{Div}[\boldsymbol{P}^{\mathrm{T}}\delta\boldsymbol{u}] = \mathrm{Div}[\boldsymbol{P}] \cdot \delta\boldsymbol{u} + \boldsymbol{P} : \mathrm{Grad}[\delta\boldsymbol{u}]$ and use of the divergence theorem $\int_{\mathcal{B}} \mathrm{Div}[\boldsymbol{P}^{\mathrm{T}}\delta\boldsymbol{u}]\,\mathrm{d}V = \int_{\partial\mathcal{B}_{\boldsymbol{\sigma}}} \boldsymbol{P}^{\mathrm{T}}\delta\boldsymbol{u} \cdot \boldsymbol{N}\,\mathrm{d}A$, the condition from Eq. 4.3 can be written as

$$\int_{\partial\mathcal{B}_{\boldsymbol{\sigma}}} \bar{\boldsymbol{T}} \cdot \delta\boldsymbol{u}\,\mathrm{d}A - \int_{\mathcal{B}} \boldsymbol{P} : \mathrm{Grad}[\delta\boldsymbol{u}]\,\mathrm{d}V + \int_{\mathcal{B}} \bar{\rho}_0 \left(\boldsymbol{b} - \ddot{\boldsymbol{x}}\right) \cdot \delta\boldsymbol{u}\,\mathrm{d}V = 0, \tag{4.4}$$

where the boundary condition $\boldsymbol{T} = \bar{\boldsymbol{T}}$ on $\partial\mathcal{B}_{\boldsymbol{\sigma}}$ has been taken into account. The second term can be reformulated by replacing $\mathrm{Grad}[\delta\boldsymbol{u}]$ by $\delta\boldsymbol{F}$, which are equivalent due to the property $\delta(\mathrm{Grad}[\boldsymbol{u}]) = \mathrm{Grad}[\delta\boldsymbol{u}]$, that is $\delta\boldsymbol{F} = \delta(\mathrm{Grad}[\boldsymbol{u}] + \boldsymbol{I}) = \mathrm{Grad}[\delta\boldsymbol{u}]$. Since the unit tensor does not depend on a virtual change of $\boldsymbol{u}$, it holds $\delta\boldsymbol{I} = \boldsymbol{0}$. The expression $\boldsymbol{P} : \delta\boldsymbol{F} = \boldsymbol{F}\boldsymbol{S} : \delta\boldsymbol{F}$ can then be written as $\boldsymbol{S} : \boldsymbol{F}^{\mathrm{T}}\delta\boldsymbol{F}$, which is equal to $\boldsymbol{S} : \mathrm{sym}[\boldsymbol{F}^{\mathrm{T}}\delta\boldsymbol{F}] = \boldsymbol{S} : \frac{1}{2}\left(\boldsymbol{F}^{\mathrm{T}}\delta\boldsymbol{F} + \delta\boldsymbol{F}^{\mathrm{T}}\boldsymbol{F}\right)$ due to the symmetry of $\boldsymbol{S}$. The expression in brackets can be identified as $\delta\boldsymbol{C} = \delta(\boldsymbol{F}^{\mathrm{T}}\boldsymbol{F})$, such that the alternative representation

$$G := G^{\mathrm{int}} - G^{\mathrm{ext}} = 0 \qquad \text{with} \tag{4.5a}$$

$$G^{\mathrm{int}} = \int_{\mathcal{B}} \boldsymbol{S} : \tfrac{1}{2}\,\delta\boldsymbol{C}\,\mathrm{d}V \qquad \text{and} \qquad G^{\mathrm{ext}} = \int_{\partial\mathcal{B}_{\boldsymbol{\sigma}}} \bar{\boldsymbol{T}} \cdot \delta\boldsymbol{u}\,\mathrm{d}A + \int_{\mathcal{B}} \bar{\rho}_0 \left(\boldsymbol{b} - \ddot{\boldsymbol{x}}\right) \cdot \delta\boldsymbol{u}\,\mathrm{d}V \tag{4.5b}$$

is obtained for the weak form of the balance of linear momentum. Therein, G^{int} and G^{ext} denote the internal and external virtual work done as a consequence of the virtual displacement $\delta\boldsymbol{u}$.

Principle of stationary potential energy. In conservative mechanical systems, the result in Eq. 4.5 can alternatively be obtained from the principle of stationary potential energy. For such systems, the existence of a potential $\Pi = \Pi_{\text{ext}} + \Pi_{\text{int}}$ can be presumed, from which the internal and external mechanical power can be derived as

$$\mathcal{P}_{\text{int}} = \frac{\partial \Pi_{\text{int}}}{\partial t} \qquad \text{and} \qquad \mathcal{P}_{\text{ext}} = -\frac{\partial \Pi_{\text{ext}}}{\partial t} \overset{3.62}{=} \mathcal{P}. \tag{4.6}$$

This potential Π is equivalent to the total potential energy of the system and is the sum of the total strain energy

$$\Pi_{\text{int}} = \int_{\mathcal{B}} \psi(\boldsymbol{C}) \, \mathrm{d}V \tag{4.7}$$

and the potential energy of the external loading

$$\Pi_{\text{ext}} = -\int_{\mathcal{B}} \bar{\rho}_0 \, \boldsymbol{b} \cdot \boldsymbol{u} \, \mathrm{d}V - \int_{\partial \mathcal{B}_{\boldsymbol{\sigma}}} \bar{\boldsymbol{T}} \cdot \boldsymbol{u} \, \mathrm{d}A \tag{4.8}$$

in terms of deformation-independent body forces $\boldsymbol{b}$ per reference mass and stress vectors $\bar{\boldsymbol{T}}$ acting on the surface $\partial \mathcal{B}_{\boldsymbol{\sigma}}$. The unknown deformed configuration is an equilibrium state, at which the total potential energy of the system has to be stationary. This state can therefore be found by requiring the first variation of Π with respect to $\boldsymbol{u}$ to vanish, i. e.

$$\delta \Pi = 0. \tag{4.9}$$

A stable equilibrium is characterized by a miminum of the potential energy, which is given if $\delta^2 \Pi > 0$. The variations of the strain energy Π_{int} and the external potential energy Π_{ext} are computed as

$$\delta \Pi^{\text{int}} = \int_{\mathcal{B}} \frac{\partial \psi}{\partial \boldsymbol{C}} : \delta \boldsymbol{C} \, \mathrm{d}V \qquad \text{and} \qquad \delta \Pi^{\text{ext}} = -\int_{\mathcal{B}} \bar{\rho}_0 \, \boldsymbol{b} \cdot \delta \boldsymbol{u} \, \mathrm{d}V - \int_{\partial \mathcal{B}_{\boldsymbol{\sigma}}} \bar{\boldsymbol{T}} \cdot \delta \boldsymbol{u} \, \mathrm{d}A, \tag{4.10}$$

see Holzapfel (2000, pp. 386–389) for details. With $\partial \psi / \partial \boldsymbol{C} = {}^1\!/_2 \, \boldsymbol{S}$ from Eq. 3.101, the stationarity of the potential energy then leads to

$$\int_{\mathcal{B}} \tfrac{1}{2} \, \boldsymbol{S} : \delta \boldsymbol{C} \, \mathrm{d}V - \int_{\mathcal{B}} \bar{\rho}_0 \, \boldsymbol{b} \cdot \delta \boldsymbol{u} \, \mathrm{d}V - \int_{\partial \mathcal{B}_{\boldsymbol{\sigma}}} \bar{\boldsymbol{T}} \cdot \delta \boldsymbol{u} \, \mathrm{d}A = 0, \tag{4.11}$$

which has also been obtained in Eq. 4.5 as weak form of the balance of linear momentum for $\ddot{\boldsymbol{x}} = \boldsymbol{0}$. However, the principle of stationary potential energy is restricted to conservative systems. In many problems, for example if energy is dissipated or if external loads depend on the deformation, the mechanical power can not be derived from a potential.

Because of the nonlinearity of the Cauchy-Green tensor, Eq. 4.5 (or its equivalent in Eq. 4.11) is intrinsically nonlinear in the displacements $\boldsymbol{u}$. Besides this geometrical nonlinearity, an additional nonlinearity arises from the stress-deformation relation, which needs to be nonlinear for being able to capture the behavior of soft biological tissues. Those nonlinearities prevent an analytical solution and ask for a linearization of Eq. 4.5 in order to solve it numerically, for example by applying the Newton-Raphson method. An overview of algorithms for the solution of nonlinear equations is given by Wriggers (2008, pp. 152–171).

4.1.2 Linearization

The Newton-Raphson method requires a first order Taylor series expansion of Eq. 4.5 at a state with known solution for $\boldsymbol{u}$ in order to progress iteratively towards the new equilibrium state by adding incremental updates $\Delta\boldsymbol{u}$ until $G = 0$ is fulfilled with sufficient accuracy. The linearized weak form of the balance of linear momentum is thus given by

$$\operatorname{Lin} G = G + \frac{\mathrm{d}G}{\mathrm{d}\boldsymbol{u}}\,\Delta\boldsymbol{u} = 0 \qquad \text{with} \qquad \frac{\mathrm{d}G}{\mathrm{d}\boldsymbol{u}}\,\Delta\boldsymbol{u} =: \Delta G, \tag{4.12}$$

where ΔG is the increment of virtual work done for an increment $\Delta\boldsymbol{u}$ of the displacement. If the volume forces $\bar{\rho}_0\,\boldsymbol{b}$ and stress vectors $\bar{\boldsymbol{T}}$ at the boundary are supposed to be independent of the displacements, hence assuming conservative loads, and if inertia terms are neglected, i. e. $\ddot{\boldsymbol{x}} = \boldsymbol{0}$, only the internal virtual work depends on $\boldsymbol{u}$ and ΔG can be computed using the product rule as

$$\Delta G = \Delta G^{\mathrm{int}} = \int_{\mathcal{B}} \Delta\boldsymbol{S} : \tfrac{1}{2}\,\delta\boldsymbol{C}\,\mathrm{dV} + \int_{\mathcal{B}} \boldsymbol{S} : \tfrac{1}{2}\,\Delta\delta\boldsymbol{C}\,\mathrm{d}V. \tag{4.13}$$

The increments $\Delta\boldsymbol{S}$ and $\Delta\delta\boldsymbol{C}$ are thereby defined in analogy to ΔG in Eq. 4.12, which means that the symbol Δ denotes differentiation with respect to $\boldsymbol{u}$ and multiplication with $\Delta\boldsymbol{u}$. For the increment of the 2nd Piola-Kirchhoff stress, the alternative expression

$$\Delta\boldsymbol{S} = \frac{\mathrm{d}\boldsymbol{S}}{\mathrm{d}\boldsymbol{C}} : \Delta\boldsymbol{C} = \tfrac{1}{2}\,\mathbb{C} : \Delta\boldsymbol{C} \qquad \text{with} \qquad \mathbb{C} := 2\,\frac{\mathrm{d}\boldsymbol{S}}{\mathrm{d}\boldsymbol{C}} \tag{4.14}$$

can be inserted, where $\Delta\boldsymbol{C}$ is given by

$$\Delta\boldsymbol{C} = \Delta(\boldsymbol{F}^{\mathrm{T}}\boldsymbol{F}) = \Delta\boldsymbol{F}^{\mathrm{T}}\boldsymbol{F} + \boldsymbol{F}^{\mathrm{T}}\Delta\boldsymbol{F} \tag{4.15}$$

and $\mathbb{C}$ is referred to as tangent modulus. For strain energy functions that are at least cubic in $\boldsymbol{C}$, a nonlinear stress-deformation relation is obtained, see Eq. 3.101, and $\mathbb{C}$ depends inherently on $\boldsymbol{u}$. In contrast to $\delta\boldsymbol{F}$, $\delta\boldsymbol{C}$ depends on $\boldsymbol{u}$ and its increment has to be computed according to

$$\delta\boldsymbol{C} = \delta(\boldsymbol{F}^{\mathrm{T}}\boldsymbol{F}) = \delta\boldsymbol{F}^{\mathrm{T}}\boldsymbol{F} + \boldsymbol{F}^{\mathrm{T}}\delta\boldsymbol{F} \tag{4.16}$$

$$\Delta\delta\boldsymbol{C} = \Delta(\delta\boldsymbol{F}^{\mathrm{T}}\boldsymbol{F} + \boldsymbol{F}^{\mathrm{T}}\delta\boldsymbol{F}) = \delta\boldsymbol{F}^{\mathrm{T}}\Delta\boldsymbol{F} + \Delta\boldsymbol{F}^{\mathrm{T}}\delta\boldsymbol{F}. \tag{4.17}$$

With Eq. 4.5 and Eq. 4.13–4.14 inserted in Eq. 4.12, the linearized form $\operatorname{Lin} G = G + \Delta G = 0$ of $G = G^{\mathrm{int}} - G^{\mathrm{ext}} = 0$ finally is

$$\operatorname{Lin} G = \int_{\mathcal{B}} \boldsymbol{S} : \tfrac{1}{2}\,\delta\boldsymbol{C}\,\mathrm{d}V - G^{\mathrm{ext}} + \int_{\mathcal{B}} \tfrac{1}{2}\,\delta\boldsymbol{C} : \mathbb{C} : \tfrac{1}{2}\,\Delta\boldsymbol{C}\,\mathrm{dV} + \int_{\mathcal{B}} \boldsymbol{S} : \tfrac{1}{2}\,\Delta\delta\boldsymbol{C}\,\mathrm{d}V = 0. \tag{4.18}$$

For the solution of this equation with respect to the increments $\Delta\boldsymbol{u}$ of the displacements, a finite element discretization is performed in order to represent the infinite number of material points with unknown displacements by a reduced number of discrete points between which the displacements are interpolated.

4.1.3 Discretization

The main idea of the finite element method is to subdivide the body under consideration into a mesh consisting of a finite number of elements that are defined by nodal points. Between those nodal points at which the primary variables – here the displacements – are computed, interpolating ansatz functions are used for the approximation of the real distributions. As illustrated in Fig. 4.2 for the two-dimensional case, the geometry of the reference configuration $\mathcal{B}$ of the body is hence replaced by an approximation $\mathcal{B}^h$ composed of n_{ele} non-overlapping finite elements $\mathcal{B}^e$ with

$$\mathcal{B} \approx \mathcal{B}^h = \bigcup_{e=1}^{n_{\text{ele}}} \mathcal{B}^e. \tag{4.19}$$

The superscript h, denoting approximated quantities, insinuates that the goodness of these approximations depends on the characteristic length of the elements, which is likewise denoted as h. An improvement of the approximations can be obtained by h-refinement, i. e. a refinement of the mesh, or by p-refinement, increasing the polynomial degree p of the ansatz functions.
Each of the elements is defined by a number n of nodes, which depends on the number of spatial dimensions and the polynomial order of the ansatz functions used for the interpolation. Based on the displacements $\boldsymbol{d}_I = \boldsymbol{x}_I - \boldsymbol{X}_I$ at the nodes, the displacements within each finite element are then approximated as

$$\boldsymbol{u} \approx \boldsymbol{u}^h = \sum_{I=1}^{n} N_I \, \boldsymbol{d}_I, \tag{4.20}$$

where N_I denotes an ansatz function associated to node I, evaluated at the position within the element at which $\boldsymbol{u}$ has to be computed. In order to obtain the known nodal displacement $\boldsymbol{d}_I$ at node I, the ansatz functions are claimed to fulfill

$$N_I = \begin{cases} 1 & \text{at node } I \\ 0 & \text{at all other nodes} \end{cases}. \tag{4.21}$$

In Fig. 4.1, quadratic ansatz functions for a three-noded 1D line element and the interpolation of the displacement vector $\boldsymbol{u}$ are exemplarily illustrated. The geometry of the element and the ansatz functions are defined in a parameter space $\mathcal{B}_0$ with coordinates $\boldsymbol{\xi} = \begin{pmatrix} \xi & \eta & \zeta \end{pmatrix}^{\mathrm{T}}$. This reference element is then mapped to the reference configuration $\mathcal{B}^e$ for each single element.

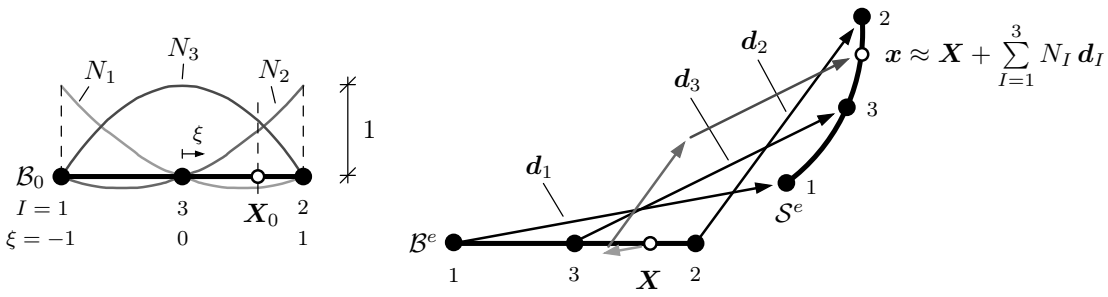

Figure 4.1: Illustration of a one-dimensional finite element with quadratic ansatz functions and the approximation of displacement $\boldsymbol{u} = \boldsymbol{x} - \boldsymbol{X}$ by a weighted sum of the nodal displacements $\boldsymbol{d}_I$.

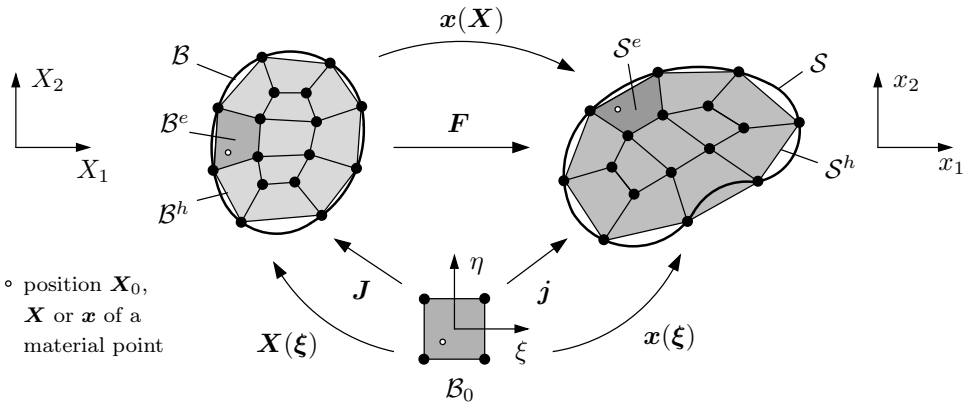

Figure 4.2: Based on a reference element defined in parameter space $\mathcal{B}_0$, the reference geometry $\mathcal{B}$ of the body is discretized into finite elements. An approximation $\mathcal{S}^h$ of the deformed geometry $\mathcal{S}$ is then found by computing the displacements at the nodes and interpolating in between. Using the isoparametric concept, displacements and geometry are interpolated by the same ansatz functions.

Making use of the isoparametric concept, the geometry within a finite element is approximated by the same ansatz functions as the displacements. The ansatz functions N_I are therefore also referred to as shape functions and the approximations for the position vectors $\boldsymbol{X}$ in the reference and $\boldsymbol{x}$ in the actual configuration are

$$\boldsymbol{X} \approx \boldsymbol{X}^h = \sum_{I=1}^{n} N_I(\boldsymbol{\xi})\, \boldsymbol{X}_I \qquad \text{and} \qquad \boldsymbol{x} \approx \boldsymbol{x}^h = \sum_{I=1}^{n} N_I(\boldsymbol{\xi})\, \boldsymbol{x}_I. \tag{4.22}$$

The relations between the coordinates $\boldsymbol{X}_0$ in the reference element, defined in parameter space $\mathcal{B}_0$, and the coordinates $\boldsymbol{X}$ and $\boldsymbol{x}$ in the reference and actual configurations $\mathcal{B}$ and $\mathcal{S}$ of the body are depicted in Fig. 4.2. In analogy to the deformation gradient, see Eq. 3.5, the Jacobians $\boldsymbol{J}$ and $\boldsymbol{j}$ are defined by

$$\boldsymbol{J} = \frac{\partial \boldsymbol{X}}{\partial \boldsymbol{\xi}} \qquad \text{and} \qquad \boldsymbol{j} = \frac{\partial \boldsymbol{x}}{\partial \boldsymbol{\xi}}, \tag{4.23}$$

where $\boldsymbol{\xi} = \begin{pmatrix} \xi & \eta & \zeta \end{pmatrix}^{\mathrm{T}}$ are the coordinates in the parameter space $\mathcal{B}_0$. The gradient of the shape functions N_I with respect to the coordinates $\boldsymbol{X}$ can then be expressed as

$$\mathrm{Grad}[N_I] = \frac{\partial N_I}{\partial \boldsymbol{X}} = \frac{\partial N_I}{\partial \boldsymbol{\xi}} \frac{\partial \boldsymbol{\xi}}{\partial \boldsymbol{X}} = \frac{\partial N_I}{\partial \boldsymbol{\xi}} \boldsymbol{J}^{-1} = \boldsymbol{J}^{-\mathrm{T}} \frac{\partial N_I}{\partial \boldsymbol{\xi}}. \tag{4.24}$$

Due to the fact that the nodal displacements are fixed for each position $\boldsymbol{X}$ within an element, the index notation of $\mathrm{Grad}[\boldsymbol{u}]$ yields the expression

$$u_{j,i} \approx \sum_{I=1}^{n} \left(N_I\, d_{Ij}\right)_{,i} = \sum_{I=1}^{n} N_{I,i}\, d_{Ij} \qquad \text{with} \qquad N_{I,i} = \frac{\partial N_I}{\partial X_i}, \tag{4.25}$$

where only the shape functions have to be differentiated with respect to $\boldsymbol{X}$.

In order to discretize Eq. 4.18, the virtual and incremental displacements $\delta\boldsymbol{u}$ and $\Delta\boldsymbol{u}$ are discretized in the same manner as the real displacements, i. e.

$$\delta\boldsymbol{u} \approx \delta\boldsymbol{u}^h = \sum_{I=1}^{n} N_I\,\delta\boldsymbol{d}_I \qquad \text{and} \qquad \Delta\boldsymbol{u} \approx \Delta\boldsymbol{u}^h = \sum_{I=1}^{n} N_I\,\Delta\boldsymbol{d}_I. \tag{4.26}$$

The components of $\delta\boldsymbol{C} = (\mathrm{Grad}[\delta\boldsymbol{u}])^{\mathrm{T}}\boldsymbol{F} + \boldsymbol{F}^{\mathrm{T}}\,\mathrm{Grad}[\delta\boldsymbol{u}]$ can then be expressed in index notation as

$$\tfrac{1}{2}\,\delta C_{ik} = \tfrac{1}{2}\,(\delta u_{j,i}\,F_{jk} + F_{ji}\,\delta u_{j,k}) \approx \sum_{I=1}^{n} \tfrac{1}{2}\,(N_{I,i}\,F_{jk} + F_{ji}\,N_{I,k})\,\delta d_{Ij}, \tag{4.27}$$

where the components δd_{Ij} of the virtual nodal displacements can be factored out. At this point, it is helpful to introduce the Voigt notation, in which symmetric tensors of second order are represented as vectors with six components. This permits a matrix notation of equations involving tensors of higher order as for example the constitutive equation $\Delta\boldsymbol{S} = \mathbb{C} : \frac{1}{2}\,\Delta\boldsymbol{C}$, for which the Voigt notation is deduced in Appendix A.3. If the virtual deformation tensor $\delta\boldsymbol{C}$ is written in Voigt notation according to

$$\delta\underline{\boldsymbol{C}} = \begin{bmatrix} \delta C_{11} \\ \delta C_{22} \\ \delta C_{33} \\ 2\,\delta C_{12} \\ 2\,\delta C_{23} \\ 2\,\delta C_{13} \end{bmatrix}, \tag{4.28}$$

where the underline is used to differentiate between standard and Voigt representation, Eq. 4.27 can be expressed by

$$\tfrac{1}{2}\,\delta\underline{\boldsymbol{C}} \approx \sum_{I=1}^{n} \underline{\boldsymbol{B}}_I\,\delta\boldsymbol{d}_I \tag{4.29}$$

with

$$\underline{\boldsymbol{B}}_I = \begin{bmatrix} F_{11}\,N_{I,1} & F_{21}\,N_{I,1} & F_{31}\,N_{I,1} \\ F_{12}\,N_{I,2} & F_{22}\,N_{I,2} & F_{32}\,N_{I,2} \\ F_{13}\,N_{I,3} & F_{23}\,N_{I,3} & F_{33}\,N_{I,3} \\ F_{11}\,N_{I,2} + F_{12}\,N_{I,1} & F_{21}\,N_{I,2} + F_{22}\,N_{I,1} & F_{31}\,N_{I,2} + F_{32}\,N_{I,1} \\ F_{12}\,N_{I,3} + F_{13}\,N_{I,2} & F_{22}\,N_{I,3} + F_{23}\,N_{I,2} & F_{32}\,N_{I,3} + F_{33}\,N_{I,2} \\ F_{11}\,N_{I,3} + F_{13}\,N_{I,1} & F_{21}\,N_{I,3} + F_{23}\,N_{I,1} & F_{31}\,N_{I,3} + F_{33}\,N_{I,1} \end{bmatrix} \tag{4.30}$$

denoting the B-matrix associated to node I. In an analogous manner, the expression

$$\tfrac{1}{2}\,\Delta\underline{\boldsymbol{C}} \approx \sum_{I=1}^{n} \underline{\boldsymbol{B}}_I\,\Delta\boldsymbol{d}_I \tag{4.31}$$

can be found for the increments of $\boldsymbol{C}$, whose Voigt notation is conform to Eq. 4.28. Assembling the virtual and incremental displacements of all nodes belonging to one element into vectors $\delta\boldsymbol{d}^e$ and $\Delta\boldsymbol{d}^e$ and the B-matrices into one elemental B-matrix $\underline{\boldsymbol{B}}^e$ according to

$$\delta\boldsymbol{d}^e = \begin{bmatrix} \delta\boldsymbol{d}_1 \\ \delta\boldsymbol{d}_2 \\ \vdots \\ \delta\boldsymbol{d}_n \end{bmatrix}, \quad \Delta\boldsymbol{d}^e = \begin{bmatrix} \Delta\boldsymbol{d}_1 \\ \Delta\boldsymbol{d}_2 \\ \vdots \\ \Delta\boldsymbol{d}_n \end{bmatrix} \qquad \text{and} \qquad \underline{\boldsymbol{B}}^e = \begin{bmatrix} \underline{\boldsymbol{B}}_1 & \underline{\boldsymbol{B}}_2 & \dots & \underline{\boldsymbol{B}}_n \end{bmatrix}, \tag{4.32}$$

the sum can be omitted and

$$\tfrac{1}{2}\,\delta\underline{\boldsymbol{C}} \approx \sum_{I=1}^{n} \underline{\boldsymbol{B}}_I\,\delta\boldsymbol{d}_I = \underline{\boldsymbol{B}}^e\,\delta\boldsymbol{d}^e \qquad \text{and} \qquad \tfrac{1}{2}\,\Delta\underline{\boldsymbol{C}} \approx \sum_{I=1}^{n} \underline{\boldsymbol{B}}_I\,\Delta\boldsymbol{d}_I = \underline{\boldsymbol{B}}^e\,\Delta\boldsymbol{d}^e \tag{4.33}$$

are obtained. The same can be done for the virtual and incremental displacements in Eq. 4.26, if the shape functions are gathered in an element shape function matrix $\underline{\boldsymbol{N}}^e$ given by

$$\underline{\boldsymbol{N}}^e = \begin{bmatrix} \underline{\boldsymbol{N}}_1 & \underline{\boldsymbol{N}}_2 & \dots & \underline{\boldsymbol{N}}_n \end{bmatrix} \qquad \text{with} \qquad \underline{\boldsymbol{N}}_I = \begin{bmatrix} N_I & 0 & 0 \\ 0 & N_I & 0 \\ 0 & 0 & N_I \end{bmatrix}. \tag{4.34}$$

This leads to the expressions

$$\delta\boldsymbol{u} \approx \sum_{I=1}^{n} N_I\,\delta\boldsymbol{d}_I = \underline{\boldsymbol{N}}^e\,\delta\boldsymbol{d}^e \qquad \text{and} \qquad \Delta\boldsymbol{u} \approx \sum_{I=1}^{n} N_I\,\Delta\boldsymbol{d}_I = \underline{\boldsymbol{N}}^e\,\Delta\boldsymbol{d}^e \tag{4.35}$$

in matrix notation. In each of the discretized quantities in Eq. 4.33 and Eq. 4.35, the dependence on the position of the material point is realized solely by the shape functions and their derivatives, which are both evaluated at the respective position within the element. The nodal displacements are discrete values, which are unknown but constant for all evaluations at different positions within the element.

In the following, the discretization of the individual summands of Eq. 4.18 is carried out. The integral over the whole domain $\mathcal{B}$ is approximated by a sum of integrals over single elements $\mathcal{B}^e$, such that only the parts of one element are considered in the first instance. Inserting Eq. 4.33, the internal virtual work $G^{e,\mathrm{int}}$ done in one element is replaced with

$$G^{e,\mathrm{int}} = \int_{\mathcal{B}^e} \boldsymbol{S} : \tfrac{1}{2}\,\delta\boldsymbol{C}\,\mathrm{d}V \approx \int_{\mathcal{B}^e} \underline{\boldsymbol{S}} \cdot \underline{\boldsymbol{B}}^e\,\delta\boldsymbol{d}^e\,\mathrm{d}V = \delta\boldsymbol{d}^{e\mathrm{T}} \int_{\mathcal{B}^e} \underline{\boldsymbol{B}}^{e\mathrm{T}}\underline{\boldsymbol{S}}\,\mathrm{d}V, \tag{4.36}$$

where the Voigt notation of the 2nd Piola-Kirchhoff stress tensor is given by

$$\underline{\boldsymbol{S}} = \begin{bmatrix} S_{11} & S_{22} & S_{33} & S_{12} & S_{23} & S_{13} \end{bmatrix}^{\mathrm{T}}. \tag{4.37}$$

Since the virtual displacement vector does not depend on the position within the element, it can be moved outside the integral. In the course of the linearization, inertia terms have been neglected. Thus, the elemental fraction $G^{e,\mathrm{ext}}$ of the external virtual work, see Eq. 4.5b, is discretized with Eq. 4.35 as

$$\begin{aligned} G^{e,\mathrm{ext}} &= \int_{\partial\mathcal{B}^e_{\boldsymbol{\sigma}}} \bar{\boldsymbol{T}} \cdot \delta\boldsymbol{u}\,\mathrm{d}A + \int_{\mathcal{B}^e} \bar{\rho}_0\,\boldsymbol{b} \cdot \delta\boldsymbol{u}\,\mathrm{d}V \\ &\approx \int_{\partial\mathcal{B}^e_{\boldsymbol{\sigma}}} \bar{\boldsymbol{T}} \cdot \underline{\boldsymbol{N}}^e\,\delta\boldsymbol{d}^e\,\mathrm{d}A + \int_{\mathcal{B}^e} \bar{\rho}_0\,\boldsymbol{b} \cdot \underline{\boldsymbol{N}}^e\,\delta\boldsymbol{d}^e\,\mathrm{d}V \\ &= \delta\boldsymbol{d}^{e\mathrm{T}} \int_{\partial\mathcal{B}^e_{\boldsymbol{\sigma}}} \underline{\boldsymbol{N}}^{e\mathrm{T}}\bar{\boldsymbol{T}}\,\mathrm{d}A + \delta\boldsymbol{d}^{e\mathrm{T}} \int_{\mathcal{B}^e} \underline{\boldsymbol{N}}^{e\mathrm{T}}\bar{\rho}_0\,\boldsymbol{b}\,\mathrm{d}V. \end{aligned} \tag{4.38}$$

For the next term in Eq. 4.18, the discretizations in Eq. 4.33 lead to the expression

$$\int_{\mathcal{B}^e} \tfrac{1}{2}\,\delta\boldsymbol{C} : \mathbb{C} : \tfrac{1}{2}\,\Delta\boldsymbol{C}\,\mathrm{d}V \approx \int_{\mathcal{B}^e} (\underline{\boldsymbol{B}}^e\,\delta\boldsymbol{d}^e)\cdot(\underline{\mathbb{C}}\,\underline{\boldsymbol{B}}^e\,\Delta\boldsymbol{d}^e)\,\mathrm{d}V = \delta\boldsymbol{d}^{e\mathrm{T}}\int_{\mathcal{B}^e}\underline{\boldsymbol{B}}^{e\mathrm{T}}\underline{\mathbb{C}}\,\underline{\boldsymbol{B}}^e\,\mathrm{d}V\,\Delta\boldsymbol{d}^e \tag{4.39}$$

on the element level. The last term of Eq. 4.18 can not directly be evaluated in matrix notation. Inserting $\delta\boldsymbol{F} = \mathrm{Grad}[\delta\boldsymbol{u}]$ and $\Delta\boldsymbol{F} = \mathrm{Grad}[\Delta\boldsymbol{u}]$ in Eq. 4.17 and using Eq. 4.26 with Eq. 4.25, the expression

$$\tfrac{1}{2}\,\Delta\delta C_{ij} = \tfrac{1}{2}\,(\delta u_{k,i}\,\Delta u_{k,j} + \Delta u_{k,i}\,\delta_{k,j}) \approx \sum_{I=1}^{n}\sum_{J=1}^{n}\delta d_{Ik}\,N_{I,i}\,N_{J,j}\,\Delta d_{Jk} \tag{4.40}$$

is obtained in index notation after some manipulations. This leads to

$$\int_{\mathcal{B}^e}\boldsymbol{S} : \tfrac{1}{2}\,\Delta\delta\boldsymbol{C}\,\mathrm{d}V \approx \sum_{I=1}^{n}\sum_{J=1}^{n}\delta d_{Ik}\int_{\mathcal{B}^e} N_{I,i}\,N_{J,j}S_{ij}\,\mathrm{d}V\,\Delta d_{Jk} = \delta\boldsymbol{d}^{e\mathrm{T}}\int_{\mathcal{B}^e}\underline{\boldsymbol{G}}^e\mathrm{d}V\,\Delta\boldsymbol{d}^e, \tag{4.41}$$

where the element displacement vectors and a matrix

$$\underline{\boldsymbol{G}}^e = \begin{bmatrix} \underline{\boldsymbol{G}}_{11} & \underline{\boldsymbol{G}}_{12} & \cdots & \underline{\boldsymbol{G}}_{1n} \\ \underline{\boldsymbol{G}}_{21} & \underline{\boldsymbol{G}}_{22} & \cdots & \underline{\boldsymbol{G}}_{2n} \\ \vdots & \vdots & \ddots & \vdots \\ \underline{\boldsymbol{G}}_{n1} & \underline{\boldsymbol{G}}_{n2} & \cdots & \underline{\boldsymbol{G}}_{nn} \end{bmatrix} \qquad \text{with} \qquad \underline{\boldsymbol{G}}_{IJ} = \begin{bmatrix} G_{IJ} & 0 & 0 \\ 0 & G_{IJ} & 0 \\ 0 & 0 & G_{IJ} \end{bmatrix} \tag{4.42}$$

and with the individual components

$$G_{IJ} = N_{I,i}\,N_{J,j}\,S_{ij} \tag{4.43}$$

can be used to substitute the sigma signs.

Summarizing all terms from Eq. 4.36, Eq. 4.38, Eq. 4.39 and Eq. 4.41 according to Eq. 4.18, the linearized virtual work done in one element can be abbreviated by

$$\mathrm{Lin}\,G^e \approx \delta\boldsymbol{d}^{e\mathrm{T}}\,\underline{\boldsymbol{r}}^{\mathrm{e}} + \delta\boldsymbol{d}^{e\mathrm{T}}\,\underline{\boldsymbol{K}}^e\,\Delta\boldsymbol{d}^e \tag{4.44}$$

with the element residual vector

$$\underline{\boldsymbol{r}}^e = \int_{\mathcal{B}^e}\underline{\boldsymbol{B}}^{e\mathrm{T}}\underline{\boldsymbol{S}}\,\mathrm{d}V - \int_{\partial\mathcal{B}^e_{\boldsymbol{\sigma}}}\underline{\boldsymbol{N}}^{e\mathrm{T}}\bar{\boldsymbol{T}}\,\mathrm{d}A - \int_{\mathcal{B}^e}\underline{\boldsymbol{N}}^{e\mathrm{T}}\bar{\rho}_0\,\boldsymbol{b}\,\mathrm{d}V \tag{4.45}$$

and the element stiffness matrix

$$\underline{\boldsymbol{K}}^e = \underline{\boldsymbol{K}}^{e,\mathrm{mat}} + \underline{\boldsymbol{K}}^{e,\mathrm{geo}} = \int_{\mathcal{B}^e}\underline{\boldsymbol{B}}^{e\mathrm{T}}\underline{\mathbb{C}}\,\underline{\boldsymbol{B}}^e\,\mathrm{d}V + \int_{\mathcal{B}^e}\underline{\boldsymbol{G}}^e\mathrm{d}V, \tag{4.46}$$

which is composed by a material and a geometric part. For the sum of all element contributions, the requirement

$$\mathrm{Lin}\,G = \sum_{e=1}^{n_{\mathrm{ele}}}\mathrm{Lin}\,G^e = 0 \tag{4.47}$$

is necessary to satisfy Eq. 4.18. However, the original aim defined in Eq. 4.5a was to fulfill $G = 0$, which is equivalent to

$$G = \sum_{e=1}^{n_{\mathrm{ele}}} \delta \boldsymbol{d}^{e\mathrm{T}} \, \underline{\boldsymbol{r}}^{e} = 0. \tag{4.48}$$

Gathering all the nodal displacements into global vectors

$$\delta \boldsymbol{d} = \bigcup_{e=1}^{n_{\mathrm{ele}}} \delta \boldsymbol{d}^{e} \qquad \text{and} \qquad \Delta \boldsymbol{d} = \bigcup_{e=1}^{n_{\mathrm{ele}}} \Delta \boldsymbol{d}^{e} \tag{4.49}$$

and assembling the element residual vectors and stiffness matrices into global counterparts

$$\underline{\boldsymbol{r}} = \mathop{\mathsf{A}}_{e=1}^{n_{\mathrm{ele}}} \underline{\boldsymbol{r}}^{e} \qquad \text{and} \qquad \underline{\boldsymbol{K}} = \mathop{\mathsf{A}}_{e=1}^{n_{\mathrm{ele}}} \underline{\boldsymbol{K}}^{e}, \tag{4.50}$$

Eq. 4.47 can be reformulated in terms of the global equation $\delta \boldsymbol{d}^{\mathrm{T}} \left(\underline{\boldsymbol{r}} + \underline{\boldsymbol{K}} \, \Delta \boldsymbol{d} \right) = 0$. Since the virtual nodal displacements $\delta \boldsymbol{d}$ are arbitrary, this leads to the global system of linearized equations

$$\underline{\boldsymbol{K}} \, \Delta \boldsymbol{d} = - \, \underline{\boldsymbol{r}} \tag{4.51}$$

for the increments of the nodal displacements $\Delta \boldsymbol{d}$ and to the condition $\underline{\boldsymbol{r}} = \boldsymbol{0}$ coming from Eq. 4.48. The global vector $\boldsymbol{d}$ of the nodal displacements has to be updated iteratively by the increments $\Delta \boldsymbol{d}$ until $\underline{\boldsymbol{r}} = \boldsymbol{0}$ is fulfilled with sufficient accuracy.

The integrals which have to be evaluated to obtain the element residual vectors and stiffness matrices given in Eq. 4.45 and Eq. 4.46 can in general not be computed analytically and are therefore replaced by weighted sums over a finite number l_{int} of integration points. Those points are defined in the parameter space $\mathcal{B}_0$, such that the integral of a quantity $(\bullet)$ over the reference configuration $\mathcal{B}^e$ of the element is given by

$$\int_{\mathcal{B}^e} (\bullet) \, \mathrm{d}V = \int_{\mathcal{B}_0} (\bullet) \det[\boldsymbol{J}] \, \mathrm{d}V_0 \approx \sum_{l=1}^{l_{\mathrm{int}}} (\bullet)\big|_l \; \omega_l \; \det[\boldsymbol{J}]\Big|_l. \tag{4.52}$$

Therein, ω_l denotes the weighting factor associated to integration point l and $\det[\boldsymbol{J}]$ has to be included due to the volume difference between the configurations $\mathcal{B}_0$ and $\mathcal{B}^e$, see Fig. 4.2 and Eq. 3.7, which holds analogously here. During summation, $\det[\boldsymbol{J}]$ and the quantity $(\bullet)$ itself have to be evaluated at the particular integration point l. The numerical integration scheme actually applied in this work is the Gauß point integration. Weighting factors and coordinates of the Gauß points for different values of l_{int} as well as further information on numerical integration are for instance given by Zienkiewicz & Taylor (2000a, pp. 217 ff.)

4.2 Finite elements for rotationally symmetric problems

For special boundary value problems, a fully three-dimensional discretization as introduced above is not necessary. If geometry, material behavior and external loads are subject to symmetries, the same restrictions are imposed on the unknown displacements and stresses. In order to avoid

redundancies and thus computing effort in such symmetric problems, it is thus reasonable to use finite elements with a reduced number of degrees of freedom. For basic investigations of blood vessels or related parameter studies, an idealized cylindrical geometry as depicted in Fig. 4.3 might be taken into account. If the results are expected to be independent on the position φ along the circumference, a representative one radian sector can be considered instead of the whole cylinder. In spite of the three-dimensionality of such a sector, an a priori reduction of the general finite element formulation to two dimensions is possible due to the independence of the displacements on the circumferential coordinate.

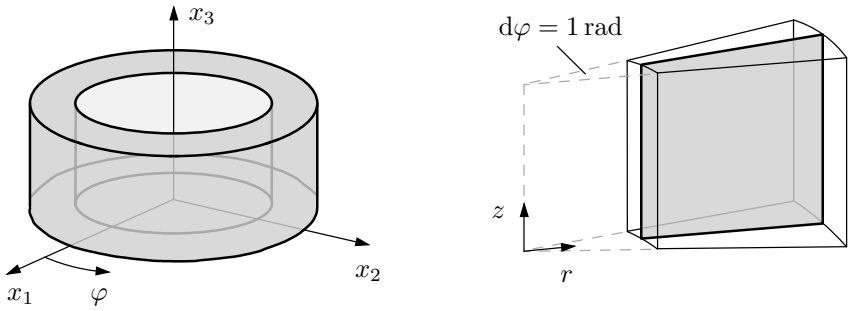

Figure 4.3: With a special finite element formulation, the simulation of a three-dimensional, rotationally symmetric boundary value problem can be reduced to two spatial dimensions without loss of information.

Supposed that the resulting stress and strain fields are even homogeneous along the axial direction, a further reduction to only one dimension is realizable. Assuming quadratic Lagrangian shape functions for the interpolation of the nodal displacements and other field quantities, such an element has only three degrees of freedom, compared to $9 \cdot 2 = 18$ in the two-dimensional or $27 \cdot 3 = 81$ in the three-dimensional element. Especially for applications where the same boundary value problem has to be evaluated many times, for example in the context of parameter optimization, the advantages achieved by such a reduction of redundant unknowns is essential.

In the following sections, a two- and a one-dimensional finite element for rotationally symmetric problems are developed based on the general three-dimensional case described in Sec. 4.1.3. The two-dimensional element is in line with the implementation of the axisymmetric element in the finite element software FEAP by Taylor (2008). Since the boundary value problem of an idealized artery, which is considered in Sec. 7.5 for the computationally intensive, optimization-based comparison of different growth models, allows a reduction to exclusively the radial direction, a suitable axisymmetric 1D element for pressurized tubular structures is proposed, which still enables the application of axial strains.
So far, neither shape functions nor the application of loads have been discussed in detail. These subjects will be covered using the example of the one-dimensional element, including hints on generalization to the two- and three-dimensional case.

4.2.1 Two-dimensional axisymmetric element

Instead of using Cartesian coordinates, a description in cylindrical coordinates is advantageous for rotationally symmetric structures. In this context, the coordinates $\boldsymbol{X} = \begin{bmatrix} X_1 & X_2 & X_3 \end{bmatrix}^{\mathrm{T}}$

are meant to refer to the radial, axial and circumferential direction, i. e.

$$\boldsymbol{X} = \begin{bmatrix} X_1 \\ X_2 \\ X_3 \end{bmatrix} \mathrel{\widehat{=}} \begin{bmatrix} r \\ z \\ \varphi \end{bmatrix}. \tag{4.53}$$

In equations, the notation with numbers is however maintained in order to be consistent with the previous notation. Since an independence on the circumferential coordinate φ is supposed to hold true, the three-dimensional geometry can be replaced by a one-radian sector, which is represented by a two-dimensional shape located in the r-z-plane, see Fig. 4.3. For the radial and axial directions, the deformation gradient is given by the 2D equivalent of Eq. 3.6 with $\boldsymbol{u}$ being now a vector with the components $u_1 = u_r$ and $u_2 = u_z$. The deformation in circumferential direction is dictated by the radial displacement. If the radius at a material point increases from X_1 to $X_1 + u_1$, the circumference is forced to increase from $2\pi\, X_1 \mathrm{d}\varphi$ to $2\pi\,(X_1 + u_1)\,\mathrm{d}\varphi$. Therefore, the component F_{33} of the deformation gradient is given by $F_{33} = 1 + u_1/X_1$ and the deformation gradient for the two-dimensional axisymmetric formulation reads

$$\boldsymbol{F} = \begin{bmatrix} 1 + u_{1,1} & u_{1,2} & 0 \\ u_{2,1} & 1 + u_{2,2} & 0 \\ 0 & 0 & 1 + {}^{\star}u_1/X_1 \end{bmatrix}. \tag{4.54}$$

Omitting the term marked by an asterisk, a plane strain formulation would be obtained, where no deformation perpendicular to the considered plane is allowed. The non-zero components of the virtual Cauchy-Green tensor and the 2nd Piola-Kirchhoff stress tensor are given in Voigt notation by

$$\tfrac{1}{2}\,\delta\underline{\boldsymbol{C}} = \begin{bmatrix} \frac{1}{2}\,\delta C_{11} \\ \frac{1}{2}\,\delta C_{22} \\ \frac{1}{2}\,\delta C_{33} \\ \delta C_{12} \end{bmatrix} \qquad \text{and} \qquad \underline{\boldsymbol{S}} = \begin{bmatrix} S_{11} \\ S_{22} \\ S_{33} \\ S_{12} \end{bmatrix}. \tag{4.55}$$

To arrive at a discretization of the virtual deformations in analogy to Eq. 4.29, the part $1/2\,\delta C_{33}$ has to be considered separately since it is not covered by the general equations applying here only for $1/2\,\delta C_{ij}$ with $i, j \in \{1, 2\}$. Evaluating Eq. 4.16 for $i = j = 3$ and the deformation gradient given in Eq. 4.54 yields

$$\tfrac{1}{2}\,\delta C_{33} = F_{33}\,\delta F_{33} = F_{33}\,\frac{\delta u_1}{X_1} \approx \sum_{I=1}^{n} F_{33}\,\frac{N_I}{X_1}\,\delta d_{I1}, \tag{4.56}$$

where the approximation of the virtual displacement δu_1 follows Eq. 4.26. For the explanation of $\delta F_{33} = \delta(1 + u_1/X_1) = \delta u_1/X_1$ it might be remarked again that the variation stands for the difference between a configuration $(1 + \bar{u}_1/X_1)$ in the direct neighborhood of F_{33} and F_{33} itself, thus $\delta F_{33} = (1 + \bar{u}_1/X_1) - (1 + u_1/X_1) \equiv \delta u_1/X_1$. Reducing the B-matrix from Eq. 4.30 appropriately and complementing the third row for the special case of axisymmetry, the nodal B-matrix follows as

$$\underline{\boldsymbol{B}}_I = \begin{bmatrix} F_{11}\,N_{I,1} & F_{21}\,N_{I,1} \\ F_{12}\,N_{I,2} & F_{22}\,N_{I,2} \\ {}^{\star}F_{33}\,N_I/X_1 & 0 \\ F_{11}\,N_{I,2} + F_{12}\,N_{I,1} & F_{21}\,N_{I,2} + F_{22}\,N_{I,1} \end{bmatrix}. \tag{4.57}$$

Besides these adaptations, all further equations except for the matrix $\underline{\boldsymbol{G}}_{IJ}$ can be taken from Sec. 4.1.3 after having been reduced to the two-dimensional case where required. For the discretization of the last term in Eq. 4.18, leading to the geometrical part of the stiffness matrix, a separate inspection is again necessary for the component $\frac{1}{2}\,\Delta\delta C_{33}$. According to Eq. 4.17 and Eq. 4.54, the expression

$$\tfrac{1}{2}\,\Delta\delta C_{33} = \Delta F_{33}\,\delta F_{33} = \frac{\Delta u_1}{X_1}\,\frac{\delta u_1}{X_1} \approx \sum_{I=1}^{n}\sum_{J=1}^{n} \delta d_{I1}\,\frac{N_I}{X_1}\,\frac{N_J}{X_1}\,\Delta d_{J1} \tag{4.58}$$

is obtained with Eq. 4.26, whereas Eq. 4.40 only holds for components with $i, j \in \{1, 2\}$. This leads to the discretization

$$\int_{\mathcal{B}^e} \boldsymbol{S} : \tfrac{1}{2}\,\Delta\delta\boldsymbol{C}\,\mathrm{d}V \approx \delta\boldsymbol{d}^{e\mathrm{T}} \int_{\mathcal{B}^e} \underline{\boldsymbol{G}}^e\,\mathrm{d}V\,\Delta\boldsymbol{d}^e, \tag{4.59}$$

where the submatrices in matrix $\underline{\boldsymbol{G}}^e$, see Eq. 4.42, are given by

$$\underline{\boldsymbol{G}}_{IJ} = \begin{bmatrix} G_{IJ} + {}^{\star}\tilde{G}_{IJ} & 0 \\ 0 & G_{IJ} \end{bmatrix} \qquad \text{with} \qquad \tilde{G}_{IJ} = \frac{N_I}{X_1}\,\frac{N_J}{X_1}\,S_{33} \tag{4.60}$$

and with G_{IJ} as defined in Eq. 4.43. Here again and also in Eq. 4.57, leaving out the terms marked by the asterisk would lead to the inherent plane strain formulation.

In order to reflect the three-dimensionality of the discretized structure, the infinitesimal volume elements computed at each Gauß point within the scope of numerical integration have to be multiplied with the thickness in circumferential direction, which is defined by the arc length $X_1\,\mathrm{d}\varphi = X_1$. The integral over an axisymmetric element $\mathcal{B}^e$ is thus computed by

$$\int_{\mathcal{B}^e} (\bullet)\,\mathrm{d}V \approx \sum_{l=1}^{l_{\mathrm{int}}} (\bullet)\big|_l\;\omega_l\,X_{1l}\;\det[\boldsymbol{J}]\Big|_l, \tag{4.61}$$

where X_{1l} denotes the X_1-coordinate of Gauß point l in the reference configuration.

4.2.2 One-dimensional axisymmetric element

In special cases, the two-dimensional axisymmetric element can be replaced by a one-dimensional one which has only one degree of freedom per node, namely the displacement u_1 in radial direction $X_1 \mathrel{\widehat{=}} r$. Just for the record, a possibility of how to construct shape functions is at first exemplified on the basis of this element. Then, the deformation gradient and the matrices $\underline{\boldsymbol{B}}_I$ and $\underline{\boldsymbol{G}}_{IJ}$ will be derived. Finally, the application of non-conservative surface loads is discussed.

Shape functions. In Fig. 4.4, the illustration of a one-dimensional finite element and its shape functions is given for a discretization with three and four nodes. At each of the n nodes, a constraint for each shape function is defined by Eq. 4.21. The shape function can thus be assumed to be a polynomial of degree $(n-1)$ with n unknown coefficients α_i, i. e.

$$N_I = \sum_{i=0}^{n-1} \alpha_i\,\xi^i. \tag{4.62}$$

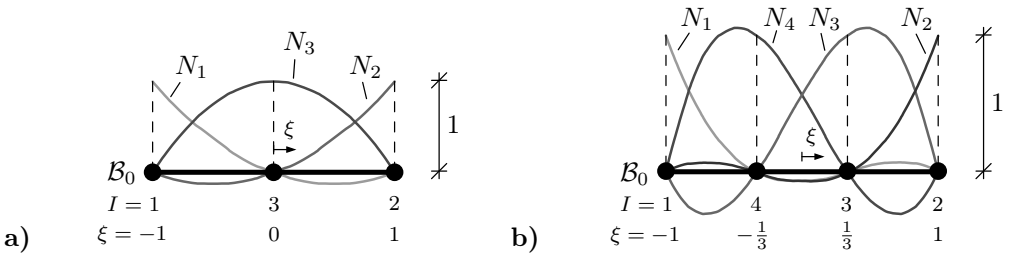

Figure 4.4: Illustration of node positions and shape functions for a one-dimensional finite element with **a)** quadratic or **b)** cubic interpolation of the nodal values.

For the 3-noded element, the quadratic shape functions

$$N_1 = \frac{\xi}{2}(\xi - 1), \qquad N_2 = \frac{\xi}{2}(\xi + 1), \qquad N_3 = 1 - \xi^2 \tag{4.63}$$

with their derivatives

$$N_{1,\xi} = \xi - \frac{1}{2}, \qquad N_{2,\xi} = \xi + \frac{1}{2}, \qquad N_{3,\xi} = -2\,\xi \tag{4.64}$$

can be determined from those conditions. If a cubic interpolation is desired, four nodes have to be included and the shape functions and their derivatives in the parameter space are

$$N_1 = \frac{1}{16}\left(-9\,\xi^3 + 9\,\xi^2 + \xi - 1\right), \qquad N_{1,\xi} = \frac{1}{16}\left(-27\,\xi^2 + 18\,\xi + 1\right), \tag{4.65a}$$

$$N_2 = \frac{1}{16}\left(+9\,\xi^3 + 9\,\xi^2 - \xi - 1\right), \qquad N_{2,\xi} = \frac{1}{16}\left(+27\,\xi^2 + 18\,\xi - 1\right), \tag{4.65b}$$

$$N_3 = \frac{9}{16}\left(-3\,\xi^3 - \xi^2 + 3\,\xi + 1\right), \qquad N_{3,\xi} = \frac{9}{16}\left(-9\,\xi^2 - 2\,\xi + 3\right), \tag{4.65c}$$

$$N_4 = \frac{9}{16}\left(+3\,\xi^3 - \xi^2 - 3\,\xi + 1\right), \qquad N_{4,\xi} = \frac{9}{16}\left(+9\,\xi^2 - 2\,\xi - 3\right). \tag{4.65d}$$

For the one-dimensional element, the derivative of a shape function with respect to the coordinate X, as defined in Eq. 4.24 for the three-dimensional case, is then simply given by

$$\frac{\partial N_I}{\partial X} = \frac{1}{J}\,N_{I,\xi} \qquad \text{with} \qquad J = \frac{\partial X}{\partial \xi}. \tag{4.66}$$

Shape functions for two- and three-dimensional elements can be obtained as products of the polynomials listed above in two and three coordinates, respectively. This type of shape functions is referred to as Lagrangian polynomials. Apart from that, other types of multidimensional shape functions with a reduced number of degrees of freedom or other advantages are known. A useful reference in this context has been published by Zienkiewicz & Taylor (2000a, ch. 8).

Adaptations for axisymmetry. In the one-dimensional finite element for rotationally symmetric geometries, only the radial displacement u_1 is assumed to be unknown and any dependencies on the circumferential and axial coordinates X_3 and X_2 are excluded. The general equations are therefore only valid for the first spatial direction and the deformation gradient can be simplified starting from Eq. 4.54 to

$$\boldsymbol{F} = \begin{bmatrix} 1 + u_{1,1} & 0 & 0 \\ 0 & 1 + f_2\,\varepsilon_2 & 0 \\ 0 & 0 & 1 + {}^{\star}u_1/X_1 \end{bmatrix}, \tag{4.67}$$

where the asterisk again marks terms which occur for axisymmetry, but not for the related case of plane strain in X_3-direction. The variable ε_2 denotes a prescribed axial strain acting uniformly at each radial position, which is applied as specified by the load factor f_2. With no shear components remaining, the relevant deformations and stresses in Voigt notation are

$$\tfrac{1}{2}\,\delta\underline{\boldsymbol{C}} = \begin{bmatrix} \frac{1}{2}\,\delta C_{11} \\ \frac{1}{2}\,\delta C_{22} \\ \frac{1}{2}\,\delta C_{33} \end{bmatrix} \qquad \text{and} \qquad \underline{\boldsymbol{S}} = \begin{bmatrix} S_{11} \\ S_{22} \\ S_{33} \end{bmatrix}. \tag{4.68}$$

Evaluation of Eq. 4.16 for the deformation gradient defined in Eq. 4.67 and insertion of the approximation for δu_1, see Eq. 4.26, leads to

$$\tfrac{1}{2}\,\delta C_{22} = F_{22}\,\delta F_{22} = 0 \qquad \text{and} \qquad \tfrac{1}{2}\,\delta C_{33} = F_{33}\,\delta F_{33} \approx \sum_{I=1}^{n} F_{33}\,\frac{N_I}{X_1}\,\delta d_{I1}. \tag{4.69}$$

The nodal B-matrix relating the virtual deformations to the nodal displacements as provided by Eq. 4.29 then has to read

$$\underline{\boldsymbol{B}}_I = \begin{bmatrix} F_{11}\,N_{I,1} \\ 0 \\ {}^{\star}F_{33}\,N_I/X_1 \end{bmatrix}. \tag{4.70}$$

Besides that, only the geometrical part of the stiffness matrix is affected by the incorporation of axisymmetry. According to Eq. 4.17 and Eq. 4.67, the equations

$$\tfrac{1}{2}\,\Delta\delta C_{22} = \Delta F_{22}\,\delta F_{22} = 0 \quad \text{and} \quad \tfrac{1}{2}\,\Delta\delta C_{33} = \Delta F_{33}\,\delta F_{33} \approx \sum_{I=1}^{n}\sum_{J=1}^{n} \delta d_{I1}\,\frac{N_I}{X_1}\,\frac{N_J}{X_1}\,\Delta d_{J1} \tag{4.71}$$

are now valid, such that the submatrices $\underline{\boldsymbol{G}}_{IJ}$ of the matrix $\underline{\boldsymbol{G}}^e$ defined in Eq. 4.42 have to be

$$\underline{\boldsymbol{G}}_{IJ} = \left[G_{IJ} + {}^{\star}\tilde{G}_{IJ}\right] \qquad \text{with} \qquad \tilde{G}_{IJ} = \frac{N_I}{X_1}\,\frac{N_J}{X_1}\,S_{33} \tag{4.72}$$

in order to fulfill the outcome of Eq. 4.41. With respect to the Gauß point integration, Eq. 4.61 identically holds for the one-dimensional axisymmetric element because the height of the undeformed volume element is equal to one.

Application of surface loads in radial direction. During linearization of the weak form of balance of momentum, conservative loads which do not depend on the actual displacements have been assumed in Sec. 4.1.2. As a consequence, the external virtual work is independent of the actual displacements $\boldsymbol{u}^{n+1}$ and no further terms than specified in Eq. 4.46 occur in the element stiffness matrix. However, the application of a hydrostatic internal pressure, keeping its value for different states of deformation or growth of the simulated artery, violates this assumption. In order to maintain a constant pressure in an expanding and axially extending tube, the force applied to the associated node has to increase depending on the radial displacement of that node as well as on the axial strain, see Fig. 4.5, and hence indeed depends on $\boldsymbol{u}^{n+1}$. A hydrostatic pressure can though be applied within the given framework if the converged displacement $\boldsymbol{u}^n$ of the previous load step is used to approximate the actual cross section in step $(n+1)$. In the context of growth, the load will anyway be held constant until a growth equilibrium state with unchanging shape is attained. The change of a cross section from one to the following step is thus vanishing over time and the exactness of the applied pressure increases.

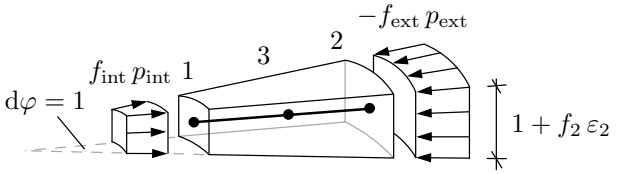

Figure 4.5: The one-dimensional axisymmetric element represents a one-radian radial cutout of a cylinder. In the actual configuration, the areas of front and back surface depend on the radial displacement of nodes 1 and 2, which determine the circumferential length, and on the actual height of the segment dictated by the axial strain.

For a n-noded 1D finite element, the part $\underline{\boldsymbol{p}}^e = \int_{\partial\mathcal{B}^e_\sigma} \underline{\boldsymbol{N}}^{e\mathrm{T}} \bar{\boldsymbol{T}}\,\mathrm{d}A$ in the element residual vector from Eq. 4.45 consists of n components representing the external forces acting on the nodes in radial direction. These forces can directly be computed from the prescribed pressures $f_{\text{int}}\,p_{\text{int}}$ at node 1 and $f_{\text{ext}}\,p_{\text{ext}}$ at node 2 multiplied with the correlated surface areas; numerical integration is not required since each surface consists of a single node I at which $N_I = 1$. Approximating the actual radii at the internal and external surface of the element by

$$r_{\text{int}} = x_1^{n+1}(1) \approx X_1(1) + u_1^n(1) \qquad \text{and} \qquad r_{\text{ext}} = x_1^{n+1}(2) \approx X_1(2) + u_1^n(2), \tag{4.73}$$

where the numbers in brackets denote the correspondent nodes, the element vector of external nodal forces is obtained as

$$\underline{\boldsymbol{p}}^e = \begin{bmatrix} f_{\text{int}}\,p_{\text{int}}\,r_{\text{int}}\,(1 + f_2\,\varepsilon_2) \\ f_{\text{ext}}\,p_{\text{ext}}\,r_{\text{ext}}\,(1 + f_2\,\varepsilon_2) \\ 0 \\ \vdots \end{bmatrix}. \tag{4.74}$$

As suggested by the dots, the contributions of all possibly added further nodes located inside the element are zero. If a pressurized cylindrical geometry is discretized into more than one element, the variables p_{int} and p_{ext} have to be set zero at all unloaded, internal nodes. This means that the attributes of the elements located at the inner and outer surfaces differ from those of the elements in between. A more general way of applying pressure surface loads is to define a separate layer of surface elements to compute the nodal forces and additional terms of the stiffness matrix, see Wriggers (2008, pp. 142 ff.) or Zienkiewicz, Taylor & Fox (2014, pp. 173–175) and the references cited therein, for instance the application to the axisymmetric case by Simo, Taylor & Wriggers (1991). For 3D and 2D problems, including axisymmetry, this method is part of the finite element program FEAP (Taylor, 2008) used in this work. A detailed explanation is therefore skipped with reference to the literature mentioned above.

5 Framework for anisotropic stress-driven growth

The observations on arterial residual stresses and adaptation in arteries summarized in Chapter 2 lead to the conclusion that growth and remodeling should be considered as anisotropic, multiaxial processes which are likely to be substantially regulated by mechanical stimuli. However, there is still no final agreement on the question if strain or stress is the decisive mechanical quantity. It seems to be more common by now to assume that growth and remodeling in soft biological tissues are stress-driven (Comellas, Carriero, et al., 2018). This hypothesis is supported by experimental findings as those mentioned in Sec. 2.3 or recapitulated by Cyron & Humphrey (2017), which indicate that adaptation processes often are governed by the aim of restoring homeostatic stress, not strain levels. Several researchers came to the same estimation when they compared the outcome of their models for strain- and stress-driven adaptation. For example, Taber & Humphrey (2001) concluded by comparison with experimental data that strain, which is a kinematically dictated quantity, provides less flexibility for the growing tissue than stress. Unlike strain, stress is not restricted to vary monotonically across the wall and shows higher local variation. A stress-driven growth mechanism can thus be supposed to be more precise and sensitive than its strain-driven equivalent. Similarly, but regarding the mechanical stimulus for fiber remodeling, Kuhl & Holzapfel (2007) are of the opinion that stress should be preferred to strain since it results in a larger spectrum of fiber orientation angles due to the nonlinear stress-strain relation. Motivated by these considerations, it seems to be appropriate to choose stress as a driving force for growth and remodeling processes.

In this chapter, a generalized framework for anisotropic, stress-driven growth will be presented. After consideration of basic forms of growth, a generalized model for various forms of growth related to a set of three preferred directions is introduced and explained in detail with regard to its algorithmic treatment. In order to demonstrate how different hypotheses on the mechanism of growth in arterial walls can be realized within the generalized formulation, three specific model variants are deduced. Although growth and remodeling are likely to cohere, both phenomena are treated separately. Remodeling, which is incorporated by stress-driven reorientation of the collagen fibers, will be discussed in Chaper 6.

5.1 General framework

The framework for anisotropic growth presented in this section has been developed based on the theory of multiplicative growth introduced in Sec. 3.1.2 and has essentially been inspired by the work of Himpel, Kuhl, et al. (2005) and Kuhl, Maas, et al. (2007). Preliminary steps towards the current formulation are documented in several publications (Zahn & Balzani, 2016, 2017, 2018a). One of the main intentions is the provision of a general local formulation for anisotropic

growth, which operates without manual definition of growth directions requiring structural or geometric information. For example, if an artery subjected to hypertension was assumed to grow in radial direction, it would be necessary to identify this direction at each material point from the geometry in order to allow for this type of growth. However, drawing a deduction from the information gathered in Chapter 2, the arrangement of tissue components is clearly motivated rather mechanically than geometrically. If growth is supposed to be stress-driven, the information available on the stress state should thus indeed be sufficient to identify its multiaxial characteristics. Moreover, a local formulation involves the advantage of in principle being applicable to any boundary value problem, for instance to patient-specific arteries with irregular geometry.

The theory of multiplicative growth relies on the decomposition $\boldsymbol{F} = \boldsymbol{F}_\mathrm{e}\boldsymbol{F}_\mathrm{g}$ introduced in Eq. 3.19. As explained there, the growth tensor $\boldsymbol{F}_\mathrm{g}$ represents the growth part of the deformation and the remaining part $\boldsymbol{F}_\mathrm{e}$ accounts for the effect of external loads and ensures the compatibility of the overall deformation by reassembling the individually grown material points to a continuous body. In addition to the undeformed reference configuration $\mathcal{B}$ and the actual configuration $\mathcal{S}$, the stress-free intermediate configuration $\mathcal{B}_\mathrm{i}$ is involved. This fictive intermediate state corresponds to a situation at which growth prescribed by the growth tensor $\boldsymbol{F}_\mathrm{g}$ has been able to evolve without any hindrance. The information on intensity and anisotropy of the growth process is thereby contained in the tensorial form of $\boldsymbol{F}_\mathrm{g}$.

5.1.1 Basic forms of the growth tensor

The form of the growth tensor has to be postulated. Among many specific proposals available in the literature, as for example reviewed by Kuhl (2014), three basic forms can be identified. These basic forms are defined by

$$\boldsymbol{F}_\mathrm{g}^{\square} = \vartheta \boldsymbol{I} \qquad \text{for isotropic growth,} \tag{5.1a}$$

$$\boldsymbol{F}_\mathrm{g}^{\parallel} = \boldsymbol{I} + (\vartheta - 1)\, \boldsymbol{A}_\mathrm{g} \otimes \boldsymbol{A}_\mathrm{g} \qquad \text{for growth in the direction of } \boldsymbol{A}_\mathrm{g} \text{ and} \tag{5.1b}$$

$$\boldsymbol{F}_\mathrm{g}^{\perp} = \vartheta \boldsymbol{I} + (1 - \vartheta)\, \boldsymbol{A}_\mathrm{g} \otimes \boldsymbol{A}_\mathrm{g} \qquad \text{for growth perpendicular to } \boldsymbol{A}_\mathrm{g}. \tag{5.1c}$$

In these equations, the scalar ϑ, which from now on will be denoted as growth factor, is related to the amount of growth, and the unit vector $\boldsymbol{A}_\mathrm{g}$ with $|\boldsymbol{A}_\mathrm{g}| = 1$ causes different types of anisotropy and marks a direction which behaves different from the others. The vector $\boldsymbol{A}_\mathrm{g}$ will therefore be referred to as growth orientation vector.

Illustrative example. For better understanding of the basic types of growth defined in Eq. 5.1, the growth deformation of a unit cube, represented by the vector $\boldsymbol{v} = \boldsymbol{e}_1 + \boldsymbol{e}_2 + \boldsymbol{e}_3$, shall be considered. The cube is supposed to have a preferred direction $\boldsymbol{A}_\mathrm{g} = \boldsymbol{e}_2$ parallel to the x_2-axis which behaves stiffer than the other two directions. Subjected to a load in x_2-direction, a stress σ_{22} might exist, which, by a relation that still has to be defined, is assumed to cause growth characterized by growth factor ϑ. If the cube grows isotropically, its intermediate configuration is defined by the vector $\boldsymbol{v}_\mathrm{i}^{\square}$ computed as

$$\boldsymbol{v}_\mathrm{i}^{\square} = \boldsymbol{F}_\mathrm{g}^{\square}\, \boldsymbol{v} = \begin{bmatrix} \vartheta & 0 & 0 \\ 0 & \vartheta & 0 \\ 0 & 0 & \vartheta \end{bmatrix} \begin{bmatrix} 1 \\ 1 \\ 1 \end{bmatrix} = \begin{bmatrix} \vartheta \\ \vartheta \\ \vartheta \end{bmatrix}. \tag{5.2}$$

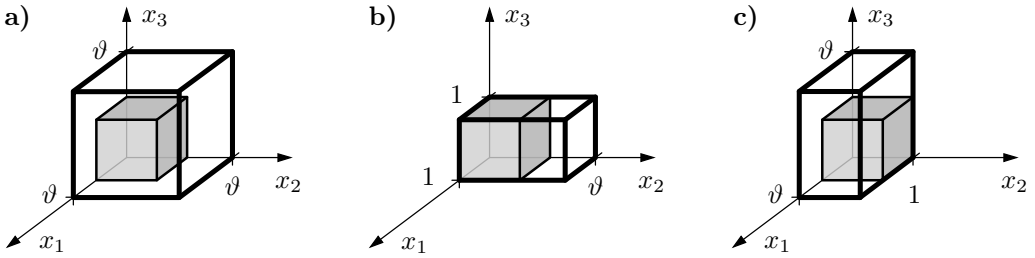

Figure 5.1: Illustration of the basic growth tensor forms **a)** $\boldsymbol{F}_\mathrm{g}^{\square}$ for isotropic growth, **b)** $\boldsymbol{F}_\mathrm{g}^{\parallel}$ for growth in the direction of $\boldsymbol{A}_\mathrm{g} = \boldsymbol{e}_2$ and **c)** $\boldsymbol{F}_\mathrm{g}^{\perp}$ for growth perpendicular to the direction of $\boldsymbol{A}_\mathrm{g} = \boldsymbol{e}_2$ by means of a grown cube whose reference configuration (gray unit cube) is spanned by the vector $\boldsymbol{v} = \boldsymbol{e}_1 + \boldsymbol{e}_2 + \boldsymbol{e}_3$.

As depicted in Fig. 5.1 a), the cube keeps its original shape, but each of its edges is lengthened by factor ϑ. For the other two basic types of growth, the structural tensor

$$\boldsymbol{A}_\mathrm{g} \otimes \boldsymbol{A}_\mathrm{g} = \boldsymbol{e}_2 \otimes \boldsymbol{e}_2 = \begin{bmatrix} 0 & 0 & 0 \\ 0 & 1 & 0 \\ 0 & 0 & 0 \end{bmatrix} \tag{5.3}$$

induces anisotropy. The grown cubes are then defined by the vectors

$$\boldsymbol{v}_\mathrm{i}^{\parallel} = \boldsymbol{F}_\mathrm{g}^{\parallel}\,\boldsymbol{v} = \begin{bmatrix} 1 & 0 & 0 \\ 0 & \vartheta & 0 \\ 0 & 0 & 1 \end{bmatrix} \begin{bmatrix} 1 \\ 1 \\ 1 \end{bmatrix} = \begin{bmatrix} 1 \\ \vartheta \\ 1 \end{bmatrix} \quad \text{and} \quad \boldsymbol{v}_\mathrm{i}^{\perp} = \boldsymbol{F}_\mathrm{g}^{\perp}\,\boldsymbol{v} = \begin{bmatrix} \vartheta & 0 & 0 \\ 0 & 1 & 0 \\ 0 & 0 & \vartheta \end{bmatrix} \begin{bmatrix} 1 \\ 1 \\ 1 \end{bmatrix} = \begin{bmatrix} \vartheta \\ 1 \\ \vartheta \end{bmatrix}, \tag{5.4}$$

see Fig. 5.1 b) and c). In both cases, the shape of the grown cube differs from the original one: either it is elongated exclusively in the preferred direction or perpendicular to it. The volume increase of the three cubes is obviously not the same. As mentioned in Eq. 3.21 and confirmed by this example, the ratio $\mathrm{d}V_\mathrm{i}/\mathrm{d}V$ of grown to reference volume is defined by $\det[\boldsymbol{F}_\mathrm{g}]$ and equal to ϑ^3, ϑ and ϑ^2 in the cases a), b) and c) as denoted in Fig. 5.1, respectively.
To conclude the example, a few remarks on the effect of growth on the stress σ_{22} shall be added. It essentially depends on the type of loading if a reduction of the stress can be achieved or not. Supposed that the stress arises from a constant force applied to the cube, an increase of the cross sectional area in the x_1-x_3-plane as occurring in cases a) and c) leads to a reduction of σ_{22}, but growth in the direction of the load has no effect. The opposite is the case if the stress is caused by a prescribed displacement in x_2-direction. Then, mainly the x_2-component of growth contributes to a drastic reduction of the stress since it compensates the imposed deformation. Compared to this, the reduction by increase of the cross section in case c) is negligible. Both loading scenarios at the same time are thus best covered by isotropic growth, but this is at the expense of an unnecessarily high volume increase which is accompanied by potentially avoidable energetic costs.

As clarified in the example above, the structural tensor $\boldsymbol{A}_\mathrm{g} \otimes \boldsymbol{A}_\mathrm{g}$ filters out contributions in the direction of a preferred direction $\boldsymbol{A}_\mathrm{g}$. Whereas this can easily be understood for special cases in which the preferred direction is parallel to a coordinate axis (for example for $\boldsymbol{A}_\mathrm{g} = \boldsymbol{e}_2$), it is less clear for an arbitrary preferred direction with a more complex structural tensor. It can be shown by a coordinate transformation, which rotates an arbitrary vector $\boldsymbol{A}_\mathrm{g}$ via $\boldsymbol{Q}\boldsymbol{A}_\mathrm{g} = \boldsymbol{A}_\mathrm{g}^{*} = \boldsymbol{e}_2$ to

the considered axis, that the observed behavior is valid in general. The growth tensor $\boldsymbol{F}_{\mathrm{g}}^{\perp}$ in the rotated coordinate system is given by

$$\begin{aligned}\boldsymbol{F}_{\mathrm{g}}^{\perp *} &= \boldsymbol{Q}\boldsymbol{F}_{\mathrm{g}}^{\perp}\boldsymbol{Q}^{\mathrm{T}} \\ &= \vartheta\,\boldsymbol{Q}\boldsymbol{I}\boldsymbol{Q}^{\mathrm{T}} + (1-\vartheta)\,\boldsymbol{Q}\,(\boldsymbol{A}_{\mathrm{g}}\otimes\boldsymbol{A}_{\mathrm{g}})\,\boldsymbol{Q}^{\mathrm{T}} \qquad \text{with} \quad \boldsymbol{Q}^{\mathrm{T}} = \boldsymbol{Q}^{-1} \\ &= \vartheta\boldsymbol{I} + (1-\vartheta)\,(\boldsymbol{Q}\boldsymbol{A}_{\mathrm{g}})\otimes(\boldsymbol{Q}\boldsymbol{A}_{\mathrm{g}}) \\ &= \vartheta\boldsymbol{I} + (1-\vartheta)\,\boldsymbol{A}_{\mathrm{g}}^{*}\otimes\boldsymbol{A}_{\mathrm{g}}^{*}\end{aligned} \tag{5.5}$$

and has thus the same structure as in the original coordinate system, see Eq. 5.1c. Analogously, the rotated counterpart of $\boldsymbol{F}_{\mathrm{g}}^{\parallel}$ from Eq. 5.1b can be computed as

$$\boldsymbol{F}_{\mathrm{g}}^{\parallel *} = \boldsymbol{Q}\boldsymbol{F}_{\mathrm{g}}^{\parallel}\boldsymbol{Q}^{\mathrm{T}} = \boldsymbol{I} + (\vartheta-1)\,\boldsymbol{A}_{\mathrm{g}}^{*}\otimes\boldsymbol{A}_{\mathrm{g}}^{*}. \tag{5.6}$$

These transformations confirm that the growth tensors $\boldsymbol{F}_{\mathrm{g}}^{\perp}$ and $\boldsymbol{F}_{\mathrm{g}}^{\parallel}$ describe growth perpendicular to or in the direction of $\boldsymbol{A}_{\mathrm{g}}$ for any preferred direction $\boldsymbol{A}_{\mathrm{g}}$.

The multiaxial character of growth in soft biological tissues suggests that one single preferred direction cannot be sufficient to model the observed growth phenomena. For this reason, a generalized formulation for anisotropic growth is proposed, which takes up to three preferred directions into account.

5.1.2 Generalized formulation for anisotropic growth

In order to enable the incorporation of up to three preferred directions, which might be able to reflect the complex growth processes in arteries, the growth tensor $\boldsymbol{F}_{\mathrm{g}}$ is decomposed multiplicatively into three parts according to

$$\boldsymbol{F}_{\mathrm{g}} = \boldsymbol{F}_{\mathrm{g}}^{(3)}\boldsymbol{F}_{\mathrm{g}}^{(2)}\boldsymbol{F}_{\mathrm{g}}^{(1)}. \tag{5.7}$$

Each of these multiplicative parts $\boldsymbol{F}_{\mathrm{g}}^{(a)}$ with $a \in [1,2,3]$ is allowed to adopt one of the basic forms defined in Eq. 5.1 or to be equal to the unit tensor $\boldsymbol{I}$ provided that only a reduced number of directions is intended to be included. Each part might thus involve an individual growth factor $\vartheta^{(a)}$ and an individual growth orientation vector $\boldsymbol{A}_{\mathrm{g}}^{(a)}$. This structure offers a high flexibility as it enables the consideration and comparison of a multitude of different growth mechanisms ranging from isotropic growth to orthotropic growth in three directions. Only the small example on p. 60 already makes clear that stress reduction induced by growth is a very complex process with many influencing factors. First, it is not clear to which extent relevant loads in arteries are of stress-, force-, strain- or displacement-driven type. This however affects the effectiveness of a particular growth mechanism. Apart from that, the amount of newly grown material might differ drastically between different forms of growth. Since growth-induced volume changes are associated to energetic costs, an effective growth mechanism is likely to aim at keeping them as low as possible. In the modeling context, isotropic growth is the simplest way to account for different loading scenarios, but it comes along with large volume changes and is not realistic since growth in arteries is obviously anisotropic. Growth in the direction of a relevant load has the advantage of effectively reducing stresses in strain-driven loading situations with comparatively very low volume changes, but it has no effect if the load consists of a constant force. By an increase of the cross sectional area, growth perpendicular to the preferred direction

can reduce stresses in both loading scenarios, but it is less effective. The general form of the growth tensor introduced in Eq. 5.7 enables the analysis of various approaches and might thus lead to a conclusion with respect to the real, unknown mechanism.

From a technical point of view, it is necessary to demand commutativity of the right hand side of Eq. 5.7. Only then, the growth mechanisms associated to different directions are independent of each other and the overall growth tensor does not depend on the chronological order in which those directions have been defined. With reference to the basic forms predefined in Eq. 5.1, the only terms in each possible product $\boldsymbol{F}_{\mathrm{g}}^{(a)}\boldsymbol{F}_{\mathrm{g}}^{(b)}$ with $a \neq b$, which are not a priori commutative, are the terms involving products of the form $\left(\boldsymbol{A}_{\mathrm{g}}^{(a)} \otimes \boldsymbol{A}_{\mathrm{g}}^{(a)}\right)\left(\boldsymbol{A}_{\mathrm{g}}^{(b)} \otimes \boldsymbol{A}_{\mathrm{g}}^{(b)}\right)$. The commutativity of Eq. 5.7 is thus ensured if the growth orientation (unit) vectors fulfill the condition $\boldsymbol{A}_{\mathrm{g}}^{(a)} \cdot \boldsymbol{A}_{\mathrm{g}}^{(b)} = 0$ for $a \neq b$, which means that they must constitute a set of orthogonal directions with the property

$$\boldsymbol{A}_{\mathrm{g}}^{(a)} \cdot \boldsymbol{A}_{\mathrm{g}}^{(b)} = \delta_{ab}. \tag{5.8}$$

The overall growth tensor can then be expanded to a sum of terms given by scalar multiples of the unit tensor $\boldsymbol{I}$ and of the structural tensors $\boldsymbol{A}_{\mathrm{g}}^{(a)} \otimes \boldsymbol{A}_{\mathrm{g}}^{(a)}$ with $a \in [1, 2, 3]$. Its general form can thus be expressed by

$$\boldsymbol{F}_{\mathrm{g}} = \alpha_0\, \boldsymbol{I} + \sum_{a=1}^{3} \alpha_a\, \boldsymbol{A}_{\mathrm{g}}^{(a)} \otimes \boldsymbol{A}_{\mathrm{g}}^{(a)}, \tag{5.9}$$

where the coefficients α_a are functions of the growth factors $\vartheta^{(a)}$ and depend on the choice of the basic form for the individual parts $\boldsymbol{F}_{\mathrm{g}}^{(a)}$ from Eq. 5.1. Due to the symmetry of its individual summands, the growth tensor turns out to be symmetric, i. e. $\boldsymbol{F}_{\mathrm{g}}^{\mathrm{T}} = \boldsymbol{F}_{\mathrm{g}}$. Another important outcome of the orthogonality of the growth orientation vectors is the property that they are eigenvectors of the growth tensor per definition. As obvious from

$$\boldsymbol{F}_{\mathrm{g}}\boldsymbol{A}_{\mathrm{g}}^{(b)} = \alpha_0\, \boldsymbol{A}_{\mathrm{g}}^{(b)} + \alpha_b\, \boldsymbol{A}_{\mathrm{g}}^{(b)} = (\alpha_0 + \alpha_b)\, \boldsymbol{A}_{\mathrm{g}}^{(b)}, \tag{5.10}$$

which follows from Eq. 5.9 due to Eq. 5.8, only the length but not the orientation of the growth orientation vectors is changed during the transformation from the reference to the intermediate configuration.

Together with the choice of stress as growth driving quantity, the requirement of orthogonality and the interpretation of the growth orientation vectors as eigenvectors suggest to define the latter as principal directions of a suitable stress tensor. This ensures the local character of the formulation and enables the simulation of growth processes which are directly (and exclusively) governed by local mechanical state variables. Following Himpel, Kuhl, et al. (2005), the Mandel stress in the intermediate configuration, which is defined by

$$\boldsymbol{\Sigma}_{\mathrm{e}} := \boldsymbol{C}_{\mathrm{e}}\boldsymbol{S}_{\mathrm{e}}, \tag{5.11}$$

is chosen as growth and remodeling driving quantity. Himpel, Kuhl, et al. motivated that choice by the observation that $\boldsymbol{\Sigma}_{\mathrm{e}}$ is energetically conjugated to the growth velocity gradient in Eq. 3.108. The growth velocity gradient $\boldsymbol{L}_{\mathrm{g}}$ in turn, introduced in Eq. 3.26, is directly linked to the temporal evolution of the growth tensor through $\dot{\boldsymbol{F}}_{\mathrm{g}} = \boldsymbol{L}_{\mathrm{g}}\boldsymbol{F}_{\mathrm{g}}$. In spite of being a product of two symmetric tensors, $\boldsymbol{\Sigma}_{\mathrm{e}}$ is in general non-symmetric and its eigenvectors do not form an

orthogonal system. In order to ensure the orthogonality requirement, the growth orientation vectors $\boldsymbol{A}_{\mathrm{g}}^{(a)}$ are defined as principal directions of the symmetric part

$$\bar{\boldsymbol{\Sigma}}_{\mathrm{e}} = \mathrm{sym}[\boldsymbol{\Sigma}_{\mathrm{e}}] = \tfrac{1}{2}\left(\boldsymbol{C}_{\mathrm{e}}\boldsymbol{S}_{\mathrm{e}} + \boldsymbol{S}_{\mathrm{e}}\boldsymbol{C}_{\mathrm{e}}\right) \tag{5.12}$$

of the Mandel stress tensor $\boldsymbol{\Sigma}_{\mathrm{e}}$. The antimetric part is assumed to be neglectable, such that the principal stress state of $\boldsymbol{\Sigma}_{\mathrm{e}}$ is well represented by $\bar{\boldsymbol{\Sigma}}_{\mathrm{e}}$. This assumption is even thoroughly correct as long as only rotationally symmetric arteries are considered, where the antimetric part of $\boldsymbol{\Sigma}_{\mathrm{e}}$ disappears completely. In that case, the principal directions of $\boldsymbol{C}_{\mathrm{e}}$ and $\boldsymbol{S}_{\mathrm{e}}$ coincide and are aligned in circumferential, axial and radial direction.
At this point, only the values of the growth factors $\vartheta^{(a)}$, which determine the amount of growth, remain unknown for completeness of the growth tensor $\boldsymbol{F}_{\mathrm{g}}$. It proved convenient to prescribe the evolution of the growth factors by a set of equations of the form

$$\dot{\vartheta}^{(a)} = k_{\vartheta}^{(a)}(\vartheta^{(a)})\,\phi^{(a)}(\boldsymbol{\Sigma}_{\mathrm{e}}) \qquad \text{with} \qquad a \in [1,2,3], \tag{5.13}$$

as initially proposed by Lubarda & Hoger (2002). According to this evolution equation, the actual value of growth factor $\vartheta^{(a)}$ depends on the growth-driving Mandel stress tensor through a function $\phi^{(a)}(\boldsymbol{\Sigma}_{\mathrm{e}})$ and is subjected to some limiting restrictions imposed by a growth function $k_{\vartheta}^{(a)}(\vartheta^{(a)})$. The latter function, defined by

$$k_{\vartheta}^{(a)}(\vartheta^{(a)}) = \begin{cases} k_{\vartheta,(a)}^{+}\left[\dfrac{\vartheta_{(a)}^{+} - \vartheta^{(a)}}{\vartheta_{(a)}^{+} - 1}\right]^{m_{\vartheta,(a)}^{+}} & \text{for} \quad \phi^{(a)}(\boldsymbol{\Sigma}_{\mathrm{e}}) > 0 \\ k_{\vartheta,(a)}^{-}\left[\dfrac{\vartheta^{(a)} - \vartheta_{(a)}^{-}}{1 - \vartheta_{(a)}^{-}}\right]^{m_{\vartheta,(a)}^{-}} & \text{for} \quad \phi^{(a)}(\boldsymbol{\Sigma}_{\mathrm{e}}) < 0 \\ 0 & \text{for} \quad \phi^{(a)}(\boldsymbol{\Sigma}_{\mathrm{e}}) = 0, \end{cases} \tag{5.14}$$

is adopted from Lubarda & Hoger and visualized in Fig. 5.2 for a positive value of $\phi^{(a)}$ and different values of its parameters $\vartheta_{(a)}^{+}$ and $m_{\vartheta,(a)}^{+}$. The effect of the growth function is twofold. On the one hand, it restricts the admissible range of each growth factor to

$$\vartheta^{(a)} \in \left[\vartheta_{(a)}^{-}, \vartheta_{(a)}^{+}\right] \qquad \text{with} \qquad \vartheta_{(a)}^{-} < 1 \quad \text{and} \quad \vartheta_{(a)}^{+} > 1 \tag{5.15}$$

as it approaches zero when these limiting values are reached. On the other hand, it scales the growth velocity by a factor $k_{\vartheta,(a)}^{+/-}$. The parameters $m_{\vartheta,(a)}^{+/-}$ determine the degree of the growth function in its nonzero range, and might for example lead to the linear and cubic graphs shown in Fig. 5.2.

The function $\phi^{(a)}(\boldsymbol{\Sigma}_{\mathrm{e}})$ accounts for the mechanical stimulus provoking growth related to the direction a and will for this reason be denoted as driving force from now on. Different proposals for its explicit functional form will be presented and motivated in Sec. 5.1.4. Prior to this, the algorithmic treatment of the generalized growth model will be explained. For these considerations, it is enough to note that the function $\phi^{(a)}(\boldsymbol{\Sigma}_{\mathrm{e}})$ depends on $\boldsymbol{F}_{\mathrm{g}}$ through Eq. 5.11 as obvious from Eq. 3.22 and Eq. 3.101, and is thus a function of all growth factors $\vartheta^{(1)}$, $\vartheta^{(2)}$ and $\vartheta^{(3)}$. This implies that Eq. 5.13 constitutes a coupled set of nonlinear differential equations, which has to be solved for the actual values of the growth factors $\vartheta^{(a)}$.

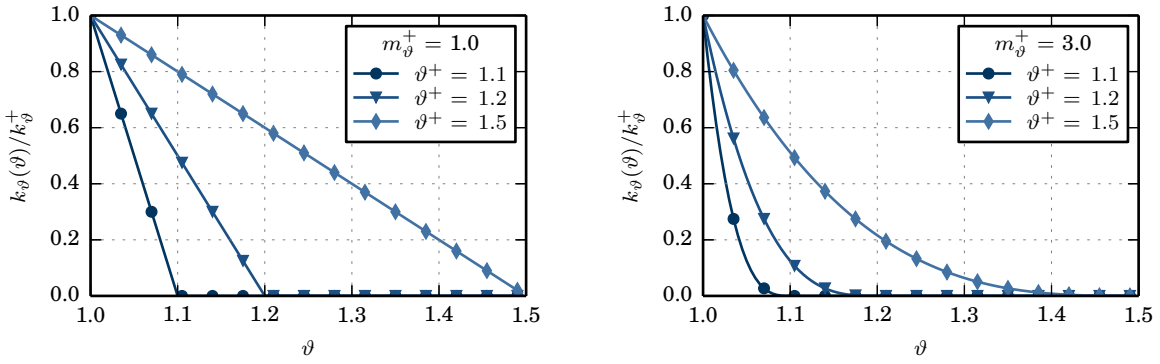

Figure 5.2: Graphs of the growth function $k_\vartheta(\vartheta)$ for $\phi(\boldsymbol{\Sigma}_\mathrm{e}) > 0$ in the range of positive growth with $\vartheta > 1$ for different values of the parameters ϑ^+ and m_ϑ^+. The index (a), denoting the direction to which the function and its parameters are assigned, is omitted here in favor of clarity.

5.1.3 Algorithmic treatment of the generalized formulation

For the solution of Eq. 5.13, time integration has to be applied. Given that all variables are known at time t_n, the values $\vartheta_{n+1}^{(a)}$ of the growth factors at actual time t_{n+1} can be computed from

$$\int_{t_n}^{t_{n+1}} \dot{\vartheta}^{(a)}\,\mathrm{d}t = \vartheta_{n+1}^{(a)} - \vartheta_n^{(a)} = \int_{t_n}^{t_{n+1}} k_\vartheta^{(a)}(\vartheta^{(a)})\,\phi^{(a)}(\boldsymbol{\Sigma}_\mathrm{e})\,\mathrm{d}t \tag{5.16}$$

if the integral on the right hand side is evaluated between t_n and t_{n+1}. Since a closed analytical solution is not available for this integral, an approximation is introduced as illustrated in Fig. 5.3. The integral is replaced by an approximation of the area below the curve, which can be obtained in different ways, either based on known values belonging to time step n, on unknown values belonging to time step $n+1$ or using both of them. The approximation

$$\vartheta_{n+1}^{(a)} - \vartheta_n^{(a)} \approx \left(\kappa\,\dot{\vartheta}_{n+1}^{(a)} + (1-\kappa)\;\dot{\vartheta}_n^{(a)}\right)\Delta t \tag{5.17}$$

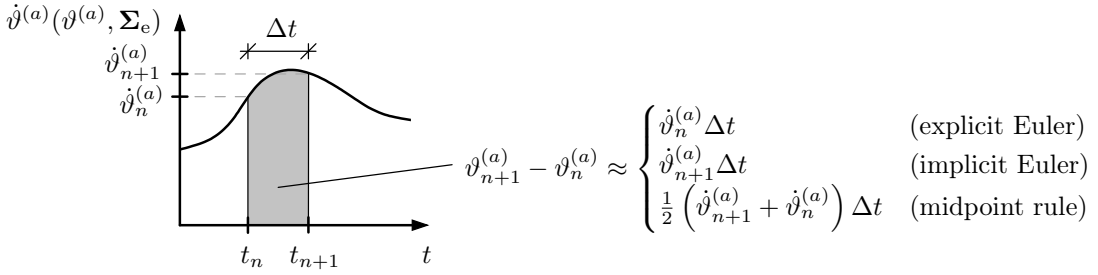

Figure 5.3: For numerical time integration of the function $\dot{\vartheta}^{(a)}(\vartheta^{(a)}, \boldsymbol{\Sigma}_\mathrm{e})$, the gray area below the curve between t_n and t_{n+1} can be approximated in different ways. Using the explicit Euler forward scheme, the function which has to be integrated has only to be evaluated at time step t_n, where its value is known. Implicit Euler backward scheme and midpoint rule involve function evaluations at the actual time step t_{n+1}, which necessitates an iteration.

with $\Delta t = t_{n+1} - t_n$ captures those three cases by means of the variable $\kappa \in [0, 1/2, 1]$. For $\kappa = 0$ and $\kappa = 1$, the explicit and implicit Euler integration schemes are obtained, respectively. Choice of $\kappa = 1/2$ leads to the midpoint rule, which approximates the area by a trapezoid instead of a rectangle. Using the approximation in Eq. 5.17, the system of equations from Eq. 5.13 turns into a set of equations defined by the residuals

$$R^{(a)} := -\vartheta^{(a)}_{n+1} + \vartheta^{(a)}_n + \left(\kappa \, k^{(a)}_\vartheta \, \phi^{(a)} \Big|_{t_{n+1}} + (1-\kappa) \, k^{(a)}_\vartheta \, \phi^{(a)} \Big|_{t_n} \right) \Delta t = 0 \tag{5.18}$$

with $a \in [1, 2, 3]$. With the exception of the case $\kappa = 0$, this system of equations is coupled and nonlinear. By linearization of the residuals associated to time step $n+1$, the system of equations

$$\begin{aligned}
R^{(1)}\big|_{\vartheta^{(a)}_k} + \frac{\partial R^{(1)}}{\partial \vartheta^{(1)}}\bigg|_{\vartheta^{(a)}_k} \Delta\vartheta^{(1)}_{k+1} + \frac{\partial R^{(1)}}{\partial \vartheta^{(2)}}\bigg|_{\vartheta^{(a)}_k} \Delta\vartheta^{(2)}_{k+1} + \frac{\partial R^{(1)}}{\partial \vartheta^{(3)}}\bigg|_{\vartheta^{(a)}_k} \Delta\vartheta^{(3)}_{k+1} = 0 \\
R^{(2)}\big|_{\vartheta^{(a)}_k} + \frac{\partial R^{(2)}}{\partial \vartheta^{(1)}}\bigg|_{\vartheta^{(a)}_k} \Delta\vartheta^{(1)}_{k+1} + \frac{\partial R^{(2)}}{\partial \vartheta^{(2)}}\bigg|_{\vartheta^{(a)}_k} \Delta\vartheta^{(2)}_{k+1} + \frac{\partial R^{(2)}}{\partial \vartheta^{(3)}}\bigg|_{\vartheta^{(a)}_k} \Delta\vartheta^{(3)}_{k+1} = 0 \\
R^{(3)}\big|_{\vartheta^{(a)}_k} + \frac{\partial R^{(3)}}{\partial \vartheta^{(1)}}\bigg|_{\vartheta^{(a)}_k} \Delta\vartheta^{(1)}_{k+1} + \frac{\partial R^{(3)}}{\partial \vartheta^{(2)}}\bigg|_{\vartheta^{(a)}_k} \Delta\vartheta^{(2)}_{k+1} + \frac{\partial R^{(3)}}{\partial \vartheta^{(3)}}\bigg|_{\vartheta^{(a)}_k} \Delta\vartheta^{(3)}_{k+1} = 0
\end{aligned} \tag{5.19}$$

is obtained. It has to be solved repeatedly in a local Newton iteration, with iteration steps denoted by index k, for the incremental updates $\Delta\vartheta^{(a)}$ of the growth factors. The growth factors are updated by those increments until a suitable convergence criterion, for example $\Delta\vartheta^{(a)} \leq 10^{-8}$ for each direction a, signalizes that the iteration can be aborted. The derivatives of the residuals $R^{(i)}$ from Eq. 5.18 with respect to the growth factors $\vartheta^{(j)}$ for $i, j \in [1, 2, 3]$, which are needed in Eq. 5.19, are given by

$$\frac{\partial R^{(a)}}{\partial \vartheta^{(a)}} = -1 + \left(\frac{\partial k^{(a)}_\vartheta}{\partial \vartheta^{(a)}} \, \phi^{(a)} + k^{(a)}_\vartheta \, \frac{\partial \phi^{(a)}}{\partial \vartheta^{(a)}} \right) \kappa \, \Delta t \qquad \text{for} \qquad a \in [1, 2, 3], \tag{5.20a}$$

$$\frac{\partial R^{(i)}}{\partial \vartheta^{(j)}} = k^{(i)}_\vartheta \, \frac{\partial \phi^{(i)}}{\partial \vartheta^{(j)}} \, \kappa \, \Delta t \qquad \text{for} \qquad i, j \in [1, 2, 3] \quad \text{with} \quad i \neq j. \tag{5.20b}$$

This involves the derivatives of the growth function, which are computed as

$$\frac{\partial k^{(a)}_\vartheta(\vartheta^{(a)})}{\partial \vartheta^{(a)}} = \begin{cases} \dfrac{m^+_{\vartheta,(a)}}{\vartheta^{(a)} - \vartheta^+_{(a)}} \, k^{(a)}_\vartheta(\vartheta^{(a)}) & \text{for} \quad \phi^{(a)}(\boldsymbol{\Sigma}_\mathrm{e}) > 0 \\ \dfrac{m^-_{(a)}}{\vartheta^{(a)} - \vartheta^-_{(a)}} \, k^{(a)}_\vartheta(\vartheta^{(a)}) & \text{for} \quad \phi^{(a)}(\boldsymbol{\Sigma}_\mathrm{e}) < 0 \\ 0 & \text{for} \quad \phi^{(a)}(\boldsymbol{\Sigma}_\mathrm{e}) = 0, \end{cases} \tag{5.21}$$

and the derivatives $\partial\phi^{(i)}(\boldsymbol{\Sigma}_\mathrm{e})/\partial\vartheta^{(j)}$ of the driving force, which will be specified separately in Sec. 5.1.4. Considering briefly the special case $\kappa = 0$, that is assuming explicit time integration, $\partial R^{(a)}/\partial\vartheta^{(a)} = -1$ and $\partial R^{(i)}/\partial\vartheta^{(j)} = 0$ follow from Eq. 5.20. The latter means that all coupling terms disappear from the system of equations in Eq. 5.19 and that the incremental updates of all growth factors can directly be identified. Since $\kappa = 0$ means that the original system of equations in Eq. 5.18 is no longer nonlinear in $\vartheta^{(a)}_{n+1}$, one single iteration step is enough to obtain

the values of the growth factors at time t_{n+1}, which are explicitly given in terms of known quantities. This clarifies that explicit time integration comes along with reduced numerical and implementation effort. It is however afflicted with the disadvantage that numerical stability is only ensured for a sufficiently small time step size Δt. This restriction can be avoided by using the implicit Euler backward integration scheme, which is unconditionally stable. An even better approximation combined with numerical stability can be obtained by means of the midpoint rule, but it must be pointed out that this scheme – just as Euler forward scheme – requires entrainment of additional history variables compared to Euler backward scheme. For each direction, the value of the driving force at time step t_n has to be stored for evaluation of Eq. 5.18. In summary, numerical effort increases from explicit over implicit Euler method to the midpoint rule, and numerical stability is only guaranteed for the latter two. As confirmed by several publications of the work group around Kuhl (Himpel, Kuhl, et al., 2005; Kuhl, Maas, et al., 2007; Göktepe, Abilez & Kuhl, 2010; Sáez, Peña, et al., 2014), Euler backward scheme is a reliable choice for the solution of evolution equations of the type of Eq. 5.13. Since no major amelioration of the performance due to use of the midpoint rule could be stated, the examples presented in this work likewise make use of Euler backward scheme, i. e. $\kappa = 1$.

In the algorithm described above, the growth orientation vectors as well as the fiber vectors are considered as fixed during the local iteration. Actually, the growth orientation vectors, computed as principal directions of the symmetric part $\bar{\boldsymbol{\Sigma}}_\mathrm{e}$ of the Mandel stress tensor, depend implicitly on the current value of the growth tensor. The same holds for the fiber vectors, provided that fiber reorientation driven by $\boldsymbol{\Sigma}_\mathrm{e}$ is assumed. Because of the complexity of the mutual dependencies between growth factors $\vartheta^{(a)}$, growth orientation vectors $\boldsymbol{A}_\mathrm{g}^{(a)}$ (both with $a \in [1,2,3]$) and fiber orientation vectors $\boldsymbol{A}^{(a)}$ (with $a \in [1,\ldots,n_\mathrm{f}]$), the latter two are taken over from the previous time step. After completion of the local Newton iteration, which ends up in the actual value of the growth tensor and the Mandel stress, the new growth and fiber orientation vectors are computed and saved for use in the next time step. If the new principal directions of $\bar{\boldsymbol{\Sigma}}_\mathrm{e}$ differ from the old growth orientation vectors, the new growth orientation vectors are defined such that the nearest principal directions are assigned. This prevents greater jumps of the vectors in case the order of the principal stresses changes. Exemplified with the aid of a pressurized cylindrical tube, where the axial stress is lower than the circumferential stress, this might for example happen if an increasing axial load leads to an axial stress which exceeds the circumferential one. In this situation, growth associated to the two directions, represented by the multiplicative parts of the growth tensor, should not be interchanged even though the order of the principal stresses switches. This can be realized by always assigning the nearest new directions.
Handling of the fiber orientation vectors is described in Chapter 6, where reorientation of the fibers is discussed. In principle, the two adaptation processes, i. e. growth and fiber reorientation, are treated in a two step mechanism, which does not take direct coupling effects within one time step into account.

Knowledge of the growth tensor now allows to compute the 2nd Piola-Kirchhoff stress tensor $\boldsymbol{S} = \boldsymbol{F}_\mathrm{g}^{-1}\boldsymbol{S}_\mathrm{e}\boldsymbol{F}_\mathrm{g}^{-\mathrm{T}}$ and also the real stress $\boldsymbol{\sigma} = {}^1\!/_J\, \boldsymbol{F}\boldsymbol{S}\boldsymbol{F}^\mathrm{T}$, see Sec. 3.2 and Sec. 3.5 for recapitulation. For a complete explanation of the algorithmic treatment, the derivation of the tangent modulus $\mathbb{C}$, which is needed for the element stiffness matrix in Eq. 4.46, is still missing. The tangent modulus can be computed analytically, but this involves various potentially difficult derivatives, which have to be recomputed whenever the model is adapted or extended, for example when a new

driving force is included. Since deduction and implementation of the analytical tangent modulus are time-consuming and prone to errors, a numerical method might be a valuable alternative or at least a replenishment to crosscheck the analytical formulation. The implementation of the numerical tangent modulus is straightforward and, if once elaborated successfully, works regardless of model adaptations. The burden for this advantage is a significant increase of the computing time in comparison to the analytical formulation. In the following paragraphs, analytical and numerical computation of the tangent modulus are described.

Analytical tangent modulus. In Eq. 4.14, the tangent modulus has been introduced as $\mathbb{C} = 2\,\mathrm{d}\boldsymbol{S}/\mathrm{d}\boldsymbol{C}$, which means that computation of the total derivative of $\boldsymbol{S}$ with respect to $\boldsymbol{C}$ is required. The tangent modulus is therefore obtained from

$$\mathbb{C} = 2\,\frac{\mathrm{d}\boldsymbol{S}}{\mathrm{d}\boldsymbol{C}} = \underbrace{2\,\frac{\partial \boldsymbol{S}}{\partial \boldsymbol{C}}}_{\mathbb{C}^{\mathrm{e}}} + \underbrace{2\sum_{a=1}^{3}\frac{\partial \boldsymbol{S}}{\partial \vartheta^{(a)}} \otimes \frac{\partial \vartheta^{(a)}}{\partial \boldsymbol{C}}}_{\mathbb{C}^{\mathrm{g}}}, \tag{5.22}$$

where $\mathbb{C}^{\mathrm{e}}$ is the standard elastic part and $\mathbb{C}^{\mathrm{g}}$ contains the additional effect of growth. Starting from the elastic part of the tangent modulus in the intermediate configuration, which is defined by

$$\mathbb{C}^{\mathrm{e}}_{\mathrm{i}} := 2\,\frac{\partial \boldsymbol{S}_{\mathrm{e}}}{\partial \boldsymbol{C}_{\mathrm{e}}} = 4\,\frac{\partial^2 \psi}{\partial \boldsymbol{C}_{\mathrm{e}} \partial \boldsymbol{C}_{\mathrm{e}}}, \tag{5.23}$$

the elastic part $\mathbb{C}^{\mathrm{e}}$ can be computed performing the pullback operation

$$\mathbb{C}^{\mathrm{e}} = \left(\boldsymbol{F}_{\mathrm{g}}^{-1} \boxtimes \boldsymbol{F}_{\mathrm{g}}^{-1}\right) : \mathbb{C}^{\mathrm{e}}_{\mathrm{i}} : \left(\boldsymbol{F}_{\mathrm{g}}^{-\mathrm{T}} \boxtimes \boldsymbol{F}_{\mathrm{g}}^{-\mathrm{T}}\right) \tag{5.24}$$

from the intermediate to the reference configuration.[1] The inverse of the growth tensor from Eq.5.7 can be expressed explicitly due to the special form of the multiplicative parts $\boldsymbol{F}_{\mathrm{g}}^{(a)}$ as

$$\boldsymbol{F}_{\mathrm{g}}^{-1} = \left(\boldsymbol{F}_{\mathrm{g}}^{(1)}\right)^{-1}\left(\boldsymbol{F}_{\mathrm{g}}^{(2)}\right)^{-1}\left(\boldsymbol{F}_{\mathrm{g}}^{(3)}\right)^{-1} \tag{5.25}$$

with the individual inverses

$$\left(\boldsymbol{F}_{\mathrm{g}}^{(a)}\right)^{-1} = \begin{cases} \dfrac{1}{\vartheta^{(a)}}\,\boldsymbol{I} & \text{for } \boldsymbol{F}_{\mathrm{g}}^{(a)} \text{ from Eq. 5.1a} \\ \boldsymbol{I} + \dfrac{1-\vartheta^{(a)}}{\vartheta^{(a)}}\,\boldsymbol{A}_{\mathrm{g}}^{(a)} \otimes \boldsymbol{A}_{\mathrm{g}}^{(a)} & \text{for } \boldsymbol{F}_{\mathrm{g}}^{(a)} \text{ from Eq. 5.1b} \\ \dfrac{1}{\vartheta^{(a)}}\,\boldsymbol{I} + \dfrac{\vartheta^{(a)}-1}{\vartheta^{(a)}}\,\boldsymbol{A}_{\mathrm{g}}^{(a)} \otimes \boldsymbol{A}_{\mathrm{g}}^{(a)} & \text{for } \boldsymbol{F}_{\mathrm{g}}^{(a)} \text{ from Eq. 5.1c} \end{cases} \tag{5.26}$$

following from the Sherman-Morrison formula as specified in Appendix A.2.4. Showing the same structure as the original tensor, also the inverse of the growth tensor is commutative and symmetric provided that Eq. 5.8 is fulfilled. The distinction between $\boldsymbol{F}_{\mathrm{g}}^{-1}$ and $\boldsymbol{F}_{\mathrm{g}}^{-\mathrm{T}}$ is nevertheless retained for formal reasons in order to enclose the general case in relations like Eq. 5.24. This particular equation analogously holds for the transformation between the actual and the reference configuration, but then involves the non-symmetric deformation gradient $\boldsymbol{F}$ instead of $\boldsymbol{F}_{\mathrm{g}}$.

[1] The universal rules for the transformation of a tensor of second order between two configurations, caused by a deformation gradient $\boldsymbol{F}$, can be retraced with the help of Eq. A.4 by considering the original tensor $\mathbb{C} = \boldsymbol{a} \otimes \boldsymbol{b} \otimes \boldsymbol{c} \otimes \boldsymbol{d}$ and its transformation $\mathbb{A} = \boldsymbol{F}\boldsymbol{a} \otimes \boldsymbol{F}\boldsymbol{b} \otimes \boldsymbol{F}\boldsymbol{c} \otimes \boldsymbol{F}\boldsymbol{d} = (\boldsymbol{F} \boxtimes \boldsymbol{F}) : \mathbb{C} : \left(\boldsymbol{F}^{\mathrm{T}} \boxtimes \boldsymbol{F}^{\mathrm{T}}\right)$.

For the growth part $\mathbb{C}^{\mathrm{g}}$ of the tangent modulus, the derivative of $\boldsymbol{S}$ with respect to growth factor $\vartheta^{(a)}$ is required. It is obtained from the chain rule expression

$$\frac{\partial \boldsymbol{S}}{\partial \vartheta^{(a)}} = \frac{\mathrm{d}\boldsymbol{S}}{\mathrm{d}\boldsymbol{F}_{\mathrm{g}}} : \frac{\partial \boldsymbol{F}_{\mathrm{g}}}{\partial \boldsymbol{F}_{\mathrm{g}}^{(a)}} : \frac{\partial \boldsymbol{F}_{\mathrm{g}}^{(a)}}{\partial \vartheta^{(a)}}, \tag{5.27}$$

where the 2nd Piola-Kirchhoff stress tensor $\boldsymbol{S} = \boldsymbol{F}_{\mathrm{g}}^{-1}\boldsymbol{S}_{\mathrm{e}}\boldsymbol{F}_{\mathrm{g}}^{-\mathrm{T}} = \left(\boldsymbol{F}_{\mathrm{g}}^{-1} \boxtimes \boldsymbol{F}_{\mathrm{g}}^{-1}\right) : \boldsymbol{S}_{\mathrm{e}}$ depends explicitly and implicitly on $\boldsymbol{F}_{\mathrm{g}}$, such that the total derivative has to be computed according to

$$\frac{\mathrm{d}\boldsymbol{S}}{\mathrm{d}\boldsymbol{F}_{\mathrm{g}}} = \frac{\partial \boldsymbol{S}}{\partial \boldsymbol{F}_{\mathrm{g}}} + \frac{\partial \boldsymbol{S}}{\partial \boldsymbol{S}_{\mathrm{e}}} : \frac{\partial \boldsymbol{S}_{\mathrm{e}}}{\partial \boldsymbol{C}_{\mathrm{e}}} : \frac{\partial \boldsymbol{C}_{\mathrm{e}}}{\partial \boldsymbol{F}_{\mathrm{g}}}. \tag{5.28}$$

Using the derivatives provided in Eq. A.19 and Eq. A.21 as well as the symmetry of $\boldsymbol{S}$ and $\boldsymbol{C}_{\mathrm{e}}$, the derivatives $\partial\boldsymbol{S}/\partial\boldsymbol{F}_{\mathrm{g}}$ and $\partial\boldsymbol{C}_{\mathrm{e}}/\partial\boldsymbol{F}_{\mathrm{g}}$ can be computed in index notation. Converting them to symbolic notation, the set of expressions

$$\frac{\partial \boldsymbol{S}}{\partial \boldsymbol{F}_{\mathrm{g}}} = -\boldsymbol{F}_{\mathrm{g}}^{-1} \boxtimes \boldsymbol{S} - \boldsymbol{S} \boxdot \boldsymbol{F}_{\mathrm{g}}^{-1}, \tag{5.29}$$

$$\frac{\partial \boldsymbol{S}}{\partial \boldsymbol{S}_{\mathrm{e}}} = \boldsymbol{F}_{\mathrm{g}}^{-1} \boxtimes \boldsymbol{F}_{\mathrm{g}}^{-1}, \tag{5.30}$$

$$\frac{\partial \boldsymbol{C}_{\mathrm{e}}}{\partial \boldsymbol{F}_{\mathrm{g}}} = -\boldsymbol{F}_{\mathrm{g}}^{-\mathrm{T}} \boxdot \boldsymbol{C}_{\mathrm{e}} - \boldsymbol{C}_{\mathrm{e}} \boxtimes \boldsymbol{F}_{\mathrm{g}}^{-\mathrm{T}} \tag{5.31}$$

is obtained. In the same manner, the derivatives of the overall growth tensor with respect to its multiplicative parts can be evaluated and expressed as

$$\frac{\partial \boldsymbol{F}_{\mathrm{g}}}{\partial \boldsymbol{F}_{\mathrm{g}}^{(1)}} = \left(\boldsymbol{F}_{\mathrm{g}}^{(3)}\boldsymbol{F}_{\mathrm{g}}^{(2)}\right) \boxtimes \boldsymbol{I}, \tag{5.32a}$$

$$\frac{\partial \boldsymbol{F}_{\mathrm{g}}}{\partial \boldsymbol{F}_{\mathrm{g}}^{(2)}} = \boldsymbol{F}_{\mathrm{g}}^{(3)} \boxtimes \left(\boldsymbol{F}_{\mathrm{g}}^{(1)}\right)^{\mathrm{T}}, \tag{5.32b}$$

$$\frac{\partial \boldsymbol{F}_{\mathrm{g}}}{\partial \boldsymbol{F}_{\mathrm{g}}^{(3)}} = \boldsymbol{I} \boxtimes \left(\boldsymbol{F}_{\mathrm{g}}^{(2)}\boldsymbol{F}_{\mathrm{g}}^{(1)}\right)^{\mathrm{T}}. \tag{5.32c}$$

The last unknown term in Eq. 5.27 requires differentiation of the multiplicative part $\boldsymbol{F}_{\mathrm{g}}^{(a)}$ of the growth tensor with respect to the growth factor $\vartheta^{(a)}$. This derivative depends on the specific form of $\boldsymbol{F}_{\mathrm{g}}^{(a)}$ and can be summarized by

$$\frac{\partial \boldsymbol{F}_{\mathrm{g}}^{(a)}}{\partial \vartheta^{(a)}} = \begin{cases} \boldsymbol{I} & \text{for } \boldsymbol{F}_{\mathrm{g}}^{(a)} \text{ from Eq. 5.1a} \\ \boldsymbol{M}_{\mathrm{g}}^{(a)} & \text{for } \boldsymbol{F}_{\mathrm{g}}^{(a)} \text{ from Eq. 5.1b} \\ \boldsymbol{I} - \boldsymbol{M}_{\mathrm{g}}^{(a)} & \text{for } \boldsymbol{F}_{\mathrm{g}}^{(a)} \text{ from Eq. 5.1c} \end{cases} \quad \text{for} \quad a \in [1,2,3]\,, \tag{5.33}$$

where $\boldsymbol{M}_{\mathrm{g}}^{(a)}$ represents the structural tensor

$$\boldsymbol{M}_{\mathrm{g}}^{(a)} = \boldsymbol{A}_{\mathrm{g}}^{(a)} \otimes \boldsymbol{A}_{\mathrm{g}}^{(a)} \qquad \text{for} \qquad a \in [1,2,3] \tag{5.34}$$

built by the growth orientation vector $\boldsymbol{A}_{\mathrm{g}}^{(a)}$ associated to direction a. Combining Eq. 5.32 with Eq. 5.33, the derivatives of the overall growth tensor $\boldsymbol{F}_{\mathrm{g}}$ with respect to the individual growth factors $\vartheta^{(a)}$ are obtained. A summary of these derivatives is given in Tab. 5.1.

Table 5.1: Derivatives $\partial \boldsymbol{F}_\mathrm{g}/\partial \vartheta^{(a)}$ of the growth tensor $\boldsymbol{F}_\mathrm{g} = \boldsymbol{F}_\mathrm{g}^{(3)}\boldsymbol{F}_\mathrm{g}^{(2)}\boldsymbol{F}_\mathrm{g}^{(1)}$ with respect to the growth factors $\vartheta^{(a)}$ for different forms of the multiplicative parts $\boldsymbol{F}_\mathrm{g}^{(a)}$.

form of $\boldsymbol{F}_\mathrm{g}^{(a)}$	$\partial \boldsymbol{F}_\mathrm{g}/\partial \vartheta^{(a)}$ for $a=1$	$\partial \boldsymbol{F}_\mathrm{g}/\partial \vartheta^{(a)}$ for $a=2$	$\partial \boldsymbol{F}_\mathrm{g}/\partial \vartheta^{(a)}$ for $a=3$
Eq. 5.1a	$\boldsymbol{F}_\mathrm{g}^{(3)}\boldsymbol{F}_\mathrm{g}^{(2)}$	$\boldsymbol{F}_\mathrm{g}^{(3)}\boldsymbol{F}_\mathrm{g}^{(1)}$	$\boldsymbol{F}_\mathrm{g}^{(2)}\boldsymbol{F}_\mathrm{g}^{(1)}$
Eq. 5.1b	$\boldsymbol{F}_\mathrm{g}^{(3)}\boldsymbol{F}_\mathrm{g}^{(2)}\boldsymbol{M}_\mathrm{g}^{(1)}$	$\boldsymbol{F}_\mathrm{g}^{(3)}\boldsymbol{M}_\mathrm{g}^{(2)}\boldsymbol{F}_\mathrm{g}^{(1)}$	$\boldsymbol{M}_\mathrm{g}^{(3)}\boldsymbol{F}_\mathrm{g}^{(2)}\boldsymbol{F}_\mathrm{g}^{(1)}$
Eq. 5.1c	$\boldsymbol{F}_\mathrm{g}^{(3)}\boldsymbol{F}_\mathrm{g}^{(2)}\left(\boldsymbol{I}-\boldsymbol{M}_\mathrm{g}^{(1)}\right)$	$\boldsymbol{F}_\mathrm{g}^{(3)}\left(\boldsymbol{I}-\boldsymbol{M}_\mathrm{g}^{(2)}\right)\boldsymbol{F}_\mathrm{g}^{(1)}$	$\left(\boldsymbol{I}-\boldsymbol{M}_\mathrm{g}^{(3)}\right)\boldsymbol{F}_\mathrm{g}^{(2)}\boldsymbol{F}_\mathrm{g}^{(1)}$

Using all those intermediate results and the definition $\partial \boldsymbol{S}_\mathrm{e}/\partial \boldsymbol{C}_\mathrm{e} = {}^1\!/_2\,\mathbb{C}_\mathrm{i}^\mathrm{e}$ from Eq. 5.23, the derivative in Eq. 5.27 can be expressed as

$$\begin{aligned}\frac{\partial \boldsymbol{S}}{\partial \vartheta^{(a)}} = -\left(\boldsymbol{F}_\mathrm{g}^{-1}\boxtimes\boldsymbol{F}_\mathrm{g}^{-1}\right) : \big[\boldsymbol{F}_\mathrm{g}^{-1}\boxtimes\boldsymbol{S}_\mathrm{e} + \boldsymbol{S}_\mathrm{e}\boxdot\boldsymbol{F}_\mathrm{g}^{-1} + \dots \\ \dots \tfrac{1}{2}\,\mathbb{C}_\mathrm{i}^\mathrm{e} : \left(\boldsymbol{F}_\mathrm{g}^{-\mathrm{T}}\boxdot\boldsymbol{C}_\mathrm{e} + \boldsymbol{C}_\mathrm{e}\boxtimes\boldsymbol{F}_\mathrm{g}^{-\mathrm{T}}\right)\big] : \frac{\partial \boldsymbol{F}_\mathrm{g}}{\partial \vartheta^{(a)}}\end{aligned} \tag{5.35}$$

with $\partial \boldsymbol{F}_\mathrm{g}/\partial \vartheta^{(a)}$ from Tab. 5.1. In order to factor out $\boldsymbol{F}_\mathrm{g}^{-1}\boxtimes\boldsymbol{F}_\mathrm{g}^{-1}$ on the left, the commutativity of the product $\boldsymbol{F}_\mathrm{g}\left(\partial \boldsymbol{F}_\mathrm{g}/\partial \vartheta^{(a)}\right)$ has been used. This commutativity is assured since the growth tensor itself and also its derivatives with respect to the growth factors can be represented in the general form mentioned in Eq. 5.9, where the individual growth orientation vectors are perpendicular to each other according to Eq. 5.8. Disregarding this last transformation step, which demands certain presuppositions on the form of $\boldsymbol{F}_\mathrm{g}$, the result is confirmed by Sáez, Peña, et al. (2014).

Recalling Eq. 5.22, the derivatives of each growth factor with respect to the Cauchy-Green tensor $\boldsymbol{C}$ are still required. As defined in Eq. 5.17, the growth factors at actual time t_{n+1} are approximated by

$$\vartheta_{n+1}^{(a)} = \vartheta_n^{(a)} + \left(\kappa\,\dot{\vartheta}_{n+1}^{(a)} + (1-\kappa)\;\dot{\vartheta}_n^{(a)}\right)\Delta t \qquad \text{for} \qquad a \in [1,2,3]\,, \tag{5.36}$$

where the time derivative of each growth factor depends on all growth factors through the driving force $\phi^{(a)}(\boldsymbol{\Sigma}_\mathrm{e})$ as obvious from Eq. 5.13. The derivatives of the individual growth factors $\vartheta^{(a)}$ with respect to $\boldsymbol{C}$ at time step $n+1$ are therefore given by

$$\frac{\partial \vartheta^{(1)}}{\partial \boldsymbol{C}} = \left(\frac{\partial \dot{\vartheta}^{(1)}}{\partial \boldsymbol{C}} + \frac{\partial \dot{\vartheta}^{(1)}}{\partial \vartheta^{(1)}}\frac{\partial \vartheta^{(1)}}{\partial \boldsymbol{C}} + \frac{\partial \dot{\vartheta}^{(1)}}{\partial \vartheta^{(2)}}\frac{\partial \vartheta^{(2)}}{\partial \boldsymbol{C}} + \frac{\partial \dot{\vartheta}^{(1)}}{\partial \vartheta^{(3)}}\frac{\partial \vartheta^{(3)}}{\partial \boldsymbol{C}}\right)\kappa\,\Delta t, \tag{5.37a}$$

$$\frac{\partial \vartheta^{(2)}}{\partial \boldsymbol{C}} = \left(\frac{\partial \dot{\vartheta}^{(2)}}{\partial \boldsymbol{C}} + \frac{\partial \dot{\vartheta}^{(2)}}{\partial \vartheta^{(1)}}\frac{\partial \vartheta^{(1)}}{\partial \boldsymbol{C}} + \frac{\partial \dot{\vartheta}^{(2)}}{\partial \vartheta^{(2)}}\frac{\partial \vartheta^{(2)}}{\partial \boldsymbol{C}} + \frac{\partial \dot{\vartheta}^{(2)}}{\partial \vartheta^{(3)}}\frac{\partial \vartheta^{(3)}}{\partial \boldsymbol{C}}\right)\kappa\,\Delta t, \tag{5.37b}$$

$$\frac{\partial \vartheta^{(3)}}{\partial \boldsymbol{C}} = \left(\frac{\partial \dot{\vartheta}^{(3)}}{\partial \boldsymbol{C}} + \frac{\partial \dot{\vartheta}^{(3)}}{\partial \vartheta^{(1)}}\frac{\partial \vartheta^{(1)}}{\partial \boldsymbol{C}} + \frac{\partial \dot{\vartheta}^{(3)}}{\partial \vartheta^{(2)}}\frac{\partial \vartheta^{(2)}}{\partial \boldsymbol{C}} + \frac{\partial \dot{\vartheta}^{(3)}}{\partial \vartheta^{(3)}}\frac{\partial \vartheta^{(3)}}{\partial \boldsymbol{C}}\right)\kappa\,\Delta t. \tag{5.37c}$$

Reformulating the derivatives from Eq. 5.20 with the help of the abbreviations

$$A_\vartheta^{(i,j)} = -\frac{\partial R^{(i)}}{\partial \vartheta^{(j)}}, \tag{5.38}$$

this system of equations can be transformed to

$$A_\vartheta^{(1,1)} \frac{\partial \vartheta^{(1)}}{\partial \boldsymbol{C}} + A_\vartheta^{(1,2)} \frac{\partial \vartheta^{(2)}}{\partial \boldsymbol{C}} + A_\vartheta^{(1,3)} \frac{\partial \vartheta^{(3)}}{\partial \boldsymbol{C}} = k_\vartheta^{(1)} \frac{\partial \phi^{(1)}}{\partial \boldsymbol{C}} \kappa \, \Delta t, \tag{5.39a}$$

$$A_\vartheta^{(2,1)} \frac{\partial \vartheta^{(1)}}{\partial \boldsymbol{C}} + A_\vartheta^{(2,2)} \frac{\partial \vartheta^{(2)}}{\partial \boldsymbol{C}} + A_\vartheta^{(2,3)} \frac{\partial \vartheta^{(3)}}{\partial \boldsymbol{C}} = k_\vartheta^{(2)} \frac{\partial \phi^{(2)}}{\partial \boldsymbol{C}} \kappa \, \Delta t, \tag{5.39b}$$

$$A_\vartheta^{(3,1)} \frac{\partial \vartheta^{(1)}}{\partial \boldsymbol{C}} + A_\vartheta^{(3,2)} \frac{\partial \vartheta^{(2)}}{\partial \boldsymbol{C}} + A_\vartheta^{(3,3)} \frac{\partial \vartheta^{(3)}}{\partial \boldsymbol{C}} = k_\vartheta^{(3)} \frac{\partial \phi^{(3)}}{\partial \boldsymbol{C}} \kappa \, \Delta t. \tag{5.39c}$$

In this form, the system of equations can be solved for the wanted terms $\partial \vartheta^{(a)} / \partial \boldsymbol{C}$. The derivatives of the driving forces $\phi^{(a)}$ with respect to $\boldsymbol{C}$ needed on the right hand side cannot be provided unless the explicit functions $\phi^{(a)}$ are specified. Both will be done in Sec. 5.1.4.

Considering the special case of explicit time integration of the evolution equation for the growth factors, it can be stated that due to $\kappa = 0$ and $A_\vartheta^{(i,j)} = \delta_{ij}$ the result $\partial \vartheta^{(a)} / \partial \boldsymbol{C} = \boldsymbol{0}$ is obtained from Eq. 5.39, which finally leads to $\mathbb{C}^{\mathrm{g}} = \mathbb{0}$. The tangent modulus given in Eq. 5.22 is thus not affected by growth since the growth factors do only depend on variables from the previous time step. Here again, it becomes apparent that explicit time integration is conceptually more simple than methods involving variables of the actual time step.

Numerical tangent modulus. The tangent modulus $\mathbb{C} = 2 \, \mathrm{d}\boldsymbol{S} / \mathrm{d}\boldsymbol{C}$ is nothing else than a derivative and can thus be computed based on classical methods of numerical differentiation, for example the finite difference scheme. Applying a truncated Taylor series expansion to a function $f(x)$ to find its value at $x + h$, i. e. $f(x + h) \approx f(x) + {}^{h}/_{1!} \, f'(x)$, the approximation

$$f'(x) \approx \frac{f(x + h) - f(x)}{h} \tag{5.40}$$

is obtained for the derivative $f'(x)$. In principle, the quality of the approximation improves if the parameter h approaches zero. But from the computational point of view, an increasing rounding error in the term $x + h$ occurs with decreasing value of h due to the limited number of available digits. In order to find the optimal value of the parameter h leading to the lowest overall error, approximation errors have to be weighed up against rounding errors. To make things even worse, the optimal value of h depends on x and is thus changing in the course of a finite element simulation. These drawbacks of the finite difference scheme can be prevented by using an alternative method for numerical differentiation: the complex step derivative approximation developed by Lyness & Moler (1967) and Lyness (1968) for scalar functions. By writing the perturbation h to the imaginary part of the variable x, i. e. $f(x + \mathrm{i}h) \approx f(x) + {}^{\mathrm{i}h}/_{1!} \, f'(x)$, the rounding error can completely be eliminated. Extracting the imaginary part leads to the approximation

$$f'(x) \approx \frac{\Im[f(x + \mathrm{i}h)]}{h}, \tag{5.41}$$

where h can be chosen arbitrarily small without generation of rounding errors. The concept of complex step derivative approximation has been transferred to the derivation of tangent moduli from stresses at finite strains by Tanaka, Fujikawa, et al. (2014). The directional derivative of a tensor-valued tensor field $\boldsymbol{S}(\boldsymbol{C})$ of second order in the direction of $\boldsymbol{D}$ is thereby approximated by

$$\frac{\mathrm{d}\boldsymbol{S}}{\mathrm{d}\boldsymbol{C}} : \boldsymbol{D} \approx \frac{\Im[\boldsymbol{S}(\boldsymbol{C} + \mathrm{i}h\boldsymbol{D})]}{h}, \tag{5.42}$$

where $\boldsymbol{D}$ is an arbitrary tensor of second order. If the perturbation tensor $\boldsymbol{D}$ is chosen appropriately, the tangent modulus $\mathbb{C} = 2\,\mathrm{d}\boldsymbol{S}/\mathrm{d}\boldsymbol{C}$ can be computed from this equation. Replacing $\boldsymbol{D}$ by

$$\overset{\star}{\boldsymbol{C}}_{(k)(l)} = \tfrac{1}{2}\left(\boldsymbol{E}_{(k)} \otimes \boldsymbol{E}_{(l)} + \boldsymbol{E}_{(l)} \otimes \boldsymbol{E}_{(k)}\right), \tag{5.43}$$

where the indices k and l are written in brackets in order to clarify that they are no summation indices but just denoting the basis vectors, the left hand side of the equation can be written as $\tfrac{1}{2}\,\mathbb{C}_{ij(k)(l)}\,\boldsymbol{E}_i \otimes \boldsymbol{E}_j$ when taking notice of the right subsymmetry of $\mathbb{C}$ mentioned in Eq. A.31. For fixed k and l, this expression represents 9 of the 81 coefficients of $\mathbb{C}$, and inserting all combinations of $k, l \in [1, 2, 3]$, all components of $\mathbb{C}$ are covered. Writing both sides of Eq. 5.42 with $\boldsymbol{D}$ replaced by Eq. 5.43 in index notation, the expression

$$\mathbb{C}_{ij(k)(l)} \approx 2\,\frac{\Im[S_{ij}(\boldsymbol{C} + \mathrm{i}h\,\overset{\star}{\boldsymbol{C}}_{(k)(l)})]}{h} \tag{5.44}$$

is obtained, which means that the coefficients of $\mathbb{C}$ can formally be computed in nine steps from the imaginary part of the stress resulting from an appropriately perturbed Cauchy-Green tensor, multiplied by $2/h$. Due to the right subsymmetry $\mathbb{C}_{ij(k)(l)} = \mathbb{C}_{ij(l)(k)}$ and the Voigt representation of $\mathbb{C}$ given in Eq. A.32, six perturbation steps each for six coefficients in one column of $\underline{\mathbb{C}}$ are sufficient in practice. In order to fulfill the right subsymmetry of the tangent modulus, the indices of the perturbation tensor have to be transposable without altering the result. For this reason, the perturbation tensor has to be symmetric as defined in Eq. 5.43 and a single pair of basis vectors is not enough.

Instead of applying the perturbation to the Cauchy-Green tensor $\boldsymbol{C}$, it might be advantageous to apply it to the deformation gradient $\boldsymbol{F}$, from where it is passed on to all subordinated fields. As described by Tanaka, Sasagawa, et al. (2015), the required perturbation tensor can be found starting from

$$\frac{\mathrm{d}\boldsymbol{S}}{\mathrm{d}\boldsymbol{F}} : \overset{\star}{\boldsymbol{F}}_{(k)(l)} \approx \frac{\Im[\boldsymbol{S}(\boldsymbol{F} + \mathrm{i}h\,\overset{\star}{\boldsymbol{F}}_{(k)(l)})]}{h}. \tag{5.45}$$

This equation is valid in analogy to Eq. 5.42 and can be transformed such that an expression for $\mathrm{d}\boldsymbol{S}/\mathrm{d}\boldsymbol{C}$ is obtained. Using the derivative $\mathrm{d}\boldsymbol{C}/\mathrm{d}\boldsymbol{F} = \left(\boldsymbol{I} \boxdot \boldsymbol{F}^{\mathrm{T}} + \boldsymbol{F}^{\mathrm{T}} \boxtimes \boldsymbol{I}\right)$, which can be computed in index notation, the left hand side of Eq. 5.45 can be reformulated according to

$$\begin{aligned}
\frac{\mathrm{d}\boldsymbol{S}}{\mathrm{d}\boldsymbol{F}} : \overset{\star}{\boldsymbol{F}}_{(k)(l)} &= \frac{\mathrm{d}\boldsymbol{S}}{\mathrm{d}\boldsymbol{C}} : \frac{\mathrm{d}\boldsymbol{C}}{\mathrm{d}\boldsymbol{F}} : \overset{\star}{\boldsymbol{F}}_{(k)(l)} \\
&= \frac{\mathrm{d}\boldsymbol{S}}{\mathrm{d}\boldsymbol{C}} : \left(\boldsymbol{I} \boxdot \boldsymbol{F}^{\mathrm{T}} + \boldsymbol{F}^{\mathrm{T}} \boxtimes \boldsymbol{I}\right) : \overset{\star}{\boldsymbol{F}}_{(k)(l)} \\
&= \tfrac{1}{2}\,\mathbb{C} : \left(\overset{\star}{\boldsymbol{F}}{}^{\mathrm{T}}_{(k)(l)}\boldsymbol{F} + \boldsymbol{F}^{\mathrm{T}}\overset{\star}{\boldsymbol{F}}_{(k)(l)}\right).
\end{aligned} \tag{5.46}$$

If now $\overset{\star}{\boldsymbol{F}}_{(k)(l)}$ is chosen such that

$$\tfrac{1}{2}\left(\overset{\star}{\boldsymbol{F}}{}^{\mathrm{T}}_{(k)(l)}\boldsymbol{F} + \boldsymbol{F}^{\mathrm{T}}\overset{\star}{\boldsymbol{F}}_{(k)(l)}\right) = \overset{\star}{\boldsymbol{C}}_{(k)(l)} \tag{5.47}$$

is fulfilled, the identity

$$\frac{\mathrm{d}\boldsymbol{S}}{\mathrm{d}\boldsymbol{F}} : \overset{\star}{\boldsymbol{F}}_{(k)(l)} = \mathbb{C} : \overset{\star}{\boldsymbol{C}}_{(k)(l)} = \mathbb{C}_{ij(k)(l)}\,\boldsymbol{E}_i \otimes \boldsymbol{E}_j \tag{5.48}$$

is valid and index notation of Eq. 5.45 leads to

$$\mathbb{C}_{ij(k)(l)} \approx \frac{\Im[S_{ij}(\boldsymbol{F} + \mathrm{i}h \overset{\star}{\boldsymbol{F}}_{(k)(l)})]}{h}. \tag{5.49}$$

This expression is suited for computing the columns of the tangent modulus $\underline{\mathbb{C}}$ as described above for perturbation of $\boldsymbol{C}$. The condition from Eq. 5.47 is satisfied if the perturbation tensor is set to

$$\overset{\star}{\boldsymbol{F}}_{(k)(l)} = \boldsymbol{F}^{-\mathrm{T}} \overset{\star}{\boldsymbol{C}}_{(k)(l)} = \tfrac{1}{2} \left(F^{-\mathrm{T}}_{i(k)} \boldsymbol{E}_i \otimes \boldsymbol{E}_{(l)} + F^{-\mathrm{T}}_{i(l)} \boldsymbol{E}_i \otimes \boldsymbol{E}_{(k)} \right). \tag{5.50}$$

In the given context, both possibilities for the numerical evaluation of the tangent modulus, that is use of Eq. 5.44 with Eq. 5.43 for perturbation of the Cauchy-Green tensor $\boldsymbol{C}$ or use of Eq. 5.49 with Eq. 5.50 for perturbation of the deformation gradient $\boldsymbol{F}$, are applicable.

5.1.4 Driving forces for growth

General considerations at the beginning of this chapter led to the assumption that adaptations in arterial tissues are likely to be stress-driven. Afterwards, the Mandel stress tensor $\boldsymbol{\Sigma}_\mathrm{e} = \boldsymbol{C}_\mathrm{e} \boldsymbol{S}_\mathrm{e}$ in the intermediate configuration has been chosen explicitly, motivated by technical reasons imposed by the general framework of multiplicative growth. Finally, the chosen stimulus for growth finds its way into the model via the functions $\phi^{(a)}(\boldsymbol{\Sigma}_\mathrm{e})$ in Eq. 5.13, which describes the evolution of the internal variables $\vartheta^{(a)}$ reflecting the amount of growth associated to the three directions $\boldsymbol{A}^{(a)}_\mathrm{g}$. Since growth in arterial tissues is known to be multiaxial, the generalized formulation for stress-driven growth presented in this work enables the combination of up to three different growth mechanisms for those three directions: isotropic growth, growth in the direction of $\boldsymbol{A}^{(a)}_\mathrm{g}$ and growth perpendicular to the direction of $\boldsymbol{A}^{(a)}_\mathrm{g}$. Depending on this choice, different functional forms of $\phi^{(a)}(\boldsymbol{\Sigma}_\mathrm{e})$ seem to be reasonable. Three suggestions will be considered in the following paragraphs. Besides a motivation of the different driving force functions, their derivatives with respect to the growth factors $\vartheta^{(a)}$ and to the Cauchy-Green tensor $\boldsymbol{C}$, needed in Eq. 5.20 and Eq. 5.39, respectively, will be provided. At the end of the section, a simple modification of the driving force function, which allows to deactivate growth if the considered stress falls below a critical level, will be proposed.

Trace of the Mandel stress tensor. In the context of isotropic growth, the trace of the Mandel stress tensor is frequently used as an isotropic measure for the stress acting on the tissue, for example by Himpel, Kuhl, et al. (2005), Göktepe, Abilez & Kuhl (2010) or Sáez, Peña, et al. (2014). Although pure isotropic growth is unrealistic for arterial walls, the isotropic driving force

$$\phi^{(a)}(\boldsymbol{\Sigma}_\mathrm{e}) = \boldsymbol{\Sigma}_\mathrm{e} : \boldsymbol{I} = \mathrm{tr}[\boldsymbol{\Sigma}_\mathrm{e}] \qquad \text{for} \qquad a \in [1,2,3] \tag{5.51}$$

is included into the framework in order to enable a comparison of anisotropic mechanisms to the isotropic reference model. Furthermore, even an anisotropic growth mechanism might be driven by an isotropic stress quantity representing the average stress state. The derivative of this driving force function with respect to growth factor $\vartheta^{(j)}$ results in

$$\frac{\partial \phi^{(i)}}{\partial \vartheta^{(j)}} = \frac{\partial \boldsymbol{C}_\mathrm{e}}{\partial \vartheta^{(j)}} : \boldsymbol{S}_\mathrm{e} + \boldsymbol{C}_\mathrm{e} : \tfrac{1}{2}\, \mathbb{C}^\mathrm{e}_\mathrm{i} : \frac{\partial \boldsymbol{C}_\mathrm{e}}{\partial \vartheta^{(j)}} \qquad \text{with} \qquad i,j \in [1,2,3], \tag{5.52}$$

where the definition of the tangent modulus in Eq. 5.23 has been used. The part $\partial \boldsymbol{C}_\mathrm{e}/\partial\vartheta^{(j)}$ can be computed according to

$$\frac{\partial \boldsymbol{C}_\mathrm{e}}{\partial\vartheta^{(j)}} = \frac{\partial \boldsymbol{C}_\mathrm{e}}{\partial \boldsymbol{F}_\mathrm{g}} : \frac{\partial \boldsymbol{F}_\mathrm{g}}{\partial\vartheta^{(j)}} = -\left(\boldsymbol{F}_\mathrm{g}^{-\mathrm{T}} \boxdot \boldsymbol{C}_\mathrm{e} + \boldsymbol{C}_\mathrm{e} \boxtimes \boldsymbol{F}_\mathrm{g}^{-\mathrm{T}}\right) : \frac{\partial \boldsymbol{F}_\mathrm{g}}{\partial\vartheta^{(j)}} \tag{5.53}$$

with the help of Eq. 5.31 and the derivatives of the growth tensor with respect to the growth factors summarized in Tab. 5.1. Differentiating Eq. 5.51 with respect to $\boldsymbol{C}$ yields

$$\frac{\partial \phi^{(a)}}{\partial \boldsymbol{C}} = \frac{\partial \phi^{(a)}}{\partial \boldsymbol{C}_\mathrm{e}} : \frac{\partial \boldsymbol{C}_\mathrm{e}}{\partial \boldsymbol{C}} = \left(\boldsymbol{S}_\mathrm{e} + \boldsymbol{C}_\mathrm{e} : \tfrac{1}{2}\,\mathbb{C}_\mathrm{i}^\mathrm{e}\right) : \left(\boldsymbol{F}_\mathrm{g}^{-\mathrm{T}} \boxtimes \boldsymbol{F}_\mathrm{g}^{-\mathrm{T}}\right) \tag{5.54}$$

with $a \in [1,2,3]$, where the derivative

$$\frac{\partial \boldsymbol{C}_\mathrm{e}}{\partial \boldsymbol{C}} = \boldsymbol{F}_\mathrm{g}^{-\mathrm{T}} \boxtimes \boldsymbol{F}_\mathrm{g}^{-\mathrm{T}} \tag{5.55}$$

has been obtained with the reformulation $\boldsymbol{C}_\mathrm{e} = \left(\boldsymbol{F}_\mathrm{g}^{-\mathrm{T}} \boxtimes \boldsymbol{F}_\mathrm{g}^{-\mathrm{T}}\right) : \boldsymbol{C}$ of Eq. 3.22 with Eq. A.5.

Principal stress associated to the growth orientation vector. In all cases of anisotropic growth related to a particular direction a characterized by the growth orientation vector $\boldsymbol{A}_\mathrm{g}^{(a)}$, a directional scalar measure of the Mandel stress tensor $\boldsymbol{\Sigma}_\mathrm{e}$ might be more appropriate than an isotropic one. If for example growth perpendicular to a particular direction is assumed to occur in order to reduce the stress in that direction by an increase of the cross sectional area, it suggests itself to choose exactly this stress as growth-inducing stimulus. A projection of the stress $\boldsymbol{\Sigma}_\mathrm{e}$ to the direction of the growth orientation vector can be realized by the double contraction $\boldsymbol{\Sigma}_\mathrm{e} : \boldsymbol{M}_\mathrm{g}^{(a)}$, where the structural tensor $\boldsymbol{M}_\mathrm{g}^{(a)} = \boldsymbol{A}_\mathrm{g}^{(a)} \otimes \boldsymbol{A}_\mathrm{g}^{(a)}$ first defined in Eq. 5.34 filters out the intended contributions. Due to the fact that the unit growth orientation vectors $\boldsymbol{A}_\mathrm{g}^{(a)}$ are defined as principal directions of the symmetric part $\bar{\boldsymbol{\Sigma}}_\mathrm{e}$ of the Mandel stress tensor $\boldsymbol{\Sigma}_\mathrm{e}$, the special relations

$$\bar{\boldsymbol{\Sigma}}_\mathrm{e} \boldsymbol{A}_\mathrm{g}^{(a)} = \bar{\Sigma}_\mathrm{e}^{(a)} \boldsymbol{A}_\mathrm{g}^{(a)}, \qquad \text{i. e.} \qquad \boldsymbol{\Sigma}_\mathrm{e} : \boldsymbol{M}_\mathrm{g}^{(a)} = \bar{\boldsymbol{\Sigma}}_\mathrm{e} : \boldsymbol{M}_\mathrm{g}^{(a)} = \left(\bar{\boldsymbol{\Sigma}}_\mathrm{e} \boldsymbol{A}_\mathrm{g}^{(a)}\right) \cdot \boldsymbol{A}_\mathrm{g}^{(a)} = \bar{\Sigma}_\mathrm{e}^{(a)} \tag{5.56}$$

with $\bar{\Sigma}_\mathrm{e}^{(a)}$ denoting the respective eigenvalues of $\bar{\boldsymbol{\Sigma}}_\mathrm{e}$ are valid for $a \in [1,2,3]$.[2] The driving force function

$$\phi^{(a)}(\boldsymbol{\Sigma}_\mathrm{e}) = \boldsymbol{\Sigma}_\mathrm{e} : \boldsymbol{M}_\mathrm{g}^{(a)} \equiv \bar{\Sigma}_\mathrm{e}^{(a)} \qquad \text{for} \qquad a \in [1,2,3] \tag{5.57}$$

can thus be adopted if growth is assumed to be driven by the stresses acting in the directions of the growth orientation vectors, which are equivalent to the eigenvalues of $\bar{\boldsymbol{\Sigma}}_\mathrm{e}$. It should be remarked that for formal reasons, the unit growth orientation vectors in the intermediate configuration, i. e. $\boldsymbol{F}_\mathrm{g}\boldsymbol{A}_\mathrm{g}^{(a)}/|\boldsymbol{F}_\mathrm{g}\boldsymbol{A}_\mathrm{g}^{(a)}|$, would technically have to be used for the definition of the structural tensor in Eq. 5.57 because the driving force is defined in the intermediate configuration. However, as shown in Eq. 5.10, the growth orientation vectors also are eigenvectors of the growth tensor, which means that their unit vectors are equal in both configurations. This property is important for the required derivatives of Eq. 5.57, which would comprise additional terms if

[2] In any double contraction of $\boldsymbol{\Sigma}_\mathrm{e}$ with a symmetric tensor, $\boldsymbol{\Sigma}_\mathrm{e}$ can be replaced by its symmetric part $\mathrm{sym}[\boldsymbol{\Sigma}_\mathrm{e}] = \bar{\boldsymbol{\Sigma}}_\mathrm{e}$ without change of the result. Since this applies to all driving force functions used in this section, there is no need to differentiate between the Mandel stress tensor and its symmetric part in the given context.

the structural tensor was depending on the growth factors and on the deformation tensor. The derivative of Eq. 5.57 with respect to growth factor $\vartheta^{(j)}$ is

$$\frac{\partial \phi^{(i)}}{\partial \vartheta^{(j)}} = \left(\frac{\partial \boldsymbol{C}_\mathrm{e}}{\partial \vartheta^{(j)}} \boldsymbol{S}_\mathrm{e} + \boldsymbol{C}_\mathrm{e} \left(\tfrac{1}{2}\, \mathbb{C}_\mathrm{i}^\mathrm{e} : \frac{\partial \boldsymbol{C}_\mathrm{e}}{\partial \vartheta^{(j)}} \right) \right) : \boldsymbol{M}_\mathrm{g}^{(i)} \qquad \text{for} \qquad i,j \in [1,2,3], \tag{5.58}$$

where $\partial \boldsymbol{C}_\mathrm{e} / \partial \vartheta^{(j)}$ can be taken from Eq. 5.53 in combination with Tab. 5.1. Using the chain rule and $\partial \boldsymbol{C}_\mathrm{e} / \partial \boldsymbol{C}$ from Eq. 5.55, the derivative

$$\frac{\partial \phi^{(a)}}{\partial \boldsymbol{C}} = \left(\boldsymbol{M}_\mathrm{g}^{(a)} \boldsymbol{S}_\mathrm{e} + \left(\boldsymbol{C}_\mathrm{e} \boldsymbol{M}_\mathrm{g}^{(a)} \right) : \tfrac{1}{2}\, \mathbb{C}_\mathrm{i}^\mathrm{e} \right) : \left(\boldsymbol{F}_\mathrm{g}^{-\mathrm{T}} \boxtimes \boldsymbol{F}_\mathrm{g}^{-\mathrm{T}} \right) \qquad \text{for} \qquad a \in [1,2,3] \tag{5.59}$$

of the driving force with respect to the Cauchy-Green tensor can be computed.

Tensile principal stress associated to the growth orientation vector. As argued in Chapter 2, the in vivo state of arteries is significantly dominated by tensile stresses in the circumferential-axial plane of the wall. Compared to the high tensile stresses born by the collagen fibers, the compressive stress in radial direction is quite small and possibly negligible. Moreover, the radial stress in tubular structures is mainly dictated by the internal and external pressure and can thus be supposed to be not controllable by adaptation of the geometry. Paying attention to these facts, the driving force function

$$\phi^{(a)}(\boldsymbol{\Sigma}_\mathrm{e}) = \left\langle \boldsymbol{\Sigma}_\mathrm{e} : \boldsymbol{M}_\mathrm{g}^{(a)} \right\rangle \equiv \left\langle \bar{\Sigma}_\mathrm{e}^{(a)} \right\rangle \qquad \text{for} \qquad a \in [1,2,3] \tag{5.60}$$

is proposed, which reflects the hypothesis that only tensile stresses acting in the direction of the growth orientation vectors trigger a growth process. Due to the special relations mentioned in Eq. 5.56, those stresses equal the tensile, positive principal stresses $\left\langle \bar{\Sigma}_\mathrm{e}^{(a)} \right\rangle$. Negative values are excluded by means of the Macaulay bracket, which is defined by

$$\left\langle \bullet \right\rangle = \tfrac{1}{2} \left(\bullet + |\bullet| \right). \tag{5.61}$$

The required derivatives of Eq. 5.60 are given by

$$\frac{\partial \phi^{(i)}}{\partial \vartheta^{(j)}} = \frac{\left\langle \bar{\Sigma}_\mathrm{e}^{(i)} \right\rangle}{\bar{\Sigma}_\mathrm{e}^{(i)}} \left(\frac{\partial \boldsymbol{C}_\mathrm{e}}{\partial \vartheta^{(j)}} \boldsymbol{S}_\mathrm{e} + \boldsymbol{C}_\mathrm{e} \left(\tfrac{1}{2}\, \mathbb{C}_\mathrm{i}^\mathrm{e} : \frac{\partial \boldsymbol{C}_\mathrm{e}}{\partial \vartheta^{(j)}} \right) \right) : \boldsymbol{M}_\mathrm{g}^{(i)} \tag{5.62}$$

with $i,j \in [1,2,3]$ and $\partial \boldsymbol{C}_\mathrm{e} / \partial \vartheta^{(j)}$ from Eq. 5.53 in combination with Tab. 5.1 and by

$$\frac{\partial \phi^{(a)}}{\partial \boldsymbol{C}} = \frac{\left\langle \bar{\Sigma}_\mathrm{e}^{(a)} \right\rangle}{\bar{\Sigma}_\mathrm{e}^{(a)}} \left(\boldsymbol{M}_\mathrm{g}^{(a)} \boldsymbol{S}_\mathrm{e} + \left(\boldsymbol{C}_\mathrm{e} \boldsymbol{M}_\mathrm{g}^{(a)} \right) : \tfrac{1}{2}\, \mathbb{C}_\mathrm{i}^\mathrm{e} \right) : \left(\boldsymbol{F}_\mathrm{g}^{-\mathrm{T}} \boxtimes \boldsymbol{F}_\mathrm{g}^{-\mathrm{T}} \right) \tag{5.63}$$

with $a \in [1,2,3]$. Both derivatives do only differ from their equivalents in Eq. 5.58 and Eq. 5.59 by a coefficient of value one or zero in case of tensile or compressive values of the driving force function.

Regardless of the explicit form of the driving force function, it seems likely that a certain threshold of the considered stress quantity has to be exceeded before a counteracting growth process is initiated in order to restore the homeostatic stress level. This could be taken into

account in a general, simplified manner by replacing the driving force function $\phi^{(a)}(\boldsymbol{\Sigma}_\mathrm{e})$ with a modified function

$$\bar{\phi}^{(a)}(\boldsymbol{\Sigma}_\mathrm{e}) = \begin{cases} 0 & \text{if} \quad \left|\phi^{(a)}(\boldsymbol{\Sigma}_\mathrm{e})\right| \leq \phi^{(a)}_\mathrm{crit} \\ \phi^{(a)}(\boldsymbol{\Sigma}_\mathrm{e}) - \phi^{(a)}_\mathrm{crit} & \text{if} \quad \phi^{(a)}(\boldsymbol{\Sigma}_\mathrm{e}) > \phi^{(a)}_\mathrm{crit} \\ \phi^{(a)}(\boldsymbol{\Sigma}_\mathrm{e}) + \phi^{(a)}_\mathrm{crit} & \text{if} \quad \phi^{(a)}(\boldsymbol{\Sigma}_\mathrm{e}) < -\phi^{(a)}_\mathrm{crit} \end{cases} \qquad \text{for} \qquad a \in [1,2,3], \tag{5.64}$$

which is zero if the original function is within the range $[-\phi^{(a)}_\mathrm{crit}, \phi^{(a)}_\mathrm{crit}]$. Of course, more complex adaptations are imaginable, for example the definition of a driving force which is zero in an asymmetric range $[\phi_\mathrm{h} - \Delta\phi^{-}_\mathrm{crit}, \phi_\mathrm{h} + \Delta\phi^{+}_\mathrm{crit}]$ around a homeostatic value ϕ_h, negative below that range, and positive above. However, such specific approaches would involve more unknown material parameters and case distinctions and are not pursued in this work.

5.2 Selected model variants

In order to illustrate the potential of the generalized formulation for growth in soft biological tissues, three exemplary growth models obtained as deductions from the general framework will be specified. Beginning with the simplest of all growth mechanisms realizable within the model, the general equations will be simplified towards isotropic growth. Since this standard form of multiplicative growth has been considered in a large number of publications, for example by Lubarda & Hoger (2002), Himpel, Kuhl, et al. (2005), Kuhl, Maas, et al. (2007), Göktepe, Abilez & Kuhl (2010) or Lee, Genet, et al. (2015), its detailed deduction from the generalized formulation primarily serves as a verification. Moreover, a recapitulation of isotropic growth is reasonable because it will be used as a standard for the evaluation of other growth mechanisms regarding their effectiveness and ability to reduce stresses. The observations in the context of arterial adaptation summarized in Sec. 2.3 however imply that growth in arterial walls is not at all isotropic, but rather governed by a complex system of stress restoring mechanisms leading to an anisotropic total result. The generalized formulation for multiplicative growth makes it possible to analyze different hypotheses concerning those mechanisms of stress reduction by decoupling the overall amount of growth into three portions assigned to the three principal stresses and their directions. To give two examples of such hypothetical models, growth in the direction of the third, generally compressive principal stress, and growth perpendicular to the directions of the first and second, mostly tensile principal stresses, will be specified in detail in addition to isotropic growth. The explicit equations are thereby only indicated for the purpose of illustration. Since the model can be implemented in its generalized form, it is not necessary to derive explicit expressions for the tangent moduli or other derivatives. The character of this section is thus purely informative.

5.2.1 Isotropic growth

For the description of isotropic growth, the multiplicative decomposition of the deformation gradient indicated in Eq. 5.7 is obsolete as no information about different directions is required. By setting

$$\boldsymbol{F}^{(2)}_\mathrm{g} = \boldsymbol{F}^{(3)}_\mathrm{g} = \boldsymbol{I} \qquad \text{and} \qquad \boldsymbol{F}_\mathrm{g} = \boldsymbol{F}^{(1)}_\mathrm{g} = \vartheta^{(1)}\boldsymbol{I}, \tag{5.65}$$

an isotropic growth tensor in the form of Eq. 5.1a incorporating a single growth factor $\vartheta^{(1)}$ is obtained from the general equation. Provided that all directional effects are to be excluded, the isotropic driving force defined in Eq. 5.51 is the only admissible choice among the proposed functions governing the evolution of this growth factor. Since only terms related to $a = 1$ have to be taken into account in all subsequent equations, the system of equations for the incremental updates of the growth factors in Eq. 5.19 can be reduced to the single equation

$$R^{(1)}\Big|_{\vartheta_k^{(1)}} - A_\vartheta^{(1,1)}\Big|_{\vartheta_k^{(1)}} \Delta\vartheta_{k+1}^{(1)} = 0, \tag{5.66}$$

where the abbreviation $A_\vartheta^{(1,1)}$ defined in Eq. 5.38 has been inserted. This equation can directly be solved for

$$\Delta\vartheta_{k+1}^{(1)} = \frac{R^{(1)}}{A_\vartheta^{(1,1)}}\bigg|_{\vartheta_k^{(1)}}. \tag{5.67}$$

For the evaluation of $A_\vartheta^{(1,1)}$, the derivative of the driving force function $\phi^{(1)}(\boldsymbol{\Sigma}_\mathrm{e})$ with respect to the growth factor $\vartheta^{(1)}$, given in Eq. 5.52 with Eq. 5.53, has to be computed. With $\partial \boldsymbol{F}_\mathrm{g}/\partial\vartheta^{(1)} = \boldsymbol{I}$ from Tab. 5.1 as well as the symmetry of $\boldsymbol{C}_\mathrm{e}$ and with the inverses

$$\boldsymbol{F}_\mathrm{g}^{-1} = \boldsymbol{F}_\mathrm{g}^{-\mathrm{T}} = \frac{1}{\vartheta^{(1)}}\,\boldsymbol{I} \tag{5.68}$$

from Eq. 5.26, the expression from Eq. 5.53 simplifies to

$$\frac{\partial \boldsymbol{C}_\mathrm{e}}{\partial\vartheta^{(1)}} = -\boldsymbol{F}_\mathrm{g}^{-\mathrm{T}}\boldsymbol{C}_\mathrm{e} - \boldsymbol{C}_\mathrm{e}\boldsymbol{F}_\mathrm{g}^{-1} = -\frac{2}{\vartheta^{(1)}}\,\boldsymbol{C}_\mathrm{e}. \tag{5.69}$$

Inserting this into Eq. 5.52 leads to

$$\frac{\partial\phi^{(1)}}{\partial\vartheta^{(1)}} = -\frac{1}{\vartheta^{(1)}}\left(2\,\boldsymbol{C}_\mathrm{e} : \boldsymbol{S}_\mathrm{e} + \boldsymbol{C}_\mathrm{e} : \mathbb{C}_\mathrm{i}^\mathrm{e} : \boldsymbol{C}_\mathrm{e}\right), \tag{5.70}$$

which equals the expressions obtained by Himpel, Kuhl, et al. (2005) and Göktepe, Abilez & Kuhl (2010) for their isotropic growth models. For the growth part of the tangent modulus, $\partial\vartheta^{(1)}/\partial\boldsymbol{C}$ has to be computed from the reduced form of Eq. 5.39a, which is given by

$$A_\vartheta^{(1,1)}\,\frac{\partial\vartheta^{(1)}}{\partial\boldsymbol{C}} = k_\vartheta^{(1)}\,\frac{\partial\phi^{(1)}}{\partial\boldsymbol{C}}\,\kappa\,\Delta t. \tag{5.71}$$

With $\partial\phi^{(1)}/\partial\boldsymbol{C}$ from Eq. 5.54, the expression

$$\frac{\partial\vartheta^{(1)}}{\partial\boldsymbol{C}} = \frac{k_\vartheta^{(1)}}{A_\vartheta^{(1,1)}}\,\frac{\partial\phi^{(1)}}{\partial\boldsymbol{C}}\,\kappa\,\Delta t = \frac{k_\vartheta^{(1)}\kappa\,\Delta t}{A_\vartheta^{(1,1)}}\left(\boldsymbol{S}_\mathrm{e} + \boldsymbol{C}_\mathrm{e} : \tfrac{1}{2}\,\mathbb{C}_\mathrm{i}^\mathrm{e}\right) : \left(\boldsymbol{F}_\mathrm{g}^{-\mathrm{T}} \boxtimes \boldsymbol{F}_\mathrm{g}^{-\mathrm{T}}\right) \tag{5.72}$$

is obtained. Inserting $\partial\boldsymbol{F}_\mathrm{g}/\partial\vartheta^{(1)} = \boldsymbol{I}$ from Tab. 5.1 into Eq. 5.35, using the symmetry of $\boldsymbol{S}_\mathrm{e}$ and $\boldsymbol{C}_\mathrm{e}$ and combining the result with Eq. 5.72 as prescribed by Eq. 5.22, the growth part of the tangent modulus can finally be formulated as

$$\mathbb{C}^\mathrm{g} = -\frac{4\,k_\vartheta^{(1)}\kappa\,\Delta t}{\vartheta^{(1)}A_\vartheta^{(1,1)}}\left(\boldsymbol{F}_\mathrm{g}^{-1} \boxtimes \boldsymbol{F}_\mathrm{g}^{-1}\right) : \left(\boldsymbol{S}_\mathrm{e} + \tfrac{1}{2}\,\mathbb{C}_\mathrm{i}^\mathrm{e} : \boldsymbol{C}_\mathrm{e}\right) \otimes \left(\boldsymbol{S}_\mathrm{e} + \boldsymbol{C}_\mathrm{e} : \tfrac{1}{2}\,\mathbb{C}_\mathrm{i}^\mathrm{e}\right) : \left(\boldsymbol{F}_\mathrm{g}^{-\mathrm{T}} \boxtimes \boldsymbol{F}_\mathrm{g}^{-\mathrm{T}}\right). \tag{5.73}$$

For formal reasons, the inverses $\boldsymbol{F}_{\mathrm{g}}^{-1}$ and $\boldsymbol{F}_{\mathrm{g}}^{-\mathrm{T}}$ have not yet been replaced by the explicit expression $1/\vartheta^{(1)}\,\boldsymbol{I}$ from Eq. 5.68. Comparing Eq. 5.73 in the given form with Eq. 5.24, the growth part of the tangent modulus in the intermediate configuration, i. e.

$$\mathbb{C}_{\mathrm{i}}^{\mathrm{g}} = -\frac{4\,k_{\vartheta}^{(1)}\kappa\,\Delta t}{\vartheta^{(1)}\,A_{\vartheta}^{(1,1)}}\left(\boldsymbol{S}_{\mathrm{e}} + \tfrac{1}{2}\,\mathbb{C}_{\mathrm{i}}^{\mathrm{e}} : \boldsymbol{C}_{\mathrm{e}}\right) \otimes \left(\boldsymbol{S}_{\mathrm{e}} + \boldsymbol{C}_{\mathrm{e}} : \tfrac{1}{2}\,\mathbb{C}_{\mathrm{i}}^{\mathrm{e}}\right) \tag{5.74}$$

can be identified. Together with the elastic part $\mathbb{C}_{\mathrm{i}}^{\mathrm{e}} = 4\,\partial^2\psi/\partial\boldsymbol{C}_{\mathrm{e}}^2$, the complete tangent modulus in the intermediate configuration is known. The tangent modulus $\mathbb{C}$ in the reference configuration, which is finally required for the evaluation of the element stiffness matrix $\underline{\boldsymbol{K}}^e$ in Eq. 4.46, can in general be computed by the pullback operation

$$\mathbb{C} = \left(\boldsymbol{F}_{\mathrm{g}}^{-1} \boxtimes \boldsymbol{F}_{\mathrm{g}}^{-1}\right) : \left(\mathbb{C}_{\mathrm{i}}^{\mathrm{e}} + \mathbb{C}_{\mathrm{i}}^{\mathrm{g}}\right) : \left(\boldsymbol{F}_{\mathrm{g}}^{-\mathrm{T}} \boxtimes \boldsymbol{F}_{\mathrm{g}}^{-\mathrm{T}}\right). \tag{5.75}$$

In the special case of isotropic growth described here, the simplified relation

$$\mathbb{C} = \left(\vartheta^{(1)}\right)^{-4}\left(\mathbb{C}_{\mathrm{i}}^{\mathrm{e}} + \mathbb{C}_{\mathrm{i}}^{\mathrm{g}}\right) \tag{5.76}$$

is valid. In this form and with $\kappa = 1$, the tangent modulus is equal to the expression previously found by Göktepe, Abilez & Kuhl (2010), but slightly deviates from the results of Himpel, Kuhl, et al. (2005) and Kuhl, Maas, et al. (2007), where the derivative of the 2nd Piola-Kirchhoff stress tensor with respect to the growth factor seems to be incomplete.

5.2.2 Growth in the direction of the third principal stress

According to the experimental observations mentioned in Sec. 2.3, an increase of the blood pressure in arteries seems to be primarily related to an increase of the wall thickness, which effectively normalizes the circumferential stress towards its homeostatic level. Although it can be concluded from those studies that pure radial growth in hypertensive arteries is implausible, its numerical analysis might help to reveal hints on the real mechanism. In several publications dealing with multiplicative growth, models for growth in radial direction have been presented, for example by Göktepe, Abilez & Kuhl (2010) and Sáez, Peña, et al. (2014) with application to the heart and to the carotid artery, respectively. In those models, the direction of growth is identified based on structural characteristics of the geometries under investigation and is thus not directly linked to the principal stress state. Establishing that link, it shows up that growth in hypertensive arteries seems to occur favorably in the direction of the third, compressive principal stress. A motivation for this behavior could be the fact that this direction is perpendicular to the plane of the other two, usually tensile principal stresses, which is formed by the fiber-reinforced arterial layers. Increasing the cross sectional area with respect to these stresses, growth in the direction of the third principal stress can therefore be supposed to effectively reduce the tensile stresses which occur within the axial-circumferential plane of the arterial wall. To describe growth in the direction of the third principal stress, the growth tensor defined in Eq. 5.7 is specified by setting

$$\boldsymbol{F}_{\mathrm{g}}^{(1)} = \boldsymbol{F}_{\mathrm{g}}^{(2)} = \boldsymbol{I} \qquad \text{and} \qquad \boldsymbol{F}_{\mathrm{g}} = \boldsymbol{F}_{\mathrm{g}}^{(3)} = \boldsymbol{I} + \left(\vartheta^{(3)} - 1\right)\boldsymbol{M}_{\mathrm{g}}^{(3)} \tag{5.77}$$

with $\boldsymbol{M}_{\mathrm{g}}^{(3)} = \boldsymbol{A}_{\mathrm{g}}^{(3)} \otimes \boldsymbol{A}_{\mathrm{g}}^{(3)}$ from Eq. 5.34. The third multiplicative part of the growth tensor is thus set according to Eq. 5.1b in order to model growth in the direction of $\boldsymbol{A}_{\mathrm{g}}^{(3)}$, which is initially

defined as the third principal direction of $\bar{\boldsymbol{\Sigma}}_\mathrm{e}$. The third principal stress can in general be assumed to coincide with the compressive radial stress, which is dictated by the blood pressure and will therefore remain unaffected by growth. For this reason, that stress does not come into consideration as driving force for positive growth in the associated direction, such that only the isotropic driving force function from Eq. 5.51, which includes the other two principal stresses, is reasonable in the given context. With only one growth factor, the system of equations from Eq. 5.19 reduces to a single equation, which can directly be solved for the incremental update

$$\Delta\vartheta^{(3)}_{k+1} = \left.\frac{R^{(3)}}{A^{(3,3)}_\vartheta}\right|_{\vartheta^{(3)}_k} \tag{5.78}$$

of the growth factor $\vartheta^{(3)}$. For the evaluation of the term $A^{(3,3)}_\vartheta$, the derivative of the driving force function $\phi^{(3)}(\boldsymbol{\Sigma}_\mathrm{e})$ with respect to the growth factor $\vartheta^{(3)}$ is required, see Eq. 5.38 and Eq. 5.20a. It can be computed from Eq. 5.52 in combination with Eq. 5.53. With $\partial\boldsymbol{F}_\mathrm{g}/\partial\vartheta^{(3)} = \boldsymbol{M}^{(3)}_\mathrm{g}$ from Tab. 5.1 and the inverses

$$\boldsymbol{F}_\mathrm{g}^{-1} = \boldsymbol{F}_\mathrm{g}^{-\mathrm{T}} = \boldsymbol{I} + \frac{1-\vartheta^{(3)}}{\vartheta^{(3)}}\,\boldsymbol{M}^{(3)}_\mathrm{g} \tag{5.79}$$

from Eq. 5.26, Eq. 5.53 can be simplified to

$$\frac{\partial\boldsymbol{C}_\mathrm{e}}{\partial\vartheta^{(3)}} = -\frac{1}{\vartheta^{(3)}}\left(\boldsymbol{M}^{(3)}_\mathrm{g}\boldsymbol{C}_\mathrm{e} + \boldsymbol{C}_\mathrm{e}\boldsymbol{M}^{(3)}_\mathrm{g}\right). \tag{5.80}$$

Thereby, the symmetries of $\boldsymbol{M}^{(3)}_\mathrm{g}$ and $\boldsymbol{C}_\mathrm{e}$ as well as the property $\boldsymbol{A}^{(3)}_\mathrm{g}\cdot\boldsymbol{A}^{(3)}_\mathrm{g} = 1$ have been used. Inserting this result into Eq. 5.52 leads to

$$\frac{\partial\phi^{(3)}}{\partial\vartheta^{(3)}} = -\frac{1}{\vartheta^{(3)}}\left[\left(\boldsymbol{M}^{(3)}_\mathrm{g}\boldsymbol{C}_\mathrm{e} + \boldsymbol{C}_\mathrm{e}\boldsymbol{M}^{(3)}_\mathrm{g}\right) : \boldsymbol{S}_\mathrm{e} + \boldsymbol{C}_\mathrm{e} : \tfrac{1}{2}\,\mathbb{C}^\mathrm{e}_\mathrm{i} : \left(\boldsymbol{M}^{(3)}_\mathrm{g}\boldsymbol{C}_\mathrm{e} + \boldsymbol{C}_\mathrm{e}\boldsymbol{M}^{(3)}_\mathrm{g}\right)\right]. \tag{5.81}$$

With $\partial\phi^{(3)}/\partial\boldsymbol{C}$ from Eq. 5.54, the reduced form of Eq. 5.39c can directly be solved for the derivative

$$\frac{\partial\vartheta^{(3)}}{\partial\boldsymbol{C}} = \frac{k^{(3)}_\vartheta\,\kappa\,\Delta t}{A^{(3,3)}_\vartheta}\left(\boldsymbol{S}_\mathrm{e} + \boldsymbol{C}_\mathrm{e} : \tfrac{1}{2}\,\mathbb{C}^\mathrm{e}_\mathrm{i}\right) : \left(\boldsymbol{F}_\mathrm{g}^{-\mathrm{T}} \boxtimes \boldsymbol{F}_\mathrm{g}^{-\mathrm{T}}\right), \tag{5.82}$$

which has to be provided for the growth part of the tangent modulus. Furthermore, the general form of derivative of the 2nd Piola-Kirchhoff stress tensor with respect to the growth factor given in Eq. 5.35 can be specified by insertion of $\partial\boldsymbol{F}_\mathrm{g}/\partial\vartheta^{(3)} = \boldsymbol{M}^{(3)}_\mathrm{g}$, which yields

$$\frac{\partial\boldsymbol{S}}{\partial\vartheta^{(3)}} = -\left(\boldsymbol{F}_\mathrm{g}^{-1} \boxtimes \boldsymbol{F}_\mathrm{g}^{-1}\right) : \frac{1}{\vartheta^{(3)}}\left[\boldsymbol{M}^{(3)}_\mathrm{g}\boldsymbol{S}_\mathrm{e} + \boldsymbol{S}_\mathrm{e}\boldsymbol{M}^{(3)}_\mathrm{g} + \tfrac{1}{2}\,\mathbb{C}^\mathrm{e}_\mathrm{i} : \left(\boldsymbol{M}^{(3)}_\mathrm{g}\boldsymbol{C}_\mathrm{e} + \boldsymbol{C}_\mathrm{e}\boldsymbol{M}^{(3)}_\mathrm{g}\right)\right]. \tag{5.83}$$

Focusing on the growth part $\mathbb{C}^\mathrm{g}_\mathrm{i}$ of the tangent modulus in the intermediate configuration, the explicit expression

$$\mathbb{C}^\mathrm{g}_\mathrm{i} = -\frac{2\,k^{(3)}_\vartheta\,\kappa\,\Delta t}{\vartheta^{(3)}A^{(3,3)}_\vartheta}\left[\boldsymbol{M}^{(3)}_\mathrm{g}\boldsymbol{S}_\mathrm{e} + \boldsymbol{S}_\mathrm{e}\boldsymbol{M}^{(3)}_\mathrm{g} + \tfrac{1}{2}\,\mathbb{C}^\mathrm{e}_\mathrm{i} : \left(\boldsymbol{M}^{(3)}_\mathrm{g}\boldsymbol{C}_\mathrm{e} + \boldsymbol{C}_\mathrm{e}\boldsymbol{M}^{(3)}_\mathrm{g}\right)\right] \otimes \left(\boldsymbol{S}_\mathrm{e} + \boldsymbol{C}_\mathrm{e} : \tfrac{1}{2}\,\mathbb{C}^\mathrm{e}_\mathrm{i}\right).$$

is finally obtained by combination of Eq. 5.83 and Eq. 5.82. Performing a pullback to the reference configuration, the entire tangent modulus as defined in Eq. 5.22 can be computed according to

$$\mathbb{C} = \left(\boldsymbol{F}_\mathrm{g}^{-1} \boxtimes \boldsymbol{F}_\mathrm{g}^{-1}\right) : \left(\mathbb{C}^\mathrm{e}_\mathrm{i} + \mathbb{C}^\mathrm{g}_\mathrm{i}\right) : \left(\boldsymbol{F}_\mathrm{g}^{-\mathrm{T}} \boxtimes \boldsymbol{F}_\mathrm{g}^{-\mathrm{T}}\right), \tag{5.84}$$

where the elastic part $\mathbb{C}^\mathrm{e}_\mathrm{i} = 4\,\partial^2\psi/\partial\boldsymbol{C}^2_\mathrm{e}$ is defined by the constitutive material model.

5.2.3 Growth perpendicular to the directions of the first and second principal stress

As brought up several times, the principal stress state in pressurized arteries can be idealized by the idea of two tensile principal stresses in the plane of the vessel wall, which are largely absorbed by the collagen fibers arranged in that plane, and of one compressive principal stress in radial direction, which is directly linked to the blood pressure and is thus not susceptible to adaptations of the tissue volume or properties. Based on this idea, an anisotropic growth model focusing on the aim of reducing high tensile stresses in the arterial wall can be developed (Zahn & Balzani, 2017). To this end, the directions of the first and second principal stresses $\bar{\Sigma}_{\mathrm{e}}^{\mathrm{I}}$ and $\bar{\Sigma}_{\mathrm{e}}^{\mathrm{II}}$ are taken into account for the definition of the growth tensor. Pursuing a reduction of the associated principal stresses by an increase of the cross sectional area, growth perpendicular to those directions, governed by the stresses themselves, is assumed. The three parts of the generalized growth tensor from Eq. 5.7 are therefore set according to

$$\boldsymbol{F}_{\mathrm{g}}^{(a)} = \vartheta^{(a)}\boldsymbol{I} + \left(1-\vartheta^{(a)}\right)\boldsymbol{M}_{\mathrm{g}}^{(a)} \quad \text{for} \quad a \in [1,2] \qquad \text{and} \qquad \boldsymbol{F}_{\mathrm{g}}^{(3)} = \boldsymbol{I} \tag{5.85}$$

with the structural tensors $\boldsymbol{M}_{\mathrm{g}}^{(a)} = \boldsymbol{A}_{\mathrm{g}}^{(a)} \otimes \boldsymbol{A}_{\mathrm{g}}^{(a)}$. The first and second part are adopting the basic form of growth perpendicular to the direction $\boldsymbol{A}_{\mathrm{g}}^{(a)}$ as introduced in Eq. 5.1c, which is supposed to be controlled by the anisotropic driving force function from Eq. 5.57. During the local Newton iteration, the incremental updates of the growth factors are obtained from the system of equations given in Eq. 5.19 for the general case, which can now be reduced to two equations with the solutions

$$\Delta\vartheta_{k+1}^{(1)} = \left.\frac{A_{\vartheta}^{(2,2)}R^{(1)} - A_{\vartheta}^{(1,2)}R^{(2)}}{A_{\vartheta}^{(1,1)}A_{\vartheta}^{(2,2)} - A_{\vartheta}^{(1,2)}A_{\vartheta}^{(2,1)}}\right|_{\vartheta_k^{(a)}}, \qquad \Delta\vartheta_{k+1}^{(2)} = \left.\frac{A_{\vartheta}^{(1,1)}R^{(2)} - A_{\vartheta}^{(2,1)}R^{(1)}}{A_{\vartheta}^{(1,1)}A_{\vartheta}^{(2,2)} - A_{\vartheta}^{(1,2)}A_{\vartheta}^{(2,1)}}\right|_{\vartheta_k^{(a)}}, \tag{5.86}$$

which have to be evaluated based on the values $\vartheta_k^{(1)}$ and $\vartheta_k^{(2)}$ of the previous iteration step. This involves the abbreviations defined in Eq. 5.38, which require knowledge of the derivatives $\partial\phi^{(i)}/\partial\vartheta^{(j)}$. For their specification, the expression from Eq. 5.58 together with $\partial\boldsymbol{C}_{\mathrm{e}}/\partial\vartheta^{(j)}$ from Eq. 5.53 has to be considered. Inserting the explicit form

$$\boldsymbol{F}_{\mathrm{g}}^{-1} = \boldsymbol{F}_{\mathrm{g}}^{-\mathrm{T}} = \frac{1}{\vartheta^{(1)}\,\vartheta^{(2)}}\left(\boldsymbol{I} + \left(\vartheta^{(1)}-1\right)\boldsymbol{M}_{\mathrm{g}}^{(1)} + \left(\vartheta^{(2)}-1\right)\boldsymbol{M}_{\mathrm{g}}^{(2)}\right) \tag{5.87}$$

of the inverse of the growth tensor from Eq. 5.25 with Eq. 5.26 and the derivatives

$$\frac{\partial\boldsymbol{F}_{\mathrm{g}}}{\partial\vartheta^{(1)}} = \boldsymbol{F}_{\mathrm{g}}^{(2)}\left(\boldsymbol{I} - \boldsymbol{M}_{\mathrm{g}}^{(1)}\right) = \vartheta^{(2)}\boldsymbol{I} - \vartheta^{(2)}\boldsymbol{M}_{\mathrm{g}}^{(1)} + \left(1-\vartheta^{(2)}\right)\boldsymbol{M}_{\mathrm{g}}^{(2)} \tag{5.88a}$$

$$\frac{\partial\boldsymbol{F}_{\mathrm{g}}}{\partial\vartheta^{(2)}} = \left(\boldsymbol{I} - \boldsymbol{M}_{\mathrm{g}}^{(2)}\right)\boldsymbol{F}_{\mathrm{g}}^{(1)} = \vartheta^{(1)}\boldsymbol{I} + \left(1-\vartheta^{(1)}\right)\boldsymbol{M}_{\mathrm{g}}^{(1)} - \vartheta^{(1)}\boldsymbol{M}_{\mathrm{g}}^{(2)} \tag{5.88b}$$

from Tab. 5.1 into Eq. 5.53 and expanding all terms finally leads to the compact result

$$\frac{\partial\boldsymbol{C}_{\mathrm{e}}}{\partial\vartheta^{(j)}} = \frac{1}{\vartheta^{(j)}}\left(-2\,\boldsymbol{C}_{\mathrm{e}} + \boldsymbol{M}_{\mathrm{g}}^{(j)}\boldsymbol{C}_{\mathrm{e}} + \boldsymbol{C}_{\mathrm{e}}\boldsymbol{M}_{\mathrm{g}}^{(j)}\right) \tag{5.89}$$

for both growth factors with $j \in [1,2]$. This expression now allows the evaluation of Eq. 5.58 for $i,j \in [1,2]$. For the growth part of the tangent modulus, the derivatives of the stress tensor $\boldsymbol{S}$

with respect to the growth factors from Eq. 5.35 and the derivatives of the growth factors with respect to the Cauchy-Green tensor $\boldsymbol{C}$ from Eq. 5.39 have to be specified. With the result from Eq. 5.88, Eq. 5.35 can be simplified towards

$$\begin{aligned}\frac{\partial \boldsymbol{S}}{\partial \vartheta^{(a)}} = -\left(\boldsymbol{F}_{\mathrm{g}}^{-1} \boxtimes \boldsymbol{F}_{\mathrm{g}}^{-1}\right) : \frac{1}{\vartheta^{(a)}} \Big[2\,\boldsymbol{S}_{\mathrm{e}} - \boldsymbol{M}_{\mathrm{g}}^{(a)} \boldsymbol{S}_{\mathrm{e}} - \boldsymbol{S}_{\mathrm{e}} \boldsymbol{M}_{\mathrm{g}}^{(a)} + \dots \\ \dots \tfrac{1}{2}\,\mathbb{C}_{\mathrm{i}}^{\mathrm{e}} : \left(2\,\boldsymbol{C}_{\mathrm{e}} - \boldsymbol{M}_{\mathrm{g}}^{(a)} \boldsymbol{C}_{\mathrm{e}} - \boldsymbol{C}_{\mathrm{e}} \boldsymbol{M}_{\mathrm{g}}^{(a)} \right) \Big],\end{aligned} \tag{5.90}$$

which is valid for both $a \in [1, 2]$. Solving the reduced form of the system of equations from Eq. 5.39 for the wanted terms, the results

$$\frac{\partial \vartheta^{(1)}}{\partial \boldsymbol{C}} = \frac{\kappa\,\Delta t}{A_\vartheta^{(1,1)} A_\vartheta^{(2,2)} - A_\vartheta^{(1,2)} A_\vartheta^{(2,1)}} \left(A_\vartheta^{(2,2)} k_\vartheta^{(1)} \frac{\partial \phi^{(1)}}{\partial \boldsymbol{C}} - A_\vartheta^{(1,2)} k_\vartheta^{(2)} \frac{\partial \phi^{(2)}}{\partial \boldsymbol{C}} \right), \tag{5.91a}$$

$$\frac{\partial \vartheta^{(2)}}{\partial \boldsymbol{C}} = \frac{\kappa\,\Delta t}{A_\vartheta^{(1,1)} A_\vartheta^{(2,2)} - A_\vartheta^{(1,2)} A_\vartheta^{(2,1)}} \left(A_\vartheta^{(1,1)} k_\vartheta^{(2)} \frac{\partial \phi^{(2)}}{\partial \boldsymbol{C}} - A_\vartheta^{(2,1)} k_\vartheta^{(1)} \frac{\partial \phi^{(1)}}{\partial \boldsymbol{C}} \right) \tag{5.91b}$$

with $\partial \phi^{(a)} / \partial \boldsymbol{C}$ from Eq. 5.59 are obtained. Using these expressions, an explicit representation of the growth part of the tangent modulus defined in Eq. 5.22 can be found, if the abbreviations

$$\begin{aligned}\boldsymbol{S}_{\mathbb{C}^{\mathrm{g}}}^{(a)} &:= 2\,\boldsymbol{S}_{\mathrm{e}} - \boldsymbol{M}_{\mathrm{g}}^{(a)} \boldsymbol{S}_{\mathrm{e}} - \boldsymbol{S}_{\mathrm{e}} \boldsymbol{M}_{\mathrm{g}}^{(a)} + \tfrac{1}{2}\,\mathbb{C}_{\mathrm{i}}^{\mathrm{e}} : \left(2\,\boldsymbol{C}_{\mathrm{e}} - \boldsymbol{M}_{\mathrm{g}}^{(a)} \boldsymbol{C}_{\mathrm{e}} - \boldsymbol{C}_{\mathrm{e}} \boldsymbol{M}_{\mathrm{g}}^{(a)} \right) \quad \text{for} \quad a \in [1, 2], \\ \boldsymbol{\Theta}_{\mathbb{C}^{\mathrm{g}}}^{(1)} &:= A_\vartheta^{(2,2)} k_\vartheta^{(1)} \left(\boldsymbol{M}_{\mathrm{g}}^{(1)} \boldsymbol{S}_{\mathrm{e}} + \left(\boldsymbol{C}_{\mathrm{e}} \boldsymbol{M}_{\mathrm{g}}^{(1)} \right) : \tfrac{1}{2}\,\mathbb{C}_{\mathrm{i}}^{\mathrm{e}} \right) - A_\vartheta^{(1,2)} k_\vartheta^{(2)} \left(\boldsymbol{M}_{\mathrm{g}}^{(2)} \boldsymbol{S}_{\mathrm{e}} + \left(\boldsymbol{C}_{\mathrm{e}} \boldsymbol{M}_{\mathrm{g}}^{(2)} \right) : \tfrac{1}{2}\,\mathbb{C}_{\mathrm{i}}^{\mathrm{e}} \right), \\ \boldsymbol{\Theta}_{\mathbb{C}^{\mathrm{g}}}^{(2)} &:= A_\vartheta^{(1,1)} k_\vartheta^{(2)} \left(\boldsymbol{M}_{\mathrm{g}}^{(2)} \boldsymbol{S}_{\mathrm{e}} + \left(\boldsymbol{C}_{\mathrm{e}} \boldsymbol{M}_{\mathrm{g}}^{(2)} \right) : \tfrac{1}{2}\,\mathbb{C}_{\mathrm{i}}^{\mathrm{e}} \right) - A_\vartheta^{(2,1)} k_\vartheta^{(1)} \left(\boldsymbol{M}_{\mathrm{g}}^{(1)} \boldsymbol{S}_{\mathrm{e}} + \left(\boldsymbol{C}_{\mathrm{e}} \boldsymbol{M}_{\mathrm{g}}^{(1)} \right) : \tfrac{1}{2}\,\mathbb{C}_{\mathrm{i}}^{\mathrm{e}} \right)\end{aligned}$$

are introduced. Then, the growth part of the tangent modulus in the intermediate configuration is given by

$$\mathbb{C}_{\mathrm{i}}^{\mathrm{g}} = -\frac{2\,\kappa\,\Delta t}{A_\vartheta^{(1,1)} A_\vartheta^{(2,2)} - A_\vartheta^{(1,2)} A_\vartheta^{(2,1)}} \sum_{a=1}^{2} \frac{1}{\vartheta^{(a)}}\, \boldsymbol{S}_{\mathbb{C}^{\mathrm{g}}}^{(a)} \otimes \boldsymbol{\Theta}_{\mathbb{C}^{\mathrm{g}}}^{(a)} \tag{5.92}$$

and the entire tangent modulus in the reference configuration is again obtained by applying the pullback operation

$$\mathbb{C} = \left(\boldsymbol{F}_{\mathrm{g}}^{-1} \boxtimes \boldsymbol{F}_{\mathrm{g}}^{-1} \right) : \left(\mathbb{C}_{\mathrm{i}}^{\mathrm{e}} + \mathbb{C}_{\mathrm{i}}^{\mathrm{g}} \right) : \left(\boldsymbol{F}_{\mathrm{g}}^{-\mathrm{T}} \boxtimes \boldsymbol{F}_{\mathrm{g}}^{-\mathrm{T}} \right). \tag{5.93}$$

By comparison of Eq. 5.92 to its equivalents on p. 78 and p. 79 for isotropic growth and for growth in the direction of the compressive principal stress, it can be observed that the complexity clearly increases with taking into account one or even more anisotropy directions. By advantage of the generalized formulation, it is however not necessary to specify each imaginable model variant in detail as exemplified here, since all of them are covered by the general equations. With a suitable implementation of the generalized framework, various combinations of different forms of the growth tensor with different driving force functions can thus be analyzed without additional implementation effort.

6 Stress-driven fiber reorientation

Besides tissue growth, remodeling in terms of a change of the internal structure of the tissue is a relevant adaptation process in arterial walls. In the context of the phenomenological material model for fiber-reinforced soft biological tissues by Balzani, Neff, et al. (2006), which considers the tissue as an isotropic matrix with two embedded families of collagen fibers, remodeling can be realized by a load-dependent reorientation of the collagen fibers. In default of a general agreement on the mechanical stimulus, reorientation of the fibers just as growth is supposed to be stress-driven based on the general motivation at the beginning of Chapter 5. As described in Sec. 2.1 and confirmed by the studies of Schriefl, Zeindlinger, et al. (2012), collagen fibers in healthy arteries are primarily found in the plane of the vessel wall, where they are arranged in two distinguishable helices around the vessel axis. Assuming an ideal tubular geometry, this is the plane, where the highest tensile stresses occur, and the arrangement of the fibers is thus well in agreement with their nature of being especially suited for carrying tensile loads. In such an idealized situation, which is illustrated on the right hand side of Fig. 6.1, the two fiber families can be represented by the vectors $\boldsymbol{A}^{(1)}$ and $\boldsymbol{A}^{(2)}$, whose orientation within the axial-circumferential plane is defined by the angles $\beta_{\mathrm{f}}^{(1)}$ and $\beta_{\mathrm{f}}^{(2)} = -\beta_{\mathrm{f}}^{(1)}$ between the fibers and the circumferential direction. But even in healthy arteries, those fiber angles have been observed in experimental investigations to vary nonlinearly over the wall thickness, as for example documented by Schriefl, Zeindlinger, et al. (2012) or Schriefl, Wolinski, et al. (2013). Moreover, the definition of the fiber orientation vectors gets much more complex in patient-specific arteries. On the one hand, the irregular geometry of such arteries can no longer be idealized as thick-walled tube, which complicates the geometry-based identification of the plane representing the vessel wall. On the other hand, a lot of patient-specific arteries might show structural aberrations due to diseases like atherosclerosis, that locally affect the material properties, the mechanical behavior and hence also the arrangement of the fibers. As shown by Akyildiz, Chai, et al. (2017) for atherosclerotic carotid plaques or by Niestrawska, Viertler, et al. (2016) for aneurysmatic compared to healthy abdominal aortas, the collagen fibers may significantly disperse out of the axial-circumferential plane in such cases, which means that a single fiber angle β_{f} is then not sufficient for the definition of a fiber orientation vector. The aim behind a reorientation algorithm is thus twofold: First, it is expected to allow for an automated identification of realistic fiber orientation vectors at each material point based on a mechanically motivated hypothesis for an optimized fiber arrangement, which does not require measurements or information about the orientation of the material points within the radial-circumferential-axial coordinate system. Starting with an initial guess, the fiber arrangement might be tuned prior to adjacent investigations by application of representative average loads. As a second aspect however, the factual reorientation of the fibers in terms of a "real time" adaptation to changing mechanical conditions is enabled as well.

The most important prerequisite for the development of a fiber reorientation algorithm is the definition of the target fiber orientations. Focusing on the assumption of a stress-driven

reorientation, this can be accomplished by a hypothesis on an explicit correlation between stress state and fiber arrangement. Once the favored fiber arrangement is identified, an algorithmic concept for the replacement of the initially chosen by the desired fiber vectors has to be determined. Apart from not being feasible for computational reasons, a sudden replacement is not in line with experimental observations on arterial adaptation. From that point of view, an approach for the continuous reorientation over time should be pursued.

6.1 Target fiber orientation

In order to arrive at a mechanically motivated prediction of the fiber arrangement in arterial walls, it should be recalled that the main function of the embedded collagen fibers is to bear tensile stresses. It can thus be presumed that the fibers are arranged in such a way that they can most effectively perform this task. The local stress state at each material point is characterized by three principal stresses, which are ordered by descending size, and the associated principal directions. The existence of fibers is justifiable if at least one of these principal stresses is positive. In that case, it is obvious that both fiber families should be aligned with the first principal direction. The existence of two distiguishable fiber families gets relevant as soon as two of the principal stresses are positive. Then, not only a single direction but a whole plane is dominated by tensile stresses. For an optimized arrangement of the two fiber families within that plane, Hariton, deBotton, et al. (2007a) postulated the hypothesis that the load-bearing behavior in arterial walls is promoted if the fibers are arranged symmetrically with respect to the two maximum tensile principal stresses. Their angle with respect to the direction of the first principal stress is thereby dictated by the ratio of the second to the first principal stress. Considering the principal stresses as force vectors as illustrated in Fig. 6.1, this means that the fibers are preferably aligned with the resultants of the tensile principal stresses. Hariton, deBotton, et al. (2007a) focused on the Cauchy stress tensor $\boldsymbol{\sigma}$ to define their target fiber orientations. This is indeed reasonable because it establishes a relation between the fiber arrangement and the true stresses acting in the tissue. In the reorientation model presented

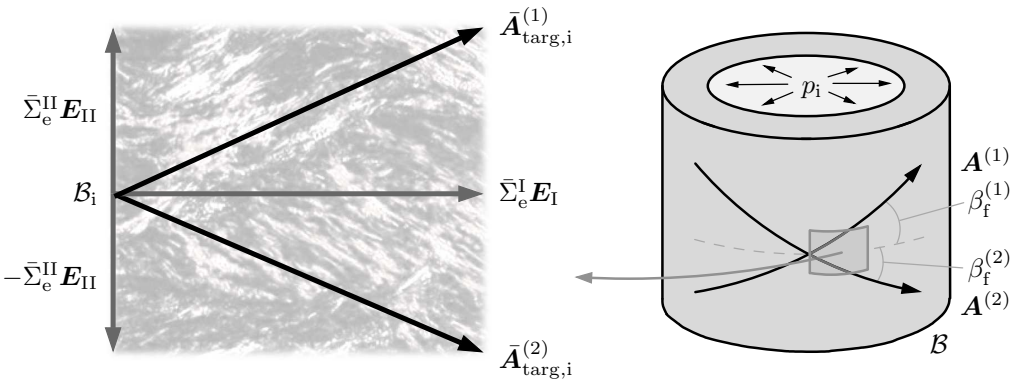

Figure 6.1: Following Hariton et al. (2007), the target fiber orientation vectors $\bar{\boldsymbol{A}}^{(1)}_{\mathrm{targ,i}}$ and $\bar{\boldsymbol{A}}^{(2)}_{\mathrm{targ,i}}$ are defined such that they point into the direction of the resultants of the tensile principal stresses. The collagen fiber network adumbrated in the background of the draft is extracted from a polarized light micrograph showing the media of a human thoracic aorta published by Schriefl, Zeindlinger, et al. (2012).

here, consistency with the stress-driven growth model treated in Chapter 5 shall be maintained. For this reason, the symmetric part $\bar{\boldsymbol{\Sigma}}_\mathrm{e} = {}^1\!/_2\,(\boldsymbol{C}_\mathrm{e}\boldsymbol{S}_\mathrm{e} + \boldsymbol{S}_\mathrm{e}\boldsymbol{C}_\mathrm{e})$ of the Mandel stress tensor in the intermediate configuration, first introduced in Eq. 5.12, is used for the definition of the target fiber orientation vectors. Solving the eigenvalue problem $\det[\bar{\boldsymbol{\Sigma}}_\mathrm{e} - \bar{\Sigma}_\mathrm{e}\boldsymbol{I}] = 0$ of this stress tensor, the eigenvalues $\bar{\Sigma}_\mathrm{e}^\mathrm{I} \geq \bar{\Sigma}_\mathrm{e}^\mathrm{II} \geq \bar{\Sigma}_\mathrm{e}^\mathrm{III}$ and the corresponding unit eigenvectors $\boldsymbol{E}_\mathrm{I}$, $\boldsymbol{E}_\mathrm{II}$ and $\boldsymbol{E}_\mathrm{III}$ are obtained. Based on these quantities and the hypothesis for an optimized arrangement of the fibers described above, the target fiber orientation vectors shown in Fig. 6.1 can be defined by

$$\bar{\boldsymbol{A}}^{(1)}_\mathrm{targ,i} = \left\langle \bar{\Sigma}_\mathrm{e}^\mathrm{I} \right\rangle \boldsymbol{E}_\mathrm{I} + \left\langle \bar{\Sigma}_\mathrm{e}^\mathrm{II} \right\rangle \boldsymbol{E}_\mathrm{II} \qquad \text{and} \qquad \bar{\boldsymbol{A}}^{(2)}_\mathrm{targ,i} = \left\langle \bar{\Sigma}_\mathrm{e}^\mathrm{I} \right\rangle \boldsymbol{E}_\mathrm{I} - \left\langle \bar{\Sigma}_\mathrm{e}^\mathrm{II} \right\rangle \boldsymbol{E}_\mathrm{II} \tag{6.1}$$

provided that at least $\bar{\Sigma}_\mathrm{e}^\mathrm{I}$ is positive. The index "i" points out that these vectors are defined in the intermediate configuration and the Macaulay bracket defined in Eq. 5.61 secures that only tensile values of the principal stresses are taken into account. If only the largest principal stress is tensile, both target vectors are aligned with the direction of that stress and both fiber families will consequently seek to reorient towards this direction. In case that all principal stresses are compressive, the fibers cannot contribute to a redistribution of the loads and the existing target vectors from preceding simulation steps should be kept unchanged.

The reorientation of the fiber vectors $\boldsymbol{A}^{(1)}$ and $\boldsymbol{A}^{(2)}$ will be regarded in the reference configuration. To this end, the pullback operation and normalization

$$\bar{\boldsymbol{A}}^{(a)}_\mathrm{targ} = \frac{\boldsymbol{F}_\mathrm{g}^{-1}\bar{\boldsymbol{A}}^{(a)}_\mathrm{targ,i}}{\left|\boldsymbol{F}_\mathrm{g}^{-1}\bar{\boldsymbol{A}}^{(a)}_\mathrm{targ,i}\right|} \qquad \text{for} \qquad a \in [1,2] \tag{6.2}$$

has to be applied to the target fiber orientation vectors. Prior to starting the reorientation, a reasonable assignment of the target vectors to the existing fiber orientation vectors has to be carried out. Fiber family 1 might in general not necessarily reorient towards the first, but rather to the second target vector if this vector is closer to the original one. In order to minimize the reorientation angles, the target vectors are therefore exchanged and/or rotated by 180° if required, such that finally the vectors $\boldsymbol{A}^{(1)}_\mathrm{targ}$ and $\boldsymbol{A}^{(2)}_\mathrm{targ}$, now without a bar, are obtained as target vectors of the fiber families $\boldsymbol{A}^{(1)}$ and $\boldsymbol{A}^{(2)}$, respectively. In view of a nonlinear finite element implementation, it is almost sure that a simple replacement of the existing by the target fiber orientation vectors at full level of the external loads is not applicable. Abrupt changes in the fiber arrangement can be expected to provoke significant changes in the stress and strain distributions, which are likely to endanger the convergence of the Newton iteration required to obtain the new nodal displacements for the updated fiber arrangement. A nearby way out, such pursued by Hariton, deBotton, et al. (2007a), is a recomputation of the boundary value problem with the new fiber orientations, beginning from the very first load step. Once the full load level is attained again, a repeated computation of the target fiber orientations will probably reveal that they have changed due to the update of the boundary value problem. In order to arrive at a final fiber arrangement being in accordance with the favored one, several iterative steps each including the entire load step procedure, might be required.
Another possibility to avoid large changes in the fiber arrangement during the global Newton iteration is to perform a stepwise rotation of the pre-existing fiber orientation vectors towards their target orientation at retained level of the external loads. Such an approach promises to be computationally more efficient.

6.2 Algorithms for the fiber reorientation

On the basis of a stepwise reorientation, Fausten, Balzani & Schröder (2016) proposed an enhanced algorithmic scheme for the update of the fiber orientation vectors, which indeed improves the computational efficiency of the original approach by Hariton, deBotton, et al. (2007a). The main advantage of their algorithm is that a recomputation of the entire boundary value problem including load stepping can be prevented, which results in a reduced total number of global Newton iterations. Apart from their approach, an alternative proposal for an iterative reorientation (Zahn & Balzani, 2018a) will be the subject of this section. Considering the reorientation as a time-delayed process by prescribing a scalar evolution equation for the angle between the existing and the target fiber orientation vector, this algorithm also ensures that no abrupt changes of the fiber arrangement occur. Especially in combination with the growth model from Chapter 5 or other models which anyway call for the maintenance of a constant load level until a steady state is reached, this method is straightforward. Furthermore, it harmonizes well with the idea of a "real time" adaptation to changing mechanical conditions in contrast to the approach by Fausten, Balzani & Schröder (2016), which considers the reorientation as a purely technical problem. A comparison of both algorithms will be provided in Sec. 7.3.2 based on a simple numerical example.

6.2.1 Algorithm 1: Incremental reorientation (Fausten et al., 2016)

Given an existing fiber orientation vector $\boldsymbol{A}_{j-1}^{(a)}$ and its target orientation $\boldsymbol{A}_{\text{targ}}^{(a)}$, the target difference vector

$$\Delta \boldsymbol{A}_{j,\text{targ}}^{(a)} = \boldsymbol{A}_{\text{targ}}^{(a)} - \boldsymbol{A}_{j-1}^{(a)} \qquad \text{for} \qquad a \in [1,2] \tag{6.3}$$

can be defined. This vector would formally have to be added to the existing fiber vector $\boldsymbol{A}_{j-1}^{(a)}$ for rotating it towards its target position. As explained above, this can not be done in a single step without endangering the convergence of the subsequent Newton iteration needed to recover equilibrium. In order to prevent this, Fausten, Balzani & Schröder (2016) perform an incremental remodeling loop, where the index j denotes the incremental reorientation steps. Two such steps are visualized in Fig. 6.2. Instead of the whole difference vector, only a fraction

$$\Delta \boldsymbol{A}_{j}^{(a)} = b_j \, \Delta \boldsymbol{A}_{j,\text{targ}}^{(a)} \tag{6.4}$$

of this vector is added to the fiber orientation vector $\boldsymbol{A}_{j-1}^{(a)}$ to obtain the updated vector $\boldsymbol{A}_{j}^{(a)}$. The coefficient b_j is thereby computed such that the rotation angle

$$\beta_{\text{r},j}^{(a)} = \arccos\left(\boldsymbol{A}_{j}^{(a)} \cdot \boldsymbol{A}_{j-1}^{(a)}\right) \qquad \text{with} \qquad \beta_{\text{r},j}^{(a)} \leq \beta_{\text{r,max}} \tag{6.5}$$

does not exceed a user-defined maximal rotation angle $\beta_{\text{r,max}}$. Beginning with the initial fiber vector defined by $j = 0$, a series of incrementally updated fiber orientation vectors

$$\boldsymbol{A}_{j}^{(a)} = \frac{\boldsymbol{A}_{j-1}^{(a)} + \Delta \boldsymbol{A}_{j}^{(a)}}{\left|\boldsymbol{A}_{j-1}^{(a)} + \Delta \boldsymbol{A}_{j}^{(a)}\right|} \qquad \text{with} \qquad j \in [1, 2, \ldots] \tag{6.6}$$

is computed until the target orientation $\boldsymbol{A}_{\text{targ}}^{(a)}$ is reached. After each reorientation step, a standard Newton iteration is performed to re-establish equilibrium. The fiber as well as the

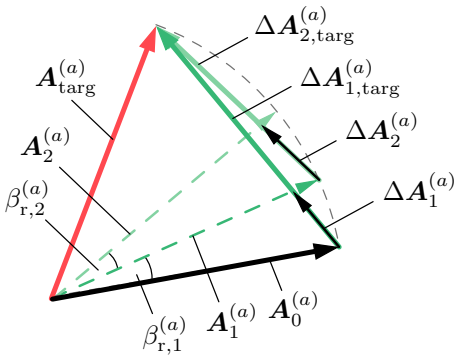

Figure 6.2: Illustration of the stepwise reorientation of an existing fiber orientation vector towards its target orientation by means of the incremental reorientation steps $j = 1$ and $j = 2$. After each step, equilibrium is established in a global Newton iteration. The figure is based on Fig. 2 by Fausten, Balzani & Schröder (2016).

target fiber orientation vectors thereby have to be saved as history variables in order to be available in the next reorientation step.
Once the target fiber arrangement is attained at all Gauß points, the target fiber orientation vectors can be computed again based on the new stress state. If they deviate from the existing fiber vectors at any Gauß point, another incremental reorientation loop has to be started. This procedure with an outer loop providing the new target orientations and an inner loop, which incrementally rotates the fiber vectors towards those target orientations, is repeated until the norm of the target difference vector defined in Eq. 6.3 is lower than a predefined tolerance near zero for both fiber families at all Gauß points of the boundary value problem.

6.2.2 Algorithm 2: Continuous reorientation

The original reorientation algorithm by Hariton, deBotton, et al. (2007a) and its enhancement by Fausten, Balzani & Schröder (2016) both try to arrive at the favored fiber arrangement as fast as possible and do not include the temporal component of the reorientation process. Even if mainly the final arrangement of the fibers is matter of interest, modeling its continuous development over time is a simple way to avoid abrupt changes and, provided that a simulation over time is anyhow required by the material model, additional Newton iterations. Furthermore, such an approach can be handled exclusively within the material subroutine without any interventions to the standard workflow outside. The proposed algorithm for continuous reorientation of the fibers (Zahn & Balzani, 2018a) is based on the definition of the two angles

$$\eta^{(a)} = \arccos\left(\boldsymbol{A}^{(a)} \cdot \boldsymbol{A}^{(a)}_{\mathrm{targ}}\right) \qquad \text{for} \qquad a \in [1,2] \tag{6.7}$$

between the existing fiber vectors $\boldsymbol{A}^{(a)}$ and their target orientations $\boldsymbol{A}^{(a)}_{\mathrm{targ}}$. These angles are scalar measures for the deviation between the existing and the favored fiber arrangement and are intended to evolve continuously towards zero over time. This can be realized by the definition of two scalar evolution equations

$$\dot{\eta}^{(a)} = k_\eta\left(|\eta^{(a)}|\right) \leq 0 \qquad \text{for} \qquad a \in [1,2] \tag{6.8}$$

for the time derivatives of the angles $\eta^{(a)}$, where the remodeling function k_η has to be negative for all non-zero values of $\eta^{(a)}$ and zero for vanishing angles $\eta^{(a)} = 0$. Transferring the illustration from Fig. 5.3 to the given situation, the approximation $\eta_{n+1}^{(a)} - \eta_n^{(a)} \approx \dot{\eta}_n^{(a)} \Delta t$ is obtained when applying explicit Euler time integration to Eq. 6.8. The wanted values of the angles at time step $n+1$ are thus given by

$$\eta_{n+1}^{(a)} \approx \dot{\eta}_n^{(a)} \Delta t + \eta_n^{(a)} \qquad \text{with} \qquad \Delta t = t_{n+1} - t_n \tag{6.9}$$

and can directly be computed without iteration since they do only depend on known values from the previous time step n. Due to use of explicit time integration, numerical stability can only be ensured for sufficiently small time step sizes Δt. Considering remodeling in parallel with the growth model from Chapter 5 however leads to the conclusion that the time step sizes required for convergence of the local Newton iteration mentioned in Sec. 5.1.3 are small enough for a stable reorientation of the fibers. An implicit time integration scheme, being unconditionally stable but associated to increased computational effort, can therefore be estimated as dispensable in the given context. In consequence of explicit time integration, the remodeling part $\mathbb{C}^{\mathrm{r}}$ of the tangent modulus $\mathbb{C} = \mathbb{C}^{\mathrm{e}} + \mathbb{C}^{\mathrm{g}} + \mathbb{C}^{\mathrm{r}}$, which would formally have to be defined as

$$\mathbb{C}^{\mathrm{r}} = 2 \sum_{a=1}^{2} \frac{\partial \boldsymbol{S}}{\partial \eta^{(a)}} \otimes \frac{\partial \eta^{(a)}}{\partial \boldsymbol{C}} \tag{6.10}$$

in analogy to Eq. 5.22, is zero due to $\partial \eta_{n+1}^{(a)} / \partial \boldsymbol{C}_{n+1} = \boldsymbol{0}$. As obvious from Eq. 6.9, the angles $\eta^{(a)}$ between the existing and the target fiber orientation vectors decrease over time provided that the derivatives $\dot{\eta}_n^{(a)}$ from Eq. 6.8 are negative. This is fulfilled for a remodeling function $k_\eta \leq 0$. Two suggestions for the remodeling function, and the computation of the updated fiber orientation vectors from Eq. 6.9 are the subject of the following paragraphs. There is no distinction of the remodeling functions and their parameters with respect to both fiber families. For that reason, the index a at variable $\eta^{(a)}$, denoting the fiber family, is skipped in favor of better legibility.

Remodeling functions. In order to enable the definition of a maximal remodeling velocity $|\dot{\eta}| = k_\eta^+$, which decelerates with a horizontal tangent towards zero for decreasing angles η, the broken rational remodeling function

$$k_\eta(\eta) = -\frac{k_\eta^+ \, \eta^2}{\eta^2 + m_\eta^+} \qquad \text{with} \qquad \eta \text{ in rad}, \quad k_\eta^+ > 0 \quad \text{and} \quad m_\eta^+ > 0 \tag{6.11}$$

is designed. As visualized in Fig. 6.3, the asymptotical convergence of this function towards $-k_\eta^+$ for large angles η can be regulated by the second parameter m_η^+. For $m_\eta^+ \to 0$, the constant function $k_\eta = -k_\eta^+$, which is however undefined for $\eta = 0°$, is approached.

An angular point at $\eta = 0°$, leading to a reduction of the reorientation velocity in the final phase, might be a realistic scenario, but is not essential if mainly the result and not the temporal progress of the reorientation process is the matter of interest. For such cases, the logarithmic remodeling function

$$k_\eta(\eta) = -k_\eta^+ \, \ln(m_\eta^+ |\eta| + 1) \qquad \text{with} \qquad \eta \text{ in rad}, \quad k_\eta^+ > 0 \quad \text{and} \quad m_\eta^+ > 0, \tag{6.12}$$

shown in Fig. 6.4, is proposed. Both parameters m_η^+ and k_η^+ affect the reorientation velocity. For $m_\eta^+ \to 0$, the whole function approaches zero, whereas the parameter k_η^+ is a pure scaling factor. In contrast to the broken rational remodeling function, the logarithmic one is not bounded by an asymptote giving a limit for the maximal reorientation velocity.

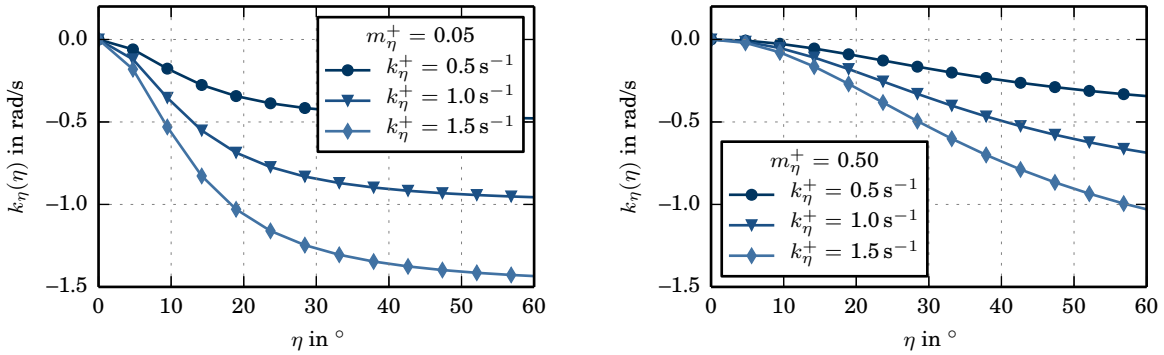

Figure 6.3: Effect of the parameters k_η^+ and m_η^+ on the graph of the broken rational remodeling function from Eq. 6.11 (previously published in Fig. 3, Zahn & Balzani, 2018a).

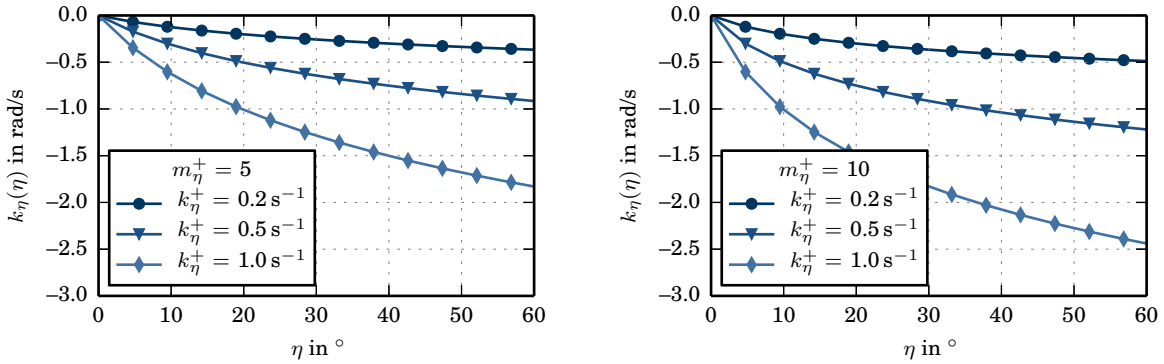

Figure 6.4: Effect of the parameters k_η^+ and m_η^+ on the graph of the logarithmic remodeling function from Eq. 6.12 (previously published in Fig. 4, Zahn & Balzani, 2018a).

Computation of the updated fiber orientation vectors. After evaluation of the evolution equation for the angle between the existing and the target fiber orientation vector, the actual value $\eta_{n+1}^{(a)}$ of this angle but not yet the fiber vector $\boldsymbol{A}_{n+1}^{(a)}$ belonging to it is known. The illustration in Fig. 6.5 shows, that it can be computed from the target vector minus a certain multiple of the unit difference vector

$$\Delta \boldsymbol{A}_{\text{targ}}^{(a)} = \frac{\Delta \tilde{\boldsymbol{A}}_{\text{targ}}^{(a)}}{\left|\Delta \tilde{\boldsymbol{A}}_{\text{targ}}^{(a)}\right|} \qquad \text{with} \qquad \Delta \tilde{\boldsymbol{A}}_{\text{targ}}^{(a)} = \boldsymbol{A}_{\text{targ},n+1}^{(a)} - \boldsymbol{A}_{n}^{(a)}. \tag{6.13}$$

Using the angular sum of 180° and the relation $a/\sin(\alpha) = b/\sin(\beta)$ valid in a general triangle, the angle

$$\gamma^{(a)} = 180° - \eta_{n+1}^{(a)} - \arccos\left(\boldsymbol{A}_{\text{targ},n+1}^{(a)} \cdot \Delta \boldsymbol{A}_{\text{targ}}^{(a)}\right) \tag{6.14}$$

and the vector

$$\tilde{\boldsymbol{A}}_{n+1}^{(a)} = \boldsymbol{A}_{\text{targ},n+1}^{(a)} - \frac{\sin\left(\eta_{n+1}^{(a)}\right)}{\sin\left(\gamma^{(a)}\right)} \Delta \boldsymbol{A}_{\text{targ}}^{(a)} \tag{6.15}$$

are obtained. The normalized fiber orientation vector at time step $n+1$ is finally given by

$$\boldsymbol{A}_{n+1}^{(a)} = \frac{\tilde{\boldsymbol{A}}_{n+1}^{(a)}}{\left|\tilde{\boldsymbol{A}}_{n+1}^{(a)}\right|}. \tag{6.16}$$

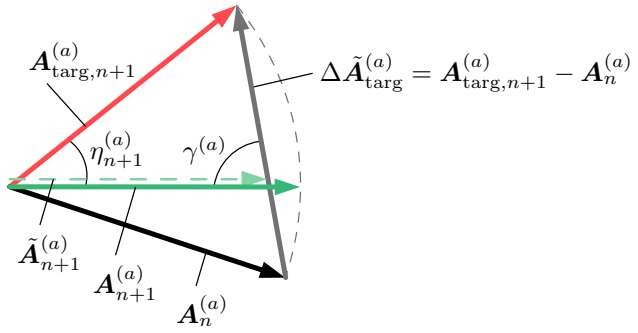

Figure 6.5: Illustration of the rotation of a fiber orientation vector $\boldsymbol{A}^{(a)}_{n}$ towards its new position at time step $n+1$ (previously published in Fig. 2, Zahn & Balzani, 2018a).

Compared with algorithm 1, the algorithmic treatment of the continuous fiber reorientation is straightforward. In each iteration step within the global Newton iteration associated to time step $n+1$, the fiber orientation vectors computed in the previous time step n are used to determine the actual stress state. Based thereon, the target fiber orientation vectors $\boldsymbol{A}^{(a)}_{\mathrm{targ},n+1}$ are computed. Presuming that those vectors converge towards stationary values over time, the existing angles $\eta^{(a)}_{n}$ can be approximated by

$$\eta^{(a)}_{n} \approx \arccos\left(\boldsymbol{A}^{(a)}_{n} \cdot \boldsymbol{A}^{(a)}_{\mathrm{targ},n+1}\right), \tag{6.17}$$

even though the target fiber orientation vectors of the previous time step would formally have to be inserted. With the updated angles $\eta^{(a)}_{n+1}$ from Eq. 6.9, the future fiber orientation vectors $\boldsymbol{A}^{(a)}_{n+1}$ can be provided. Those vectors will actually not be needed until the next time step is reached, and have thus to be saved as history variables.

7 Growth and fiber reorientation in idealized arterial segments

The purpose of this chapter is the illustration and evaluation of the combined framework for stress-driven growth and fiber reorientation by means of numerical examples on idealized arterial segments. In two preliminary sections, the constitutive material model used in all simulations and the boundary value problem as well as general information, which applies to all examples, are introduced. After the investigation of some numerical aspects, basic effects of growth and fiber reorientation on stresses and fiber arrangement in the arterial wall are analyzed for different forms of growth. This analysis will emphasize that a reliable comparison and assessment of different growth mechanisms can only be achieved if the growth parameters are set appropriately and if a method for the consistent evaluation of certain criteria characterizing the quality of the model variants is found. In order to meet these demands, a method for the optimization-based comparison of model variants within the general framework is developed and applied to one- and two-layered, idealized arterial segments. In a final numerical example in that section, the most important findings of the chapter are summarized. Finally, a first attempt towards a virtual opening angle experiment is presented.

7.1 Constitutive material model for soft biological tissues

As motivated in Sec. 2.2, the phenomena analyzed in this work are based on a phenomenological, hyperelastic stress-strain formulation with exclusion of the active response. In the existing literature, many of such material models designed to describe the passive response of arterial walls within the framework of hyperelasticity are available, for example those which are analyzed in the comparative study by Holzapfel, Gasser & Ogden (2000) or explained in the summaries by Humphrey (2002, 2008). A major number of those models are not a priori convex, which means that they cannot guarantee a mechanically and mathematically reliable behavior (Holzapfel, Gasser & Ogden, 2000). The model used in this work is therefore chosen among the polyconvex framework for soft biological tissues proposed by Balzani, Neff, et al. (2006), where all energy functions satisfy some generalized convexity conditions ensuring physical reasonability and numerical stability.

Concretely, the free energy function $\psi = \bar{\rho}_0 \, \bar{\psi}$ per unit reference volume is supposed to be the sum of four parts, with three of them representing the behavior of mechanically relevant tissue components and the fourth one enforcing incompressibility. The framework of multiplicative growth implies that only the elastic part of the deformation, represented by the deformation tensor $\boldsymbol{C}_{\mathrm{e}}$, generates stresses. The functional form of the strain energy function is thus assumed

to be

$$\psi(\boldsymbol{C}_\mathrm{e}, \boldsymbol{M}_\mathrm{i}^{(1)}, \boldsymbol{M}_\mathrm{i}^{(2)}) = \psi_\mathrm{iso}(I_1, I_3) + \psi_\mathrm{pen}(I_3) + \sum_{a=1}^{2} \psi_\mathrm{ti}^{(a)}(I_1, J_4^{(a)}, J_5^{(a)}), \tag{7.1}$$

which is in accordance with Eq. 3.96 if the dependence of $\bar{\psi}$ on $\bar{\rho}_0$ is supposed to be of the type $\bar{\psi}(\bar{\rho}_0, \boldsymbol{C}_\mathrm{e}, \boldsymbol{M}_\mathrm{i}^{(a)}) = {}^1\!/_{\bar{\rho}_0}\, \psi(\boldsymbol{C}_\mathrm{e}, \boldsymbol{M}_\mathrm{i}^{(a)})$. As previously defined, the included invariants are given by

$$I_1 = \mathrm{tr}[\boldsymbol{C}_\mathrm{e}], \qquad I_3 = \det[\boldsymbol{C}_\mathrm{e}], \qquad J_4^{(a)} = \mathrm{tr}[\boldsymbol{C}_\mathrm{e}\boldsymbol{M}_\mathrm{i}^{(a)}] \quad \text{and} \quad J_5^{(a)} = \mathrm{tr}[\boldsymbol{C}_\mathrm{e}^2\boldsymbol{M}_\mathrm{i}^{(a)}], \tag{7.2}$$

where $\boldsymbol{M}_\mathrm{i}^{(a)} = \boldsymbol{A}_\mathrm{i}^{(a)} \otimes \boldsymbol{A}_\mathrm{i}^{(a)}$ is a structural tensor representing fiber family a, built from the fiber orientation vector in the intermediate configuration. The first term of ψ, formulated in terms of the isotropic invariants I_1 and I_3, describes the material response of the isotropic matrix material. A common approach for large strain isotropic behavior is the Neo-Hookean model. Balzani, Neff, et al. (2006) propose the explicit expression

$$\psi_\mathrm{iso} = c_1 \left(I_1\, I_3^{-\frac{1}{3}} - 3 \right) \quad \text{with} \quad c_1 > 0, \tag{7.3}$$

which only accounts for the isochoric, i. e. volume preserving part of the deformation and has already been used by Holzapfel, Gasser & Ogden (2000). In order to satisfy the quasi-incompressibility constraint, Balzani, Neff, et al. (2006) include the penalty function

$$\psi_\mathrm{pen} = \epsilon_1 \left(I_3^{\epsilon_2} + I_3^{-\epsilon_2} - 2 \right) \quad \text{with} \quad \epsilon_1 > 0, \quad \epsilon_2 > 1, \tag{7.4}$$

which penalizes volumetric deformations. Here, only volumetric deformations arising from the elastic part of the deformation are concerned, which means that the determinant $J_\mathrm{e} = \sqrt{I_3}$ of $\boldsymbol{F}_\mathrm{e}$ is forced towards unity whereas the value of J_g, describing the volume change defined by the growth tensor $\boldsymbol{F}_\mathrm{g}$, is not restricted. To understand the effect of the penalty term, it is helpful to recall that the total energy potential introduced on p. 45 has to attain a minimum in a stable equilibrium state, which means

$$\Pi = \int_\mathcal{B} \left(\psi_\mathrm{iso} + \psi_\mathrm{pen} + \sum_{a=1}^{2} \psi_\mathrm{ti}^{(a)} \right) \mathrm{d}V + \Pi_\mathrm{ext} \quad \overset{!}{\rightarrow} \quad \min. \tag{7.5}$$

with Π_ext given in Eq. 4.8. The global minimum of the penalty function is reached just for the case that the postulation $J_\mathrm{e} = 1$ is satisfied. An infinitely high value of ϵ_1 would thus enforce $J_\mathrm{e} = 1$ in order to erase the accordingly extensive contribution of the penalty term in Eq. 7.5. This limit can however never be reached for numerical reasons since it leads to an ill-conditioned system of equations. Nevertheless, by setting the parameters ϵ_1 and ϵ_2 reasonably, the quasi-incompressibility constraint can sufficiently be fulfilled by the penalty method. It should be pointed out that this method, see e. g. Holzapfel (2000, pp. 389–391) for further information, is not the only way to model incompressibility. A common approach in this context, intelligibly explained by Humphrey (2002, pp. 93–95), is the introduction of a Lagrange multiplier p enforcing the constraint. In contrast to the parameters ϵ_1 and ϵ_2 in Eq. 7.4, this parameter depends on time, position and boundary conditions and has to be accounted for by an additional degree of freedom in a mixed finite element method. Appropriate special finite element formulations for incompressible materials are for example described by Wriggers (2008, pp. 406 ff.) or Zienkiewicz & Taylor (2000a, pp. 307 ff.).

The remaining terms in Eq. 7.1 represent two families of collagen fibers, which are taken into account by two transversely isotropic contributions characterized by

$$\psi_{\mathrm{ti}}^{(a)} = \alpha_1 \big\langle K_3^{(a)} - 2 \big\rangle^{\alpha_2} \quad \text{with} \quad \alpha_1 \geq 0, \quad \alpha_2 > 1 \quad \text{and} \quad K_3^{(a)} = I_1\, J_4^{(a)} - J_5^{(a)} \tag{7.6}$$

for $a = 1, 2$. As stated by Schröder & Neff (2003), who describe the construction and physical interpretation of $K_3^{(a)}$, the square root of this polyconvex function controls the deformation of an area element with a normal in the isotropy plane, i. e. with a normal perpendicular to the preferred direction $\boldsymbol{A}_{\mathrm{i}}^{(a)}$. According to Balzani, Neff, et al. (2006, Fig. 1), $K_3^{(a)}$ increases if an incompressible material is elongated in the direction of $\boldsymbol{A}_{\mathrm{i}}^{(a)}$. In the reference state for $\boldsymbol{C}_{\mathrm{e}} = \boldsymbol{I}$ with $I_1 = 3$ and $J_4^{(a)} = J_5^{(a)} = 1$, the value of $K_3^{(a)}$ is 2. As a consequence of the Macaulay bracket in Eq. 7.6, fiber family a only contributes to the overall stress response if it is under tension, which is true for $K_3^{(a)} > 2$.

Based on the free energy function in Eq. 7.1, the stress tensor $\boldsymbol{S}_{\mathrm{e}}$ is obtained from Eq. 3.101 using the chain rule and the derivatives

$$\frac{\partial I_1}{\partial \boldsymbol{C}_{\mathrm{e}}} = \boldsymbol{I} \qquad \text{and} \qquad \frac{\partial I_3}{\partial \boldsymbol{C}_{\mathrm{e}}} = I_3\, \boldsymbol{C}_{\mathrm{e}}^{-1} \tag{7.7}$$

of the isotropic invariants as well as the derivatives

$$\frac{\partial J_4^{(a)}}{\partial \boldsymbol{C}_{\mathrm{e}}} = \boldsymbol{M}_{\mathrm{i}}^{(a)} \qquad \text{and} \qquad \frac{\partial J_5^{(a)}}{\partial \boldsymbol{C}_{\mathrm{e}}} = \boldsymbol{C}_{\mathrm{e}} \boldsymbol{M}_{\mathrm{i}}^{(a)} + \boldsymbol{M}_{\mathrm{i}}^{(a)} \boldsymbol{C}_{\mathrm{e}} \tag{7.8}$$

of the mixed invariants. For the elastic part of the tangent modulus in the intermediate configuration defined in Eq. 5.23, the nonzero second derivatives

$$\frac{\partial^2 I_3}{\partial \boldsymbol{C}_{\mathrm{e}}^2} = I_3 \left(\boldsymbol{C}_{\mathrm{e}}^{-1} \otimes \boldsymbol{C}_{\mathrm{e}}^{-1} - \boldsymbol{C}_{\mathrm{e}}^{-1} \boxtimes \boldsymbol{C}_{\mathrm{e}}^{-1} \right) \qquad \text{and} \qquad \frac{\partial^2 J_5^{(a)}}{\partial \boldsymbol{C}_{\mathrm{e}}^2} = \boldsymbol{I} \boxtimes \boldsymbol{M}_{\mathrm{i}}^{(a)} + \boldsymbol{M}_{\mathrm{i}}^{(a)} \boxtimes \boldsymbol{I} \tag{7.9}$$

of the invariants are additionally required. The explicit expressions for stresses and tangent modulus are skipped by reason of not being relevant here.

Apart from the penalty parameters ϵ_1 and ϵ_2, the material model has three parameters per arterial layer which have to be fitted to experimental data: the isotropic parameter c_1 and the parameters α_1 and α_2 governing the response of the fibers. Brands, Klawonn, et al. (2008) adjusted the model to experimental data of media and adventitia of a human abdominal aorta, which was taken over from Holzapfel (2006). The condition $\det[\boldsymbol{F}] = \det[\boldsymbol{F}_{\mathrm{e}}] = 1$ was thereby used as a side constraint. They obtained the parameter sets given in Tab. 7.1, which will be used for the numerical simulations in this work.

Table 7.1: Parameters of the material model by Balzani, Neff, et al. (2006), adjusted to human tissue by Brands, Klawonn, et al. (2008).

	c_1	ϵ_1	ϵ_2	α_1	α_2
media	17.5 kPa	499.8 kPa	2.4	30 001.9 kPa	5.1
adventitia	6.6 kPa	23.9 kPa	10.0	1503.0 kPa	6.3

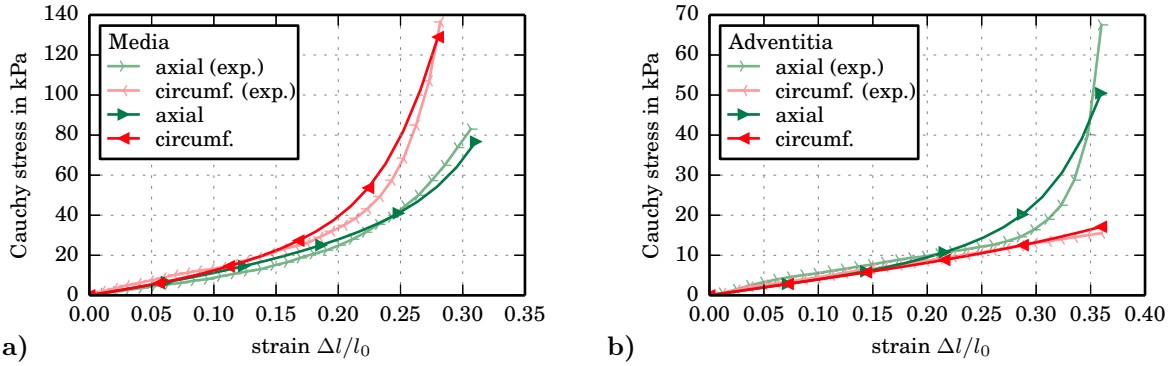

Figure 7.1: Comparison of experimental data and simulation for **a)** media ($\beta_f = \pm 43.39°$) and **b)** adventitia ($\beta_f = \pm 49.0°$) based on the material parameters from Tab. 7.1. The experimental data has been reproduced from Brands, Klawonn, et al. (2008, Fig. 2 + 3), but originally stems from Holzapfel (2006).

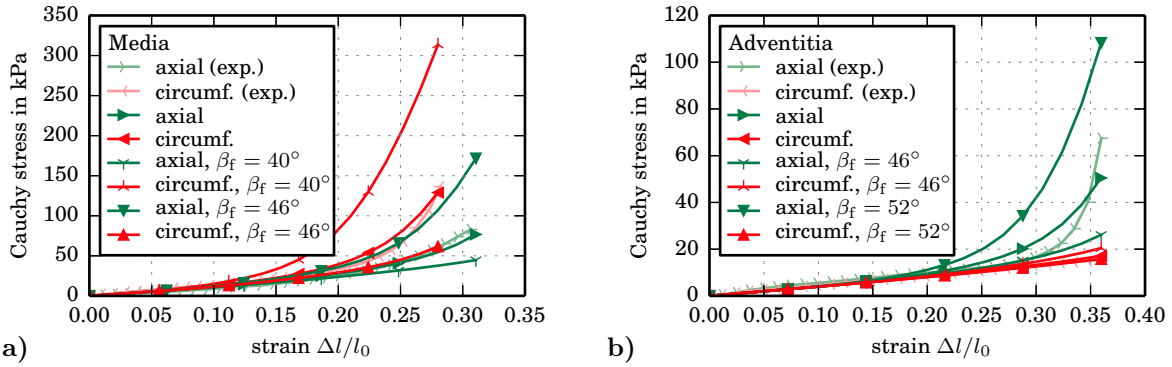

Figure 7.2: Only a small decrease or increase of the fiber angle, for which the parameters in Tab. 7.1 were obtained, leads to a strong change of the response of the material model adjusted to **a)** media and **b)** adventitia. If an angle of $\pm 45°$ is exceeded or underrun, this even reverses the stiffness ratio of circumferential and axial direction, as happening in the media for an angle of $\pm 46°$.

A comparison of experiment and simulation of a homogeneous unconstrained uniaxial tension test is illustrated in Fig. 7.1. Both anisotropy and nonlinearity of the experimental curves are captured well by the model. It should however be noted that the fiber angle, which has been set to $\beta_f = \pm 43.39°$ for the media as reported by Balzani, Neff, et al. (2006) and to $\beta_f = \pm 49.0°$ for the adventitia, has a tremendous effect on the material behavior and does not correspond to the mean fiber angle detected by Holzapfel (2006), which is $\pm 37.8°$ in the media and $\pm 58.9°$ in the adventitia. Even a comparatively small deviation of only $\pm 3°$ leads to stresses which are far from the experimental curves, see Fig. 7.2. In the context of this work, the fiber angle is however not assumed to be an input parameter of the material model, but primarily seen as a parameter which regulates itself following the mechanical demands. If the resulting angles differ from the angles for which the model was adjusted, a significant discrepancy between the behavior of the simulated and an average real artery has thus to be expected. For the analysis of fundamental effects of growth and fiber reorientation on a qualitative level, use of the described material model with the parameters given in Tab. 7.1 is nevertheless supposed to be justified since the basic characteristics of the material behavior are captured.

7.2 Boundary value problem of an idealized arterial segment

For the study of basic effects of growth and fiber reorientation in arteries, a series of simulations in idealized arterial geometries is performed. Notwithstanding that real arteries consist of three distinguishable layers, a cylindrical one-layered tube representing the media is considered in this context in order to keep the number of parameters small and to obtain clear statements on the basic behavior. The material parameters are set as specified for media in Tab. 7.1. In accordance with the data of human aortas reported by Wolinsky & Glagov (1967), the inner and outer radii of the arterial segment are set to $r_\mathrm{i} = 6.5\,\mathrm{mm}$ and $r_\mathrm{o} = 7.5\,\mathrm{mm}$. The initial fiber angles of the two fiber families, which by the way do not affect the final result of the reorientation, are set consistently to $\pm 30°$ with respect to the circumferential direction. Unless stated elsewise, an internal pressure of $p = 120\,\mathrm{mmHg} = 16\,\mathrm{kPa}$ and an axial strain $\varepsilon_z \geq 0\,\%$ are applied to the idealized arteries. Applying symmetry boundary conditions, a section of 90° instead of the whole ring is sufficient for a 3D simulation of such an arterial segment. Discretizing that quarter of the artery into f elements each in radial and axial, as well as $6f$ elements in circumferential direction, a total number of $6f^3$ brick elements is required. Due to rotational symmetry and homogeneous conditions in axial direction, the simulations can be reduced to one dimension as illustrated in Fig. 7.3 when using the special finite element described in Sec. 4.2.2. The same arterial segment is then represented by only f one-dimensional axisymmetric elements lined up in radial direction. If a dependence of the results on the axial direction is expected, the compromise of a two-dimensional axisymmetric representation (see Sec. 4.2.1), getting along with f^2 elements, can be adopted. The more the mesh size factor f increases, the greater is the percentage decrease of the number of elements with respect to the original 3D problem. The effect of this reduction on the computing time will be analyzed in Sec. 7.3.1 for finite elements with quadratic shape functions. At the same time, a reasonable value of the mesh size factor f for use in all subsequent simulations will be determined.

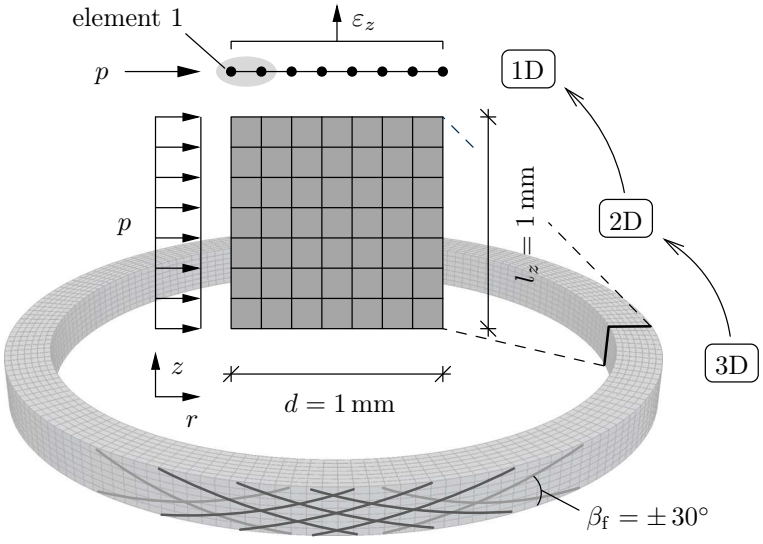

Figure 7.3: The boundary value problem of an idealized arterial segment can be reduced to one dimension if rotationally symmetric finite elements are used and if the loading allows this simplification. If the axial direction can not be renounced, for example due to a pressure that is not constant over z, a reduction to two dimensions is recommended, which still drastically reduces the number of degrees of freedom.

The standard procedure for the simulations presented in this chapter is as follows: Within the first second of the simulation time, the loads are applied to the arterial segments without activating growth and/or fiber reorientation. Afterwards, the loads are held constant and the segments are allowed to adapt, which changes the stress state and the arrangement of the fibers. The main focus is on the final result of those adaptation processes, which means that there is no ambition of reproducing the real temporal development. All parameters, which are supposed to essentially affect the temporal progression but not the final result, are therefore set without experimental evidence such that growth and remodeling act on the same time scale. For the growth function from Eq. 5.14, those parameters are

$$k_\vartheta^+ = k_\vartheta^- = 1.0\,\mathrm{s}^{-1} \qquad \text{and} \qquad m_\vartheta^+ = m_\vartheta^- = 3.0, \tag{7.10}$$

and the corresponding parameters of the logarithmic remodeling function from Eq. 6.12 are by default set to

$$k_\eta^+ = 0.6\,\mathrm{s}^{-1} \qquad \text{and} \qquad m_\eta^+ = 5.0. \tag{7.11}$$

The broken-rational remodeling function proposed in Eq. 6.11 will not be applied in the numerical examples of this chapter, and for incremental reorientation of the fiber vectors according to algorithm 1, no parameters related to the temporal behavior have to be set. Although the parameters $\phi_{\mathrm{crit}}^{(a)}$ introduced in Eq. 5.64 are supposed to affect the result of the adaptation process, their effect will not be analyzed and the non-modified driving force functions without consideration of critical stress levels will be used throughout.

For the comparison of different growth mechanisms, a consistent criterion for the abortion of the simulation has to be defined. Under constant load, the adaptation process is assumed to end up in a steady state at which neither growth nor remodeling are active anymore. This equilibrium state is indicated by a vanishing rate of all growth factors and zero difference angles between the actual and the target fiber orientation vectors. Growth equilibrium is supposed to be attained as soon as the condition

$$\frac{1}{n_{\mathrm{ele}}\, l_{\mathrm{int}}\, n_\vartheta} \sum_{n_{\mathrm{ele}}} \sum_{l_{\mathrm{int}}} \sum_{a=1}^{3} \frac{\left| \vartheta_{t+\Delta t}^{(a)} - \vartheta_t^{(a)} \right|}{\vartheta_t^{(a)} \Delta t} < \epsilon_\vartheta \tag{7.12}$$

is fulfilled. In this equation, n_{ele} and l_{int} are the numbers of elements and Gauß points per element, n_ϑ denotes the number of multiplicative parts of the growth tensor, and the tolerance ϵ_ϑ is set to $\epsilon_\vartheta = 10^{-4}/\mathrm{s} = 0.01\,\%/\mathrm{s}$. Anticipating that only algorithm 2 will be used later on for the reorientation of the fibers, the final fiber arrangement is assumed to be indicated by the condition

$$\frac{1}{n_{\mathrm{ele}}\, l_{\mathrm{int}}\, n_{\mathrm{f}}} \sum_{n_{\mathrm{ele}}} \sum_{l_{\mathrm{int}}} \sum_{a=1}^{n_{\mathrm{f}}} \left| \eta_t^{(a)} \right| < \epsilon_\eta \tag{7.13}$$

with the number of fiber families n_{f} and the tolerance ϵ_η for vanishing angles $\eta^{(a)}$, which is set to $\epsilon_\eta = 10^{-4} = 0.006°$. A steady state of the entire adaptation process is attained if both conditions, i. e. Eq. 7.12 and Eq. 7.13, are fulfilled simultaneously.

7.3 Numerical aspects

In this section, some basic numerical aspects which are relevant in the context of the arterial wall simulations performed in this work will be investigated. The first numerical example focuses on two major impact factors on the computing time: the reduction of a three-dimensional, rotationally symmetric boundary value problem to two or even to one dimension, and the usage of the analytic equations for the tangent modulus instead of its numerical computation. Since these effects are analyzed for different values of the mesh size factor f, the study also allows to evaluate the convergence behavior depending on the spatial discretization and to determine a reasonable value of f for all subsequent simulations. In a second example, the two algorithms for the reorientation of the fiber vectors are compared with respect to their robustness and the quality of the results, but also with respect to technical aspects and efficiency. Based on this analysis, a decision on which of both algorithms should be preferred in future simulations will be made.

7.3.1 Computing time and spatial discretization

All the arterial segments considered in this chapter are rotationally symmetric and can therefore be analyzed in one-dimensional boundary value problems without loss of information. In cases where the computing time is an important limiting factor, for example in the optimization-based, comparative study of different model variants presented in Sec. 7.5, this simplification leads to an enormous gain in time and computing capacity. Not as significant in its implication but still not less important is the method for the computation of the tangent modulus. Computing the tangent modulus numerically by means of complex step derivative approximation (CSDA) instead of analytically necessitates six additional loops within the material subroutine and use of complex data types at least on the material level, see the explanations on p. 71 f. In order to come to an estimation on the order of computing time reduction caused by these two effects, an arterial segment as defined in Sec. 7.2 with an axial strain of $\varepsilon_z = 10\,\%$ is simulated up to the growth equilibrium state in 3D, 2D and 1D with both methods to compute the tangent modulus and for different mesh size factors f between 1 and 10. The growth model from Sec. 5.2.3 with $\vartheta^+_{(1)} = 1.10$, $\vartheta^+_{(2)} = 1.049$ and $\vartheta^-_{(1)} = \vartheta^-_{(2)} = 0.98$ is applied and the fibers are allowed to reorient continuously according to Sec. 6.2.2. Specifically, the following finite elements are compared:

- 20-noded 3D brick element with quadratic shape functions and 14 Gauß points,
- 9-noded 2D quadrilateral, axisymmetric element with quadratic shape functions and 9 Gauß points,
- 3-noded 1D axisymmetric element with quadratic shape functions and 3 Gauß points.

If the tangent modulus is computed numerically, the element and material subroutines involve as many complex data type variables as required for a CSDA approach applied to the material tangent modulus or even to the entire element stiffness matrix. For the analytical approach, both subroutines do only make use of real data types instead. All simulations are performed on the same machine (a fair quality laptop) and with the same predefined sequence of time step sizes. The absolute values of the computing time and the final values of circumferential and axial stress at a Gauß point with the lowest distance to the vessel axis are summarized in Tab. 7.2.

Table 7.2: Computing times and stresses at a Gauß point near the inner surface, computed at steady state of growth and fiber reorientation, for 3D, 2D and 1D simulations with analytical and numerical computation of the tangent modulus and different mesh size factors f.

	Computing time in s						**Stress near inner surface**			
	analytical tangent			numerical tangent			σ_φ in kPa		σ_z in kPa	
f	3D	2D	1D	3D	2D	1D	3D	2/1D	3D	2/1D
1	6.94	0.89	0.42	29.77	2.45	1.01	127.6	127.1	13.92	13.90
2	60.29	2.17	0.57	219.6	10.32	1.55	130.5	130.2	12.98	13.00
3	218.0	4.04	0.72	752.5	21.31	2.12	131.5	131.3	12.75	12.77
4	609.1	8.72	0.86	1848	37.65	2.73	131.9	131.8	12.64	12.66
5	1437	13.43	0.88	–	58.96	3.22	132.2	132.1	12.59	12.60
6	3223	19.14	1.07	–	82.75	3.76	132.4	132.3	12.55	12.56
7	7035	25.93	1.21	–	110.8	4.31	132.6	132.5	12.53	12.54
8	15330	33.60	1.29	–	143.1	5.41	132.7	132.6	12.51	12.52
9	–*	42.32	1.46	–	180.3	5.93	–	132.7	–	12.50
10	–	51.75	1.57	–	220.8	5.85	–	132.7	–	12.49

*A missing number indicates that the simulation has not been performed because of its long duration.

As the performance depends on the computer, the informative value of the absolute numbers is limited. Nevertheless, two general trends can be stated when setting them into relation: If the tangent modulus is computed numerically, the computing time increases by a factor of roughly 4. In contrast to this, the computing time of a 3D simulation compared to a 1D simulation is multiplied by a factor beginning with 17 for $f = 1$, which then increases exponentially with f, reaching already about 12 000 for $f = 8$. This difference has been expectable since the question of analytical or numerical tangent modulus only affects the time needed to assemble the unchanged global system of equations, whereas the number of spatial dimensions predominantly affects the number of unknowns. Instead of f elements in 1D, f^2 elements are required in 2D and $6f^3$ elements in 3D. The increase in the number of elements compared to the 1D simulation is depicted in Fig. 7.4 a) for mesh size factors $f \in [1, 10]$. It should be noted that the number of unknown nodal displacement components is still higher, such that the increase in computing time, shown in Fig. 7.4 b), is even larger than the increase in elements.

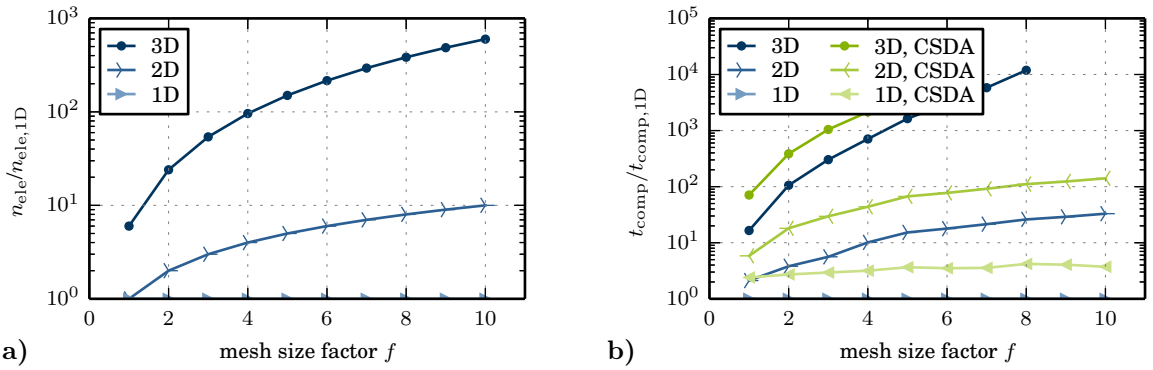

Figure 7.4: Illustration of the increase in **a)** the number of finite elements and **b)** computing time for analytical and numerical computation of the tangent modulus, both for 3D and 2D simulations relative to the reference 1D simulation and depending on the mesh size factor f.

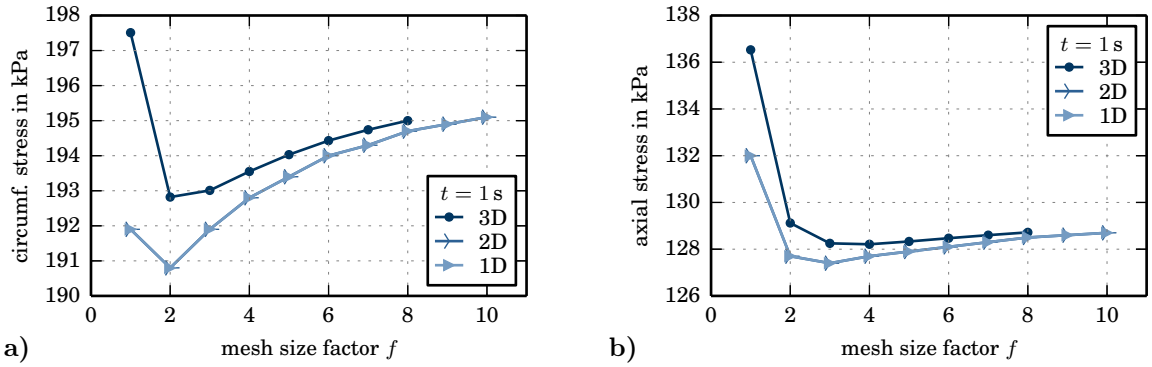

Figure 7.5: Convergence of **a)** circumferential and **b)** axial stress at a Gauß point near the inner surface with increasing mesh refinement, computed at $t = 1\,\mathrm{s}$ after full application of the load but prior to growth and remodeling.

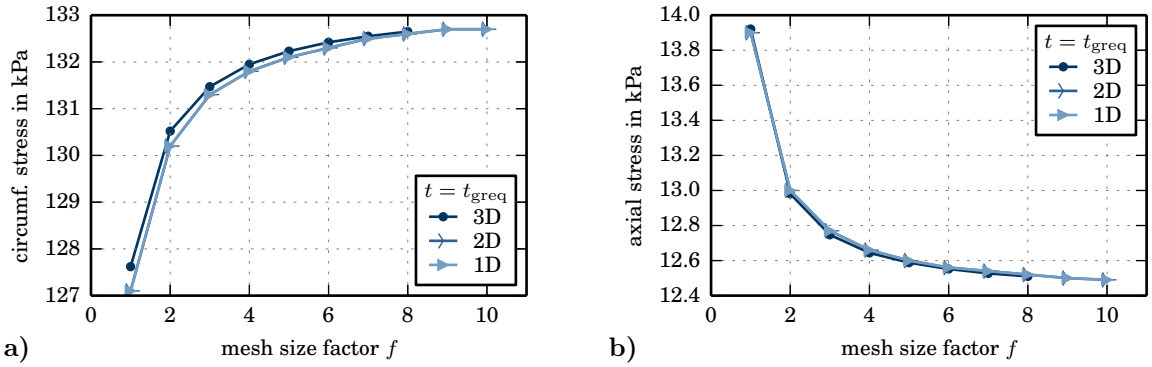

Figure 7.6: Convergence of **a)** circumferential and **b)** axial stress at a Gauß point near the inner surface with increasing mesh refinement, computed at steady state of growth and fiber reorientation.

Apart from observations on the computing time, the data obtained in the above study can be consulted to arrive at a statement on the required mesh refinement. The convergence of the circumferential and axial stresses at a Gauß point near the inner surface of the arterial segment for an increasing mesh size factor f is illustrated in Fig. 7.5 for $t = 1\,\mathrm{s}$ and in Fig. 7.6 for the final steady state. Regardless of point in time and number of spatial dimensions of the mesh, both stresses seem to converge towards fixed values. The deviations between the 3D and the 2D/1D results are caused by the deviant Gauß point position within the 3D element due to use of a 14 point instead of a 27 point integration scheme. Compared to 2D/1D, the Gauß point is located closer to the arterial lumen, where the peak values of circumferential and axial stress are expected in a non-adapting artery. This explains that the curves showing the 3D results in Fig. 7.5, that is before activation of growth and fiber reorientation, are above the other two curves. With increasing number of elements, the difference in the Gauß point positions decreases, such that the asymptotic values of the stresses do not depend on the number of spatial dimensions. Since growth and fiber reorientation induce a reduction of the stress gradients, in ideal circumstances towards a constant value, the deviating positions of the Gauß points have only a small effect on the results shown in Fig. 7.6.
After all, a mesh size factor of $f = 7$, i. e. seven elements in radial direction in the 1D simulation, can be supposed to be a good compromise between accuracy and numerical effort and is therefore

fixed for the subsequent numerical examples. For this value of f, a 1D simulation is complete in only 0.02 % of the time needed for a 3D simulation or in 4–5 % of the time needed for a 2D simulation. Using the analytic equations for the tangent modulus instead of CSDA reduces the computing time to about 28 %.
It should be noted for completeness that simulations with growth and fiber remodeling are running less stable in 3D than in 2D or 1D. It might happen that the principal directions start to deviate slightly from the circumferential, axial and radial directions over time, such that the rotational symmetry gets lost. This might possibly be caused by numerical inaccuracies due to the difference between the principal stress directions and the axes of the Cartesian coordinate system based on which the 3D elements are defined, and can be prevented by transforming the principal directions to a cylindrical coordinate system, truncating them to two decimal places and transforming them back. With regard to general 3D problems, which are however not considered in this chapter, a solution is still outstanding.

7.3.2 Comparison of the fiber reorientation algorithms

The two algorithms for the reorientation of the fiber vectors, i. e. incremental update according to Fausten et al. (algorithm 1) and continuous reorientation over time (algorithm 2), are compared on the basis of a non-growing 1D arterial segment loaded by an internal pressure of 120 mmHg and different levels of axial strain between 0 % and 15 %. As a consequence of different ratios between both loads, the final arrangement of the fibers is expected to differ, but for the same load case, both algorithms should lead to the same result. For algorithm 1, a maximal rotation angle of $\beta_{\mathrm{r,max}} = 10°$ is assumed for each reorientation step. A reorientation is only performed if the deviation with respect to the target orientation is greater than $\beta_{\mathrm{r,min}} = 1°$. The remodeling parameters for algorithm 2 are set as mentioned in Eq. 7.11.
In Fig. 7.7 and Fig. 7.8, the time response of both approaches is set in contrast by means of the fiber angles, the circumferential and the axial stress at Gauß point 1 of element 1. With only one exception, each of the considered quantities converges to a final value, which depends on the level of axial strain and is more or less the same for both approaches. When using algorithm 1, the reorientation is accomplished within about half a second – afterwards, the target fiber orientation vectors, which are recomputed at each time step with $\Delta t = 0.05\,\mathrm{s}$, remain unchanged and likewise do the fiber angles and the stresses. In contrast to that, a continuous reorientation of the fiber vectors spans over a period of several seconds, which can be adapted by choice of the remodeling parameters. This leads to smoother curves with less abrupt changes of the fiber angles and the mechanical quantities. As mentioned above, there is one exception at which no convergence over time can be achieved. In the case of 15 % of axial strain, algorithm 1 leads to a slight oscillation of the fiber angles, see Fig. 7.7 a), which in turn provokes a strong oscillation of the stresses around a mean value. Algorithm 2 proves to be more robust: in spite of the high level of axial strain, a convergence towards constant values in the range expected from algorithm 1 is obtained.
Similar observations can be made when analyzing the distribution of fiber angles and stresses over the radial position at a fixed point in time. The comparison of Fig. 7.9 and Fig. 7.10, which show the situation at $t = 8\,\mathrm{s}$ for use of algorithms 1 and 2, respectively, confirms that continuous reorientation of the fibers in general allows for more reliable results. For all considered levels of axial strain, smooth fiber and stress distributions are obtained, whereas an incremental update of the fiber vectors seems to be more prone to instabilities.

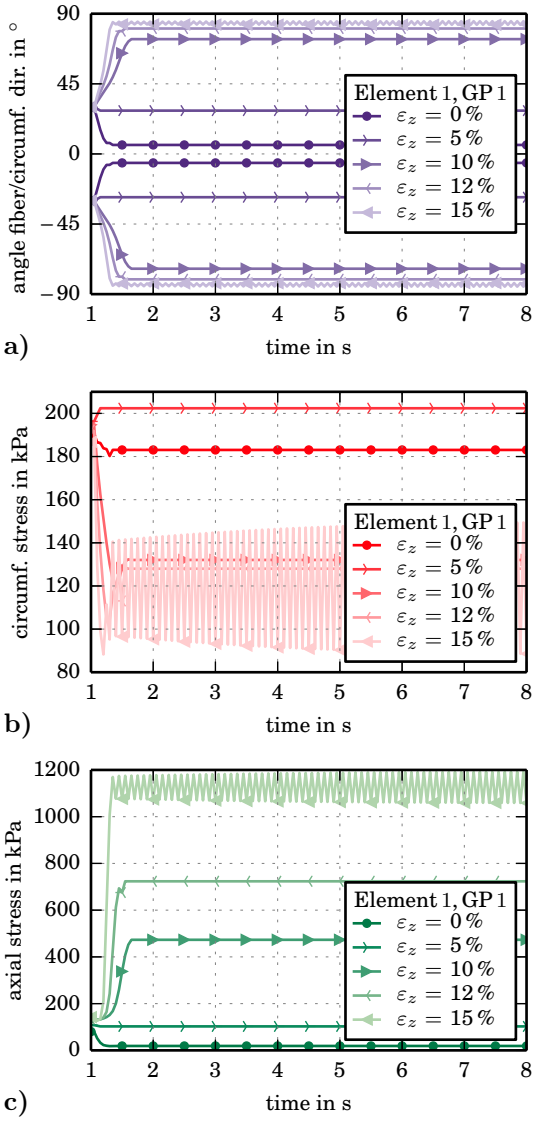

Figure 7.7: Temporal development of **a)** fiber angles, **b)** circumferential stress and **c)** axial stress at Gauß point 1 of element 1 in an arterial segment with incremental update of the fiber orientation vectors (**algorithm 1**).

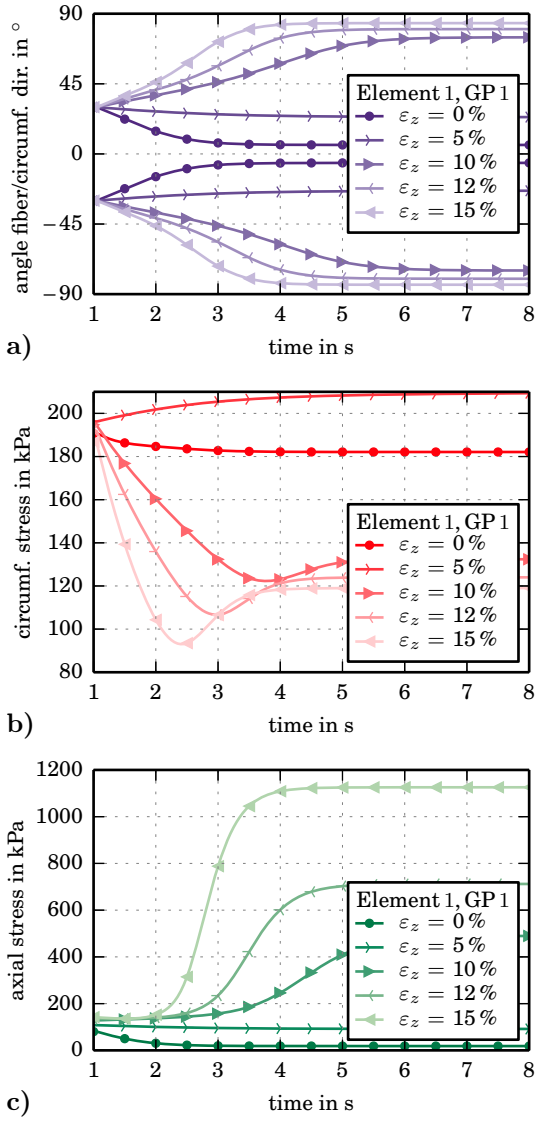

Figure 7.8: Temporal development of **a)** fiber angles, **b)** circumferential stress and **c)** axial stress at Gauß point 1 of element 1 in an arterial segment with continuous update of the fiber orientation vectors (**algorithm 2**).

Apart from better robustness, further points argue for preferential use of algorithm 2. From a technical point of view, algorithm 2 comes along with reduced memory requirements: instead of the fiber and the target fiber orientation vectors, only the fiber orientation vectors have to be saved as history variables, which reduces the number of the latter from $6\,n_\mathrm{f}$ to $3\,n_\mathrm{f}$, here with $n_\mathrm{f} = 2$. Furthermore, the implementation of algorithm 2 is straightforward compared to algorithm 1. It necessitates intervention on the material level only and does not even demand a local Newton iteration due to explicit integration of the evolution equation. In contrast to that, algorithm 1 requires implementation of an additional global Newton iteration loop around the standard one, where an abort criterion for the incremental reorientation loop should be

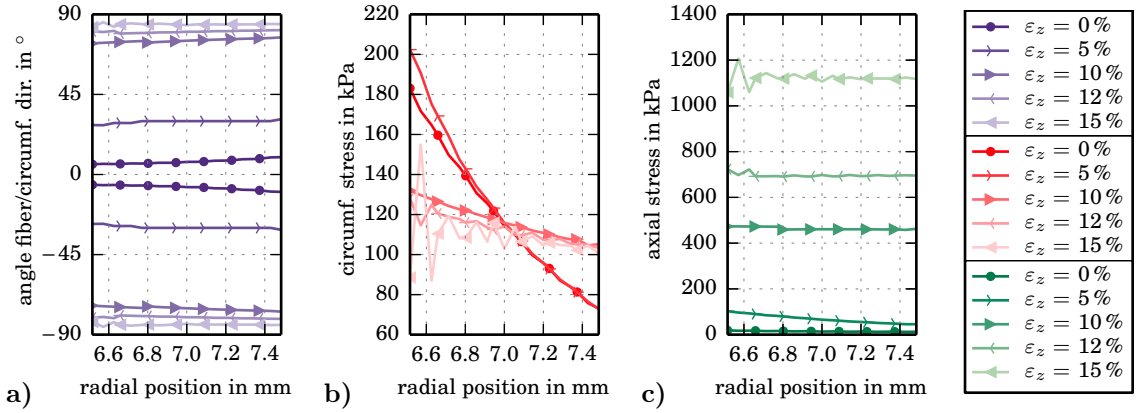

Figure 7.9: Distribution of **a)** fiber angles, **b)** circumferential stresses and **c)** axial stresses over the wall thickness at $t = 8\,\mathrm{s}$ in an arterial segment with incremental update of the fiber orientation vectors (**algorithm 1**).

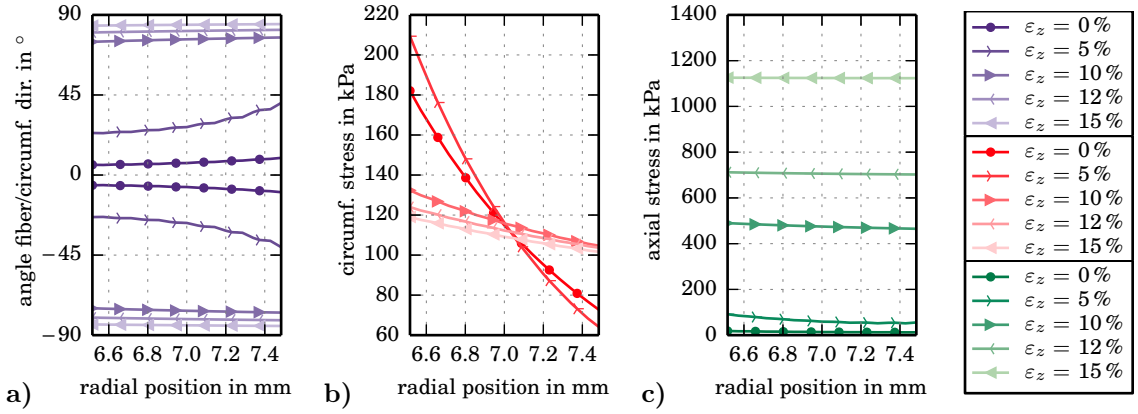

Figure 7.10: Distribution of **a)** fiber angles, **b)** circumferential stresses and **c)** axial stresses over the wall thickness at $t = 8\,\mathrm{s}$ in an arterial segment with continuous update of the fiber orientation vectors (**algorithm 2**).

included to avoid needless computation steps. In the context of the finite element program FEAP, this task has to be solved with the aid of a user macro, which considerably increases the implementation effort compared to algorithm 2. Finally, algorithm 2 is also advantageous regarding computational efficiency. At first glance, the example shown above indicates that the number of required time steps to arrive at the final fiber arrangement is much lower for algorithm 1, which means that the additional Newton iterations of algorithm 1 might be negligible compared to the additionally needed time steps of algorithm 2. If fiber reorientation is however combined with growth or another time-dependent process, the principal stress state is likely to change over time such that the reorientation is no longer restricted to a small number of time steps. Then, the additional Newton iterations noticeably increase the computing time. A rough evaluation of 1D simulations with isotropic growth and fiber reorientation up to the growth equilibrium state confirms that algorithm 1 needs on average 34 % more time than algorithm 2. It can be concluded that for all concerns from simplicity to robustness and efficiency, algorithm 2 with continuous reorientation of the fiber vectors should be preferred against algorithm 1. In all subsequent numerical examples, algorithm 2 will therefore be used.

7.4 Basic effects of growth and fiber reorientation

The numerical examples in this section are thought to illustrate basic effects of growth and fiber reorientation in arteries based on idealized, one-layered arterial segments. In an introductory example, basic forms of growth are first applied to a uniaxially loaded unit cube in order to investigate different possibilities of stress reduction. In a second example, the effect of fiber reorientation on the stress state in a non-growing artery is analyzed. The example points out that not only a reduction, but also a strong increase of stress components may appear. Afterwards, a simple comparative study of different growth mechanisms with and without reorientation of the fibers is performed. It highlights that the potential of the considered model variants to counteract stress peaks and gradients is strongly dependent on the level of axial strain and on the growth parameters. This leads to the conclusion that a more sophisticated strategy is needed for a fair comparison and evaluation of different model variants within the general framework.

7.4.1 Basic forms of growth

Supplementing the illustrative example from p. 60 on different basic forms of growth applied to a unit cube, the three basic forms of the growth tensor introduced in Eq. 5.1 are compared to each other in a simple study. A unit cube made of isotropic matrix material with the material parameters of media, but without embedded fibers, is charged with a uniaxial load of either 10 % of strain or 10 kPa of stress within the first second of the simulation time. The load is held constant up to $t = 20\,\mathrm{s}$ and then increased within one second to 20 %/20 kPa. In the time between $t = 1\,\mathrm{s}$ and $t = 40\,\mathrm{s}$, the cube is allowed to grow isotropically, in the direction of the load or perpendicular to the direction of the load as described by the growth tensors $\boldsymbol{F}_{\mathrm{g}}^{\square}$, $\boldsymbol{F}_{\mathrm{g}}^{\parallel}$ and $\boldsymbol{F}_{\mathrm{g}}^{\perp}$, respectively. The limiting values of the growth factors are set such that the maximally permitted volume increase, represented by the determinant of the growth tensor, is equal for each form of growth. With $\vartheta_{\square}^{+} = 1.1$, $\vartheta_{\parallel}^{+} = 1.331$ and $\vartheta_{\perp}^{+} = 1.1537$, this limit is at 33.1 %. A distinction of driving force functions is not required in this simple setting since all of them are equal due to the uniaxial, tensile stress state.

The development of the non-zero stress component and the determinant of the growth tensor over time is shown in Fig. 7.11 for strain-driven and in Fig. 7.12 for stress-driven application of the load. In both figures, the reference values for a non-growing cube are depicted as dashed lines. As guessed before in the theoretical consideration on p. 61 and obvious from Fig. 7.11, growth in the direction of the load can most effectively reduce the stress in case of a prescribed strain: in spite of the lowest volume increase, the lowest stress level is obtained. The rigorous reduction is due to a compensation of the deformation by an elongation of the reference configuration, which might even lead to a zero stress if the simulation was extended up to a steady state and the allowed amount of growth was high enough. For growth perpendicular to the load, where the reduction of the stress results from an increase of the cross sectional area, this is impossible if the volume increase is limited to reasonable values. Although the volume increase is clearly higher than for growth in the direction of the load, the effect on the stress is limited. Isotropic growth can be seen as a combination of the other two forms of growth. Consequently, it leads to an average result with an appreciable reduction of the stress but an unnecessarily high increase of the volume.

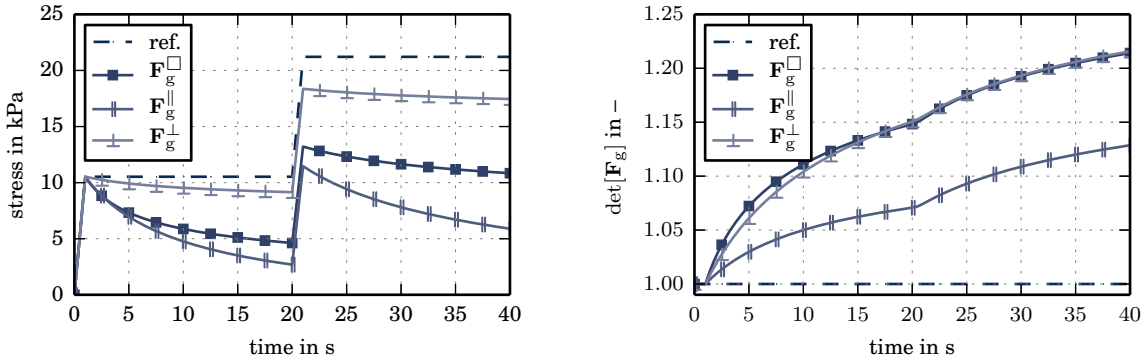

Figure 7.11: Stress and determinant of the growth tensor, representing the volume increase, over time in a unit cube loaded in two steps by 10 % and 20 % of uniaxial strain. Growth is activated at $t = 1\,\mathrm{s}$.

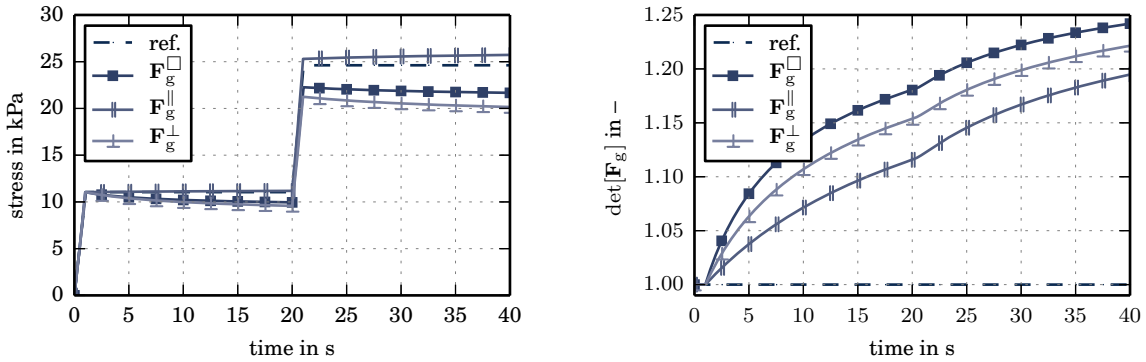

Figure 7.12: Stress and determinant of the growth tensor, representing the volume increase, over time in a unit cube loaded in two steps by a uniaxial stress of 10 kPa and 20 kPa, which is referred to the reference configuration. Growth is activated at $t = 1\,\mathrm{s}$.

If the load is applied in terms of a constant force, i. e. a constant stress referred to the reference configuration, contrary results are obtained. In that case, *only* an increase of the cross sectional area can lead to a reduction of the Cauchy stress, which means that growth perpendicular to the loading direction is the best choice, see Fig. 7.12. Growth in the direction of the load is even followed by a slight increase of the stress because it gives rise to a higher lateral contraction than observed in the non-growing reference cube. Again, isotropic growth combines both effects: due to its component perpendicular to the load, a reduction of the stress can be realized, but the component in the direction of the stress is dispensable.
It should be mentioned that further loading situations are imaginable. If for example a constant Cauchy stress – i. e. a constant stress referred to the actual configuration – was applied, none of the growth mechanisms would cause a reduction of the stress. The capability of a certain form of growth to reduce or homogenize stresses is thus strongly dependent on the type of loading, especially for anisotropic forms of growth.

7.4.2 Fiber reorientation in a non-growing arterial segment

The concept of the following example and the content of the accompanying text are adopted almost without changes from Zahn & Balzani (2018a). However, the simulations are recom-

puted in 1D instead of 3D, which leads to slight quantitative, but not qualitative deviations of the results. Proceeding as described in Sec. 7.2, two one-dimensional arterial segments are loaded with an internal pressure and an axial strain of either 0 % or 12 % within the first second of the simulation time. Afterwards, the fibers are allowed to reorient at constant level of the loads. As a result of the explicit time integration of the evolution equations for the angles $\eta^{(a)}$ between the existing and the target fiber orientation vectors, a dependence of the development of the stresses and fiber angles over time on the time step size Δt should in general be expected. In order to check to what extent this might be relevant, the computations are run with different choices for the time increment.

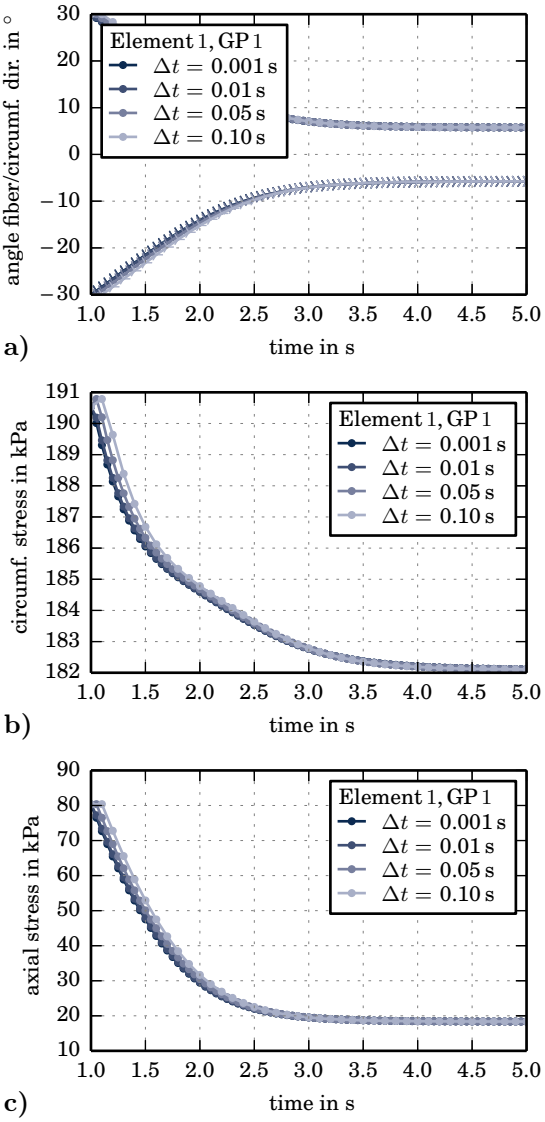

Figure 7.13: Temporal development of **a)** fiber angles, **b)** circumferential stress and **c)** axial stress at Gauß point 1 of element 1 in a remodeling arterial segment subjected to an internal pressure of 120 mmHg.

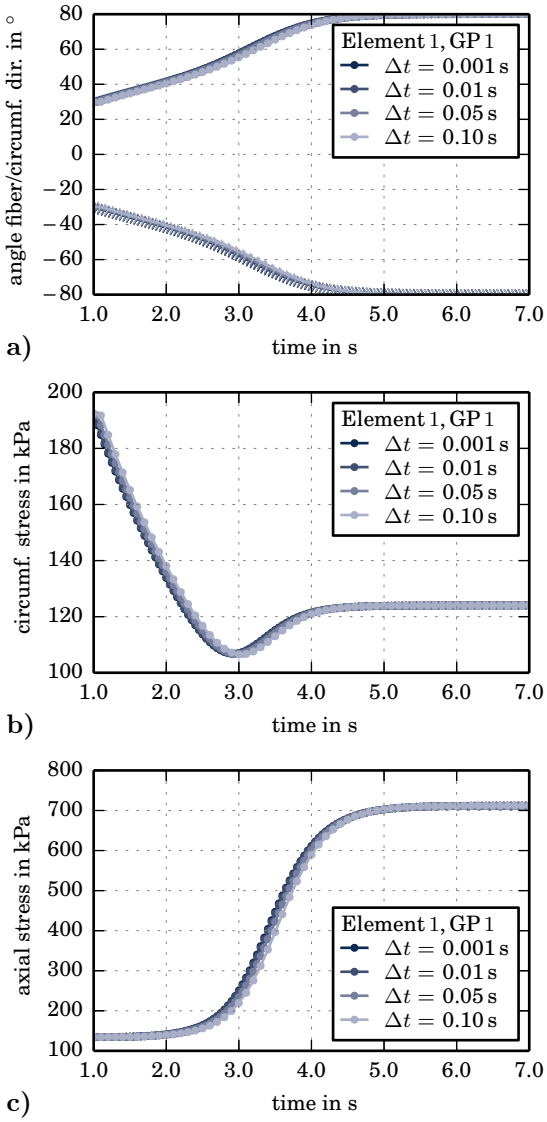

Figure 7.14: Temporal development of **a)** fiber angles, **b)** circumferential stress and **c)** axial stress at Gauß point 1 of element 1 in a remodeling arterial segment subjected to an internal pressure of 120 mmHg and an axial strain of 12 %.

In Fig. 7.13 and Fig. 7.14, the fiber angles as well as the Cauchy stress in circumferential and axial direction at Gauß point 1 of element 1 are plotted over time for the arterial segments loaded with 0 % and 12 % of axial strain, respectively. As indicated in Fig. 7.3, element 1 is located at the internal surface of the segment. A distinction of the curves obtained with different sizes of the time increment is only possible in periods with a high positive or negative slope of the considered quantity. The final converged state at $t = 5\,\mathrm{s}$ in Fig. 7.13 and at $t = 7\,\mathrm{s}$ in Fig. 7.14 does not depend on the time step size, such that a major effect of Δt on the result can be excluded. Beyond that, as shown in Fig. 7.15, the converged state is independent on the initially chosen fiber angles. The same final values are also reached for initial fiber angles of e. g. $\pm 10°$, $\pm 50°$ or $\pm 70°$.

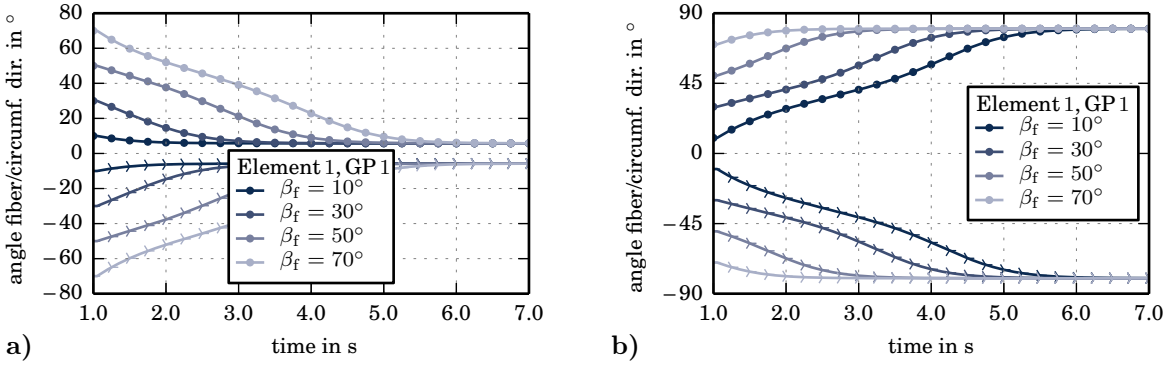

Figure 7.15: Temporal development of the fiber angles for different initial values at Gauß point 1 of element 1 in a remodeling arterial segment subjected to an internal pressure of 120 mmHg and an axial strain of **a)** 0 % or **b)** 12 %.

A comparison of the numeric results in Fig. 7.13 and Fig. 7.14 reveals that the level of axial strain is of particular importance. In absence of a deformation in axial direction, the circumferential stress near the arterial lumen is only slightly reduced by about 5 %, see Fig. 7.13 b), whereas the axial stress decreases strongly to remaining 25 % of its initial value, see Fig. 7.13 c). Both reductions are caused by a decrease of the fiber angles from $\pm 30°$ to $\pm 5.75°$ with respect to the circumferential direction, which is shown in Fig. 7.13 a). Since this reorientation of the load-bearing fibers towards the circumferential direction leads to a higher material stiffness in that direction, a reduction of the circumferential stress is not even self-evident.
Indeed, as occurring in the arterial segment loaded with 12 % instead of 0 % of axial strain, a reorientation of the fibers can also lead to the increase of single stress components due to a drastic change of the material behavior. As illustrated in Fig. 7.14 b) and Fig. 7.14 c), a strong decrease of the circumferential stress and a rather constant level of the axial stress, with a tendency to increase, can be observed in the first two seconds. But then, at a time where the steady state has almost been reached in the first arterial segment, the axial stress starts to increase towards an extremely high level of 700 kPa and the circumferential stress, which had its minimum at about $t = 3\,\mathrm{s}$, rises again, converging to a value of 124 kPa. The strong increase of the axial stress can be attributed to the reorientation of the fibers towards the axial direction, which is shown in Fig. 7.14 a). At about $t = 2.5\,\mathrm{s}$, the fiber angles pass over $\pm 45°$ and the fibers start to bear more axial than circumferential loads. As a result of a stiffening in axial direction, the stresses increase and the fibers are forced to arrange more and more in axial direction until an equilibrium state with fiber angles of $\pm 80°$ is found.

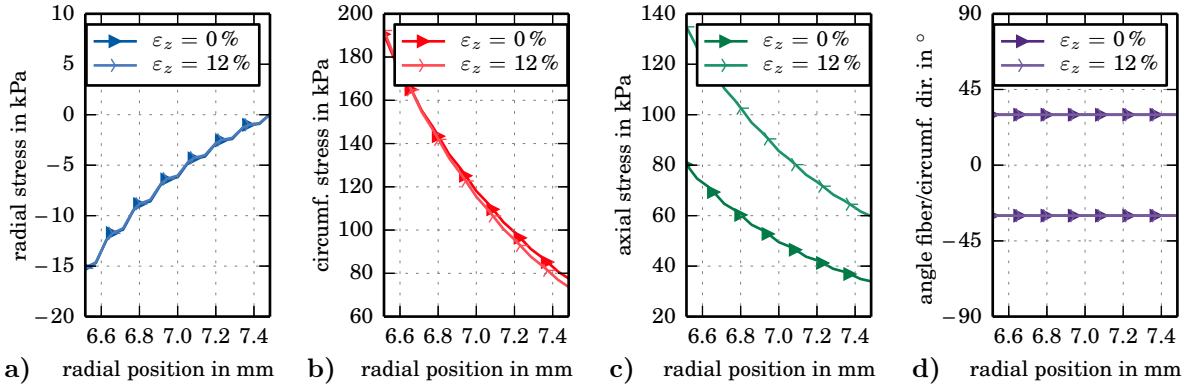

Figure 7.16: Distribution of **a)** radial stresses, **b)** circumferential stresses, **c)** axial stresses and **d)** fiber angles over the wall thickness before remodeling at $t = 1\,\mathrm{s}$.

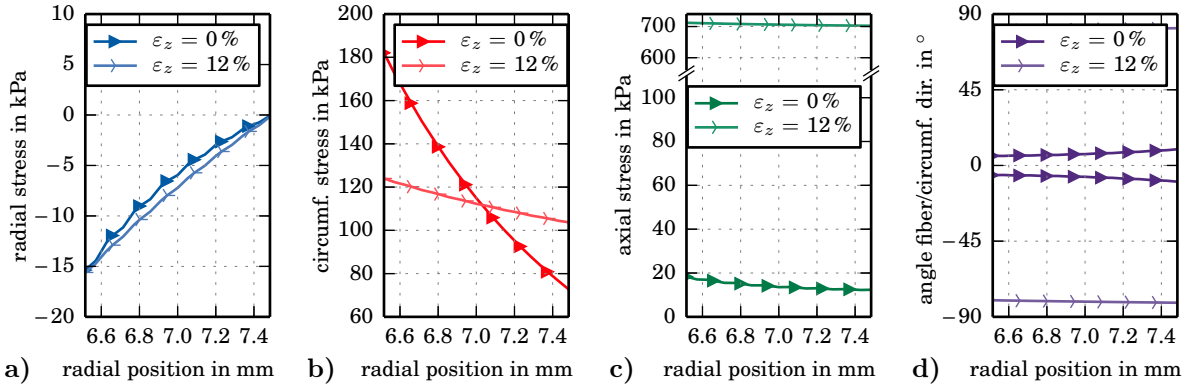

Figure 7.17: Distribution of **a)** radial stresses, **b)** circumferential stresses, **c)** axial stresses and **d)** fiber angles over the wall thickness after convergence of remodeling at $t = 7\,\mathrm{s}$.

The analysis of one single Gauß point cannot shed light on the distributions of stresses and fiber angles over the entire wall thickness. For that reason, those distributions are given separately for $t = 1\,\mathrm{s}$ and $t = 7\,\mathrm{s}$ in Fig. 7.16 and Fig. 7.17, respectively. Since no differences related to the choice of the time increment are existent at these points in time, only the data obtained with $\Delta t = 0.5\,\mathrm{s}$ is given. Note that the raw Gauß point values without any smoothing are plotted, which is the reason for the slight oscillations of the curves visible in some cases. Fig. 7.16 represents the initial state at full load before reorientation of the fibers. It is apparent that the level of axial strain mainly affects the axial, but not the circumferential or the radial stress. The latter is anyway forced to take the predefined values of $-16\,\mathrm{kPa}$ at the inner and $0\,\mathrm{kPa}$ at the outer surface of the vessel.

The diagrams in Fig. 7.17 confirm that the level of axial strain, which severely affects the principal stress state, is of particular importance for a stress-driven reorientation of the fibers. At low axial strains, a final fiber arrangement near the circumferential direction, a significant decrease of the axial stress and a slight reduction of the circumferential stress can be observed. At high axial strains, the fibers reorient towards the axial direction and a considerable reduction of peak and gradient of the circumferential stress is obtained, but the axial stress rises to a level far above the initial one. For a certain intermediate level of axial strain between $0\,\%$ and $12\,\%$, it might be possible that circumferential and axial stress both are affected beneficially. If the

reorientation of the fibers is combined with a stress-induced increase of the tissue volume by growth, the axial component of growth is another important factor since it reduces the effect of axial strain.

7.4.3 Growth and fiber reorientation in an idealized arterial segment

For the analysis of the effects of growth on the mechanical behavior of idealized arterial segments in response to an internal pressure and different levels of axial strain, three specifications of the general formulation, namely those which have been presented in Sec. 5.2, will be considered. Due to axisymmetry of the boundary value problem, the principal directions equate to the axes of the cylindrical coordinate system, i. e. the radial, circumferential and axial direction. The initial mapping between the principal directions and the growth orientation vectors is done based on the stress state in the non-adapting arterial segment, which is known from Fig. 7.16 in the previous example. This implies that the first multiplicative part of the growth tensor with $a = 1$ is associated to the circumferential direction, the second one with $a = 2$ to the axial direction and the third one with $a = 3$ to the radial direction. The three growth models, which now are referred to as "isotropic", "radial" and "anisotropic", can then be recapitulated as follows and as summarized in Tab. 7.3. The growth tensor for isotropic growth is not intended to include any directional information. It is thus not important, that just the first instead of the second or third multiplicative part is chosen to represent the isotropic volume change by setting it according to Eq. 5.1a. In order to obtain radial growth, growth in the direction of the third principal stress has to be allowed by defining the third part of the growth tensor as indicated in Eq. 5.1b. Isotropic as well as radial growth are assumed to be governed by the isotropic driving force function from Eq. 5.51. The third growth model is constructed based on the assumption that the (tensile) principal stresses in circumferential and axial direction can effectively be reduced by growth in the plane perpendicular to those directions, which is described by Eq. 5.1c. By use of Eq. 5.57, the stresses in circumferential and axial direction are supposed to be the respective driving forces. In addition, the driving force function from Eq. 5.60 is taken into account for the same, anisotropic growth tensor. This function is zero if the stress in the associated direction reaches negative values, which means that negative growth is excluded.

Table 7.3: Summary of the analyzed growth models. Non-tabulated multiplicative parts of the growth tensor equal the unit tensor.

growth model	a	$\boldsymbol{F}_{\mathrm{g}}^{(a)}$	$\phi^{(a)}(\boldsymbol{\Sigma}_{\mathrm{e}})$	$\vartheta_{(a)}^{+}$	$\vartheta_{(a)}^{-}$
isotropic	1	$\boldsymbol{F}_{\mathrm{g}}^{\square}$ (Eq. 5.1a)	Eq. 5.51	1.100	0.98
radial	3	$\boldsymbol{F}_{\mathrm{g}}^{\parallel}$ (Eq. 5.1b)	Eq. 5.51	1.331	0.98
anisotropic	1	$\boldsymbol{F}_{\mathrm{g}}^{\perp}$ (Eq. 5.1c)	Eq. 5.57/5.60	1.100	0.98
	2	$\boldsymbol{F}_{\mathrm{g}}^{\perp}$ (Eq. 5.1c)	Eq. 5.57/5.60	1.049	0.98

In order to ensure a certain degree of comparability of the growth models, the upper limiting values $\vartheta_{(a)}^{+}$ of the growth factors are set such that the determinant of the growth tensor is limited to $\max[J_{\mathrm{g}}] = 1.331$. As a consequence of the quasi-incompressibility constraint imposed by Eq. 7.4, which enforces $J_{\mathrm{e}} \approx 1$, the volume increase of each arterial segment is thus restricted

to 33.1 %. Since negative values of the driving force are only expected as an exception for anisotropic growth driven by Eq. 5.57, the lower limiting values $\vartheta^{-}_{(a)}$ are less relevant. By setting them uniformly to 0.98, a decrease of the volume to a minor degree is theoretically enabled. All remaining parameters are set as described in Sec. 7.2, where the boundary value problem of the idealized arterial segment is introduced. A first set of simulations is performed in 1D and for four different levels of axial strain: 0 %, 5 %, 10 % and 15 %. For a first comparison of isotropic, radial and the two variants of anisotropic growth under the effect of axial strain, the temporal development of axial and circumferential stress as well as fiber angles and determinant of the growth tensor at the innermost Gauß point near the arterial lumen is illustrated in Fig. 7.18 to Fig. 7.21 for each of the four model variants. The initial values at $t = 1\,\mathrm{s}$ represent the reference state of fully loaded, non-adapting arterial segments before onset of growth and remodeling. The simulation time required to reach the steady state is in parts strongly dependent on the level of axial strain. In order to obtain meaningful diagrams, the time axis is therefore scaled logarithmically. This makes it possible to focus on the first few seconds, where the major changes occur, and still to show a large range of time.

Isotropic growth. As obvious from Fig. 7.18 a) and Fig. 7.19 a), the initial effect of isotropic growth is a significant percentage drop of both the circumferential and the axial stress. The subsequent behavior depends on the level of axial strain: if no axial strain is applied, both stresses continue to decrease, but in case of $\varepsilon_z = 15\,\%$, both stresses rise again and even reach maximal values above the initial ones before they converge to their final values. For axial strains in between, there is a transition from one behavior to the other. In general, it can be observed that the final values of circumferential and axial stress decrease with the level of axial strain. For axial strains above 10 %, the final value of the circumferential stress might thereby be higher than in non-growing arteries. Due to the axial component of growth, which compensates the axial strain, the axial stress is reduced to such an extent, that even compressive values can finally be obtained. This is especially observed for low levels of the axial strain below about 5 %. In these cases, only one tensile principal stress is left, which gives rise to a reorientation of both fiber families to the circumferential direction, see Fig. 7.20 a). With increasing level of the axial strain, the fiber angles with respect to the circumferential direction increase, but they converge to values below the initial $\pm 30°$ in each of the considered examples. The final amount of growth, measured in terms of the determinant of the growth tensor, seems to correlate with the height of the axial strain. As shown in Fig. 7.21 a), the determinant of the growth tensor converges monotonically towards the upper limit of 1.331, which is however not reached before the steady state is attained. It should be remarked here that it is only due to the logarithmic scale of the time axis that the curves seem to end with a slope far from zero.

Radial growth. Compared to the other investigated forms of growth, the effects occurring in arterial segments which grow exclusively in radial direction are completely different. As noticeable in Fig. 7.18 b), the circumferential stress decreases nearly monotonically to very low values, and even ends up close to zero in the case of 15 % of axial strain. A direct correlation between the final value of the circumferential stress and the level of axial strain can however not be observed.
If a certain level of axial strain is exceeded, the strong reduction of the circumferential stress is linked to a pronounced increase of the axial stress, see Fig. 7.19 b). Only for low axial strains of 0 % or 5 %, the axial stress converges towards values which are lower than the initial ones.

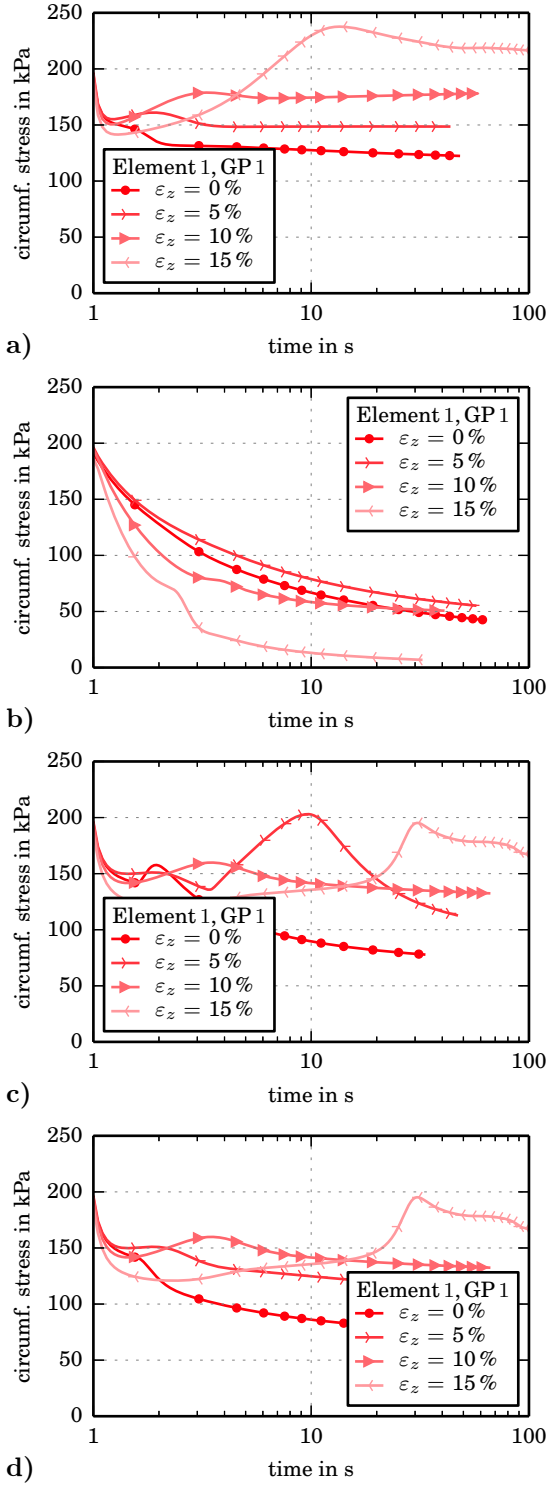

Figure 7.18: Temporal development of the circumferential stress at the innermost Gauß point of a 1D arterial segment with different levels of axial strain for **a)** isotropic growth, **b)** radial growth, **c)** anisotropic growth and **d)** anisotropic growth restricted to positive driving forces. The two fiber families are allowed to reorient.

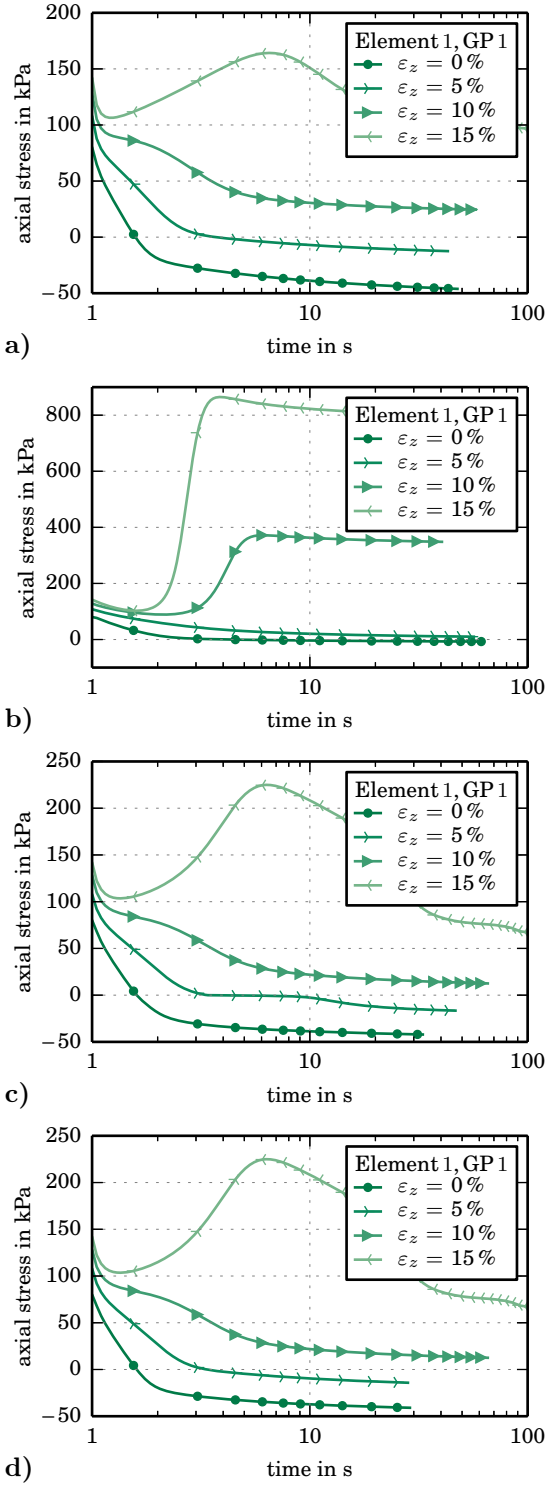

Figure 7.19: Temporal development of the axial stress at the innermost Gauß point of a 1D arterial segment with different levels of axial strain for **a)** isotropic growth, **b)** radial growth, **c)** anisotropic growth and **d)** anisotropic growth restricted to positive driving forces. The two fiber families are allowed to reorient.

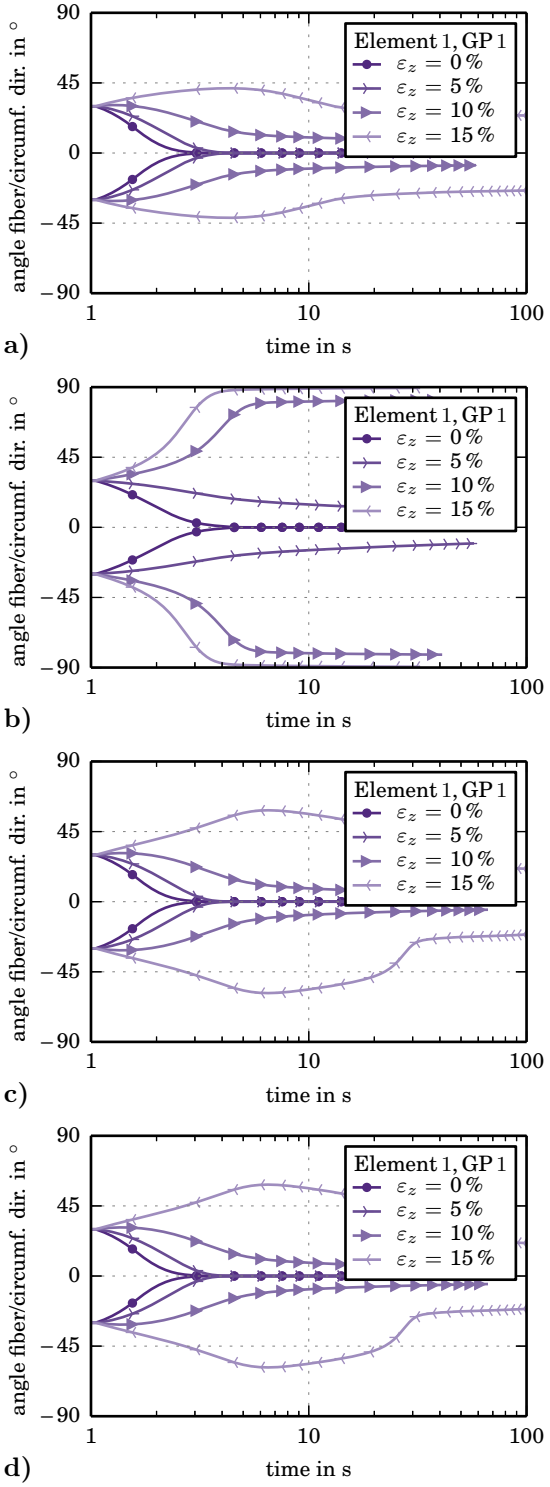

Figure 7.20: Temporal development of the fiber angles at the innermost Gauß point of a 1D arterial segment with different levels of axial strain for **a)** isotropic growth, **b)** radial growth, **c)** anisotropic growth and **d)** anisotropic growth restricted to positive driving forces.

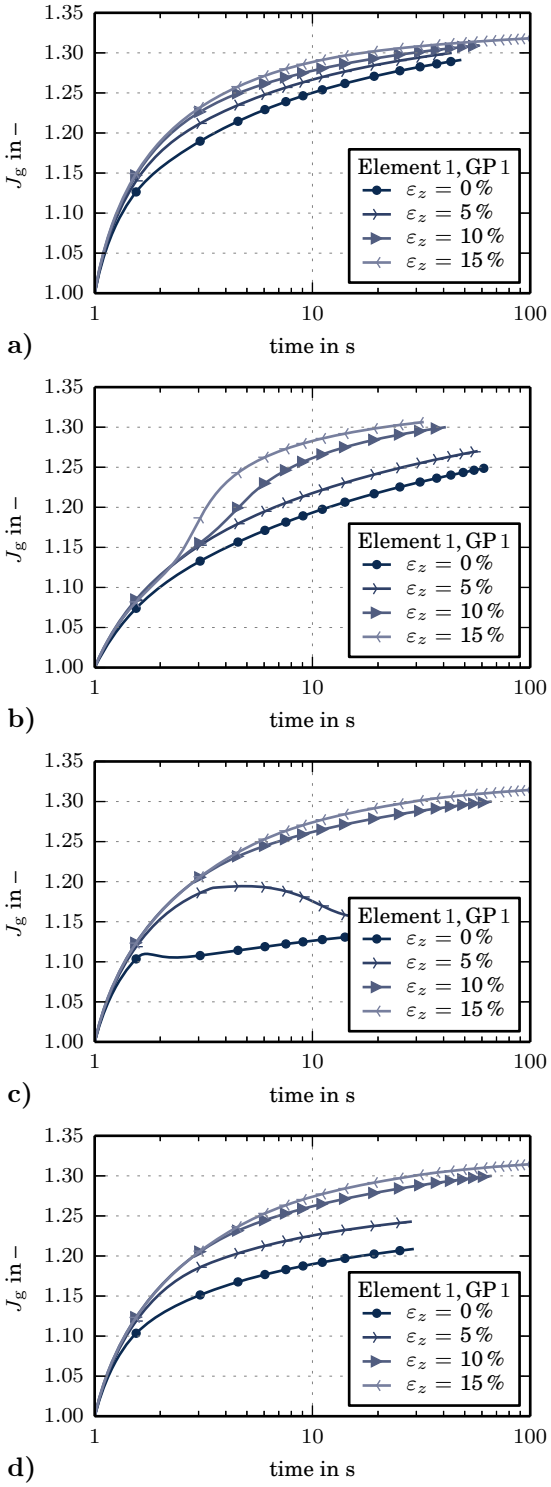

Figure 7.21: Temporal development of the determinant of the growth tensor at the innermost Gauß point of a 1D arterial segment with different levels of axial strain for **a)** isotropic growth, **b)** radial growth, **c)** anisotropic growth and **d)** anisotropic growth restricted to positive driving forces.

The enormous increase for higher values of the axial strain can be explained by the absence of growth in axial direction. As already observed in Sec. 7.4.2 for a non-growing artery, the fibers start to reorient towards the axial direction as soon as the axial stress is higher than the circumferential stress. The combination of low circumferential stresses and high axial strains, which are not compensated by growth, leads directly to this effect: according to Fig. 7.20 b), the fiber angles pass the value of $\pm 45°$ at $t \approx 2\,\mathrm{s}$ and $t \approx 3\,\mathrm{s}$ for axial strains of 15 % and 10 %, respectively. Beginning from then, the strong increase of the axial stress starts to develop. To summarize, two basic scenarios can be expected in the context of radial growth: If the axial strain is low, the fibers end up in a position around the circumferential direction and the circumferential and axial stresses decrease significantly. If the axial strain is higher than a certain value, the fibers reorient towards the axial direction and the axial stress increases to undesirably high values. This increase is even observable in the development of the growth-induced volume increase over time, which is given in Fig. 7.21 b). The sudden increase of the driving force is followed by an intensification of growth.

Anisotropic growth. The effect of anisotropic growth on the stresses is qualitatively comparable to what has been observed for isotropic growth. The final values of the circumferential and axial stresses, indicated by the end points of the curves in Fig. 7.18 c) and d) and Fig. 7.19 c) and d), are lower than the initial ones and decrease with the level of axial strain. As for isotropic growth, the axial stress gets compressive for axial strains below about 5 %. Only in these cases, differences caused by the two different driving force functions can be expected, but the effect on the final stress values seems to be negligible here. The absolute values of the circumferential stress in the steady state are lower than observed for isotropic growth, which could indicate that anisotropic growth is more effective regarding its normalizing effect on stress peaks occurring near the arterial lumen. Nevertheless, it may obviously happen that high values of circumferential and axial stress are reached in the meantime, since the path to the final state is not at all monotonic. This might be a result of the many nonlinearities which are involved: on the one hand, the material law itself is nonlinear, and on the other hand, there are additional nonlinear effects on the material behavior due to reorientation of the fibers and anisotropic changes of the volume. The temporally high values of the axial stress in case of $\varepsilon_z = 15\,\%$ can be supposed to be related to the elevated values of the fiber angles in the period between $t \approx 3\,\mathrm{s}$ and $t \approx 30\,\mathrm{s}$, see Fig. 7.20 c) and d).
A major difference between use of Eq. 5.57 or Eq. 5.60 as driving force can only be stated with regard to the volume increase caused by growth. As obvious from Fig. 7.21 c), a highly decelerated increase or even a decrease of the determinant of the growth tensor is possible if negative values of the driving force – here the axial stress – are permitted. This effect is caused by a decrease of the growth factor associated to the axial direction, which leads to negative growth in the circumferential-radial plane. If only positive values of the driving force are allowed, see Fig. 7.21 d), the increase of the volume is decelerated, but not regressive. As soon as the axial stress gets compressive, the corresponding growth factor remains constant, whereas the other one, which is associated to the circumferential direction, continues to increase. Whenever compressive axial stresses are involved in the context of anisotropic growth with directional driving forces, the final volume increase is far beyond the upper limit of 33.1 %.

With the exception of isotropic and in particular radial growth at higher axial strains, a reduction of both the circumferential and the axial stress peak near the internal surface of the artery can be achieved in each of the considered examples. The lower the level of axial strain, the lower

are the stresses in the steady state of completed growth and fiber reorientation. Arteries are however known to hold positive residual stresses in axial direction, which makes them contract when they are resected from the body. Growth mechanisms which lead to an excessive reduction of the axial stress or even a switchover to compressive values can therefore not be assumed to reflect the real behavior. Nevertheless, the above observations show that for each of the analyzed growth mechanisms, there is a particular value of the axial strain which is suitable to produce results that are qualitatively in line with the residual stress state and the fiber arrangement in real arteries. For example, isotropic growth with an axial strain of 8 %, radial growth with an axial strain of 5 % and anisotropic growth with an axial strain of 12 % are expected to result in an optimized state with reduced values of the circumferential stress but non-negative values of the axial stress and a fiber arrangement around the circumferential direction. For these three particular situations, the steady state at the end of the adaptation process will be investigated more in detail. To this end, the distribution of the stresses over the wall thickness is illustrated in Fig. 7.22 for the three mentioned growth mechanisms, again with consideration of the two different driving forces for anisotropic growth. In addition, the results for growth alone, that is with constant fiber angles of $\pm 30°$, and for a non-adapting reference artery are depicted. Since the axial strain is chosen such that the final axial stress is positive, it can be expected that both versions of anisotropic growth throughout lead to the same results. For that reason, no distinction will be made between both models in the following comments.

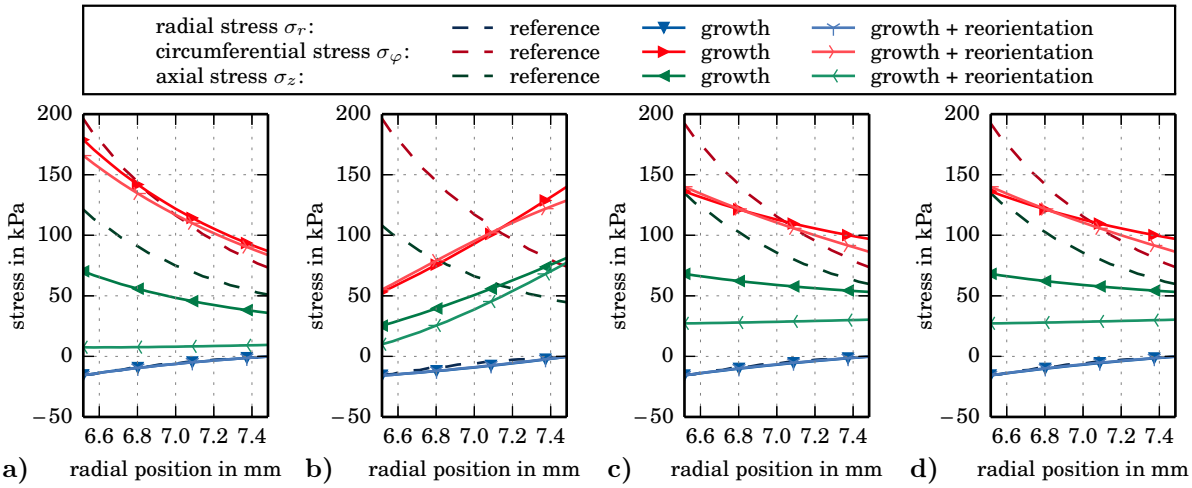

Figure 7.22: Distribution of radial, circumferential and axial stress at the end of the adaptation process for **a)** isotropic growth with $\varepsilon_z = 8\,\%$, **b)** radial growth with $\varepsilon_z = 5\,\%$, **c)** anisotropic growth with $\varepsilon_z = 12\,\%$ and **d)** anisotropic growth restricted to positive driving forces with $\varepsilon_z = 12\,\%$. Apart from the results for combined growth and fiber reorientation, the results for growth alone and for non-adapting reference arteries are given.

Examining first the circumferential stress, it can be stated that a reduction of the peak near the arterial lumen is always linked to an increase of the stress in the outer part of the wall, which means that primarily the gradient of the circumferential stress is reduced by growth. In the case of radial growth, see Fig. 7.22 b), the gradient is even reversed. This relativizes the fact that very low values of the circumferential stress have been observed at the innermost Gauß point in Fig. 7.18 b). Starting from angles of $\pm 30°$, a reorientation of the fibers has only minor effects on the distribution of the circumferential stress, but on average leads to lower mean values. In

contrast to that, the reorientation of the fibers is accompanied by a strong reduction of the axial stress, especially in combination with isotropic or anisotropic growth. Growth alone already leads to a reduction of the mean value and the gradient of the axial stress. This effect seems to be intensified by remodeling, such that the final distributions of the axial stress are nearly constant over the wall thickness. Again, radial growth is an exception, where an inversion of the stress gradient occurs, whether remodeling is taken into account or not. As suspected earlier, the radial stress is hardly affected by growth or remodeling. Forced to take the boundary values $\sigma_{\mathrm{r}} = -p$ at the inner and $\sigma_{\mathrm{r}} = 0$ at the outer surface, there is little scope for adjustments in between.

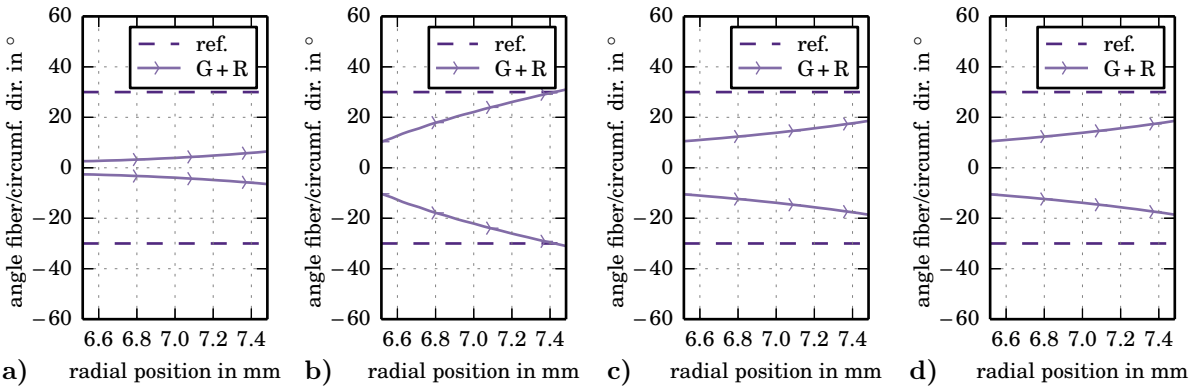

Figure 7.23: Distribution of the fiber angles at the end of the adaptation process for **a)** isotropic growth with $\varepsilon_z = 8\,\%$, **b)** radial growth with $\varepsilon_z = 5\,\%$, **c)** anisotropic growth with $\varepsilon_z = 12\,\%$ and **d)** anisotropic growth restricted to positive driving forces with $\varepsilon_z = 12\,\%$. Apart from the results for combined growth and fiber reorientation, the fiber angles of the non-adapting reference arteries are given.

Due to the specific choice of convenient levels of axial strain for each of the growth models, the final distribution of the fiber angles over the radial position can be expected to be qualitatively reasonable in each of the considered scenarios, which means that the fibers in the media should more or less be distributed around the circumferential direction. Indeed, Fig. 7.23 confirms that fiber angles below $\pm 30°$ are obtained throughout. In each simulation, they take their minimal values at the internal surface of the vessel and increase towards the outside. Since the fiber angles are dictated by the ratio of the first to the second principal stress, which here correspond to the circumferential and the axial stress, this result is not astonishing and could have been anticipated from the distributions of the stresses shown in Fig. 7.22.

In Fig. 7.24, the distribution of the determinant of the growth tensor at the end of the adaptation process, with and without reorientation of the fibers, is depicted. First, it can be stated that the effect of remodeling on the growth-induced volume change is nonsignificant in the considered examples. Only in the case of anisotropic growth, a minor difference is visible at all. The evaluation of the results at the innermost Gauß point in Fig. 7.21 has already shown that values of about 1.3 could have been expected in the inner part of the wall. Interestingly, the volume increase is even almost constant over the entire wall thickness. In consideration of the fact that higher stresses occur in the inner part of the wall, a decrease of J_{g} towards the outside would have been plausible. In contrast to that, even an increase can be observed in the case of radial growth. In combination with the stress distribution in Fig. 7.22 b), this arouses suspicion that an over-optimization could have taken place: Assuming that growth somehow leads to a

kind of counterclockwise rotation of the stress distributions, a high amount of growth might be counterproductive for the reduction of stress peaks and gradients.

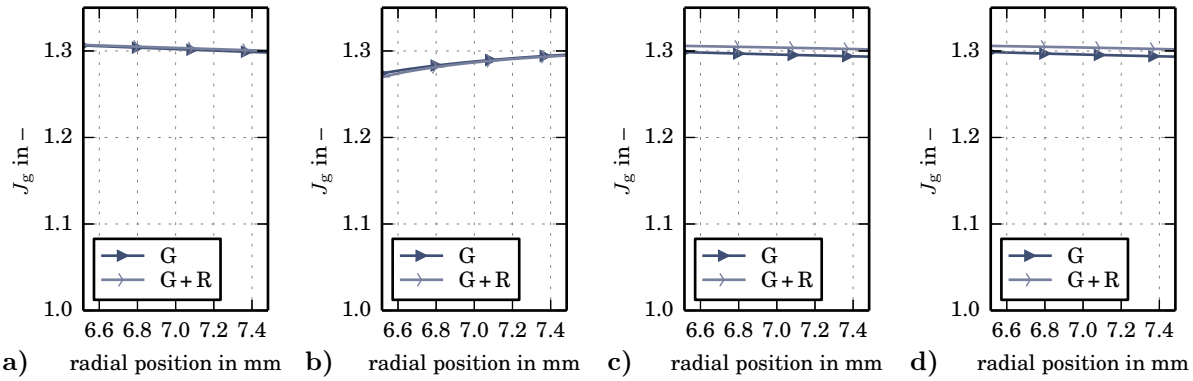

Figure 7.24: Distribution of the determinant of the growth tensor at the end of the adaptation process for **a)** isotropic growth with $\varepsilon_z = 8\,\%$, **b)** radial growth with $\varepsilon_z = 5\,\%$, **c)** anisotropic growth with $\varepsilon_z = 12\,\%$ and **d)** anisotropic growth restricted to positive driving forces with $\varepsilon_z = 12\,\%$. Apart from the results for combined growth and fiber reorientation, the results for growth alone are given.

Effect of the limiting values of the growth factors. In order to get an impression on the significance of the growth parameters $\vartheta^{+}_{(a)}$, the last-mentioned simulations are repeated for two additional parameter sets, where the determinant of the growth tensor is now restricted to 1.141 and 1.242 instead of 1.331. Details on the parameters for each of the three cases are listed in Tab. 7.4.

Table 7.4: Growth parameters $\vartheta^{+}_{(a)}$ of the models from Tab. 7.3 for different upper limits of the growth-induced volume change.

growth model	a	$\max[J_g] = 1.141$	$\max[J_g] = 1.242$	$\max[J_g] = 1.331$
isotropic	1	1.045	1.075	1.100
radial	3	1.141	1.242	1.331
anisotropic	1	1.045	1.075	1.100
	2	1.022	1.037	1.049

The effect of the maximal amount of growth on the final stress distributions is illustrated in Fig. 7.25 and the associated fiber angles are given in Fig. 7.26. As expected, the impact is notable. If growth in axial direction is involved, as for isotropic and anisotropic growth, higher amounts of growth lead to a strong decrease of gradient and average value of the axial stress. However, especially for elevated levels of the axial strain, a certain minimal amount of growth is necessary to avoid a reorientation of the fibers towards the axial direction, which is accompanied by a strong increase of the axial stress. For that reason, the upper limit of $\max[J_g] = 1.141$ is not high enough for anisotropic growth with $\varepsilon_z = 12\,\%$, see Fig. 7.25 c) and Fig. 7.26 c). For the circumferential stress, a reduction of the gradient with increasing amount of growth can in general be observed. In the considered examples of isotropic and anisotropic growth, the stress peak thereby remains at the inner surface of the artery and might even be slightly higher than in the non-growing reference artery, see Fig. 7.25 a).

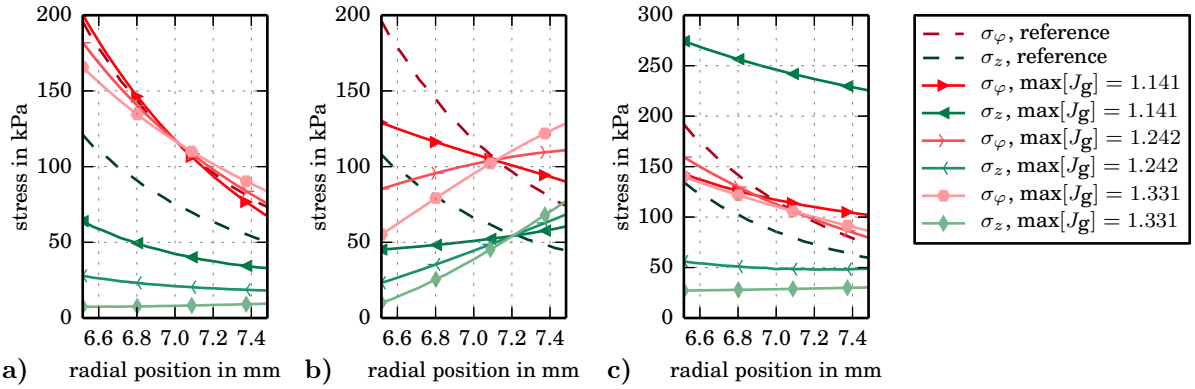

Figure 7.25: Distribution of the circumferential and axial stresses at the end of adaptation processes with different upper limits of the growth-induced volume change for **a)** isotropic growth with $\varepsilon_z = 8\,\%$, **b)** radial growth with $\varepsilon_z = 5\,\%$ and **c)** anisotropic growth with $\varepsilon_z = 12\,\%$. Apart from the results for combined growth and fiber reorientation, the stresses in non-adapting reference arteries are given.

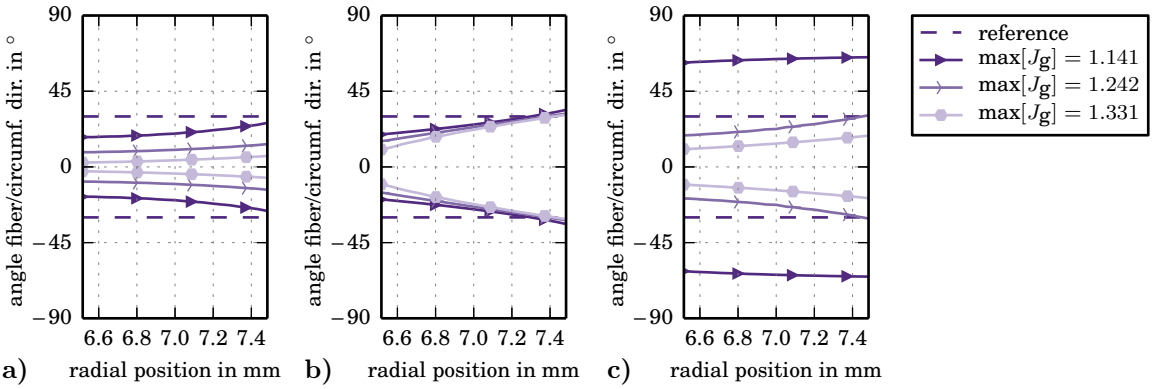

Figure 7.26: Distribution of the fiber angles at the end adaptation processes with different upper limits of the growth-induced volume change for **a)** isotropic growth with $\varepsilon_z = 8\,\%$, **b)** radial growth with $\varepsilon_z = 5\,\%$ and **c)** anisotropic growth with $\varepsilon_z = 12\,\%$. Apart from the results for combined growth and fiber reorientation, the fiber angles of non-adapting reference arteries are given.

Radial growth again has to be regarded as a special case with different basic behavior since no growth in axial direction is involved. As shown in Fig. 7.25 b), an increase of the amount of growth seems to be associated to a rotation of the distributions of the circumferential and axial stresses around an unchanging point on the reference curve. If the amount of growth is too high, the stress peaks switch from the inner to the outer surface of the wall, which leads to increasing stress gradients as soon as the most advantageous amount of growth is exceeded.

The latter analysis confirms that in the course of further investigations of different growth mechanisms, it is essential to pay more attention to the definition of the growth parameters $\vartheta^+_{(a)}$, which besides the loading situation are supposed to be among the key drivers deciding on the model performance. The above results should thus not be overrated, but only leave a first impression on the basic effects of growth and fiber reorientation. It can be summarized that in principle, each of the considered forms of growth can lead to a reduction of stress peaks

and gradients and to a qualitatively realistic distribution of the fiber angles. However, the performance of each mechanism is strongly dependent on the level of axial strain, or rather on the ratio of axial strain and internal pressure. This ratio controls the principal stress state and thus essentially affects the growth and remodeling behavior in the chosen stress-driven framework. Since arteries are able to adapt to different loading situations, an effective growth mechanism should have the capability to produce good results for a certain range of axial strains and not only for one specific value. Due to the necessity to consider different load cases, the large number of possible model variants and the question on how to set the growth parameters, search for the most promising growth mechanism within the given framework is a complex task. In order to enable a well-founded validation of each mechanism, a method for the equitable comparison of various model variants is proposed in the following section. It is based on the formulation of an objective function and the optimization of model parameters.

7.5 Optimization-based comparison of different growth mechanisms

For the evaluation of the large number of possible combinations of growth tensors and driving forces within the generalized formulation for anisotropic growth, the definition of an unambiguous, scalar comparative value would be helpful. This value should be able to adequately represent the potential of each model variant to meet certain targets which are assumed to be relevant for a realistic growth mechanism, for example the reduction of stress peaks and gradients. Of course, such a value depends on the chosen load case and on the parameters of the growth model. It can thus be used for an assessment of the behavior in different loading situations and also serves as an indicative value for optimal growth parameters.
In the context of computational optimization, the quantity which establishes comparability of model realizations is referred to as objective function. In the following sections, an objective function for the assessment of different growth mechanisms with respect to their mechano-biological plausibility is defined, and its use within three different optimization scenarios is described. The proposed method is applied to idealized one- and two-layered arterial segments, which allow for an efficient 1D finite element discretization, and the results are evaluated. The steps towards the present form of the method and intermediate results are documented in a series of conference proceedings (Zahn & Balzani, 2018b, 2019b, 2019a).

7.5.1 Formulation of the objective function

In order to represent the assumed aim of arterial growth and remodeling to reduce stress peaks and inhomogeneities within the arterial layers, an objective function with the general structure

$$f_{\mathrm{obj}} = \sum_{j=1}^{n_{\mathrm{layer}}} \sum_{i} \omega_{ji}\, q_{ji} \tag{7.14}$$

is defined, where the coefficients ω_{ji} are weighting factors that allow to adjust the impact of the individual arguments q_{ji} on the overall value of the function. Each of the arguments q_{ji}, computed separately for each layer j, represents a mechano-biological quantity which is claimed

to reach low values in a steady state of terminated growth and fiber reorientation. Precisely, those quantities are defined by the expressions

$$
\begin{aligned}
q_{j1} &= \frac{\max\limits_{r} |\sigma_\varphi|}{\tilde{\sigma}_{\text{peak}}}, & q_{j4} &= \frac{\max\limits_{r} |\sigma_\varphi| - \left|\operatorname{mean}\limits_{r} \sigma_\varphi\right|}{\tilde{\sigma}_{\text{diff}}}, \\
q_{j2} &= \frac{\max\limits_{r} |\sigma_z|}{\tilde{\sigma}_{\text{peak}}}, & q_{j5} &= \frac{\max\limits_{r} |\sigma_z| - \left|\operatorname{mean}\limits_{r} \sigma_z\right|}{\tilde{\sigma}_{\text{diff}}}, \\
q_{j3} &= \frac{\operatorname{mean}\limits_{r} |\sigma_\varphi - \sigma_z|}{\left|\operatorname{mean}\limits_{r} \sigma_\varphi\right|}, & q_{j6} &= \left|\operatorname{mean}\limits_{r} J_{\text{g}} - 1\right|
\end{aligned}
\tag{7.15}
$$

with $r \in [r_{j,\text{i}}, r_{j,\text{o}}]$, where $\tilde{\sigma}_{\text{peak}}$ and $\tilde{\sigma}_{\text{diff}}$ are introduced as normalizing values for stress peaks and differences. The operators "max" and "mean" are used to denote the maximal value and the volume average of a quantity over the radial direction r, and have to be evaluated layer-wise between the inner and outer radii $r_{j,\text{i}}$ and $r_{j,\text{o}}$ for each of the considered layers, i. e. for $j \in [1, n_{\text{layer}}]$. Each of the individual expressions in Eq. 7.15 is normalized such that a set of dimensionless quantities of the same order of magnitude and with theoretical optimal values of zero is obtained. The definition of the expressions is motivated mechano-biologically as summarized below and relies on the observations described in Sec. 2.2 and Sec. 2.3.

q_{j1}/q_{j2}: A reduction of the circumferential stress peak in each layer towards a reference level $\tilde{\sigma}_{\text{peak}}$ or less might be desired in order to increase the general resilience of the tissue. The same might hold for the peak of the axial stress. Taking into account that compressive stresses might occur, the absolute values of both stresses are considered.

q_{j3}: A reduction of the axial stress peak to zero by means of growth in axial direction is in principle possible, but it conflicts with the natural in vivo state of healthy arteries, which is characterized by axial tension. A layer-wise reduction of the average difference between the circumferential and the axial stress might therefore be a more realistic goal of arterial adaptation.

q_{j4}/q_{j5}: The material properties of the individual arterial layers and their resistance to mechanical load differ strongly, but within each layer, a uniform exposure can be assumed to be preferable. In order to obtain stress distributions that are layer-wise constant as far as possible, the maximal values per layer have to approach the corresponding mean values.

q_{j6}: From an energetic point of view, arterial tissues can be expected to avoid an unnecessarily high amount of growth, that is to keep the average growth-induced volume change as low as possible.

Finally, low values of the objective function in the steady state are associated to an efficient reduction of stress peaks, differences and gradients at low energetic cost. By minimization of the objective function for a particular model variant, the specific set of parameters leading to its best reachable mechano-biological behavior is obtained. Based thereon, a fair comparison of model variants is enabled. Since the performance of different growth mechanisms is known to be strongly dependent on the loading situation, different optimization scenarios are considered.

7.5.2 Optimization scenarios

In the previous numerical examples on combined growth and fiber reorientation, the possible effect of changes in the time scale ratio in terms of an adaptation of the velocity parameters has been disregarded. Since growth and fiber reorientation interact due to their impact on the stress state on both sides, such an effect can be assumed to exist and to be significant. Nevertheless, it will be left out of consideration here in order to keep the number of optimization variables low. Then, the limiting values of the growth factors are the only among the growth and remodeling parameters which substantially affect the mechano-biological fields in the steady state. In the relevant boundary value problem, the occurrence of growth factors below 1.0, which indicate negative growth compared to the reference configuration, can almost be excluded. Single cases in which this might occur are associated with negative axial stresses, which are estimated as unrealistic. For this reason, the parameter optimization is restricted to the upper limiting values $\vartheta^{+}_{(a)}$ of the growth factors, and the lower limits are consistently set to $\vartheta^{-}_{(a)} = 0.95$. The important impact of the level of axial strain is taken into account by considering the following optimization scenarios:

Mode O 1: Optimization of the growth parameters $\vartheta^{+}_{(a)}$ for a fixed level of axial strain in order to find the best performance for a given loading situation.

Mode O 2: Optimization of the growth parameters $\vartheta^{+}_{(a)}$ and the level of axial strain ε_z in order to find the best possible performance within the range of possible loads.

Mode O 3: Optimization of the growth parameters $\vartheta^{+}_{(a)}$ by averaging over different levels of axial strain in order to find the best mean performance over a range of possible loading situations.

By comparison of the results, the sensitivity of a growth mechanism with respect to the level of axial strain can be detected. For a non-sensitive mechanism, the values of the objective function obtained with mode O 1 for different levels of axial strain should only slightly differ. In ideal circumstances, the optimal values of the growth parameters should even remain unchanged. If the difference between the values of the objective function obtained with modes O 2 and O 3 is small, a good performance over a range of axial strains without adaptation of the growth parameters can be expected.

Basic conditions for the optimization. If the level of axial strain is not considered as optimization variable, it is fixed to a constant value among 0 %, 5 %, 10 %, 15 % or 20 %. In mode O 3, the value of the objective function is averaged over axial strains of 0 %, 5 %, 10 % and 15 % since higher values are assumed to be exceptionally high. By setting the bounds of the optimization variables to

$$\vartheta^{+}_{(a)} \in [1.0001, 1.5] \qquad \text{and} \qquad \varepsilon_z \in [0\,\%, 30\,\%], \tag{7.16}$$

it is presumed that neither growth factors larger than 1.5 nor axial strains above 30 % lead to optimal results. The normalizing values $\tilde{\sigma}_{\text{peak}}$ and $\tilde{\sigma}_{\text{diff}}$ are defined according to

$$\tilde{\sigma}_{\text{peak}} = 100\,\text{kPa} \qquad \text{and} \qquad \tilde{\sigma}_{\text{diff}} = 50\,\text{kPa} \tag{7.17}$$

based on the estimation that these values are in the order of magnitude of average stress peaks and differences in the media of adapted arteries. Presuming that the optimization goals defined in Eq. 7.15 are equally important, the weighting factors are uniformly set to

$$\omega_{ji} = 1.0 \qquad \text{for} \qquad j \in [1, n_{\text{layer}}] \quad \text{and} \quad i \in [1, 6]. \tag{7.18}$$

For the optimization itself, the functionalities of the software MATLAB (MathWorks, 2014/2018) are used. The repeated evaluation of the objective function, which requires the solution of an entire boundary value problem in FEAP, is enabled via the interface MATFEAP by Bindel (2011), which allows to set FEAP parameters and start FEAP simulations from within MATLAB. Due to the nonlinearity of the objective function and the constraints on the optimization variables, the solver "fmincon" for constrained nonlinear minimization is chosen. Using it with its default interior-point algorithm, a sequence of approximate problems with equality constraints is solved instead of the original, inequality-constrained problem.
In order to as far as possible find the global minimum, the "GlobalSearch" algorithm of MATLAB is applied. In this context, several hundreds of trial points are analyzed with the aid of a score function, but the solver "fmincon" is run only locally. For each of the investigated model variants and each optimization mode, the "GlobalSearch" algorithm is run five times starting with different, random initial values of the optimization variables. The lowest of the five final values of the objective function is supposed to best possibly represent the global minimum.

In addition to the one-layered idealized arterial segment described in Sec. 7.2, a second rotationally symmetric boundary value problem will be taken into account for the optimization-based comparison of different growth model variants. Instead of only considering the media, a second layer representing the adventitia is added. With an unchanged inner radius of $r_{\text{i}} = 6.5\,\text{mm}$, a media of 0.8 mm thickness and a contiguous adventitia of 0.3 mm thickness, the two-layered artery has an outer radius of $r_{\text{o}} = 7.6\,\text{mm}$. The initial fiber angles in media and adventitia are set to $\pm\,30°$ and $\pm\,50°$, respectively, and the material parameters of both layers are defined as specified in Tab. 7.1. The growth mechanisms in both layers are supposed to be the same, but the limiting values of the growth factors are allowed to differ, such that the number of optimization variables increases compared to the one-layered segment.
Especially in the given context of parameter optimization, where the entire boundary value problem has to be solved for each evaluation of the objective function, use of a one-dimensional finite element for rotationally symmetric geometries significantly raises the efficiency, or rather is even necessary to enable such a computationally intensive analysis in the first place. For that reason, the simulations are performed in 1D by means of the special finite element introduced in Sec. 4.2.2. Based on the results from Sec. 7.3.1, the one-layered arterial segments are discretized into 7 quadratic finite elements in radial direction. For the two-layered arterial segments, a discretization into 5 elements in the media and 2 elements in the adventitia can be assumed to be appropriate, but the optimization is by mistake performed with 10 elements in the media and 4 elements in the adventitia.
Whenever MATLAB asks for the value of the objective function, the actual values of the optimization variables, i. e. $\vartheta^{+}_{(a)}$ and, for mode O 2, ε_z, are passed to FEAP and the following simulation is initialized:

1. Application of the internal pressure of 120 mmHg and the axial strain ε_z without activation of growth and fiber reorientation.

2. Simulation of growth and fiber reorientation at constant level of the loads until

a) a steady state is attained,

b) a maximal simulation time of 3000 s is over or

c) the simulation is aborted due to unsuitable parameters.

3. Evaluation of the objective function. If no steady state has been attained, an exceptionally high value of $f_{\mathrm{obj}} = 100$ is assumed in order to penalize the improper choice of parameters or the bad performance of the model variant.

The improvements of the mechano-biological state in adapting compared to non-adapting arteries can be assessed by a comparison of the values taken by the objective function in both cases. Evaluating the objective function for the non-adapting arterial segments, the reference values given in Tab. 7.5 are obtained.

Table 7.5: Reference values $f_{\mathrm{obj,ref}}$ of the objective function for non-adapting arterial segments loaded with an internal pressure of 120 mmHg and different levels of axial strain.

	0 %	2.5 %	5 %	7.5 %	10 %	12.5 %	15 %	17.5 %	20 %
one-layered	5.2233	5.5228	5.7375	5.8645	5.9039	5.8576	5.7296	5.5248	5.2509
two-layered	6.2036	6.2369	6.2500	6.7034	7.0324	7.1994	7.2123	7.1163	6.9595

The informative value of these numbers alone is limited, since the absolute value of the objective function does not have a direct physical meaning and is not normalized with respect to the number of included layers. The higher numbers obtained for the two-layered segment are thus not caused by higher stresses, but merely by a higher number of summands in Eq. 7.14. For a clear statement, values of the objective function for the same considered arterial segment, but for different adaptation mechanisms have to be set into relation to each other.

7.5.3 Evaluation of the results

The relative performance of a growth mechanism is rated by means of a performance measure P, which establishes a relation between the mechano-biological states in adapting and non-adapting arteries. It makes use of the reference values of the objective function from Tab. 7.5 and is computed according to

$$P = -\frac{f_{\mathrm{obj}} - f_{\mathrm{obj,ref}}}{f_{\mathrm{obj,ref}}}. \tag{7.19}$$

For optimization mode O 1, where a fixed level of the axial strain is considered, the reference values for the particular level of axial strain are inserted. In the other cases, where the axial strain is an optimization variable (mode O 2) or where an averaging over different axial strains is performed (mode O 3), the reference value is averaged over axial strains of 0 %, 5 %, 10 % and 15 %. Positive values of the performance measure indicate that the considered growth mechanism leads to improvements of the mechano-biological state, negative values indicate a change for the worse.

Due to the high number of potential model variants, it is rather impossible to find a clear and brief nomenclature based on verbal description. For that reason, a system of symbolic abbreviations is introduced. It consists of up to three pairs of symbols for each approach, which

denote the types of growth tensor and driving force associated to the three principal directions as shown in the following example:

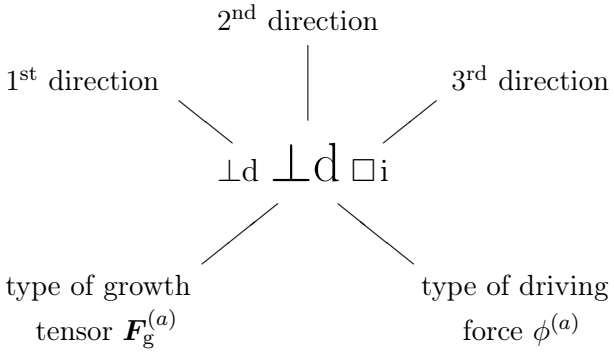

If only the first or the first and the second direction are included, leftover symbols on the right are omitted, but if only the third direction is considered, two pairs of zeros are put in front. To give an example, the three model variants described in Sec. 5.2 are referred to as □i (isotropic growth), 0 0 0 0 ∥ i (growth in the direction of the third principal stress with isotropic driving force) and ⊥d⊥d (growth perpendicular to the directions of the first and second principal stress with directional driving force). The meaning of the individual symbols is explained in Tab. 7.6.

Table 7.6: Symbols for the abbreviated designation of model variants.

symbol	type of growth tensor	$\boldsymbol{F}_{\mathrm{g}}^{(a)}$
0	no growth considered	$\boldsymbol{I}$
□	isotropic growth	Eq. 5.1a
∥	growth in the direction of $\boldsymbol{A}_{\mathrm{g}}^{(a)}$	Eq. 5.1b
⊥	growth perpendicular to $\boldsymbol{A}_{\mathrm{g}}^{(a)}$	Eq. 5.1c
symbol	**type of driving force**	$\phi^{(a)}$
0	none	–
i	isotropic	Eq. 5.51
d	directional	Eq. 5.57
t	directional with restriction to tensile values	Eq. 5.60

In the following set of figures, a selection of model variants applied to the one-layered arterial segment is evaluated by means of a graphical illustration of the performance measures obtained for the three optimization modes. Model variants, where only the first of the multiplicative parts of the growth tensor is taken into account, are considered in Fig. 7.27. The effect of the driving force on the performance seems to be minor, but there are marked differences related to the form of the growth tensor. For an explanation of these results, it is necessary to know that the direction which is considered for the definition of anisotropic forms of growth is here equal to the circumferential direction. Models with growth perpendicular to that direction perform better than isotropic forms of growth. In contrast to that, models where only growth in circumferential direction is allowed, lead in most cases to negative performance measures, which indicate a deterioration of the mechano-biological state compared to the non-growing

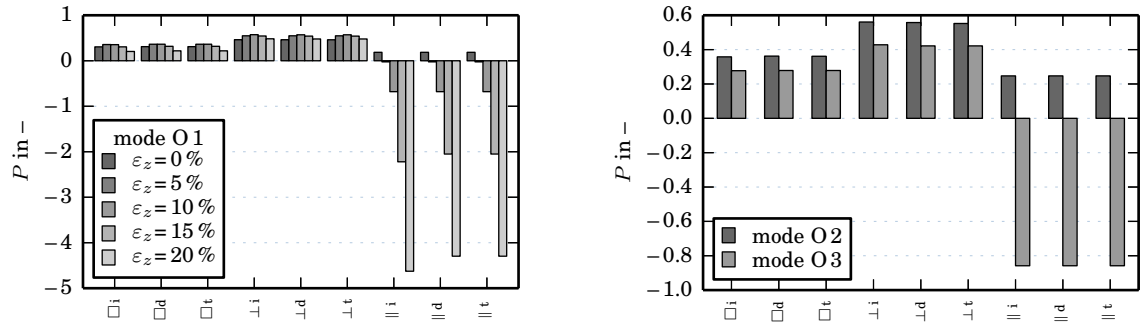

Figure 7.27: Performance measure P for model variants in one-layered arterial segments where only the first of the multiplicative parts of the growth tensor, which here is associated to the circumferential direction, is included.

reference artery. For these forms of growth, a strong dependency of the performance measure on the level of axial strain can be stated based on the data obtained in optimization mode O 1. As motivated in previous numerical examples, this can be attributed to the absence of axial growth, which provokes a nonnatural reorientation of the fibers towards the axial direction. Positive performance measures can then only be obtained in optimal loading situations with vanishing or very low values of axial strain.
The best possible performance reachable by each of the model variants within the given range of the optimization variables is identified in optimization mode O 2, where the optimal level of axial strain is determined. For isotropic forms of growth and growth in circumferential direction, this level is at about 0 %, for growth perpendicular to the circumferential direction, more realistic values between 8 % and 10 % are obtained. The exact values of the optimization variables and of the objective function for each of the performed optimizations are listed in Tab. B.1 in Appendix B.
The sensitivity of a growth mechanism with respect to the growth parameters and the level of axial strain can be estimated with the help of its performance measure for optimization mode O 3, which represents the average performance for axial strains from 0 % to 15 % with the same set of growth parameters. The shown values of P confirm that on average, growth perpendicular to the direction of the first principal stress is more favorable than isotropic growth and that missing growth is even better than growth in the direction of the first principal stress.

In Fig. 7.28, model variants with two multiplicative parts of the growth tensor, associated to the directions of the first and second principal stress, are considered. In cases with two tensile principal stresses, which can be assumed to be standard in arterial walls, there is no reason why the growth mechanisms related to those two directions should differ. Model variants with differing combinations of growth tensor and driving force for the two directions will thus not be analyzed. Again, isotropic growth, which is given as a reference in the first entry of the diagrams, is clearly outperformed by anisotropic forms of growth involving growth perpendicular to the principal directions. But also the growth mechanisms $\|\,\mathrm{d}\|\,\mathrm{d}$ and $\|\,\mathrm{t}\,\|\,\mathrm{t}$ with growth *in* the directions of the principal stresses might be promising, especially because of the small difference between the results for modes O 2 and O 3, which indicates a constant quality regardless of the level of axial strain.

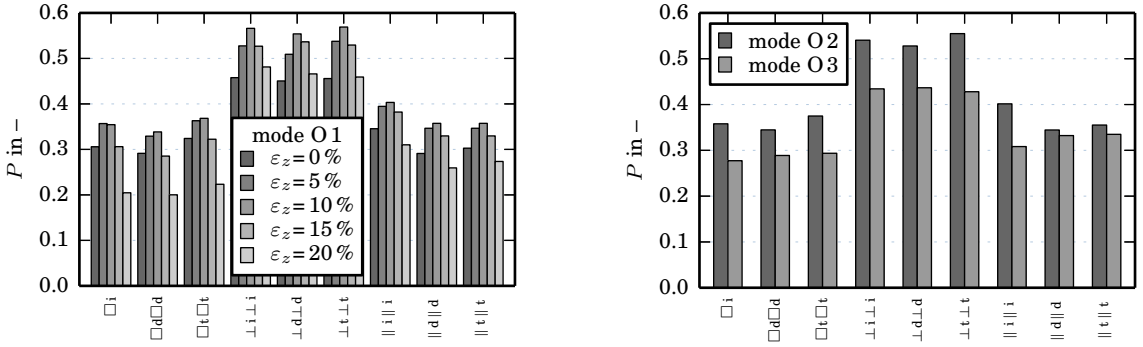

Figure 7.28: Performance measure P for model variants in one-layered arterial segments where the first and second of the multiplicative parts of the growth tensor, which here are associated to the circumferential and the axial direction, are included. The performance of isotropic growth, denoted by $\square\,\mathrm{i}$, is shown as a reference.

For the analysis of growth mechanisms including each of the three multiplicative parts of the growth tensor, some model variants with a differing mechanism in the third direction are included. Such an anisotropy could be motivated by the fact that the direction of the third principal stress, which in idealized arterial geometries equals the radial direction, differs fundamentally from the other two directions, which are aligned within the plane of the wall. It is dominated by compressive instead of tensile stresses and could thus be subjected to a differing adaptation mechanism. The performance measures of all model variants including three directions are illustrated in Fig. 7.29 a) and b), subdivided into models without and with differing mechanism in the third direction. The models considered in Fig. 7.29 a) in principle contain all the models considered previously in Fig. 7.27 and Fig. 7.28, which are obtained by accordingly setting the parameters $\vartheta^{+}_{(3)}$ and $\vartheta^{+}_{(2)}$ to their lower limit 1.0001. If the global minimum was really found, the analysis of models with less than three multiplicative parts of the growth tensor would be redundant. However, a comparison of the values of the objective function, see Tab. B.1, or of the performance measures indicates that in some cases, better results are obtained if the third direction is excluded from the beginning, which leads to the conclusion that the global minimum is not always detected. This can especially be observed for the model variants $\square\mathrm{d}\square\mathrm{d}\square\mathrm{d}$, $\perp\mathrm{d}\perp\mathrm{d}\perp\mathrm{d}$ and $\parallel\mathrm{d}\parallel\mathrm{d}\parallel\mathrm{d}$, which are mostly outperformed by their counterparts with less parts of the growth tensor. The opposite can only be stated for one specific growth mechanism, namely the model denoted by $\parallel\mathrm{i}\parallel\mathrm{i}\parallel\mathrm{i}$. Here, inclusion of the third direction leads to distinctly higher values of the performance measure.
As obvious from Fig. 7.29 b), a differing growth mechanism associated to the third direction can still improve the performance. The highest value of the performance measure in mode O 3, which represents the mean performance over a range of loading situations, is reached by growth model $\parallel\mathrm{d}\parallel\mathrm{d}\parallel\mathrm{i}$. The best possible performance of that model, obtained in mode O 2, is only slightly better, such that a low sensitivity with respect to the growth parameters and to the level of axial strain can be expected for that specific growth mechanism.

Although they are as well contained in the set of models with three parts of the growth tensor, models which only make use of the third part of the growth tensor are considered explicitly in Fig. 7.30. The poor performance of some of these models with negative performance measures could have been expected in advance. Use of the driving force function denoted by "d", which here is equivalent to the third principal stress, i. e. the compressive stress in radial direction,

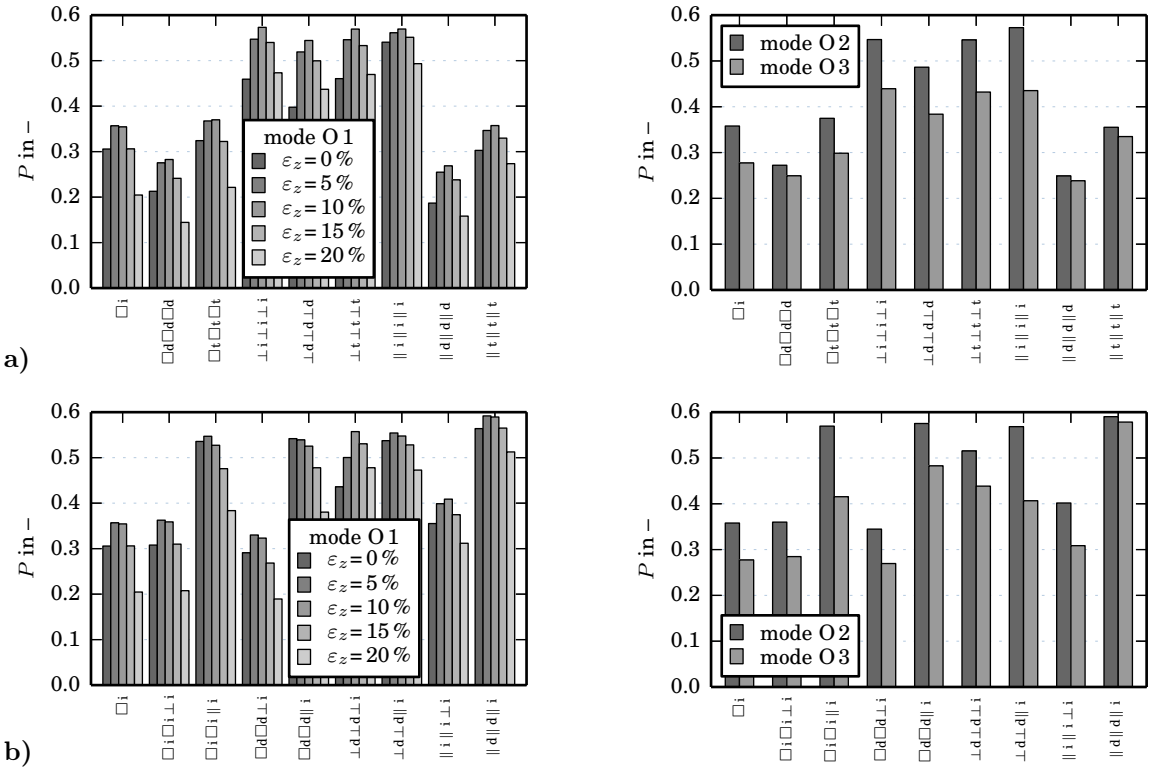

Figure 7.29: Performance measure P for model variants in one-layered arterial segments **a)** with the same growth mechanism in each of the three directions and **b)** with a differing growth mechanism in the third direction (which here is the radial direction). The performance of isotropic growth, denoted by $\square$i, is shown as a reference.

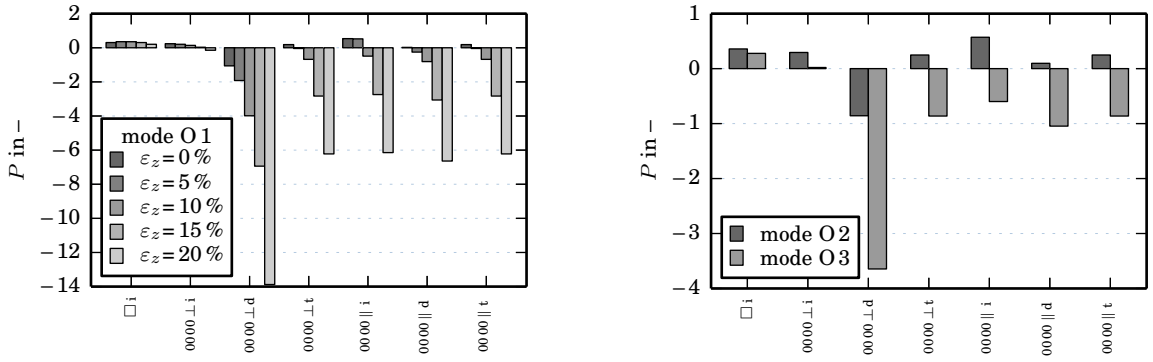

Figure 7.30: Performance measure P for model variants in one-layered arterial segments where only the third direction (which here is the radial direction) is included. The performance of isotropic growth, denoted by $\square$i, is shown as a reference.

leads to a decrease of the tissue volume, which can not be assumed to improve the mechanical behavior in the given loading situation. Similarly, use of driving force "t" equals a deactivation of growth since only tensile values of the third principal stress would have an effect. Nevertheless, the collagen fibers are still allowed to reorient, such that the objective function can take values that are higher than the reference values obtained for the non-adapting artery, which is followed by negative values of the performance measure. Based on earlier observations, the reason can be

assumed to be a strong increase of the axial stress due to a reorientation of the fibers towards the axial direction. Only one of the models, namely radial growth driven by the isotropic driving force, denoted by 0 0 0 0 ∥ i , can outperform isotropic growth, but only under ideal conditions in terms of low axial strains. The mean performance, represented by the performance measure of optimization mode O 3, is nonetheless very poor.

The comparison of a reduced number of model variants in the two-layered arterial segment on the basis of the performance measures for the three optimization modes is summarized in Fig. 7.31. Some of the models which performed bad in the one-layered artery or did not behave better than isotropic growth are not considered again. Although the performance of growth in the direction of the third principal stress is expected to be poor, this model variant is included to the analysis since it is equivalent to growth in the radial direction, which is often used to describe arterial wall thickening.
The results for the two-layered arterial segment essentially confirm what has been observed for the one-layered segment, but two details are worth mentioning: One the one hand, the performance of isotropic forms of growth is noticeably worse than in the one-layered segment. This supports the assumption that isotropy is not sufficient to adequately describe growth in boundary value problems with increasing complexity. On the other hand, except for model variant ⊥ i ⊥ i ⊥ i , the difference in the performance measures obtained in optimization modes O 2 and O 3 is clearly larger than observed for the one-layered segment. This might be attributable to the increased complexity of the objective function, which makes it more difficult to find the global minimum, especially in mode O 3, where an averaging over different levels of axial strain is performed. Due to the high impact of the axial strain on the stress distribution, this averaging in combination with a higher number of optimization variables can be assumed to significantly increase the nonlinearity of the optimization problem.

The results of the optimization-based comparison of different growth mechanisms can be summarized as follows: Apart from single exceptions, growth in general leads to an improvement of the mechanical behavior, which here is assessed based on the value of a mechano-biologically motivated objective function representing the ability of a growth mechanism to reduce stress peaks, gradients and differences at low energetic cost. A fair comparison is ensured by using optimized growth parameters, which have been determined on the basis of this function. The performance of most of the anisotropic models with either growth perpendicular to the directions of the principal stresses or growth in those directions is significantly better than the performance of isotropic growth, but the results do not allow a clear answer to the question, which of the anisotropic forms of growth might be most realistic. It can nevertheless be stated that among the analyzed models, growth mechanism ∥ d ∥ d ∥ i by far shows the best performance. This could be a hint that growth preferably occurs *in* the direction of the principal stresses. With respect to the driving force, the good performance suggests that growth in those directions is driven by the principal stresses as long as they are positive, but by an isotropic stress measure representing the mean stress state as soon as the principal stress gets compressive. However, this suspicion is only based on the numerical results above and should of course be examined in experiments before reliable conclusions on the growth mechanism in arterial walls can be drawn. Apart from the verification of the hypothesis that growth in arterial walls is likely to be anisotropic, it can be stated that purely radial growth can hardly be justified from a mechanical point of view. The performance of radial growth is strongly dependent on the level of axial strain and an improvement of the mechanical behavior compared to isotropic growth is only possible at axial strains below 5 % with specifically adjusted values of the growth parameters.

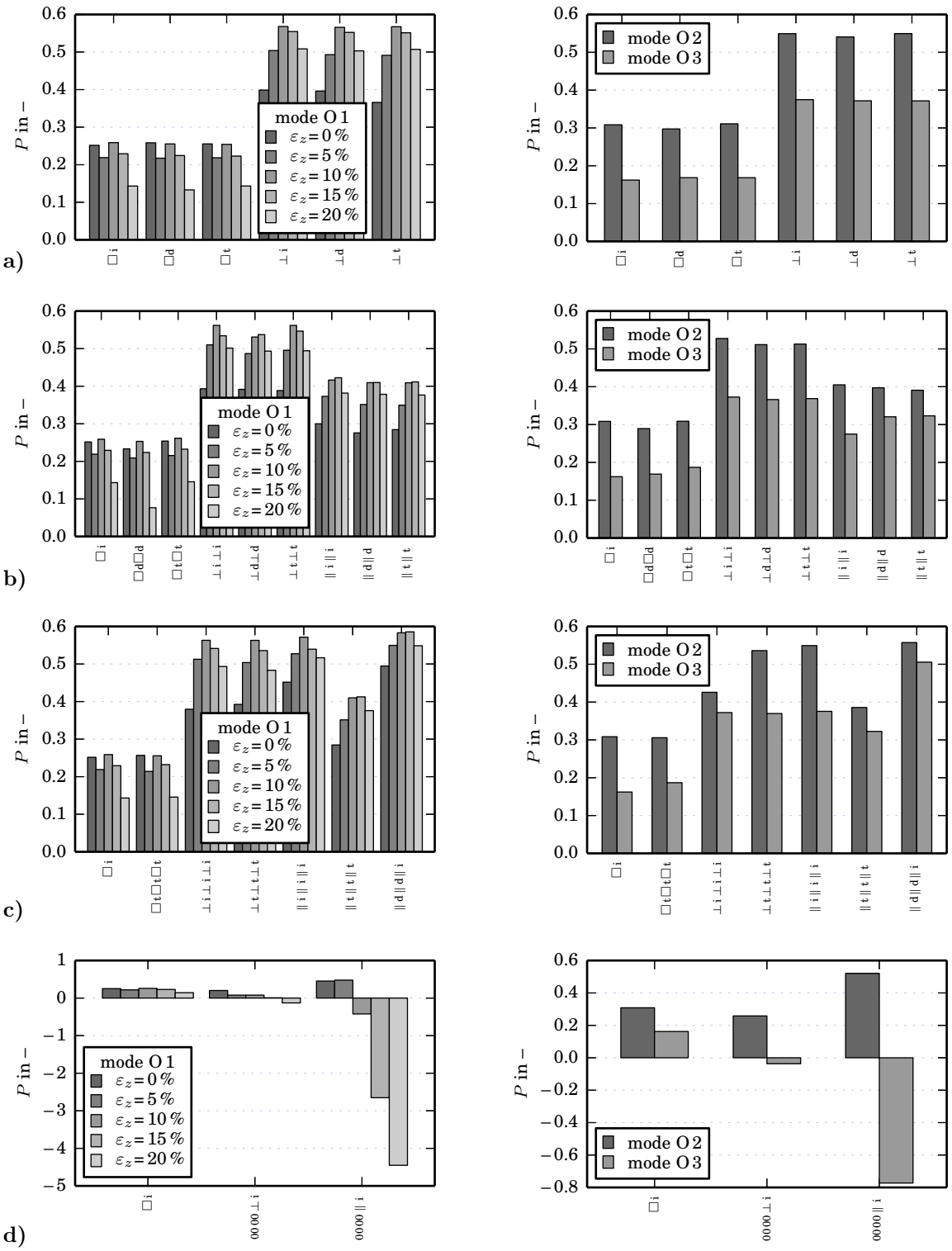

Figure 7.31: Performance measure P for selected model variants in two-layered arterial segments with growth mechanisms where **a)** only the first, **b)** the first and the second, **c)** the first, second and third or **d)** only the third of the multiplicative parts of the growth tensor is included. The performance of isotropic growth, denoted by □i, is shown as a reference.

With view to potential improvements of the performance of the analyzed growth models, it should be mentioned that the possibility of Eq. 5.64 to define critical values of the driving force functions, below which growth is deactivated, has not been considered so far. Taking such parameters into account would have increased the number of unknown model parameters and thus the complexity of the optimization problem. Since biological tissues are suspected to adapt such that preferred levels of homeostatic stresses are maintained, it might be reasonable to include critical driving force values in future investigations of a reduced number of selected growth mechanisms.

In order to point out the effect of optimized growth parameters on the distribution of the stresses in the steady growth and remodeling state, and to verify that the performance measures used above are indeed suitable to reflect the observed behavior of the growth models, four model variants are again considered in detail in the following section.

7.5.4 Optimized adaptation in idealized two-layered arterial segments

In Sec. 7.4.3, the effects of isotropic growth, radial growth and growth perpendicular to the directions of the (tensile) principal stresses have been analyzed for a one-layered idealized arterial segment. In default of better knowledge, the growth parameters had therefore been chosen rather intuitively, but such that the limit for the growth-induced volume increase was the same for each model variant. When examining the distribution of stresses and fiber angles over the wall thickness, the level of axial strain had been set such that good results could have been expected. Now, optimized parameter sets ensuring the best possible behavior at a certain level of axial strain or for a range of axial strains from 0 % to 15 % are available for one- and two-layered arterial segments. Using the parameters obtained for varying heights of the axial load, the three forms of growth are compared again for a consistent level of axial strain of 10 % in two-layered arterial segments with initial fiber angles of $\pm 30°$ in the media and $\pm 50°$ in the adventitia. Due to its excellent results in the comparative study, growth mechanism $\| \mathrm{d} \| \mathrm{d} \| \mathrm{i}$ is additionally considered. The optimized growth parameters and the associated values of the objective function for the four growth mechanisms are summarized in Tab. 7.7. Apart from those, all material, growth and remodeling parameters are set as in previous examples, that is as listed in Tab. 7.1 and defined in Eq. 7.10 and Eq. 7.11.

Table 7.7: Optimized growth parameters for different growth mechanisms in a two-layered arterial segment, obtained with averaging over different levels of axial strain (mode O 3).

growth model	f_{obj}	layer	$\vartheta^{+}_{(1)}$	$\vartheta^{+}_{(2)}$	$\vartheta^{+}_{(3)}$
$\square$ i	5.5922	media	1.1187	–	–
		adventitia	1.0881	–	–
0 0 0 0 $\|$ i	11.833	media	–	–	1.2056
		adventitia	–	–	1.4973
$\perp$d$\perp$d	4.2313	media	1.1127	1.0113	–
		adventitia	1.0709	1.0239	–
$\|$ d$\|$ d$\|$ i	3.3001	media	1.0058	1.3441	1.1501
		adventitia	1.0333	1.0766	1.0859

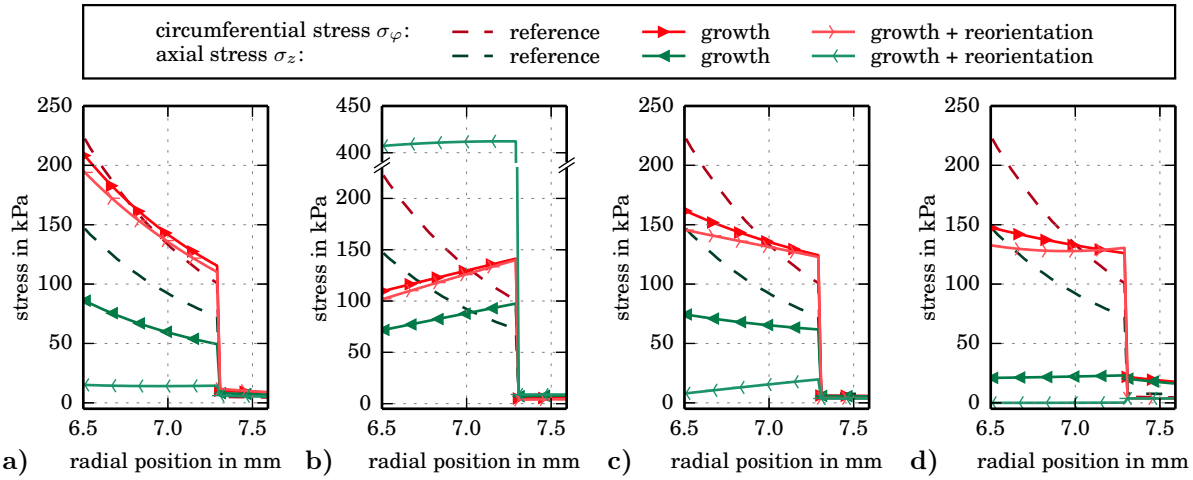

Figure 7.32: Distribution of the circumferential and axial stresses at the end of the adaptation process for the growth models **a)** □i (isotropic growth), **b)** 0 0 0 0 ‖ i (radial growth), **c)** ⊥d⊥d and **d)** ‖ d‖ d‖ i in two-layered arterial segments subjected to $p = 120\,\text{mmHg}$ and $\varepsilon_z = 10\,\%$. Apart from the results for combined growth and fiber reorientation, the results for growth alone and for non-adapting reference arteries are given.

The distributions of the circumferential and axial stresses over the wall thickness in the final adapted state are depicted in Fig. 7.32 for each of the four growth mechanisms. Besides the results for combined growth and fiber reorientation, the results for growing arteries with fiber angles fixed to the initial values and for non-adapting reference arteries are given. Since the stresses in the adventitia are negligibly low compared to the stresses in the media, only the latter will be analyzed here. The small contribution of the adventitia confirms that the media is the mechanically relevant layer at physiological blood pressures. This might however change with increasing stiffness of the adventitia at higher blood pressures.
On the basis of Fig. 7.32, the general correctness of earlier observations on the effects of different forms of growth and reorientation of the fibers as well as the main results of the optimization-based comparative study can be confirmed. Even though the growth parameters are set within the optimal range, considerable differences in the performance of isotropic, radial and anisotropic forms of growth continue to persist. With reference to the non-adapting artery, the main effect of growth on the circumferential stress is a more or less pronounced reduction of the gradient, but also of the mean value of the stress. In most cases, a reorientation of the fibers slightly supports these effects. Whereas only a minor reduction of the stress gradient is obtained with isotropic growth, see Fig. 7.32 a), radial growth shown in Fig. 7.32 b) even leads to a reversal of the sign. As obvious from Fig. 7.32 c) and d), very low gradients or nearly constant levels of the circumferential stress can be realized with more general anisotropic growth models.
Regarding the axial stress, growth alone in general causes a strong decrease of mean value and gradient. If the fibers are allowed to reorient, a considerable extra reduction, but also a very strong increase of the axial stress can occur. The latter supports the hypothesis that purely radial growth can rather not describe the true adaptation processes in arterial walls. However, zero axial stresses as in Fig. 7.32 d) or even compressive axial stresses which might occur for lower levels of the axial strain, are not the best result as well since this implies that no shortening in axial direction can probably be observed when loosening the axial fixation of the unloaded artery.

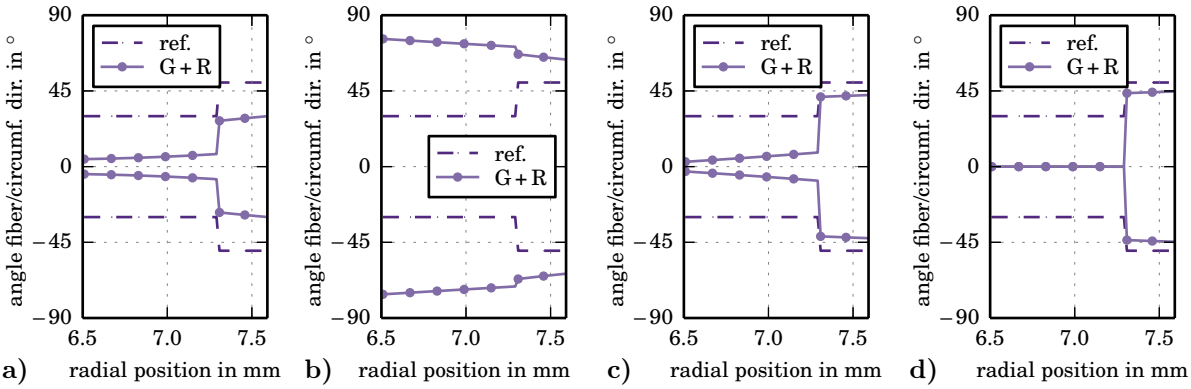

Figure 7.33: Distribution of the fiber angles at the end of the adaptation process for the growth models **a)** □i (isotropic growth), **b)** 0 0 0 0 ‖ i (radial growth), **c)** ⊥d⊥d and **d)** ‖ d‖ d‖ i in two-layered arterial segments subjected to $p = 120\,\text{mmHg}$ and $\varepsilon_z = 10\,\%$. Apart from the results for combined growth and fiber reorientation, the fiber angles of the non-adapting reference arteries are given.

The better performance of anisotropic compared to isotropic or purely radial growth can also be recognized when looking at the distribution of the fiber angles over the wall thickness, which is shown in Fig. 7.33. The high fiber angles in the media of the radially growing artery clearly contradict the experimental observation that collagen fibers in the media are rather oriented in circumferential direction. This is well captured by isotropic growth and by growth perpendicular to the tensile principal stresses, see Fig. 7.33 a) and c). For the adventitia, experimental observations suggest that the fiber orientation should rather tend towards the axial direction. In this regard, the fiber angles of about $\pm 45°$ obtained with the anisotropic forms of growth are still more realistic than those of less than $\pm 30°$ for isotropic growth.

Table 7.8: Layer-wise, growth-induced volume increase in arterial segments without and with reorientation of the fibers.

growth model	layer	G	G + R
□i	media	36.94 %	37.08 %
	adventitia	22.90 %	23.60 %
0 0 0 0 ‖ i	media	19.05 %	19.57 %
	adventitia	29.67 %	29.22 %
⊥d⊥d	media	23.99 %	24.72 %
	adventitia	13.79 %	14.74 %
‖ d‖ d‖ i	media	45.16 %	28.76 %
	adventitia	17.90 %	13.60 %

Altogether, the anisotropic growth mechanisms ⊥d⊥d and ‖ d‖ d‖ i are able to produce the most realistic results. In addition to a final fiber arrangement, which is in qualitative agreement with experimental data, a significant reduction of peaks, gradients and mean values of the circumferential and axial stresses can be realized. As obvious from Tab. 7.8, this can even be achieved with a comparatively low growth-induced increase of the tissue volume. In the adventitia, the volume increase is anyway the lowest, and in the media, lower values are

only obtained for radial growth, which due to the observations described above can however not be regarded as realistic. Interestingly, the differences in the volume increase for arterial segments without and with reorientation of the fibers are rather negligible except for growth mechanism $\| \mathrm{d} \| \mathrm{d} \| \mathrm{i}$, where the reorientation of the fibers is linked to a significant reduction of the amount of growth. This might be attributable to the fact that the circumferential and axial components of growth are relatively independent in this case. In contrast to isotropic growth or growth perpendicular to the first and second principal stresses, growth in axial direction only occurs as long as the axial stress is positive. If the axial stress is already strongly reduced due to a reorientation of the fibers towards the circumferential direction, the amount of axial growth needed for an additional reduction towards zero can be assumed to be much lower than in the case with fixed fiber orientations.

In spite of the convincing results for the considered anisotropic forms of growth in the above example, it should again be mentioned that the quality of the results should in general be expected to be strongly dependent on the ratio of internal pressure and axial strain. For a quantification of this dependency, the behavior of the four model variants at reduced and elevated level of the axial strain is illustrated in Fig. 7.34 in terms of the circumferential and axial stresses in the steady state. In addition to $\varepsilon_z = 10\,\%$, the axial loads $\varepsilon_z = 5\,\%$ and $\varepsilon_z = 15\,\%$ are now considered without changing the growth parameters.

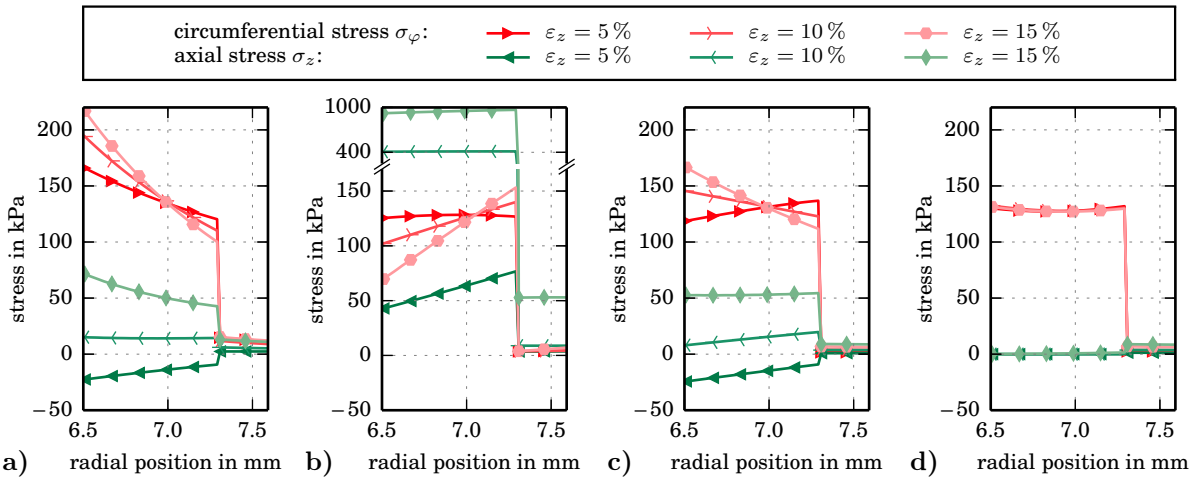

Figure 7.34: Distribution of the circumferential and axial stresses at the end of the adaptation process for the growth models **a)** $\square \mathrm{i}$ (isotropic growth), **b)** $0\,0\,0\,0 \,\|\, \mathrm{i}$ (radial growth), **c)** $\perp \mathrm{d} \perp \mathrm{d}$ and **d)** $\| \mathrm{d} \| \mathrm{d} \| \mathrm{i}$ in two-layered arterial segments subjected to $p = 120\,\mathrm{mmHg}$ and different levels of axial strain, computed with the same set of growth parameters.

The results are impressive, and at the same time they confirm that the optimization-based comparison of the model variants has been able to reveal the main differences between the growth mechanisms. For isotropic growth and growth perpendicular to the directions of the first and second principal stress, the peak of the circumferential stress at the inner border of the media and the level of axial stress increase with the height of axial strain. The same in principle holds for radial growth, but there, the peak of the circumferential stress is at the outer border of the media and the axial stress increases drastically. A completely different picture, which has not been expected in such strong intensity, arises for the fourth growth mechanism: regardless of the level of axial strain, the same final stresses, which are furthermore nearly

constant over the wall thickness, are attained in the media. On the one hand, these results are visibly well in line with the values of the objective function, see Tab. 7.7, which have been determined by averaging over axial strains of 0 %, 5 %, 10 % and 15 %. On the other hand, the differences between the performance measures obtained for the optimization modes O 2 and O 3, see Fig. 7.31, can indeed be taken as an indicator for the sensitivity of the final stress distributions with respect to the loading. This sensitivity can of course also be observed for the fiber angles, which are governed by the ratio of the tensile principal stresses. As shown in Fig. 7.35, the highest variability is obtained for radial growth and the lowest for growth mechanism ∥ d∥ d∥ i .

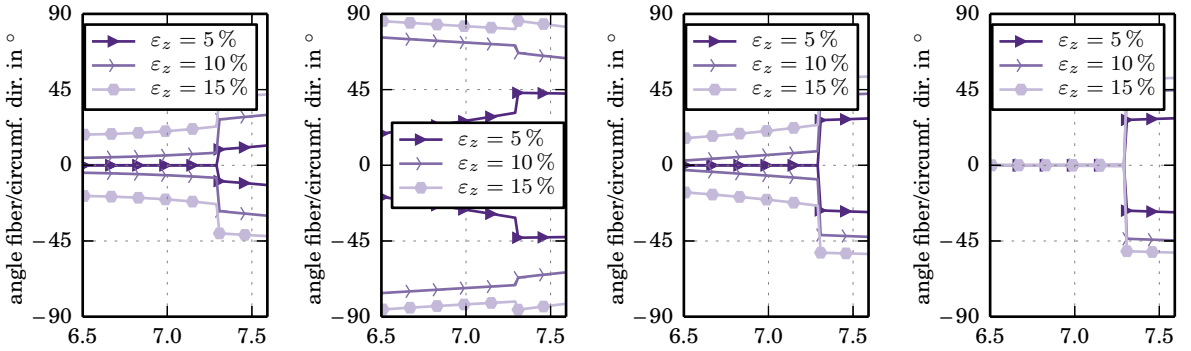

Figure 7.35: Distribution of the fiber angles at the end of the adaptation process for the growth models **a)** □i (isotropic growth), **b)** 0 0 0 0 ∥ i (radial growth), **c)** ⊥d⊥d and **d)** ∥ d∥ d∥ i in two-layered arterial segments subjected to $p = 120\,\text{mmHg}$ and different levels of axial strain, computed with the same set of growth parameters.

In this context, it is again important to notice that the latter growth mechanism allows for a rather independent regulation of the axial stress, which in the considered loading situations and without use of critical values for the driving forces always results in a zero axial stress and zero fiber angles in the media. On the basis of the experimental observations described in Chapter 2, it should rather be assumed that independent growth in the principal directions, which is directly driven by the respective principal stresses, is in general not possible in arterial walls.

7.6 Virtual opening angle experiment

The results of the arterial wall simulations including growth imply that the aim of incorporating residual stresses has been achieved without falling back to the inverse simulation of opening angle experiments. Nevertheless, a virtual forward opening angle experiment is assumed to be a useful final step in order to check the plausibility of the growth-induced residual stress state by visualization of the related deformations. To this end, a removal of the internal pressure, the release of the arterial segment from its axial fixation, as well as the radial and circumferential cuts have to be simulated numerically in a 3D simulation. The expected deformations, in ideal circumstances a contraction in axial direction and an opening of the individual layers in circumferential direction, are clearly too large to be determined in a single calculation step. For that reason, a special algorithmic procedure based on an internal update of the stress state

is proposed (cf. Zahn & Balzani, 2017; Balzani & Zahn, 2017). The following steps are involved:

1. Solve the original boundary value problem, where internal pressure and axial strain are held constant until a steady state of growth and remodeling is attained.
2. Deactivate growth and remodeling and remove the internal pressure while retaining the axial strain to obtain the unloaded in vivo state.
3. Save the obtained configuration by storing the nodal coordinates, the fiber orientation vectors and the Cauchy stress tensor $\boldsymbol{\sigma}_{\mathrm{res}} := {}^{1}/_{J}\,\boldsymbol{F}\boldsymbol{S}\boldsymbol{F}^{\mathrm{T}}$ of each Gauß point.
4. Use the nodal coordinates and fiber orientation vectors to define a new boundary value problem that allows for the expected deformations, restore $\boldsymbol{\sigma}_{\mathrm{res}}$ at each Gauß point and keep it throughout the following calculation.
5. Apply the restored stresses internally by updating the 2nd Piola-Kirchhoff stress tensor according to $\boldsymbol{S} \leftarrow \boldsymbol{S} + f_{\mathrm{load}}\,\boldsymbol{S}_{\mathrm{res}}$, where f_{load} is a load factor ranging from 0 to 1. In each step, the stress $\boldsymbol{S}_{\mathrm{res}} = J\,\boldsymbol{F}^{-1}\boldsymbol{\sigma}_{\mathrm{res}}\boldsymbol{F}^{-\mathrm{T}}$ has to be computed corresponding to the actual deformation state.

Following this procedure, the wanted deformations will arise stepwise in absence of any external load. If the boundary conditions of the secondary problem do not permit a deformation in axial direction and a bending deformation of the arterial layers, the known stress and deformation state after removal of the pressure is identically regained.

In order to give a numerical example of the opening angle experiment, three of the arterial segments from Sec. 7.5.4 are considered again. Since the final opened configuration is supposed to be symmetric with respect to the plane of the radial cut, symmetry boundary conditions can be applied, such that only one half of the segments needs to be simulated. These halves are discretized with 7 elements in radial, 42 elements in circumferential and 7 elements in axial direction. The arterial segments are allowed to adapt to an internal pressure of 120 mmHg and an axial strain of 10 % until the steady state known from Fig. 7.32 is reached. Then, the internal pressure is reduced to zero and the stresses shown in Fig. 7.36 are left.

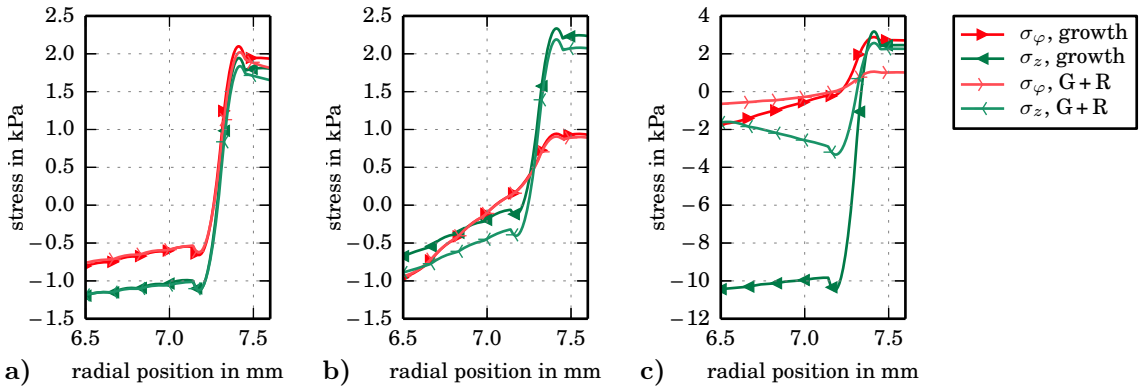

Figure 7.36: Distribution of the circumferential and axial stresses after removal of the internal pressure for the growth models **a)** □i (isotropic growth), **b)** ⊥d⊥d and **c)** ∥ d∥ d∥ i with and without reorientation of the fibers in two-layered 3D arterial segments with a retained axial strain of 10 %.

It should first be recalled that the axial stretch is still present, such that the given stresses can not be denoted as "residual" stresses in the classical meaning. They rather represent a kind of unloaded in vivo state, where the artery is still fixed in axial direction before it is cut from the body. Ranging from compressive values near the lumen to tensile values in the adventitia, the circumferential stresses should induce an opening of the segments after a radial cut as expected. After a cut in axial direction, only the adventitia can be expected to contract: regardless of the growth model, compressive axial stresses are obtained in the media. Except for growth model $\| \mathrm{d} \| \mathrm{d} \| \mathrm{i}$, where a reorientation of the collagen fibers has been stated to have a significant effect on the amount of growth (see Tab. 7.8), the obtained stresses are largely independent on remodeling.
Whereas the distribution of the stresses is in principle in line with the findings of other authors, for example Sigaeva, Sommer, et al. (2019) or Liu, Zhang, et al. (2019), the numerical values are surprisingly low. Presumably, this can be attributed to an incorrect treatment of the different configurations. Since the examples in this chapter are only academic, no attention has so far been paid to the difference in the dimensions of the undeformed reference configuration and the grown, unloaded configuration. In a proper implementation, it might be required to produce a residually stressed configuration which nevertheless has the geometry of the original reference configuration. Liu, Zhang, et al. realized this by an iterative backward update of the grown geometry. In this context, it becomes apparent that further problems arise on the path towards realistic patient-specific simulations. Apart from residual stresses, also prestresses have to be taken into account in order to match the geometries of the boundary value problem, which is usually defined in the unloaded state, and of the real artery, which is obtained from medical images showing the physiological in vivo state. For an insight into that subject, the work of Weisbecker, Pierce & Holzapfel (2014), Pierce, Fastl, et al. (2015) and Genet, Rausch, et al. (2015) is recommended. The small values of the circumferential residual stresses and the axial prestresses shown in Fig. 7.36 can thus be supposed to be the result of an incomplete methodological approach. Nevertheless, they allow the simulation of an opening angle experiment. The arising deformations in the plane normal to the longitudinal axis are illustrated in Fig. 7.37 for the entire arterial wall consisting of media and adventitia, and in Fig. 7.38 for the individual layers. Due to the low values of the applied stresses, the opening angles, which are defined as denoted in Fig. 7.37 a), are far too small as well. In real aortas, opening angles of 180° and more are observed (Holzapfel, Sommer, Auer, et al., 2007). Nonetheless, the qualitative behavior is as expected: The opened configurations of the non-separated arteries are still not free of circumferential stresses, which means that a single opening angle is not enough to characterize the residual stress state. In contrast to that, the circumferential stresses vanish completely if adventitia and media are separated. Both anisotropic growth mechanisms produced residual stresses due to which the media opens more than the adventitia. With isotropic growth, only a minor reduction of the circumferential stress gradient in the media could be realized and hence only a small opening angle of this layer is obtained. Together with the observation by Holzapfel, Sommer, Auer, et al. (2007) that the media of human aortas shows larger opening angles than the adventitia, this supports the hypothesis that anisotropic forms of growth are better suited to model residual stresses than isotropic growth.

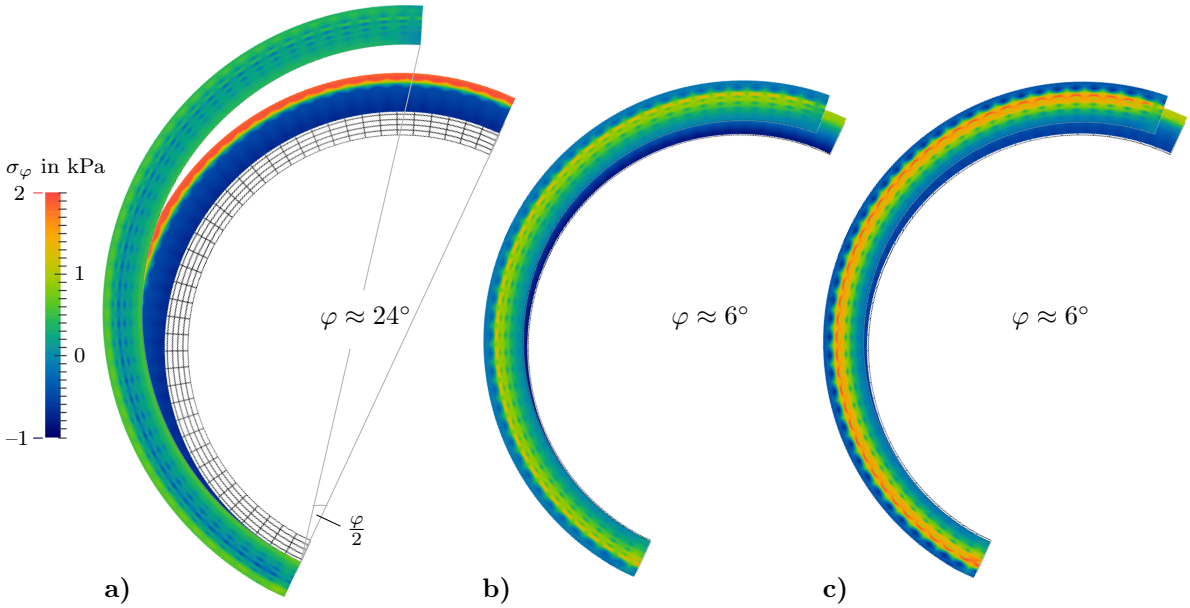

Figure 7.37: Deformation state and circumferential stress in a virtual opening angle experiment of two-layered arterial segments without separation of the layers. The residual stresses are the result of combined growth and fiber reorientation using the growth models **a)** □i (isotropic growth), **b)** ⊥d⊥d and **c)** ∥ d∥ d∥ i . The wire frame represents the undeformed reference configuration an the second chart from the inside shows the grown state after removal of the pressure but with retained axial strain.

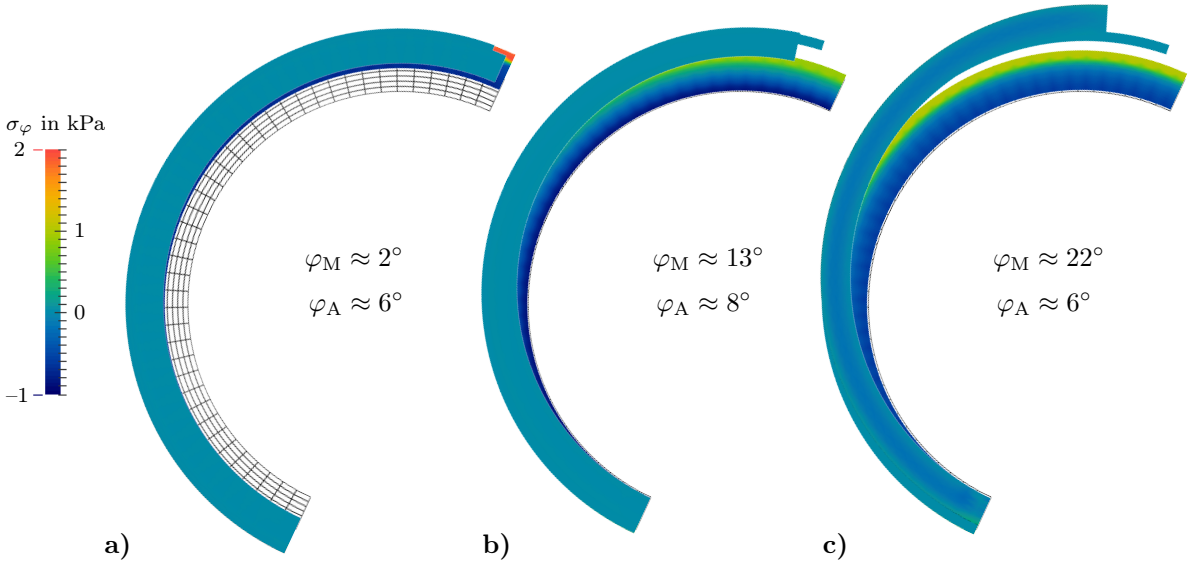

Figure 7.38: Deformation state and circumferential stress in a virtual opening angle experiment of two-layered arterial segments with separation of the layers. The residual stresses are the result of combined growth and fiber reorientation using the growth models **a)** □i (isotropic growth), **b)** ⊥d⊥d and **c)** ∥ d∥ d∥ i . The wire frame represents the undeformed reference configuration an the second chart from the inside shows the grown state after removal of the pressure but with retained axial strain.

8 Outlook to future application and extensions

In Chapter 7, the fundamental effects of fiber reorientation and different forms of growth have been analyzed on the basis of idealized, rotationally symmetric arterial segments, which allowed a reduction of the boundary value problem to one spatial dimension. Nonetheless, the combined growth and remodeling framework has been developed with the intention to provide a general tool for the approximation of residual stresses and fiber orientations in fiber-reinforced soft biological tissues without restriction to idealized geometries. For that reason, the constitutive framework is consistently formulated in three dimensions. A reduction to two- or one-dimensional rotationally symmetric geometries, if required, happens on the element level alone, see Sec. 4.2. Furthermore, directional information required for the definition of the growth tensor and the target fiber orientation vectors is exclusively based on local mechanical field quantities, precisely the principal stress state, at the considered material point. The framework should therefore in principle be applicable to irregular geometries without changes or extensions. In order to verify this assumption, a patient-specific artery will be analyzed in Sec. 8.1.
In the context of finite element method, the growth and remodeling framework virtually is situated in between the element and the material level. It provides updated fiber orientation vectors and an adjusted version of the deformation gradient, which is corrected by the stress-free part due to growth. Based thereon, any material model can be used to compute the stress response. An example for such an application to enhanced material models is given in Sec. 8.2.

8.1 Simulation of a patient-specific artery

In their contribution on the automated calculation of fiber orientations in arterial walls, Fausten, Balzani & Schröder (2016) applied their reorientation algorithm to a finite element model of a patient-specific coronary artery, which had been produced from a stack of two-dimensional intravascular ultrasound images as described by Balzani, Böse, et al. (2012). The existing finite element mesh, consisting of 8401 tetrahedral, 10-noded elements with quadratic shape functions, will now be used to prove the applicability of the proposed growth and remodeling framework in irregular geometries. As in previous examples, the artery is loaded by an internal pressure and a displacement-driven stretch in axial direction. The unhindered dilation of the pressurized artery is enabled by a statically determined support, which is illustrated in Fig. 8.1. This figure also shows that no distinction between the different arterial layers and the deposited plaque had been made when generating the finite element mesh. For that reason, the artery is considered as one-layered and the material parameters of the mechanically most relevant layer, the media, are assigned throughout.

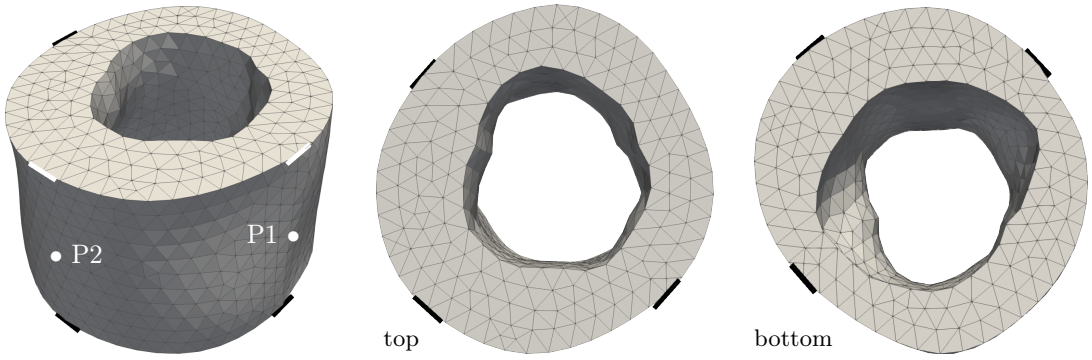

Figure 8.1: Finite element mesh and boundary conditions of the patient-specific artery. The nodes marked by lines are fixed in the indicated direction, and the top and bottom planes are fixed in axial direction. A controlled displacement of the top plane induces axial strain.

Compared to the one-layered arterial segment from Chapter 7, which is meant to represent a healthy human aorta, the patient-specific artery can be expected to show an increased stiffness due to the elevated ratio of wall thickness to diameter. A direct re-utilization of the growth parameters optimized for use in the model of the aorta is thus not recommended. In order to obtain an optimized parameter set for the model of the patient-specific artery, a rotationally symmetric substitute model with inner and outer radii of $r_\mathrm{i} = 1.2\,\mathrm{mm}$ and $r_\mathrm{o} = 2.35\,\mathrm{mm}$ is defined. On the basis of the results from Sec. 7.5, a reduced number of growth models is chosen for a new parameter optimization specialized to the new boundary value problem. Among those models, growth mechanism $\| \mathrm{d} \| \mathrm{d} \| \mathrm{i}$ with $\vartheta^+_{(1)} = 1.0058$, $\vartheta^+_{(2)} = 1.1705$ and $\vartheta^+_{(3)} = 1.0836$, obtained with averaging over the level of axial strain in optimization mode O 3, is picked out for the 3D simulation of the patient-specific artery. The parameters obtained for the other growth mechanisms and optimization modes are tabulated in Tab. B.3 of Appendix B.

The adaptation of the patient-specific artery to an internal pressure of 120 mmHg and an axial strain of 5 % is illustrated in Fig. 8.2 in terms of the contour plots and exemplary distributions of the first and second principal stress for four different points in time. Compared to the initial state at $t = 1\,\mathrm{s}$ in the first column, already one second of growth and fiber reorientation leads to a significant reduction of local stress peaks at the inner surface of the artery. This can for example be observed at point P1, where first and second principal stress at the lumen are both reduced by more than 50 %. In contrast to that, the radial distributions of the stresses at point P2 remain more or less unchanged at the original low level, such that a homogenization of the stresses over the entire artery can be observed. This homogenization process continues over time and comes along with an increase of the first principal stress in the outer part of the wall, which is already known from the examples on idealized arterial segments. At $t = 60\,\mathrm{s}$, the first principal stress ranges from about 30 kPa at the outer surface to maximally 120 kPa at local points on the inner surface of the wall and the second principal stress is nearly constant at a very low level under 20 kPa. In summary, the desired effect of stress-driven growth and fiber reorientation – a reduction of stress peaks and gradients in the arterial wall – is not only observed in idealized geometries, but also in irregular patient-specific models, where the principal directions may change from point to point and over time. It should however be mentioned that the simulation could not be continued up to the steady state of constant growth factors and fiber orientation vectors due to missing convergence in the local Newton iteration (see Sec. 5.1.3).

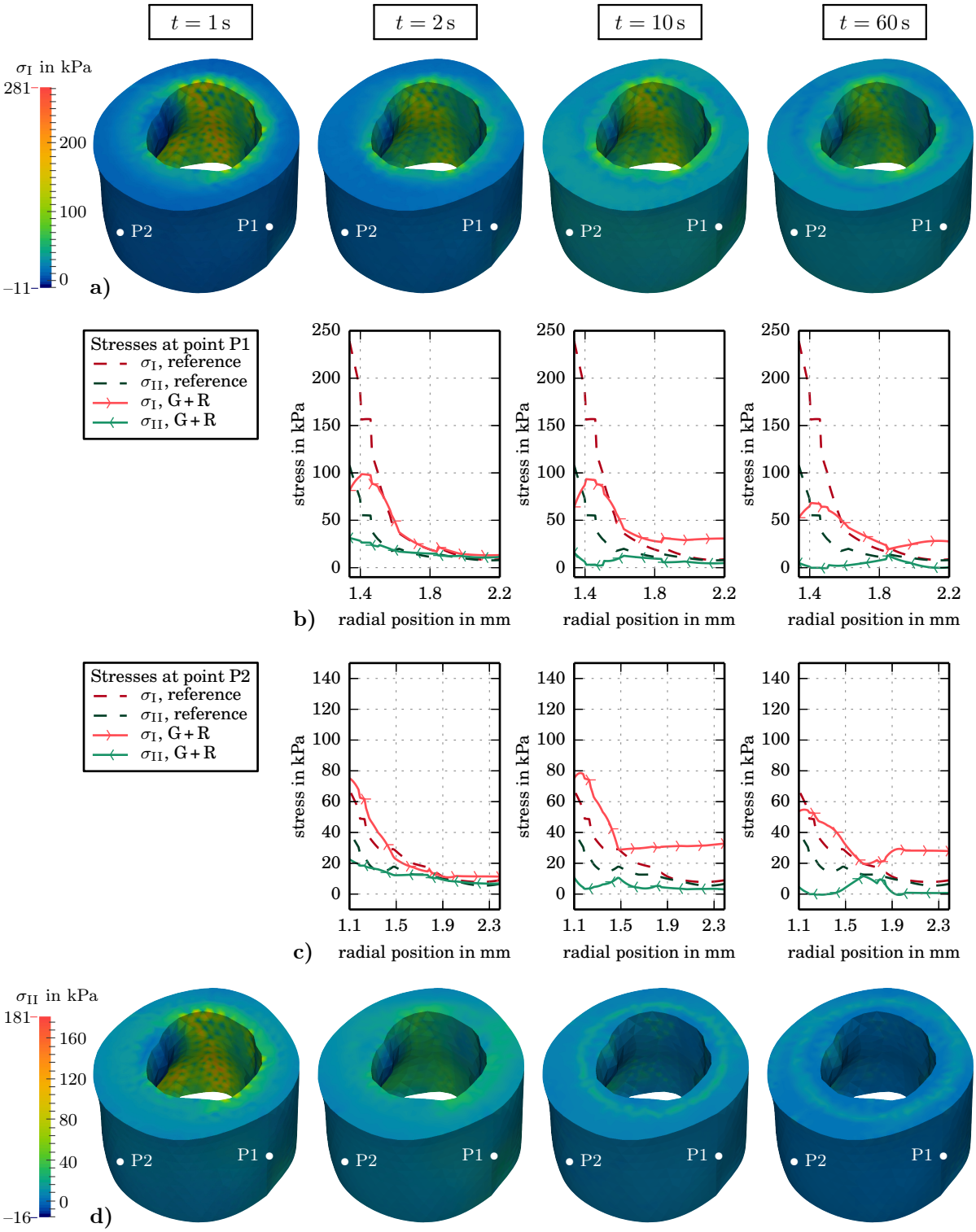

Figure 8.2: Contour plots of **a)** the first and **d)** the second principal Cauchy stress prior to adaptation at $t = 1\,\mathrm{s}$ and after one, nine and fifty-nine seconds of growth and fiber reorientation. For two exemplary points P1 and P2, the corresponding stress distributions over the wall thickness are illustrated under **b)** and **c)**.

One potential cause of trouble is the unsolved problem mentioned on p. 100 which leads to a loss of the rotational symmetry in the 3D simulation of idealized arteries. The correction of the principal directions mentioned there has been deactivated for the simulation of the patient-specific artery since the principal directions are not expected to exactly coincide with the radial, circumferential and axial directions here. This might have caused inaccuracies with unknown consequences. Furthermore, inaccuracies might have arisen from an inadvertency which has only been detected a posteriori: Instead of $\mathrm{sym}[\boldsymbol{\Sigma}_\mathrm{e}]$, a specially symmetrized Mandel stress tensor $\tilde{\boldsymbol{\Sigma}}_\mathrm{e}$ based on the upper triangular half of $\boldsymbol{\Sigma}_\mathrm{e}$ has been used to compute the principal directions. On the other hand it might also be valuable to think about the history of growth in order to improve the performance in irregular geometries. If the orientation of the principal axes changes between two time steps, for example by a rotation of some degrees around the direction of the second principal stress, the growth factors associated to those axes are taken along to the new orientations. This means that the history of growth is distorted. In rotationally symmetric structures, this effect does not occur since the principal directions do not deviate from the coordinate axes over time.

8.2 Consideration of the active material response

For the simulation of muscular arteries, a restriction to the passive material response is no longer sufficient to cover all important aspects of the material behavior. In those arteries, an active regulation of the diameter by contraction of the smooth muscle cells is observed. The presented framework for combined growth and fiber reorientation can easily be applied to enhanced constitutive equations by extending or replacing the strain energy function given in Eq. 7.1, provided that no more than two reorienting fiber families are included. In the context of active response, this can be achieved by adding the part

$$\psi_\mathrm{act} = \sum_{m=1}^{2} \psi_\mathrm{act}^{(m)}(\tilde{J}_4^{(m)}), \tag{8.1}$$

which represents the active contraction of two fibrous families of smooth muscle cells. It is formulated as a function of the fourth invariant

$$\tilde{J}_4^{(m)} = \mathrm{tr}[\boldsymbol{C}_\mathrm{e}\boldsymbol{M}_\mathrm{SMC,i}^{(m)}] \qquad \text{with} \qquad \boldsymbol{M}_\mathrm{SMC,i}^{(m)} = \boldsymbol{A}_\mathrm{SMC,i}^{(m)} \otimes \boldsymbol{A}_\mathrm{SMC,i}^{(m)}, \tag{8.2}$$

where the unit vector $\boldsymbol{A}_\mathrm{SMC,i}^{(m)}$ indicates the orientation of smooth muscle fiber family m in the intermediate configuration. The combined simulation of arterial growth, fiber reorientation and active response within this framework has been analyzed in a first fundamental study (Uhlmann, Zahn & Balzani, 2021), which attests its potential for future application and improvements. In the following paragraphs, a short introduction to the model for smooth muscle contraction and a basic numerical example are presented. More details can be found in the contribution by Uhlmann, Zahn & Balzani and the references mentioned therein.

Model for smooth muscle contraction. The contraction of smooth muscle cells involves several biochemical processes, but mechanical models mostly focus on the intracellular calcium concentration as the predominant influencing factor. A contraction is initiated by power strokes in the contractile units of the cells, which can be performed if phosphorylated myosin heads are

attached to actin filaments. The state of the myosin heads, that is, if they are phosphorylated and attached to actin or not, depends on the calcium concentration and is described by a set of coupled differential equations proposed by Hai & Murphy (1988). The transition from one functional state to another is thereby described by reaction rates k_i with $i \in [1, 7]$. Adopting the reaction rates k_1 and k_6 for phosphorylation from Murtada, Arner & Holzapfel (2012), a dependency on the calcium concentration and on the chemical parameters ED_{50}, η and h is assumed. As proposed by Uhlmann, Uhlmann, Zahn & Balzani model the calcium concentration itself as a phenomenological function of the stretch $\lambda^{(m)}$ in the direction of the muscle fibers, which is defined by

$$\lambda^{(m)} = \sqrt{\tilde{J}_4^{(m)}}. \tag{8.3}$$

In this context, three material parameters c_1, c_2 and λ_0 are introduced. The active part $\psi_{\mathrm{act}}^{(m)}$ of the strain energy function for muscle fiber direction m is formulated based on the approaches by Murtada, Kroon & Holzapfel (2010) and Murtada, Arner & Holzapfel (2012) and involves the material parameters μ_{a}, κ, γ_1, and γ_2.

Effect of active response in adapting arterial segments. An active contraction of the smooth muscle cells can be assumed to have an additional effect on the stress distributions in the arterial wall. The following numerical example will only be able to show the qualitative behavior of arterial segments with combined growth, fiber reorientation and active response, since several aspects are not taken into account. On the one hand, the considered boundary value problem of a two-layered arterial segment is based on the geometry of human aortas, which are not of muscular, but of elastic type. Muscular arteries are in general smaller in diameter and the adventitia makes up about 50 % of the wall thickness. On the other hand, the difference in the time scales of active response and adaptation is not modeled realistically and only a constant load scenario with a representative, average blood pressure of 120 mmHg and an axial strain of 15 % is considered. The material parameters for active response, which are listed in Tab. 8.1, are set without experimental evidence in such a manner that the contraction of the smooth muscle cells is significant, but not unrealistic. Since the adventitia does not contain smooth muscle cells, active response is only taken into account for the media.

Table 8.1: Parameters for the active response in the media as used by Uhlmann et al. (2021).

mechanical	μ_{a}	κ	γ_1	γ_2	c_1	c_2	λ_0
	1000 kPa	700 kPa	$0.0001\,\mathrm{s}^{-1}$	26.68 kPa	0.01 mol/l	4.0	0.98
chemical	$k_{2/5}$	k_3	k_4	k_7	ED_{50}	η	h
	$0.16\,\mathrm{s}^{-1}$	$0.07\,\mathrm{s}^{-1}$	$0.03\,\mathrm{s}^{-1}$	$0.02\,\mathrm{s}^{-1}$	0.35 µmol/l	$0.8\,\mathrm{s}^{-1}$	4.0

In default of better knowledge, the orientation of the muscle fibers is supposed to equal the orientation of the collagen fibers throughout the entire simulation. If the collagen fibers are allowed to reorient, the new orientation thus also holds for the muscle fibers. The arterial segment is assumed to grow according to the anisotropic growth mechanism denoted by $\perp\mathrm{t}\perp\mathrm{t}$, which consists of growth perpendicular to the directions of the first and the second principal stress as long as those stresses are tensile. The limiting values of the growth factors are set such that an optimal performance of the growth mechanism is ensured for the given loading scenario without consideration of the active material response. In order to match the time

scales of adaptation and active response, the velocities of growth and fiber reorientation are decelerated by a factor of 100 compared to previous numerical examples. The complete set of growth parameters is summarized in Tab. 8.2 and the remodeling parameters are $k_\eta^+ = 0.006\,\mathrm{s}^{-1}$ and $m_\eta^+ = 5.0$.

Table 8.2: Parameters for growth model $\perp\mathrm{t}\perp\mathrm{t}$ in a two-layered artery, optimized for $\varepsilon_z = 15\,\%$.

	a	$\vartheta_{(a)}^+$	$\vartheta_{(a)}^-$	$k_{\vartheta,(a)}^{+/-}$	$m_{\vartheta,(a)}^{+/-}$
media	1	1.16	0.98	$0.01\,\mathrm{s}^{-1}$	3.0
	2	1.01	0.98	$0.01\,\mathrm{s}^{-1}$	3.0
adventitia	1	1.10	0.98	$0.01\,\mathrm{s}^{-1}$	3.0
	2	1.01	0.98	$0.01\,\mathrm{s}^{-1}$	3.0

As in previous simulations, the load is applied within the first second of the simulation time without activation of growth, fiber reorientation and active response. For the analysis of the effect of active response, three different scenarios are analyzed:

Mode A 1: Growth, fiber reorientation and active response start simultaneously at $t = 1\,\mathrm{s}$.

Mode A 2: Active response starts at $t = 1\,\mathrm{s}$, growth and fiber reorientation are activated additionally as soon as a steady state of active response has been attained.

Mode A 3: Active response starts at $t = 1\,\mathrm{s}$ and is deactivated as soon as a steady state is attained. Growth and fiber reorientation are activated afterwards.

The steady state of smooth muscle contraction as a reaction to the initial loading is identified visually on the basis of the temporal development of circumferential and axial stress. It is assumed to be attained at $t = 6000\,\mathrm{s}$. This can be verified with the help of Fig. 8.3, where the development of the circumferential and the axial stress at the innermost Gauß point is visualized for the three modes of active response in combination with growth and fiber reorientation. As a reference, the behavior of an adapting arterial segment without consideration of the active material response is shown. A general observation from Fig. 8.3 is that active response obviously intensifies the effect of growth and fiber reorientation if both are active simultaneously. In modes A 1 and A 2, the final level of circumferential and axial stress at the considered Gauß point is far beyond the reference level, and it is qualitatively similar whether growth and remodeling have been active from the beginning (mode A 1) or started belatedly at $t = 6000\,\mathrm{s}$ (mode A 2). Furthermore, it can be observed that active response alone, as in the first 6000 seconds of modes A 2 and A 3, leads to an increase of both stresses compared to the initial value at $t = 1\,\mathrm{s}$. If active response is deactivated as soon as the steady state of smooth muscle contraction in response to the initial loading is attained, subsequent growth and fiber reorientation reduce both stresses as expected (mode A 3). However, the obtained level of the circumferential stress is significantly higher than in the reference case without active response. A comparison of modes A 2 and A 3 shows that growth and remodeling, which here includes a reorientation of the muscle fibers, have a significant impact on the contraction of the smooth muscle cells. Although a steady state had been attained at $t = 6000\,\mathrm{s}$ for the given level of the external loads, further smooth muscle activity is induced due to changes of the stretch in the direction of the muscle fibers caused by growth and remodeling. It should be questioned in future examinations

if this is the wanted behavior or not. Since growth and remodeling are known to be much slower than the active material response, which is a protective mechanism operating at acute overload, a permanent interaction between both processes seems to be contradictory at first glance. It might for instance be imaginable to model the calcium concentration as a function of the rate of the fiber stretch instead of the stretch itself in order to prevent a smooth muscle contraction in response to slow, growth-induced changes of the fiber stretch.

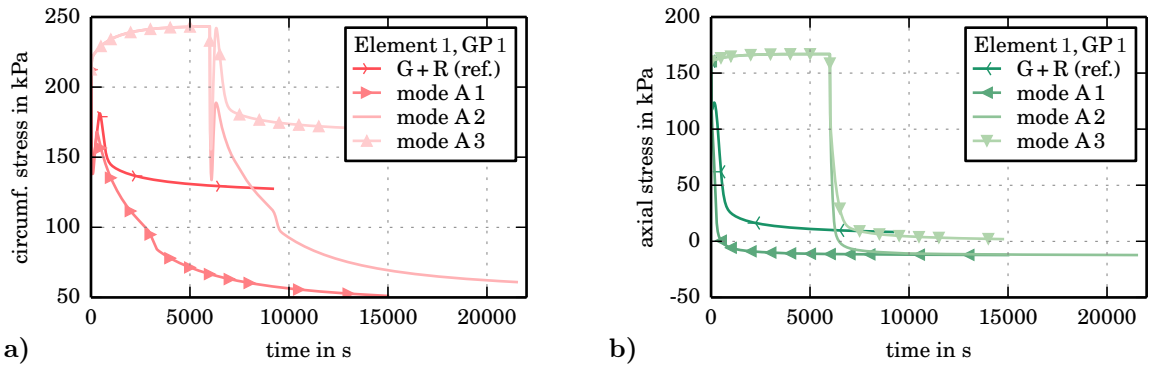

Figure 8.3: Temporal development of **a)** circumferential stress and **b)** axial stress at Gauß point 1 of element 1 in a 1D two-layered arterial segment with different combinations of growth and fiber reorientation with active material response.

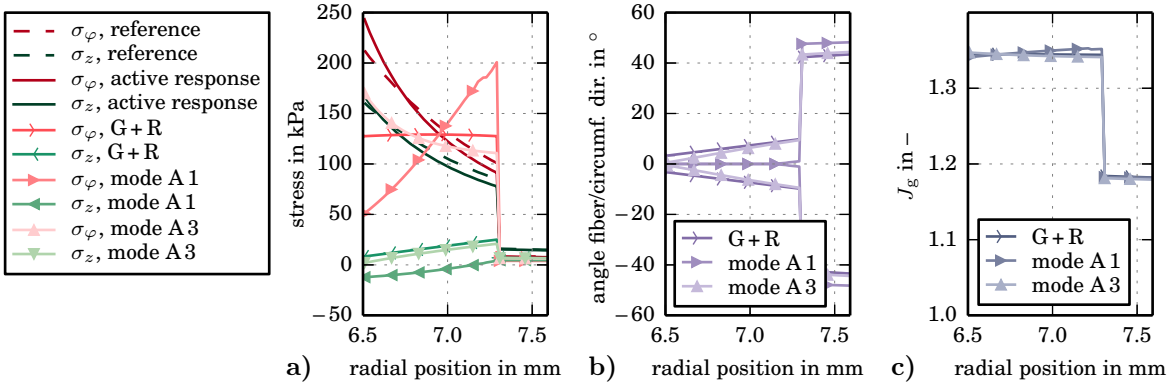

Figure 8.4: Distribution of **a)** circumferential and axial stresses, **b)** fiber angles and **c)** determinant of the growth tensor over the radial position in the final steady state of growth, fiber reorientation and active response.

The qualitative effect of active response on the distribution of the circumferential and axial stresses over the wall thickness in the steady state is illustrated in Fig. 8.4 a) for three different situations. First, a reference artery without any adaptation, i. e. at time $t = 1\,\mathrm{s}$, can be compared to an artery with active response. The contraction of the smooth muscle cells leads to an increase of peak and gradient of the circumferential and also the axial stress, but the mean values of both stresses computed over the whole volume are reduced. For the combination of active response with growth and remodeling, the two simulation modes A 1 and A 3 as well as the reference curves for growth and remodeling without active response are depicted. If growth and remodeling act under the permanent presence of smooth muscle response (mode A 1), a negative effect on the stress distributions in the media can be observed: the gradient of the circumferential stress is reversed and its peak value at the outer surface is relatively high. Furthermore, the

axial stress decreases to such an extent that it gets compressive. Both observations confirm that active response intensifies the effects of growth and fiber reorientation provided that they occur simultaneously. In contrast to that, the effects of growth and fiber reorientation are damped if the onset of the adaptation process is preceded by a contraction of the smooth muscle cells, which is maintained without changes during growth and remodeling (mode A 3). The inner peak and the gradient of the circumferential stress are higher than without preceding active response. Compared to that, the small differences in axial stress are negligible.
A pronounced effect of active response on the fiber angles can only be observed if all processes are assumed to occur simultaneously, see Fig. 8.4 b). As a result of the compressive axial stresses in the media, zero fiber angles over the entire thickness of the media are obtained. In the adventitia, the fiber angles of mode A 1 are higher than in the other two scenarios. The growth-induced volume change, which is shown in Fig. 8.4 c), is almost unaffected by active response.

When evaluating the presented results, it should be considered that the growth parameters have been optimized for the situation without activity of the smooth muscle cells, and that the parameters of active response have been set rather intuitively. In consequence, the aim of uniform stress distributions over the wall thickness and low peak values is best possibly achieved if the additional effect of active response is ignored. The above analysis can thus only be seen as a first step which demonstrates the qualitative behavior. For more advanced application, detailed thought should be given to the chronology and interaction of growth, fiber reorientation and active response, and the material parameters should be adapted to the chosen scenario.

9 Conclusion

The numerical simulation of soft biological tissues continues to be a challenging task. Many of the biological, chemical and mechanical processes, which lead to the observed tissue behavior and its changes over time or in pathological situations are still far from understood. In this work, the idea to approximate residual stresses and fiber orientations in arterial walls based on a phenomenological description of growth and fiber reorientation has been pursued. The basic assumption was that changes in tissue mass and structure occur as a reaction to changes of the mechanical environment conditions and represent the tissue's attempts to continuously adapt and improve its load-bearing behavior. Following the trend apparent in recent publications with related content, growth and fiber reorientation were assumed to be stress-driven.
For the continuum mechanical realization of volumetric growth, a multiplicative decomposition of the deformation gradient into a growth tensor and a remaining elastic part as proposed by Rodriguez, Hoger & McCulloch (1994) was applied. In order to introduce anisotropy, the growth tensor itself was decomposed multiplicatively into three parts associated to the three perpendicular principal directions of the symmetric part of the Mandel stress tensor in the intermediate configuration. The latter stress tensor was chosen as mechanical reference quantity for growth and fiber reorientation since it is energetically conjugated to the growth velocity gradient (Himpel, Kuhl, et al., 2005). Due to uncertainty about the growth mechanisms prevalent in arterial tissues, each part of the growth tensor was allowed to adopt one of four basic forms, describing either isotropic growth, growth in the direction of the associated principal stress, growth perpendicular to that direction or no growth at all. The amount of growth related to each of the three parts was described by scalar internal variables $\vartheta^{(1)}$, $\vartheta^{(2)}$ and $\vartheta^{(3)}$, which were supposed to depend on stress-based, isotropic or anisotropic driving force functions. The involved set of coupled, nonlinear evolution equations was treated in a local Newton iteration by application of implicit Euler backward scheme, linearization and analytical solution of the resulting system of equations for the incremental updates $\Delta\vartheta^{(a)}$ with $a \in [1, 2, 3]$. For the implementation of the generalized growth model in a nonlinear finite element setting, the complete set of expressions needed for an analytical computation of the tangent modulus was derived. In comparison with a numerical derivation of the tangent modulus using complex step derivative approximation (cf. Tanaka, Fujikawa, et al., 2014), this led to a reduction of the computing time in the amount of about 70 %. Starting from the general equations, a simplification towards specific forms of growth was conducted in order to check the results on the basis of previously known expressions (e. g. by Göktepe, Abilez & Kuhl, 2010; Zahn & Balzani, 2017). Nonetheless, the implementation of the growth model was kept general, such that the realization of various growth mechanisms with different combinations of basic forms of growth and driving forces for the three multiplicative parts of the growth tensor was enabled. Since the anisotropy of growth was induced solely by directional information contained in the local mechanical field quantities, none of those models requires knowledge of any kind of structural information. This is advantageous for use in irregular patient-specific geometries, where an identification of the radial, circumferential and axial directions is more

complex than in boundary value problems of idealized, cylindrical arteries. Apart from that, a general local formulation based on stress quantities was estimated to better describe the reality in adapting tissues than a model based on geometrically determined coordinate axes without direct mechanical meaning.
The decomposition of the overall deformation into a stress-free growth part and a remaining elastic part restoring compatibility can be applied regardless of the constitutive equations. In this work, a phenomenological, polyconvex material model by Balzani, Neff, et al. (2006), which idealizes arterial tissues as isotropic matrix materials with two embedded families of collagen fibers, was used to compute the stress from the elastic part of the Cauchy-Green tensor. In agreement with their supposed main task to carry tensile loads, the favored arrangement of the two fiber families was assumed to be dictated by the tensile principal stresses. Adopting the hypothesis of Hariton, deBotton, et al. (2007a), but using the symmetric part of the Mandel stress tensor in the intermediate configuration instead of the Cauchy stress tensor, the target fiber orientation vectors were chosen to be aligned symmetrically with respect to the first and second principal stress directions according to the ratio of the associated (tensile) principal stresses. For the reorientation of the existing fiber vectors towards their target orientation, an algorithm for the continuous reorientation over time was proposed and compared to an alternative approach by Fausten, Balzani & Schröder (2016), where the fiber vectors are updated incrementally in additional Newton iterations. With its simplicity due to explicit time integration of the scalar evolution equations for the angles between the existing and the target fiber orientation vectors, better robustness and increased efficiency when used in combination with a process which in any case is time-dependent, the proposed algorithm could be shown to be a valid choice.

Numerical examples on selected forms of growth and fiber reorientation in idealized arterial geometries revealed that a reduction of stress peaks, mean values and gradients can in principle be realized with isotropic, radial as well as more general forms of anisotropic growth. However, the level of axial strain and the parameters defining the maximal amount of growth could be identified as important factors which severely affect the final steady state and the potential of the model variants to describe the desired behavior. In order to nevertheless enable an equitable comparison and assessment of the many different growth mechanisms included in the generalized form of the growth tensor, an optimization-based comparative study was performed. With the definition of a mechano-biologically motivated objective function representing the ability of a growth mechanism to homogenize the stress distributions at minimum energetic effort, which was measured in terms of the growth-induced increase of the tissue volume, a scalar comparative quantity was introduced. In three different optimization modes, where the level of axial strain was either fixed to a specific value, treated as optimization variable or set to 0 %, 5 %, 10 % and 15 % in succession while averaging the objective function, the performance of the model variants under availability of optimized growth parameters as well as the sensitivity with respect to those parameters and to the level of axial strain could be assessed. The comparative study confirmed that anisotropic forms of growth often lead to improvements compared to isotropic growth: although the absolute amount of growth is lower, more homogeneous stress distributions might be obtained. Purely radial growth in combination with reorienting fibers however turned out to be unjustifiable from a mechanical point of view. For axial strains above 5 %, a non-physiological reorientation of the fibers in the media towards the axial direction was observed, which came along with a strong increase of the axial stress to values far above the initial ones. The best performance in terms of the objective function values could be realized with the combination

of growth in the directions of the first and second principal stress, driven by those stresses, with growth in the direction of the third principal stress, i. e. the radial direction, driven by an isotropic stress measure. With this model variant, identical, nearly constant stresses in the mechanically relevant layer were obtained for different levels of axial strain without change of the growth parameters. With a view to experimental observations, such a form of growth with independent behavior in radial, circumferential and axial direction however seems to be implausible. For that reason, mechanisms with growth perpendicular to the directions of the principal stresses, which also proved to perform well, might be a more realistic assumption.
The simulation of growth and fiber reorientation in a 3D model of a patient-specific artery, resulting in homogenized stress distributions as expected, confirmed that the proposed framework is in principle applicable in boundary value problems with irregular geometries. Nevertheless, it should not be kept secret that the numerical robustness in 3D simulations is still in need of improvement. Given that this can be achieved, the presented framework can be considered to be a promising tool for the approximation of residual stresses and fiber orientations in arbitrary arterial wall simulations. As shown in a final example, where the active response of smooth muscle cells was included, the framework can straightforwardly be extended to more complex material models, such that finally more and more relevant aspects of arterial wall mechanics can be taken into account.

A Notation and tensor algebra

This appendix contains additional remarks on notation and vector algebra, that are not mandatory for the overall comprehension of the document but helpful for the reconstruction of details. In the literature, contradictory definitions of particular tensors or operators might be found. It is therefore mentioned here that this work widely follows the conventions introduced by Holzapfel in his textbook *Nonlinear Solid Mechanics*.

A.1 Notes on the notation

As far as possible, the following conventions on notation are pursued within this work. Scalar quantites as a, J, v, β, ϑ are denoted by regular small or capital letters. If the same quantity is defined in more than one configuration, capital letters are used for the reference configuration, index "i" for the intermediate configuration and small letters for the actual configuration, for example $\mathrm{d}V$, $\mathrm{d}V_\mathrm{i}$, $\mathrm{d}v$. This contradicts the convention of denoting vectors and tensors of 2^{nd} order in symbolic notation by small and capital bold letters, respectively, which is however used for quantites that are not referred to in different configurations, e. g. $\boldsymbol{u}$, $\boldsymbol{\varphi}$, $\mathrm{d}\boldsymbol{f}$ and $\boldsymbol{F}$, $\boldsymbol{C}$, $\boldsymbol{S}$. In contrast to that, $\boldsymbol{E}_i$ and $\boldsymbol{X}$ (like $\boldsymbol{e}_i$ and $\boldsymbol{x}$) denote vectors and $\boldsymbol{l}$ (like $\boldsymbol{L}_\mathrm{i}$) a tensor. The Cauchy stress tensor $\boldsymbol{\sigma}$ is a further exception. Tensors of 4^{th} order are indicated by blackboard bold symbols as $\mathbb{C}$, $\mathbb{A}$, $\mathbb{I}$.

The unit tensor of 2^{nd} order is denoted by $\boldsymbol{I} = \delta_{ij}\,\boldsymbol{e}_i \otimes \boldsymbol{e}_j = \boldsymbol{e}_i \otimes \boldsymbol{e}_i$, where δ_{ij} is the Kronecker delta defined as

$$\delta_{ij} = \begin{cases} 1 & \text{if} \quad i \neq j \\ 0 & \text{if} \quad i = j \end{cases} . \tag{A.1}$$

Another special tensor is the permutation tensor $\boldsymbol{\epsilon}$ with the indices

$$\epsilon_{ijk} = \begin{cases} 1 & \text{if } (i,j,k) \text{ is a cyclic permutation of (1,2,3)} \\ -1 & \text{if } (i,j,k) \text{ is an anti-cyclic permutation of (1,2,3)} \\ 0 & \text{if at least two indices are equal} \end{cases} , \tag{A.2}$$

which is also referred to as Levi-Civita symbol. If the same index occurs twice in an expression in index notation, Einstein's summation convention has to be applied, i. e.

$$a_i\,\boldsymbol{e}_i = \sum_{i=1}^{3} a_i\,\boldsymbol{e}_i \qquad \text{or} \qquad A_{ij}\,B_{ji} = \sum_{i=1}^{3}\sum_{j=1}^{3} A_{ij}\,B_{ji}. \tag{A.3}$$

Such double indices are denoted as summation indices, whereas single indices are called free indices. Exemplary tensor operations resulting in tensors of 0^{th}, 1^{st}, 2^{nd} or 4^{th} order are listed below in symbolic and index notation.

Tensors of 0^{th} order/scalars:

$c = \boldsymbol{a} \cdot \boldsymbol{b}$	$c = a_i \, b_i$
$c = \boldsymbol{A} \cdot \boldsymbol{B} = \boldsymbol{A} : \boldsymbol{B}$	$c = A_{ij} \, B_{ij}$
$c = \mathrm{tr}[\boldsymbol{A}] = \boldsymbol{A} \cdot \boldsymbol{I}$	$c = A_{ii}$
$c = \mathrm{tr}[\boldsymbol{A}\boldsymbol{B}]$	$c = A_{ij} \, B_{ji}$
$c = \mathrm{div}[\boldsymbol{a}] = \nabla \cdot \boldsymbol{a}$	$c = a_{i,i}$

Tensors of 1^{st} order/vectors:

$\boldsymbol{c} = \boldsymbol{A} \, \boldsymbol{b}$	$c_i = A_{ij} \, b_j$
$\boldsymbol{c} = (\boldsymbol{a} \otimes \boldsymbol{b}) \, \boldsymbol{d} = (\boldsymbol{b} \cdot \boldsymbol{d}) \, \boldsymbol{a}$	$c_i = b_j \, d_j \, a_i$
$\boldsymbol{c} = \boldsymbol{a} \times \boldsymbol{b}$	$c_i = \epsilon_{ijk} \, a_i \, b_j$
$\boldsymbol{c} = \mathrm{div}[\boldsymbol{A}]$	$c_i = A_{ij,j}$
$\boldsymbol{c} = \nabla \times \boldsymbol{a}$	$c_i = \epsilon_{jki} \, a_{k,j}$

Tensors of 2^{nd} order:

$\boldsymbol{C} = \boldsymbol{a} \otimes \boldsymbol{b}$	$C_{ij} = a_i \, b_j$
$\boldsymbol{C} = \boldsymbol{A}\boldsymbol{B}$	$C_{ij} = A_{ik} \, B_{kj}$
$\boldsymbol{C} = (\boldsymbol{a} \otimes \boldsymbol{b}) \, (\boldsymbol{c} \otimes \boldsymbol{d}) = (\boldsymbol{b} \cdot \boldsymbol{c}) \, (\boldsymbol{a} \otimes \boldsymbol{d})$	$C_{ij} = b_k \, c_k \, a_i \, d_j$
$\boldsymbol{C} = \boldsymbol{A}^{\mathrm{T}}$	$C_{ij} = A_{ji}$
$\boldsymbol{C} = \mathbb{A} : \boldsymbol{B}$	$C_{ij} = \mathbb{A}_{ijkl} \, B_{kl}$
$\boldsymbol{C} = \boldsymbol{B} : \mathbb{A}$	$C_{ij} = B_{kl} \, \mathbb{A}_{klij}$
$\boldsymbol{C} = \mathrm{grad}[\boldsymbol{a}]$	$C_{ij} = a_{i,j}$
$\boldsymbol{C} = \nabla \times \boldsymbol{A}$	$C_{ij} = \epsilon_{kli} \, A_{jl,k}$

Tensors of 4^{th} order:

$\mathbb{C} = \boldsymbol{A} \otimes \boldsymbol{B}$	$\mathbb{C}_{ijkl} = A_{ij} \, B_{kl}$
$\mathbb{C} = \boldsymbol{A} \boxtimes \boldsymbol{B}$	$\mathbb{C}_{ijkl} = A_{ik} \, B_{jl}$
$\mathbb{C} = \boldsymbol{A} \boxdot \boldsymbol{B}$	$\mathbb{C}_{ijkl} = A_{il} \, B_{jk}$

The non-standard symbol $\boxtimes$ is defined such that the relation

$$(\boldsymbol{A} \boxtimes \boldsymbol{B}) : (\boldsymbol{a} \otimes \boldsymbol{b}) = \mathbb{C} : (\boldsymbol{a} \otimes \boldsymbol{b}) = \boldsymbol{A}\boldsymbol{a} \otimes \boldsymbol{B}\boldsymbol{b} \tag{A.4}$$

with the tensor components $\mathbb{C}_{ijkl} = A_{ik} \, B_{jl}$ is valid. In consequence, the identities

$$\boldsymbol{A}\boldsymbol{B}\boldsymbol{C} = \left(\boldsymbol{A} \boxtimes \boldsymbol{C}^{\mathrm{T}}\right) : \boldsymbol{B} \qquad \text{and} \qquad \boldsymbol{A}\boldsymbol{B}\boldsymbol{C} = \boldsymbol{B} : \left(\boldsymbol{A}^{\mathrm{T}} \boxtimes \boldsymbol{C}\right) \tag{A.5}$$

hold for three tensors of second order. Furthermore, the symbol $\boxdot$ is defined such that the relation

$$(\boldsymbol{A} \boxdot \boldsymbol{B}) : (\boldsymbol{a} \otimes \boldsymbol{b}) = \mathbb{C} : (\boldsymbol{a} \otimes \boldsymbol{b}) = \boldsymbol{A}\boldsymbol{b} \otimes \boldsymbol{B}\boldsymbol{a} \tag{A.6}$$

holds, where the components of $\mathbb{C}$ are now given by $\mathbb{C}_{ijkl} = A_{il}\, B_{jk}$. This leads to the calculation rules

$$\boldsymbol{A}\boldsymbol{B}\boldsymbol{C} = \left(\boldsymbol{A} \boxdot \boldsymbol{C}^{\mathrm{T}}\right) : \boldsymbol{B}^{\mathrm{T}} \qquad \text{and} \qquad \boldsymbol{A}\boldsymbol{B}\boldsymbol{C} = \boldsymbol{B}^{\mathrm{T}} : \left(\boldsymbol{C} \boxdot \boldsymbol{A}^{\mathrm{T}}\right) \tag{A.7}$$

for a sequence of three tensors of second order.

The operators "grad" and "div" might also appear as "Grad" and "Div". The initial letter indicates if the derivative has to be taken with respect to the coordinates $\boldsymbol{x}$ in the actual configuration (small initial letter) or $\boldsymbol{X}$ in the reference configuration (capital initial letter).

A.2 Tensor algebra

In this section, complementary information on the manipulation of equations presumed in the main part of the document is given, which in most cases is either part of general knowledge or irrelevant for the overall comprehension.

A.2.1 Pushforward and pullback operations

In order to clarify how the transformation of tensors between different configurations works, a detailed example is given here. For clarification purposes, the belonging of the basis vectors to the configurations is emphasized by use of different indices in index notation. Capital letters like A, B, C are used for quantities belonging to the reference configuration, small letters like i, j, k for quantities belonging to the actual configuration and greek letters like α, β, γ for quantities belonging to the intermediate configuration. Then, the deformation gradient and its multiplicative parts as well as their inverses can be written down as

$$\boldsymbol{F} = F_{iA}\, \boldsymbol{e}_i \otimes \boldsymbol{e}_A, \qquad \boldsymbol{F}^{-1} = F^{-1}_{Ai}\, \boldsymbol{e}_A \otimes \boldsymbol{e}_i, \tag{A.8a}$$

$$\boldsymbol{F}_{\mathrm{g}} = (F_{\mathrm{g}})_{\alpha A}\, \boldsymbol{e}_\alpha \otimes \boldsymbol{e}_A, \qquad \boldsymbol{F}_{\mathrm{g}}^{-1} = (F_{\mathrm{g}}^{-1})_{A\alpha}\, \boldsymbol{e}_A \otimes \boldsymbol{e}_\alpha, \tag{A.8b}$$

$$\boldsymbol{F}_{\mathrm{e}} = (F_{\mathrm{e}})_{i\alpha}\, \boldsymbol{e}_i \otimes \boldsymbol{e}_\alpha, \qquad \boldsymbol{F}_{\mathrm{e}}^{-1} = (F_{\mathrm{e}}^{-1})_{\alpha i}\, \boldsymbol{e}_\alpha \otimes \boldsymbol{e}_i. \tag{A.8c}$$

As indicated by its name, the spatial velocity gradient

$$\boldsymbol{l} = \dot{\boldsymbol{F}}\boldsymbol{F}^{-1} = \dot{F}_{iA}\, \boldsymbol{e}_i \otimes \boldsymbol{e}_A\, F^{-1}_{Bj}\, \boldsymbol{e}_B \otimes \boldsymbol{e}_j = \dot{F}_{iA} F^{-1}_{Aj}\, \boldsymbol{e}_i \otimes \boldsymbol{e}_j = l_{ij}\, \boldsymbol{e}_i \otimes \boldsymbol{e}_j \tag{A.9}$$

from Eq. 3.16 has thus two basis vectors in the actual configuration. In order to obtain its counterpart in the intermediate configuration given in Eq. 3.23, a pullback using the elastic part of the deformation gradient, i. e.

$$\begin{aligned} \boldsymbol{L}_{\mathrm{i}} &= \boldsymbol{F}_{\mathrm{e}}^{-1} \boldsymbol{l} \boldsymbol{F}_{\mathrm{e}} \\ &= (F_{\mathrm{e}}^{-1})_{\alpha i}\, \boldsymbol{e}_\alpha \otimes \boldsymbol{e}_i\, l_{kl}\, \boldsymbol{e}_k \otimes \boldsymbol{e}_l\, (F_{\mathrm{e}})_{j\beta}\, \boldsymbol{e}_j \otimes \boldsymbol{e}_\beta \\ &= (F_{\mathrm{e}}^{-1})_{\alpha i}\, l_{ij}\, (F_{\mathrm{e}})_{j\beta}\, \boldsymbol{e}_\alpha \otimes \boldsymbol{e}_\beta \\ &= (L_{\mathrm{i}})_{\alpha\beta}\, \boldsymbol{e}_\alpha \otimes \boldsymbol{e}_\beta \end{aligned} \tag{A.10}$$

has to be performed to end up with a tensor with two basis vectors belonging to the intermediate configuration.

A.2.2 Modification of Gauß' divergence theorem

For the transformation of a surface integral into a volume integral, Gauß' divergence theorem

$$\int_{\partial\mathcal{S}} \boldsymbol{\sigma}\boldsymbol{n}\,\mathrm{d}a = \int_{\mathcal{S}} \operatorname{div}[\boldsymbol{\sigma}]\,\mathrm{d}v \qquad \text{i. e.} \qquad \int_{\partial\mathcal{S}} \sigma_{ij}\,n_j\,\boldsymbol{e}_i\,\mathrm{d}a = \int_{\mathcal{S}} \frac{\partial\sigma_{ij}}{\partial x_j}\,\boldsymbol{e}_i\,\mathrm{d}v \tag{A.11}$$

for an integration over the actual configuration or

$$\int_{\partial\mathcal{B}} \boldsymbol{P}\boldsymbol{N}\,\mathrm{d}A = \int_{\mathcal{B}} \operatorname{Div}[\boldsymbol{P}]\,\mathrm{d}V \qquad \text{i. e.} \qquad \int_{\partial\mathcal{B}} P_{ij}\,N_j\,\boldsymbol{e}_i\,\mathrm{d}A = \int_{\mathcal{B}} \frac{\partial P_{ij}}{\partial X_j}\,\boldsymbol{e}_i\,\mathrm{d}V \tag{A.12}$$

for an integration over the reference configuration holds. In these equations, $\boldsymbol{n}$ and $\boldsymbol{N}$ denote the outward unit normal vectors on the surface in the actual and reference configuration, respectively. For the evaluation of the balance of angular momentum, a modification of this theorem is required in order to convert an expression like $\int_{\partial\mathcal{S}} \boldsymbol{x}\times\boldsymbol{\sigma}\boldsymbol{n}\,\mathrm{d}A$. With

$$\boldsymbol{x}\times\boldsymbol{\sigma}\boldsymbol{n} = x_i\,\boldsymbol{e}_i\times\sigma_{jr}\,n_r\boldsymbol{e}_j = \underbrace{\epsilon_{kij}\,x_i\,\sigma_{jr}}_{=:\bar{\sigma}_{kr}}\,n_r\,\boldsymbol{e}_k, \tag{A.13}$$

the integrand on the right hand side of the wanted expression can be computed in analogy to Eq. A.11 as

$$\frac{\partial\bar{\sigma}_{kr}}{\partial x_r}\,\boldsymbol{e}_k = \frac{\partial(\epsilon_{kij}\,x_i\,\sigma_{jr})}{\partial x_r}\,\boldsymbol{e}_k = \epsilon_{kij}\,\delta_{ir}\,\sigma_{jr}\,\boldsymbol{e}_k + \epsilon_{kij}\,x_i\,\frac{\partial\sigma_{jr}}{\partial x_r}\,\boldsymbol{e}_k. \tag{A.14}$$

This expression can be converted back to symbolic notation by introduction of additional basis vectors according to

$$\epsilon_{kij}\,\sigma_{ji}\,\boldsymbol{e}_k + \epsilon_{kij}\,x_i\,\frac{\partial\sigma_{jr}}{\partial x_r}\,\boldsymbol{e}_k = \epsilon_{kij}\,\boldsymbol{e}_k\otimes\boldsymbol{e}_i\otimes\boldsymbol{e}_j : \sigma^{\mathrm{T}}_{su}\,\boldsymbol{e}_s\otimes\boldsymbol{e}_u + x_i\,\boldsymbol{e}_i\times\frac{\partial\sigma_{jr}}{\partial x_r}\,\boldsymbol{e}_j, \tag{A.15}$$

which equals the expression $\boldsymbol{\epsilon} : \boldsymbol{\sigma}^{\mathrm{T}} + \boldsymbol{x}\times\operatorname{div}[\boldsymbol{\sigma}]$. The wanted modification of the divergence theorem thus results in

$$\int_{\partial\mathcal{S}} \boldsymbol{x}\times\boldsymbol{\sigma}\boldsymbol{n}\,\mathrm{d}a = \int_{\mathcal{S}} \boldsymbol{x}\times\operatorname{div}[\boldsymbol{\sigma}] + \boldsymbol{\epsilon} : \boldsymbol{\sigma}^{\mathrm{T}}\,\mathrm{d}v. \tag{A.16}$$

In an analogeous manner,

$$\int_{\partial\mathcal{B}} \boldsymbol{x}\times\boldsymbol{P}\boldsymbol{N}\,\mathrm{d}A = \int_{\mathcal{B}} \boldsymbol{x}\times\operatorname{Div}[\boldsymbol{P}] + \boldsymbol{\epsilon} : \boldsymbol{F}\boldsymbol{P}^{\mathrm{T}}\,\mathrm{d}V. \tag{A.17}$$

can be shown to hold true.

A.2.3 Special derivatives

Derivative of inverse tensors. In order to find the derivative of the inverse of a tensor with respect to the tensor itself, the expression $\partial\left(\boldsymbol{A}^{-1}\boldsymbol{A}\right)/\partial\boldsymbol{A} = \mathbb{0}$ with the 4^{th} order zero tensor $\mathbb{0}$

can be evaluated in index notation. From

$$\begin{aligned}
\frac{\partial\left(A_{ij}^{-1}\,A_{jk}\right)}{\partial A_{lm}} &= \frac{\partial A_{ij}^{-1}}{\partial A_{lm}}\,A_{jk} + A_{ij}^{-1}\,\frac{\partial A_{jk}}{\partial A_{lm}} = 0 \\
\frac{\partial A_{ij}^{-1}}{\partial A_{lm}}\,A_{jk}\,A_{kn}^{-1} &= -A_{ij}^{-1}\,\frac{\partial A_{jk}}{\partial A_{lm}}\,A_{kn}^{-1} \\
\frac{\partial A_{ij}^{-1}}{\partial A_{lm}}\,\delta_{jn} &= -A_{ij}^{-1}\,\delta_{jl}\,\delta_{km}\,A_{kn}^{-1} \\
\frac{\partial A_{in}^{-1}}{\partial A_{lm}} &= -A_{il}^{-1}\,A_{mn}^{-1}
\end{aligned} \tag{A.18}$$

it can be concluded that

$$\left(\frac{\partial \boldsymbol{A}^{-1}}{\partial \boldsymbol{A}}\right)_{ijkl} = -A_{ik}^{-1}\,A_{lj}^{-1} \tag{A.19}$$

holds for the components of $\partial \boldsymbol{A}^{-1}/\partial \boldsymbol{A}$. With the product defined in Eq. A.4, the derivative can be expressed in symbolic notation as

$$\frac{\partial \boldsymbol{A}^{-1}}{\partial \boldsymbol{A}} = -\boldsymbol{A}^{-1} \boxtimes \boldsymbol{A}^{-\mathrm{T}}. \tag{A.20}$$

In the same manner, the derivative $\partial \boldsymbol{A}^{-\mathrm{T}}/\partial \boldsymbol{A}$ with

$$\left(\frac{\partial \boldsymbol{A}^{-\mathrm{T}}}{\partial \boldsymbol{A}}\right)_{ijkl} = -A_{il}^{-\mathrm{T}}\,A_{kj}^{-\mathrm{T}} \tag{A.21}$$

can be derived, which can be given in symbolic notation with the help of the symbol $\boxdot$ defined in Eq. A.6 as

$$\frac{\partial \boldsymbol{A}^{-\mathrm{T}}}{\partial \boldsymbol{A}} = -\boldsymbol{A}^{-\mathrm{T}} \boxdot \boldsymbol{A}^{-1}. \tag{A.22}$$

Derivative of the determinant. In Eq. 3.17, the relation $\partial \det[\boldsymbol{F}]/\partial \boldsymbol{F} = \det[\boldsymbol{F}]\boldsymbol{F}^{-\mathrm{T}}$ has been used to compute the time derivative of the Jacobian and also for the computation of stresses within the theory of hyperelasticity, the derivative of the determinant is required, see Eq. 7.7. It is known that the inverse of a tensor $\boldsymbol{F}$ is computed as

$$\begin{aligned}
\boldsymbol{F}^{-1} &= \begin{pmatrix} F_{11} & F_{12} & F_{13} \\ F_{21} & F_{22} & F_{23} \\ F_{31} & F_{32} & F_{33} \end{pmatrix}^{-1} \\
&= \frac{1}{\det[\boldsymbol{F}]} \begin{pmatrix} F_{22}F_{33} - F_{23}F_{32} & F_{13}F_{32} - F_{12}F_{33} & F_{12}F_{23} - F_{22}F_{13} \\ F_{23}F_{31} - F_{21}F_{33} & F_{11}F_{33} - F_{13}F_{31} & F_{13}F_{21} - F_{23}F_{11} \\ F_{21}F_{32} - F_{22}F_{31} & F_{12}F_{31} - F_{11}F_{32} & F_{11}F_{22} - F_{12}F_{21} \end{pmatrix}.
\end{aligned} \tag{A.23}$$

With this knowledge, the derivative of $\det[\boldsymbol{F}]$ with respect to $\boldsymbol{F}$ can be expressed as

$$\begin{aligned}\frac{\partial \det[\boldsymbol{F}]}{\partial \boldsymbol{F}} &= \frac{\partial \left| \begin{pmatrix} F_{11} & F_{12} & F_{13} \\ F_{21} & F_{22} & F_{23} \\ F_{31} & F_{32} & F_{33} \end{pmatrix} \right|}{\partial \boldsymbol{F}} \\ &= \begin{pmatrix} F_{22}F_{33} - F_{23}F_{32} & F_{23}F_{31} - F_{21}F_{33} & F_{21}F_{32} - F_{22}F_{31} \\ F_{13}F_{32} - F_{12}F_{33} & F_{11}F_{33} - F_{13}F_{31} & F_{12}F_{31} - F_{11}F_{32} \\ F_{12}F_{23} - F_{22}F_{13} & F_{13}F_{21} - F_{23}F_{11} & F_{11}F_{22} - F_{12}F_{21} \end{pmatrix} \\ &= \det[\boldsymbol{F}]\, \boldsymbol{F}^{-\mathrm{T}}.\end{aligned} \tag{A.24}$$

If the derivative of the inverse of the determinant is wanted, the chain rule can be used to find

$$\frac{\partial \det[\boldsymbol{F}]^{-1}}{\partial \boldsymbol{F}} = -\frac{1}{\det[\boldsymbol{F}]^2} \frac{\partial \det[\boldsymbol{F}]}{\partial \boldsymbol{F}} = -\frac{1}{\det[\boldsymbol{F}]}\, \boldsymbol{F}^{-\mathrm{T}}. \tag{A.25}$$

For a symmetric tensor, for example $\boldsymbol{C}_\mathrm{e}$, the derivatives computed above can be expressed as

$$\frac{\partial \det[\boldsymbol{C}_\mathrm{e}]}{\partial \boldsymbol{C}_\mathrm{e}} = \det[\boldsymbol{C}_\mathrm{e}]\, \boldsymbol{C}_\mathrm{e}^{-1} \qquad \text{and} \qquad \frac{\partial \det[\boldsymbol{C}_\mathrm{e}]^{-1}}{\partial \boldsymbol{C}_\mathrm{e}} = -\frac{1}{\det[\boldsymbol{C}_\mathrm{e}]}\, \boldsymbol{C}_\mathrm{e}^{-1}. \tag{A.26}$$

A.2.4 Sherman-Morrison formula

The inverse of a tensor being the sum of an invertible tensor $\boldsymbol{A}$ and a dyad $\boldsymbol{u} \otimes \boldsymbol{v}$ can be computed if $(1 + \boldsymbol{v} \cdot \boldsymbol{A}^{-1}\boldsymbol{u}) \neq 0$. It is defined by

$$(\boldsymbol{A} + \boldsymbol{u} \otimes \boldsymbol{v})^{-1} = \boldsymbol{A}^{-1} - \frac{\boldsymbol{A}^{-1}\,(\boldsymbol{u} \otimes \boldsymbol{v})\,\boldsymbol{A}^{-1}}{1 + \boldsymbol{v} \cdot \boldsymbol{A}^{-1}\boldsymbol{u}} \tag{A.27}$$

according to the Sherman-Morrison formula. For the application to the basic forms of the growth tensor defined in Eq. 5.1b and Eq. 5.1c, this formula can be simplified. In this case, the tensor $\boldsymbol{A}$ can be expressed as $\boldsymbol{A} = \alpha\, \boldsymbol{I}$ and it holds $\boldsymbol{u} = \boldsymbol{v} = \sqrt{\beta}\, \boldsymbol{u}_0$, where $\boldsymbol{u}_0$ is a unit vector. Inserting those simplifications into Eq. A.27 leads to

$$(\alpha\, \boldsymbol{I} + \beta\, \boldsymbol{u}_0 \otimes \boldsymbol{u}_0)^{-1} = \frac{1}{\alpha}\, \boldsymbol{I} - \frac{\beta}{\alpha\,(\alpha + \beta)}\, \boldsymbol{u}_0 \otimes \boldsymbol{u}_0. \tag{A.28}$$

A.3 Voigt notation

Using Voigt notation, an effective matrix notation of equations involving tensors of fourth order, as for example the constitutive equation

$$\Delta \boldsymbol{S} = \mathbb{C} : \tfrac{1}{2}\, \Delta \boldsymbol{C} \qquad \text{or} \qquad \Delta S_{ij} = \mathbb{C}_{ijkl}\, \tfrac{1}{2}\, \Delta C_{kl} \tag{A.29}$$

from Eq. 4.14, is enabled. To this end, tensors of second order are represented by vectors and tensors of fourth order by matrices. Moreover, symmetries are exploited, such that the

dimensions can be reduced from $3^2 = 9$ to 6 and from $3^4 = 9^2 = 81$ to $6^2 = 36$ for tensors of 2^{nd} and 4^{th} order, respectively. To begin with, the generally valid notation

$$\begin{bmatrix} \Delta S_{11} \\ \Delta S_{22} \\ \Delta S_{33} \\ \Delta S_{12} \\ \Delta S_{23} \\ \Delta S_{13} \\ \Delta S_{21} \\ \Delta S_{32} \\ \Delta S_{31} \end{bmatrix} = \begin{bmatrix} \mathbb{C}_{1111} & \mathbb{C}_{1122} & \mathbb{C}_{1133} & \mathbb{C}_{1112} & \mathbb{C}_{1123} & \mathbb{C}_{1113} & \mathbb{C}_{1121} & \mathbb{C}_{1132} & \mathbb{C}_{1131} \\ \mathbb{C}_{2211} & \mathbb{C}_{2222} & \mathbb{C}_{2233} & \mathbb{C}_{2212} & \mathbb{C}_{2223} & \mathbb{C}_{2213} & \mathbb{C}_{2221} & \mathbb{C}_{2232} & \mathbb{C}_{2231} \\ \mathbb{C}_{3311} & \mathbb{C}_{3322} & \mathbb{C}_{3333} & \mathbb{C}_{3312} & \mathbb{C}_{3323} & \mathbb{C}_{3313} & \mathbb{C}_{3321} & \mathbb{C}_{3332} & \mathbb{C}_{3331} \\ \mathbb{C}_{1211} & \mathbb{C}_{1222} & \mathbb{C}_{1233} & \mathbb{C}_{1212} & \mathbb{C}_{1223} & \mathbb{C}_{1213} & \mathbb{C}_{1221} & \mathbb{C}_{1232} & \mathbb{C}_{1231} \\ \mathbb{C}_{2311} & \mathbb{C}_{2322} & \mathbb{C}_{2333} & \mathbb{C}_{2312} & \mathbb{C}_{2323} & \mathbb{C}_{2313} & \mathbb{C}_{2321} & \mathbb{C}_{2332} & \mathbb{C}_{2331} \\ \mathbb{C}_{1311} & \mathbb{C}_{1322} & \mathbb{C}_{1333} & \mathbb{C}_{1312} & \mathbb{C}_{1323} & \mathbb{C}_{1313} & \mathbb{C}_{1321} & \mathbb{C}_{1332} & \mathbb{C}_{1331} \\ \mathbb{C}_{2111} & \mathbb{C}_{2122} & \mathbb{C}_{2133} & \mathbb{C}_{2112} & \mathbb{C}_{2123} & \mathbb{C}_{2113} & \mathbb{C}_{2121} & \mathbb{C}_{2132} & \mathbb{C}_{2131} \\ \mathbb{C}_{3211} & \mathbb{C}_{3222} & \mathbb{C}_{3233} & \mathbb{C}_{3212} & \mathbb{C}_{3223} & \mathbb{C}_{3213} & \mathbb{C}_{3221} & \mathbb{C}_{3232} & \mathbb{C}_{3231} \\ \mathbb{C}_{3111} & \mathbb{C}_{3122} & \mathbb{C}_{3133} & \mathbb{C}_{3112} & \mathbb{C}_{3123} & \mathbb{C}_{3113} & \mathbb{C}_{3121} & \mathbb{C}_{3132} & \mathbb{C}_{3131} \end{bmatrix} \begin{bmatrix} \frac{1}{2}\,\Delta C_{11} \\ \frac{1}{2}\,\Delta C_{22} \\ \frac{1}{2}\,\Delta C_{33} \\ \frac{1}{2}\,\Delta C_{12} \\ \frac{1}{2}\,\Delta C_{23} \\ \frac{1}{2}\,\Delta C_{13} \\ \frac{1}{2}\,\Delta C_{21} \\ \frac{1}{2}\,\Delta C_{32} \\ \frac{1}{2}\,\Delta C_{31} \end{bmatrix}$$

of Eq. A.29 is considered. Due to the symmetry of $\boldsymbol{S}$, see Eq. 3.56, the rows 7–9 of this system of equations are redundant and can be omitted. Furthermore, the symmetry of $\boldsymbol{C}$ stated in Eq. 3.12 and various symmetries of $\mathbb{C}$ can be taken into account. Since the order of the partial derivatives in

$$\mathbb{C}_{ijkl} = 4\,\frac{\partial^2 \psi}{\partial C_{ij}\,\partial C_{kl}} = 4\,\frac{\partial^2 \psi}{\partial C_{kl}\,\partial C_{ij}}$$

is interchangable, the tangent modulus shows the main symmetry

$$\mathbb{C}_{ijkl} = \mathbb{C}_{klij}. \tag{A.30}$$

Beyond that, the symmetry of $\boldsymbol{C}$ implicates right and left subsymmetry of $\mathbb{C}$, i. e.

$$\mathbb{C}_{ijkl} = \mathbb{C}_{ijlk} \qquad \text{and} \qquad \mathbb{C}_{ijkl} = \mathbb{C}_{jikl}. \tag{A.31}$$

Including the symmetry of $\boldsymbol{C}$ and right subsymmetry of $\mathbb{C}$, the reduced system of equations, with changes highlighted in bold face, reads

$$\begin{bmatrix} \Delta S_{11} \\ \Delta S_{22} \\ \Delta S_{33} \\ \Delta S_{12} \\ \Delta S_{23} \\ \Delta S_{13} \end{bmatrix} = \begin{bmatrix} \mathbb{C}_{1111} & \mathbb{C}_{1122} & \mathbb{C}_{1133} & \mathbb{C}_{1112} & \mathbb{C}_{1123} & \mathbb{C}_{1113} & \mathbb{C}_{11\mathbf{12}} & \mathbb{C}_{11\mathbf{23}} & \mathbb{C}_{11\mathbf{13}} \\ \mathbb{C}_{2211} & \mathbb{C}_{2222} & \mathbb{C}_{2233} & \mathbb{C}_{2212} & \mathbb{C}_{2223} & \mathbb{C}_{2213} & \mathbb{C}_{22\mathbf{12}} & \mathbb{C}_{22\mathbf{23}} & \mathbb{C}_{22\mathbf{13}} \\ \mathbb{C}_{3311} & \mathbb{C}_{3322} & \mathbb{C}_{3333} & \mathbb{C}_{3312} & \mathbb{C}_{3323} & \mathbb{C}_{3313} & \mathbb{C}_{33\mathbf{12}} & \mathbb{C}_{33\mathbf{23}} & \mathbb{C}_{33\mathbf{13}} \\ \mathbb{C}_{1211} & \mathbb{C}_{1222} & \mathbb{C}_{1233} & \mathbb{C}_{1212} & \mathbb{C}_{1223} & \mathbb{C}_{1213} & \mathbb{C}_{12\mathbf{12}} & \mathbb{C}_{12\mathbf{23}} & \mathbb{C}_{12\mathbf{13}} \\ \mathbb{C}_{2311} & \mathbb{C}_{2322} & \mathbb{C}_{2333} & \mathbb{C}_{2312} & \mathbb{C}_{2323} & \mathbb{C}_{2313} & \mathbb{C}_{23\mathbf{12}} & \mathbb{C}_{23\mathbf{23}} & \mathbb{C}_{23\mathbf{13}} \\ \mathbb{C}_{1311} & \mathbb{C}_{1322} & \mathbb{C}_{1333} & \mathbb{C}_{1312} & \mathbb{C}_{1323} & \mathbb{C}_{1313} & \mathbb{C}_{13\mathbf{12}} & \mathbb{C}_{13\mathbf{23}} & \mathbb{C}_{13\mathbf{13}} \end{bmatrix} \begin{bmatrix} \frac{1}{2}\,\Delta C_{11} \\ \frac{1}{2}\,\Delta C_{22} \\ \frac{1}{2}\,\Delta C_{33} \\ \frac{1}{2}\,\Delta C_{12} \\ \frac{1}{2}\,\Delta C_{23} \\ \frac{1}{2}\,\Delta C_{13} \\ \frac{1}{2}\,\Delta C_{\mathbf{12}} \\ \frac{1}{2}\,\Delta C_{\mathbf{23}} \\ \frac{1}{2}\,\Delta C_{\mathbf{13}} \end{bmatrix}.$$

Therein, columns 7–9 of $\mathbb{C}$ can be added to columns 4–6 because the associated components of $\Delta\boldsymbol{C}$ occur twice in the vector on the right hand side. This reduces the system to

$$\begin{bmatrix} \Delta S_{11} \\ \Delta S_{22} \\ \Delta S_{33} \\ \Delta S_{12} \\ \Delta S_{23} \\ \Delta S_{13} \end{bmatrix} = \begin{bmatrix} \mathbb{C}_{1111} & \mathbb{C}_{1122} & \mathbb{C}_{1133} & 2\,\mathbb{C}_{1112} & 2\,\mathbb{C}_{1123} & 2\,\mathbb{C}_{1113} \\ \mathbb{C}_{2211} & \mathbb{C}_{2222} & \mathbb{C}_{2233} & 2\,\mathbb{C}_{2212} & 2\,\mathbb{C}_{2223} & 2\,\mathbb{C}_{2213} \\ \mathbb{C}_{3311} & \mathbb{C}_{3322} & \mathbb{C}_{3333} & 2\,\mathbb{C}_{3312} & 2\,\mathbb{C}_{3323} & 2\,\mathbb{C}_{3313} \\ \mathbb{C}_{1211} & \mathbb{C}_{1222} & \mathbb{C}_{1233} & 2\,\mathbb{C}_{1212} & 2\,\mathbb{C}_{1223} & 2\,\mathbb{C}_{1213} \\ \mathbb{C}_{2311} & \mathbb{C}_{2322} & \mathbb{C}_{2333} & 2\,\mathbb{C}_{2312} & 2\,\mathbb{C}_{2323} & 2\,\mathbb{C}_{2313} \\ \mathbb{C}_{1311} & \mathbb{C}_{1322} & \mathbb{C}_{1333} & 2\,\mathbb{C}_{1312} & 2\,\mathbb{C}_{1323} & 2\,\mathbb{C}_{1313} \end{bmatrix} \begin{bmatrix} \frac{1}{2}\,\Delta C_{11} \\ \frac{1}{2}\,\Delta C_{22} \\ \frac{1}{2}\,\Delta C_{33} \\ \frac{1}{2}\,\Delta C_{12} \\ \frac{1}{2}\,\Delta C_{23} \\ \frac{1}{2}\,\Delta C_{13} \end{bmatrix},$$

where the factor 2 can also be transferred to the vector containing the increments of the deformation. Finally, making use of Eq. A.30, the Voigt notation of Eq. A.29 is

$$\begin{bmatrix} \Delta S_{11} \\ \Delta S_{22} \\ \Delta S_{33} \\ \Delta S_{12} \\ \Delta S_{23} \\ \Delta S_{13} \end{bmatrix} = \begin{bmatrix} \mathbb{C}_{1111} & \mathbb{C}_{1122} & \mathbb{C}_{1133} & \mathbb{C}_{1112} & \mathbb{C}_{1123} & \mathbb{C}_{1113} \\ & \mathbb{C}_{2222} & \mathbb{C}_{2233} & \mathbb{C}_{2212} & \mathbb{C}_{2223} & \mathbb{C}_{2213} \\ & & \mathbb{C}_{3333} & \mathbb{C}_{3312} & \mathbb{C}_{3323} & \mathbb{C}_{3313} \\ & & & \mathbb{C}_{1212} & \mathbb{C}_{1223} & \mathbb{C}_{1213} \\ & \text{sym.} & & & \mathbb{C}_{2323} & \mathbb{C}_{2313} \\ & & & & & \mathbb{C}_{1313} \end{bmatrix} \begin{bmatrix} \frac{1}{2}\,\Delta C_{11} \\ \frac{1}{2}\,\Delta C_{22} \\ \frac{1}{2}\,\Delta C_{33} \\ \Delta C_{12} \\ \Delta C_{23} \\ \Delta C_{13} \end{bmatrix} . \tag{A.32}$$

This form of the deformation vector permits use of the standard scalar product between a stress and a deformation tensor in Voigt notation, as for example $\boldsymbol{S} : {}^1\!/_2\,\delta\boldsymbol{C} = \underline{\boldsymbol{S}} \cdot {}^1\!/_2\,\delta\underline{\boldsymbol{C}}$ in Eq. 4.36, for terms with mixed components have to appear doubly.

B Tabulated results of the parameter optimization

In this appendix, the growth parameters determined by minimization of the objective function defined in Sec. 7.5.1 and the corresponding values of this function are listed in tabular form. They are valid for one- and two-layered, idealized arterial segments as specified in Sec. 7.2, Sec. 7.5.2 and Sec. 8.1, which are loaded with an internal pressure of 120 mmHg and an axial strain ε_z. Three different modes have been considered for the optimization:

- mode O 1: optimization of $\vartheta^+_{(a)}$,
- mode O 2: optimization of $\vartheta^+_{(a)}$ and ε_z,
- mode O 3: optimization of $\vartheta^+_{(a)}$ with averaging over different levels of ε_z.

The values of the optimization variables have been restricted to the ranges $[1.0001, 1.5]$ for $\vartheta^+_{(a)}$ and $[0\,\%, 30\,\%]$ for ε_z. An explanation of the abbreviated designation of the model variants in the first colum of the following tables can be found in Tab. 7.6.
Although it should be expected that the values of the objective function obtained in mode O 2 are the lowest, this is not always the case. The applied algorithm for the minimization of the objective function can thus in general not be assumed to have found the global minimum.

Table B.1: Optimized growth parameters for the one-layered arterial segment defined in Sec. 7.2, loaded with a pressure of 120 mmHg.

model	mode	ε_z	$\vartheta^+_{(1)}$	$\vartheta^+_{(2)}$	$\vartheta^+_{(3)}$	f_{obj}
0 0	–	0 %	–	–	–	5.2233
	–	5 %	–	–	–	5.7375
	–	10 %	–	–	–	5.9039
	–	15 %	–	–	–	5.7296
	–	20 %	–	–	–	5.2509
□i	O 1	0 %	1.034647	–	–	3.6265
	O 1	5 %	1.084513	–	–	3.6903
	O 1	10 %	1.142806	–	–	3.8115
	O 1	15 %	1.201195	–	–	3.9761
	O 1	20 %	1.259895	–	–	4.1765
	O 2	0.0000 %	1.034481	–	–	3.6267
	O 3	0/5/10/15 %	1.163530	–	–	4.0820

(continued on next page)

Table B.1: Optimized growth parameters for the one-layered arterial segment defined in Sec. 7.2, loaded with a pressure of 120 mmHg *(continued)*.

model	mode	ε_z	$\vartheta^+_{(1)}$	$\vartheta^+_{(2)}$	$\vartheta^+_{(3)}$	f_{obj}
□d	O 1	0 %	1.048793	–	–	3.6022
	O 1	5 %	1.084363	–	–	3.6516
	O 1	10 %	1.142500	–	–	3.7555
	O 1	15 %	1.200742	–	–	3.9096
	O 1	20 %	1.259176	–	–	4.1036
	O 2	0.0051 %	1.045989	–	–	3.6024
	O 3	0/5/10/15 %	1.142494	–	–	4.0755
□t	O 1	0 %	1.049296	–	–	3.6022
	O 1	5 %	1.084363	–	–	3.6516
	O 1	10 %	1.142447	–	–	3.7559
	O 1	15 %	1.200804	–	–	3.9092
	O 1	20 %	1.258996	–	–	4.1042
	O 2	0.0093 %	1.034365	–	–	3.6072
	O 3	0/5/10/15 %	1.142475	–	–	4.0755
⊥i	O 1	0 %	1.064338	–	–	2.8081
	O 1	5 %	1.094243	–	–	2.5877
	O 1	10 %	1.123648	–	–	2.5177
	O 1	15 %	1.154063	–	–	2.6089
	O 1	20 %	1.180923	–	–	2.7144
	O 2	8.1482 %	1.112619	–	–	2.4812
	O 3	0/5/10/15 %	1.102878	–	–	3.2297
⊥d	O 1	0 %	1.063536	–	–	2.8118
	O 1	5 %	1.093213	–	–	2.5868
	O 1	10 %	1.122496	–	–	2.5317
	O 1	15 %	1.152802	–	–	2.6249
	O 1	20 %	1.180466	–	–	2.7347
	O 2	8.3245 %	1.112385	–	–	2.4987
	O 3	0/5/10/15 %	1.103561	–	–	3.2660
⊥t	O 1	0 %	1.063511	–	–	2.8122
	O 1	5 %	1.092966	–	–	2.5892
	O 1	10 %	1.122503	–	–	2.5317
	O 1	15 %	1.153023	–	–	2.6248
	O 1	20 %	1.180471	–	–	2.7347
	O 2	9.8384 %	1.120875	–	–	2.5294
	O 3	0/5/10/15 %	1.103557	–	–	3.2660
∥ i	O 1	0 %	1.000100	–	–	4.2523
	O 1	5 %	1.000100	–	–	5.8755
	O 1	10 %	1.000100	–	–	9.9153
	O 1	15 %	1.499997	–	–	18.456

(continued on next page)

Table B.1: Optimized growth parameters for the one-layered arterial segment defined in Sec. 7.2, loaded with a pressure of 120 mmHg *(continued)*.

model	mode	ε_z	$\vartheta^+_{(1)}$	$\vartheta^+_{(2)}$	$\vartheta^+_{(3)}$	f_{obj}
	O 1	20 %	1.499999	–	–	29.544
	O 2	0.0006 %	1.000113	–	–	4.2528
	O 3	0/5/10/15 %	1.000104	–	–	10.497
∥ d	O 1	0 %	1.000100	–	–	4.2523
	O 1	5 %	1.000100	–	–	5.8755
	O 1	10 %	1.000113	–	–	9.9153
	O 1	15 %	1.499998	–	–	17.479
	O 1	20 %	1.499999	–	–	27.810
	O 2	0.0000 %	1.000100	–	–	4.2523
	O 3	0/5/10/15 %	1.000101	–	–	10.497
∥ t	O 1	0 %	1.000103	–	–	4.2523
	O 1	5 %	1.000105	–	–	5.8755
	O 1	10 %	1.000113	–	–	9.9153
	O 1	15 %	1.500000	–	–	17.479
	O 1	20 %	1.499999	–	–	27.810
	O 2	0.0000 %	1.000100	–	–	4.2523
	O 3	0/5/10/15 %	1.000100	–	–	10.497
0 0 0 0 ⊥ i	O 1	0 %	–	–	1.027313	3.9891
	O 1	5 %	–	–	1.095845	4.5612
	O 1	10 %	–	–	1.156392	5.0776
	O 1	15 %	–	–	1.218434	5.5512
	O 1	20 %	–	–	1.280025	6.0061
	O 2	0.0018 %	–	–	1.027351	3.9889
	O 3	0/5/10/15 %	–	–	1.158164	5.5349
0 0 0 0 ⊥ d	O 1	0 %	–	–	1.001614	10.762
	O 1	5 %	–	–	1.019152	16.759
	O 1	10 %	–	–	1.202642	29.441
	O 1	15 %	–	–	1.019367	45.494
	O 1	20 %	–	–	1.002856	78.128
	O 2	1.0480 %	–	–	1.230843	10.493
	O 3	0/5/10/15 %	–	–	1.419386	26.238
0 0 0 0 ⊥ t	O 1	0 %	–	–	1.000221	4.2500
	O 1	5 %	–	–	1.000520	5.9791
	O 1	10 %	–	–	1.491884	9.9150
	O 1	15 %	–	–	1.493666	21.946
	O 1	20 %	–	–	1.484589	37.923
	O 2	0.0000 %	–	–	1.241077	4.2500
	O 3	0/5/10/15 %	–	–	1.000100	10.523
0 0 0 0 ∥ i	O 1	0 %	–	–	1.144761	2.4252

(continued on next page)

Table B.1: Optimized growth parameters for the one-layered arterial segment defined in Sec. 7.2, loaded with a pressure of 120 mmHg *(continued)*.

model	mode	ε_z	$\vartheta^+_{(1)}$	$\vartheta^+_{(2)}$	$\vartheta^+_{(3)}$	f_{obj}
	O 1	5 %	–	–	1.193658	2.7418
	O 1	10 %	–	–	1.127384	8.8012
	O 1	15 %	–	–	1.025350	21.446
	O 1	20 %	–	–	1.014602	37.521
	O 2	0.0000 %	–	–	1.144809	2.4252
	O 3	0/5/10/15 %	–	–	1.147747	9.0320
0 0 0 0 ‖ d	O 1	0 %	–	–	1.481616	5.1038
	O 1	5 %	–	–	1.107153	7.1959
	O 1	10 %	–	–	1.266417	10.691
	O 1	15 %	–	–	1.003277	23.269
	O 1	20 %	–	–	1.003726	40.116
	O 2	0.0000 %	–	–	1.240150	5.1038
	O 3	0/5/10/15 %	–	–	1.003825	11.559
0 0 0 0 ‖ t	O 1	0 %	–	–	1.018261	4.2499
	O 1	5 %	–	–	1.000511	5.9757
	O 1	10 %	–	–	1.130255	9.9149
	O 1	15 %	–	–	1.479252	21.946
	O 1	20 %	–	–	1.148732	37.923
	O 2	0.0000 %	–	–	1.245024	4.2499
	O 3	0/5/10/15 %	–	–	1.000552	10.522
□d□d	O 1	0 %	1.152916	1.282138	–	3.7015
	O 1	5 %	1.195351	1.305421	–	3.8492
	O 1	10 %	1.121014	1.008725	–	3.9057
	O 1	15 %	1.159110	1.025290	–	4.0948
	O 1	20 %	1.230028	1.015234	–	4.1999
	O 2	0.0051 %	1.152627	1.498874	–	3.7016
	O 3	0/5/10/15 %	1.172453	1.007775	–	4.0174
□t□t	O 1	0 %	1.016333	1.475580	–	3.5305
	O 1	5 %	1.086111	1.005018	–	3.6549
	O 1	10 %	1.147789	1.001279	–	3.7295
	O 1	15 %	1.208550	1.000382	–	3.8826
	O 1	20 %	1.261876	1.000355	–	4.0781
	O 2	0.0061 %	1.016594	1.495110	–	3.5308
	O 3	0/5/10/15 %	1.111504	1.062377	–	3.9900
⊥i⊥i	O 1	0 %	1.066631	1.009271	–	2.8325
	O 1	5 %	1.088062	1.012502	–	2.7106
	O 1	10 %	1.123817	1.017741	–	2.5617
	O 1	15 %	1.154456	1.038033	–	2.7108
	O 1	20 %	1.179818	1.002580	–	2.7239
	O 2	8.3757 %	1.114636	1.034965	–	2.5957

(continued on next page)

Table B.1: Optimized growth parameters for the one-layered arterial segment defined in Sec. 7.2, loaded with a pressure of 120 mmHg *(continued)*.

model	mode	ε_z	$\vartheta^+_{(1)}$	$\vartheta^+_{(2)}$	$\vartheta^+_{(3)}$	f_{obj}
	O 3	0/5/10/15 %	1.102747	1.002457	–	3.1956
⊥d⊥d	O 1	0 %	1.073563	1.000708	–	2.8704
	O 1	5 %	1.114568	1.021502	–	2.8165
	O 1	10 %	1.116128	1.000365	–	2.6335
	O 1	15 %	1.153100	1.012031	–	2.6559
	O 1	20 %	1.182553	1.027899	–	2.8041
	O 2	11.699 %	1.132105	1.017357	–	2.6668
	O 3	0/5/10/15 %	1.113562	1.002720	–	3.1822
⊥t⊥t	O 1	0 %	1.061927	1.061881	–	2.8427
	O 1	5 %	1.091068	1.002892	–	2.6527
	O 1	10 %	1.123492	1.007065	–	2.5448
	O 1	15 %	1.153225	1.023220	–	2.6964
	O 1	20 %	1.179533	1.036157	–	2.8401
	O 2	8.8198 %	1.115226	1.002529	–	2.5146
	O 3	0/5/10/15 %	1.103302	1.005122	–	3.2313
‖ i‖ i	O 1	0 %	1.001112	1.115933	–	3.4191
	O 1	5 %	1.004237	1.191331	–	3.4734
	O 1	10 %	1.003624	1.258596	–	3.5230
	O 1	15 %	1.000115	1.322997	–	3.5403
	O 1	20 %	1.001010	1.390435	–	3.6228
	O 2	0.1708 %	1.001083	1.124115	–	3.3805
	O 3	0/5/10/15 %	1.000603	1.160465	–	3.9075
‖ d‖ d	O 1	0 %	1.000100	1.499978	–	3.7030
	O 1	5 %	1.000100	1.499995	–	3.7495
	O 1	10 %	1.000102	1.497986	–	3.7945
	O 1	15 %	1.000100	1.498129	–	3.8408
	O 1	20 %	1.000100	1.463538	–	3.8890
	O 2	0.0000 %	1.000100	1.499998	–	3.7030
	O 3	0/5/10/15 %	1.000102	1.497989	–	3.7719
‖ t‖ t	O 1	0 %	1.000100	1.499996	–	3.6421
	O 1	5 %	1.000100	1.499965	–	3.7495
	O 1	10 %	1.000102	1.497990	–	3.7945
	O 1	15 %	1.000100	1.498131	–	3.8408
	O 1	20 %	1.000104	1.499600	–	3.8147
	O 2	0.0000 %	1.000100	1.499996	–	3.6421
	O 3	0/5/10/15 %	1.000103	1.497988	–	3.7567
□d□d□d	O 1	0 %	1.001536	1.122055	1.048060	4.1118
	O 1	5 %	1.000177	1.185161	1.473355	4.1577
	O 1	10 %	1.000164	1.240193	1.400551	4.2351

(continued on next page)

Table B.1: Optimized growth parameters for the one-layered arterial segment defined in Sec. 7.2, loaded with a pressure of 120 mmHg *(continued)*.

model	mode	ε_z	$\vartheta^+_{(1)}$	$\vartheta^+_{(2)}$	$\vartheta^+_{(3)}$	f_{obj}
	O 1	15 %	1.000250	1.300355	1.239198	4.3470
	O 1	20 %	1.000102	1.358668	1.341997	4.4925
	O 2	0.0054 %	1.000369	1.125495	1.235526	4.1104
	O 3	0/5/10/15 %	1.000519	1.288926	1.239453	4.2403
□t□t□t	O 1	0 %	1.016668	1.467639	1.074687	3.5302
	O 1	5 %	1.088938	1.003567	1.007788	3.6292
	O 1	10 %	1.151169	1.004472	1.245232	3.7201
	O 1	15 %	1.208848	1.007086	1.255822	3.8827
	O 1	20 %	1.257566	1.007022	1.237691	4.0883
	O 2	0.0065 %	1.017204	1.334986	1.250192	3.5316
	O 3	0/5/10/15 %	1.115430	1.052379	1.499591	3.9620
⊥i⊥i⊥i	O 1	0 %	1.066691	1.000309	1.000147	2.8245
	O 1	5 %	1.098511	1.000707	1.000184	2.5983
	O 1	10 %	1.123571	1.000731	1.000296	2.5198
	O 1	15 %	1.151534	1.002144	1.012878	2.6359
	O 1	20 %	1.182977	1.013041	1.024253	2.7658
	O 2	7.9076 %	1.114275	1.003373	1.005929	2.5605
	O 3	0/5/10/15 %	1.102526	1.000700	1.000215	3.1667
⊥d⊥d⊥d	O 1	0 %	1.050684	1.030263	1.014616	3.1463
	O 1	5 %	1.105697	1.020412	1.267420	2.7589
	O 1	10 %	1.167141	1.022606	1.019667	2.6903
	O 1	15 %	1.258967	1.004119	1.055095	2.8671
	O 1	20 %	1.290966	1.019103	1.169003	2.9561
	O 2	7.6047 %	1.177795	1.185887	1.274766	2.9013
	O 3	0/5/10/15 %	1.159761	1.211905	1.214855	3.4808
⊥t⊥t⊥t	O 1	0 %	1.064920	1.018585	1.479705	2.8183
	O 1	5 %	1.099112	1.005322	1.488755	2.6051
	O 1	10 %	1.124582	1.007720	1.243193	2.5423
	O 1	15 %	1.154871	1.021459	1.245154	2.6750
	O 1	20 %	1.178507	1.016307	1.253611	2.7851
	O 2	10.350 %	1.129316	1.014389	1.225677	2.5648
	O 3	0/5/10/15 %	1.103419	1.002697	1.030136	3.2078
‖i‖i‖i	O 1	0 %	1.005063	1.020595	1.119918	2.3998
	O 1	5 %	1.016900	1.057109	1.163843	2.5171
	O 1	10 %	1.007801	1.120313	1.137009	2.5417
	O 1	15 %	1.003387	1.189755	1.118764	2.5707
	O 1	20 %	1.006374	1.231784	1.132856	2.6605
	O 2	0.4062 %	1.007372	1.022416	1.125989	2.4135
	O 3	0/5/10/15 %	1.001006	1.100583	1.142324	3.1899

(continued on next page)

Table B.1: Optimized growth parameters for the one-layered arterial segment defined in Sec. 7.2, loaded with a pressure of 120 mmHg *(continued)*.

model	mode	ε_z	$\vartheta^+_{(1)}$	$\vartheta^+_{(2)}$	$\vartheta^+_{(3)}$	f_{obj}
∥ d∥ d∥ d	O 1	0 %	1.000100	1.499992	1.243559	4.2473
	O 1	5 %	1.000101	1.499425	1.243760	4.2755
	O 1	10 %	1.000100	1.499996	1.298126	4.3174
	O 1	15 %	1.000100	1.499997	1.449946	4.3661
	O 1	20 %	1.000100	1.499999	1.006665	4.4200
	O 2	0.3915 %	1.000101	1.487519	1.402966	4.2423
	O 3	0/5/10/15 %	1.000100	1.499996	1.310316	4.3016
∥ t∥ t∥ t	O 1	0 %	1.000100	1.499995	1.104587	3.6421
	O 1	5 %	1.000100	1.499996	1.247040	3.7495
	O 1	10 %	1.000103	1.497991	1.239202	3.7945
	O 1	15 %	1.000100	1.498134	1.119734	3.8408
	O 1	20 %	1.000103	1.499619	1.323300	3.8147
	O 2	0.0000 %	1.000100	1.499997	1.249797	3.6421
	O 3	0/5/10/15 %	1.000103	1.497994	1.022877	3.7567
□i□i⊥i	O 1	0 %	1.048793	1.000104	1.000100	3.6153
	O 1	5 %	1.094582	1.000172	1.000102	3.6574
	O 1	10 %	1.154087	1.000109	1.000157	3.7854
	O 1	15 %	1.215298	1.000182	1.000190	3.9539
	O 1	20 %	1.260986	1.000694	1.000211	4.1608
	O 2	0.0000 %	1.000113	1.048890	1.000100	3.6153
	O 3	0/5/10/15 %	1.167208	1.000293	1.000101	4.0405
□i□i∥ i	O 1	0 %	1.000304	1.000101	1.144068	2.4255
	O 1	5 %	1.002702	1.035131	1.172096	2.5990
	O 1	10 %	1.081800	1.000171	1.185103	2.7911
	O 1	15 %	1.108466	1.011878	1.200064	3.0034
	O 1	20 %	1.020444	1.149290	1.207779	3.2368
	O 2	0.0000 %	1.008594	1.001264	1.128635	2.4315
	O 3	0/5/10/15 %	1.095486	1.000391	1.126718	3.3022
□d□d⊥i	O 1	0 %	1.151438	1.020198	1.000329	3.7039
	O 1	5 %	1.197121	1.274924	1.000208	3.8442
	O 1	10 %	1.249440	1.480331	1.000293	3.9959
	O 1	15 %	1.296151	1.113895	1.002324	4.1922
	O 1	20 %	1.219424	1.018611	1.004126	4.2568
	O 2	0.0030 %	1.150786	1.266159	1.000117	3.7017
	O 3	0/5/10/15 %	1.185026	1.468979	1.000373	4.1261
□d□d∥ i	O 1	0 %	1.037131	1.016536	1.475242	2.3932
	O 1	5 %	1.094988	1.288989	1.487793	2.6444
	O 1	10 %	1.069327	1.000143	1.188214	2.8025
	O 1	15 %	1.036513	1.091172	1.214867	2.9919

(continued on next page)

Table B.1: Optimized growth parameters for the one-layered arterial segment defined in Sec. 7.2, loaded with a pressure of 120 mmHg *(continued)*.

model	mode	ε_z	$\vartheta^+_{(1)}$	$\vartheta^+_{(2)}$	$\vartheta^+_{(3)}$	f_{obj}
	O 1	20 %	1.142965	1.024898	1.193479	3.2540
	O 2	0.0000 %	1.030276	1.078043	1.492791	2.3991
	O 3	0/5/10/15 %	1.003078	1.235385	1.427467	2.9211
⊥d⊥d⊥ i	O 1	0 %	1.075106	1.484905	1.003708	2.9465
	O 1	5 %	1.115035	1.000110	1.000799	2.8671
	O 1	10 %	1.116917	1.000312	1.000420	2.6138
	O 1	15 %	1.150252	1.009893	1.011794	2.6902
	O 1	20 %	1.179214	1.000627	1.009419	2.7417
	O 2	16.544 %	1.167921	1.032572	1.015053	2.7378
	O 3	0/5/10/15 %	1.115698	1.000374	1.001158	3.1715
⊥d⊥d‖ i	O 1	0 %	1.005517	1.000225	1.128444	2.4164
	O 1	5 %	1.025299	1.001495	1.145896	2.5575
	O 1	10 %	1.062827	1.000120	1.109125	2.6709
	O 1	15 %	1.128128	1.012307	1.043204	2.7039
	O 1	20 %	1.171838	1.003695	1.008177	2.7689
	O 2	0.1449 %	1.000391	1.005983	1.149435	2.4380
	O 3	0/5/10/15 %	1.102831	1.110065	1.041245	3.3518
‖ i‖ i⊥i	O 1	0 %	1.000116	1.124166	1.000406	3.3682
	O 1	5 %	1.000111	1.188587	1.000120	3.4496
	O 1	10 %	1.000284	1.261526	1.000165	3.4903
	O 1	15 %	1.000410	1.326636	1.000424	3.5832
	O 1	20 %	1.000108	1.401325	1.000142	3.6136
	O 2	0.0001 %	1.000105	1.122073	1.000104	3.3795
	O 3	0/5/10/15 %	1.001812	1.161554	1.001141	3.9057
‖ d‖ d‖ i	O 1	0 %	1.002425	1.204309	1.146233	2.2780
	O 1	5 %	1.003431	1.324583	1.149376	2.3421
	O 1	10 %	1.007470	1.299598	1.154931	2.4243
	O 1	15 %	1.002685	1.411955	1.147400	2.4923
	O 1	20 %	1.001657	1.440732	1.145135	2.5593
	O 2	1.2551 %	1.000882	1.234826	1.141419	2.3148
	O 3	0/5/10/15 %	1.003214	1.418505	1.149910	2.3815

Table B.2: Optimized growth parameters for the two-layered arterial segment defined in Sec. 7.5.2, loaded with an internal pressure of 120 mmHg.

model	mode	ε_z	layer	$\vartheta^+_{(1)}$	$\vartheta^+_{(2)}$	$\vartheta^+_{(3)}$	f_{obj}
0 0	–	0 %	media	–	–	–	6.2036
			adventitia	–	–	–	
	–	5 %	media	–	–	–	6.2500
			adventitia	–	–	–	
	–	10 %	media	–	–	–	7.0324
			adventitia	–	–	–	
	–	15 %	media	–	–	–	7.2123
			adventitia	–	–	–	
	–	20 %	media	–	–	–	6.9595
			adventitia	–	–	–	
□i	O 1	0 %	media	1.028947	–	–	4.6424
			adventitia	1.005524	–	–	
	O 1	5 %	media	1.087554	–	–	4.8809
			adventitia	1.054811	–	–	
	O 1	10 %	media	1.123893	–	–	5.2120
			adventitia	1.097525	–	–	
	O 1	15 %	media	1.175551	–	–	5.5589
			adventitia	1.148973	–	–	
	O 1	20 %	media	1.230963	–	–	5.9623
			adventitia	1.201486	–	–	
	O 2	0.0796 %	media	1.030319	–	–	4.6165
			adventitia	1.000155	–	–	
	O 3	0/5/10/15 %	media	1.118697	–	–	5.5922
			adventitia	1.088086	–	–	
□d	O 1	0 %	media	1.029586	–	–	4.6008
			adventitia	1.000112	–	–	
	O 1	5 %	media	1.067190	–	–	4.8911
			adventitia	1.036425	–	–	
	O 1	10 %	media	1.113287	–	–	5.2366
			adventitia	1.085411	–	–	
	O 1	15 %	media	1.168124	–	–	5.5934
			adventitia	1.122291	–	–	
	O 1	20 %	media	1.210508	–	–	6.0337
			adventitia	1.228261	–	–	
	O 2	0.0019 %	media	1.019926	–	–	4.6905
			adventitia	1.000139	–	–	
	O 3	0/5/10/15 %	media	1.110237	–	–	5.5498
			adventitia	1.088275	–	–	
□t	O 1	0 %	media	1.030447	–	–	4.6190
			adventitia	1.006095	–	–	

(continued on next page)

Table B.2: Optimized growth parameters for the two-layered arterial segment defined in Sec. 7.5.2, loaded with an internal pressure of 120 mmHg *(continued)*.

model	mode	ε_z	layer	$\vartheta^+_{(1)}$	$\vartheta^+_{(2)}$	$\vartheta^+_{(3)}$	f_{obj}
	O 1	5 %	media	1.070197	–	–	4.8843
			adventitia	1.038878	–	–	
	O 1	10 %	media	1.114689	–	–	5.2445
			adventitia	1.110844	–	–	
	O 1	15 %	media	1.161803	–	–	5.6036
			adventitia	1.132264	–	–	
	O 1	20 %	media	1.218687	–	–	5.9616
			adventitia	1.179215	–	–	
	O 2	0.1345 %	media	1.031999	–	–	4.5995
			adventitia	1.001337	–	–	
	O 3	0/5/10/15 %	media	1.103859	–	–	5.5501
			adventitia	1.082677	–	–	
⊥i	O 1	0 %	media	1.067555	–	–	3.7297
			adventitia	1.000461	–	–	
	O 1	5 %	media	1.097982	–	–	3.1003
			adventitia	1.000238	–	–	
	O 1	10 %	media	1.126412	–	–	3.0383
			adventitia	1.036552	–	–	
	O 1	15 %	media	1.159174	–	–	3.2128
			adventitia	1.092235	–	–	
	O 1	20 %	media	1.186398	–	–	3.4215
			adventitia	1.156121	–	–	
	O 2	6.7659 %	media	1.107855	–	–	3.0085
			adventitia	1.011734	–	–	
	O 3	0/5/10/15 %	media	1.097523	–	–	4.1729
			adventitia	1.048113	–	–	
⊥d	O 1	0 %	media	1.066645	–	–	3.7461
			adventitia	1.001454	–	–	
	O 1	5 %	media	1.092100	–	–	3.1683
			adventitia	1.006218	–	–	
	O 1	10 %	media	1.124760	–	–	3.0537
			adventitia	1.040425	–	–	
	O 1	15 %	media	1.157225	–	–	3.2287
			adventitia	1.098681	–	–	
	O 1	20 %	media	1.185279	–	–	3.4576
			adventitia	1.157145	–	–	
	O 2	9.8139 %	media	1.125520	–	–	3.0666
			adventitia	1.047842	–	–	
	O 3	0/5/10/15 %	media	1.097507	–	–	4.1930
			adventitia	1.047543	–	–	

(continued on next page)

Table B.2: Optimized growth parameters for the two-layered arterial segment defined in Sec. 7.5.2, loaded with an internal pressure of 120 mmHg *(continued)*.

model	mode	ε_z	layer	$\vartheta^+_{(1)}$	$\vartheta^+_{(2)}$	$\vartheta^+_{(3)}$	f_{obj}
$\perp$ t	O 1	0 %	media	1.050414	–	–	3.9339
			adventitia	1.004006	–	–	
	O 1	5 %	media	1.096513	–	–	3.1799
			adventitia	1.014042	–	–	
	O 1	10 %	media	1.126880	–	–	3.0420
			adventitia	1.037616	–	–	
	O 1	15 %	media	1.155847	–	–	3.2363
			adventitia	1.100137	–	–	
	O 1	20 %	media	1.186974	–	–	3.4305
			adventitia	1.162707	–	–	
	O 2	8.7042 %	media	1.117255	–	–	3.0068
			adventitia	1.025223	–	–	
	O 3	0/5/10/15 %	media	1.097542	–	–	4.1947
			adventitia	1.046683	–	–	
0 0 0 0 $\perp$ i	O 1	0 %	media	–	–	1.017775	4.9525
			adventitia	–	–	1.000176	
	O 1	5 %	media	–	–	1.083953	5.7636
			adventitia	–	–	1.048686	
	O 1	10 %	media	–	–	1.151775	6.4825
			adventitia	–	–	1.110568	
	O 1	15 %	media	–	–	1.213131	7.1581
			adventitia	–	–	1.168511	
	O 1	20 %	media	–	–	1.273028	7.8571
			adventitia	–	–	1.246636	
	O 2	0.0025 %	media	–	–	1.017808	4.9522
			adventitia	–	–	1.000112	
	O 3	0/5/10/15 %	media	–	–	1.106532	6.9187
			adventitia	–	–	1.076036	
0 0 0 0 $\parallel$ i	O 1	0 %	media	–	–	1.151172	3.3906
			adventitia	–	–	1.058198	
	O 1	5 %	media	–	–	1.208198	3.2641
			adventitia	–	–	1.038319	
	O 1	10 %	media	–	–	1.193851	10.003
			adventitia	–	–	1.007226	
	O 1	15 %	media	–	–	1.499999	26.342
			adventitia	–	–	1.499996	
	O 1	20 %	media	–	–	1.463209	37.943
			adventitia	–	–	1.198045	
	O 2	3.4276 %	media	–	–	1.202843	3.2028
			adventitia	–	–	1.033535	

(continued on next page)

Table B.2: Optimized growth parameters for the two-layered arterial segment defined in Sec. 7.5.2, loaded with an internal pressure of 120 mmHg *(continued)*.

model	mode	ε_z	layer	$\vartheta^+_{(1)}$	$\vartheta^+_{(2)}$	$\vartheta^+_{(3)}$	f_{obj}
	O 3	0/5/10/15 %	media	–	–	1.205600	11.833
			adventitia	–	–	1.497256	
□d□d	O 1	0 %	media	1.000110	1.017519	–	4.7565
			adventitia	1.000204	1.000216	–	
	O 1	5 %	media	1.000635	1.074030	–	4.9436
			adventitia	1.000341	1.042392	–	
	O 1	10 %	media	1.011388	1.118345	–	5.2520
			adventitia	1.062506	1.025764	–	
	O 1	15 %	media	1.000282	1.183789	–	5.5984
			adventitia	1.057473	1.075557	–	
	O 1	20 %	media	1.341255	1.257734	–	6.4261
			adventitia	1.071470	1.175019	–	
	O 2	0.4682 %	media	1.002643	1.021473	–	4.7437
			adventitia	1.000195	1.000177	–	
	O 3	0/5/10/15 %	media	1.099821	1.029911	–	5.5468
			adventitia	1.021313	1.066082	–	
□t□t	O 1	0 %	media	1.012774	1.124325	–	4.6283
			adventitia	1.000322	1.003595	–	
	O 1	5 %	media	1.066434	1.006557	–	4.9034
			adventitia	1.001916	1.040486	–	
	O 1	10 %	media	1.107506	1.010700	–	5.1932
			adventitia	1.030205	1.064236	–	
	O 1	15 %	media	1.161966	1.009231	–	5.5363
			adventitia	1.040207	1.095662	–	
	O 1	20 %	media	1.195977	1.026426	–	5.9465
			adventitia	1.037705	1.171744	–	
	O 2	0.0772 %	media	1.028935	1.001742	–	4.6143
			adventitia	1.000196	1.000104	–	
	O 3	0/5/10/15 %	media	1.021270	1.121004	–	5.4270
			adventitia	1.014297	1.082925	–	
⊥i⊥i	O 1	0 %	media	1.065517	1.000783	–	3.7645
			adventitia	1.001213	1.038623	–	
	O 1	5 %	media	1.091209	1.001874	–	3.0612
			adventitia	1.006590	1.035275	–	
	O 1	10 %	media	1.128355	1.000892	–	3.0802
			adventitia	1.047004	1.021488	–	
	O 1	15 %	media	1.158329	1.011215	–	3.3587
			adventitia	1.082716	1.017412	–	
	O 1	20 %	media	1.182075	1.000277	–	3.4696
			adventitia	1.159144	1.000722	–	

(continued on next page)

Table B.2: Optimized growth parameters for the two-layered arterial segment defined in Sec. 7.5.2, loaded with an internal pressure of 120 mmHg *(continued)*.

model	mode	ε_z	layer	$\vartheta^+_{(1)}$	$\vartheta^+_{(2)}$	$\vartheta^+_{(3)}$	f_{obj}
	O 2	9.0646 %	media	1.117186	1.010899	–	3.1530
			adventitia	1.024461	1.008100	–	
	O 3	0/5/10/15 %	media	1.110136	1.002017	–	4.1871
			adventitia	1.045683	1.005198	–	
⊥d⊥d	O 1	0 %	media	1.078306	1.316935	–	3.7737
			adventitia	1.001284	1.004470	–	
	O 1	5 %	media	1.103011	1.000127	–	3.2069
			adventitia	1.371448	1.266239	–	
	O 1	10 %	media	1.119578	1.004312	–	3.2985
			adventitia	1.070055	1.004776	–	
	O 1	15 %	media	1.158117	1.007946	–	3.3369
			adventitia	1.080824	1.000378	–	
	O 1	20 %	media	1.183605	1.008359	–	3.5253
			adventitia	1.150629	1.005808	–	
	O 2	14.982 %	media	1.153935	1.001094	–	3.2618
			adventitia	1.107078	1.004985	–	
	O 3	0/5/10/15 %	media	1.112650	1.011316	–	4.2313
			adventitia	1.070875	1.023886	–	
⊥t⊥t	O 1	0 %	media	1.062542	1.043561	–	3.7936
			adventitia	1.000560	1.430148	–	
	O 1	5 %	media	1.100905	1.012141	–	3.1520
			adventitia	1.009940	1.042206	–	
	O 1	10 %	media	1.131726	1.013034	–	3.0812
			adventitia	1.049926	1.019230	–	
	O 1	15 %	media	1.159399	1.006995	–	3.2696
			adventitia	1.099295	1.010793	–	
	O 1	20 %	media	1.185682	1.001745	–	3.5186
			adventitia	1.143583	1.000487	–	
	O 2	11.632 %	media	1.146586	1.026184	–	3.2514
			adventitia	1.109724	1.067521	–	
	O 3	0/5/10/15 %	media	1.103688	1.005942	–	4.2140
			adventitia	1.053641	1.014470	–	
∥ i ∥ i	O 1	0 %	media	1.000134	1.121309	–	4.3424
			adventitia	1.071859	1.000215	–	
	O 1	5 %	media	1.000700	1.195852	–	3.9187
			adventitia	1.013808	1.001848	–	
	O 1	10 %	media	1.002383	1.241828	–	4.1045
			adventitia	1.037763	1.088735	–	
	O 1	15 %	media	1.000140	1.325977	–	4.1646
			adventitia	1.003763	1.118874	–	

(continued on next page)

Table B.2: Optimized growth parameters for the two-layered arterial segment defined in Sec. 7.5.2, loaded with an internal pressure of 120 mmHg *(continued)*.

model	mode	ε_z	layer	$\vartheta^+_{(1)}$	$\vartheta^+_{(2)}$	$\vartheta^+_{(3)}$	f_{obj}
	O 1	20 %	media	1.002157	1.387006	–	4.3036
			adventitia	1.006232	1.170970	–	
	O 2	2.3529 %	media	1.002943	1.131156	–	3.9713
			adventitia	1.065966	1.000232	–	
	O 3	0/5/10/15 %	media	1.000624	1.147998	–	4.8400
			adventitia	1.001638	1.045225	–	
‖ d‖ d	O 1	0 %	media	1.000100	1.496166	–	4.4931
			adventitia	1.118667	1.000100	–	
	O 1	5 %	media	1.000156	1.385916	–	4.0543
			adventitia	1.019229	1.000972	–	
	O 1	10 %	media	1.000656	1.337881	–	4.1531
			adventitia	1.027343	1.093842	–	
	O 1	15 %	media	1.000136	1.463313	–	4.2561
			adventitia	1.004619	1.125619	–	
	O 1	20 %	media	1.000135	1.499806	–	4.3259
			adventitia	1.013510	1.228641	–	
	O 2	2.1643 %	media	1.000102	1.347641	–	4.0232
			adventitia	1.068034	1.000110	–	
	O 3	0/5/10/15 %	media	1.000353	1.346173	–	4.5354
			adventitia	1.008609	1.063008	–	
‖ t‖ t	O 1	0 %	media	1.000100	1.499879	–	4.4392
			adventitia	1.118017	1.000100	–	
	O 1	5 %	media	1.000548	1.253939	–	4.0652
			adventitia	1.018798	1.002403	–	
	O 1	10 %	media	1.000706	1.344227	–	4.1553
			adventitia	1.017778	1.076988	–	
	O 1	15 %	media	1.000182	1.462818	–	4.2444
			adventitia	1.004863	1.132401	–	
	O 1	20 %	media	1.000779	1.491462	–	4.3394
			adventitia	1.027874	1.261299	–	
	O 2	1.8949 %	media	1.001210	1.456797	–	4.0666
			adventitia	1.077816	1.003158	–	
	O 3	0/5/10/15 %	media	1.000146	1.369653	–	4.5182
			adventitia	1.005836	1.064536	–	
□t□t□t	O 1	0 %	media	1.028512	1.001326	1.184656	4.6108
			adventitia	1.000339	1.000249	1.051553	
	O 1	5 %	media	1.060947	1.008605	1.281823	4.9122
			adventitia	1.000929	1.038415	1.194700	
	O 1	10 %	media	1.089894	1.029054	1.249530	5.2349
			adventitia	1.037149	1.046312	1.250580	

(continued on next page)

Table B.2: Optimized growth parameters for the two-layered arterial segment defined in Sec. 7.5.2, loaded with an internal pressure of 120 mmHg *(continued)*.

model	mode	ε_z	layer	$\vartheta^+_{(1)}$	$\vartheta^+_{(2)}$	$\vartheta^+_{(3)}$	f_{obj}
	O 1	15 %	media	1.164272	1.005336	1.248762	5.5378
			adventitia	1.039231	1.113726	1.248334	
	O 1	20 %	media	1.193233	1.028884	1.252055	5.9457
			adventitia	1.116429	1.071033	1.248414	
	O 2	0.0026 %	media	1.007818	1.338888	1.029226	4.6337
			adventitia	1.000859	1.005681	1.012136	
	O 3	0/5/10/15 %	media	1.016697	1.121160	1.249405	5.4275
			adventitia	1.020269	1.085191	1.250350	
⊥i⊥i⊥i	O 1	0 %	media	1.067023	1.002686	1.000954	3.8488
			adventitia	1.001851	1.114520	1.001963	
	O 1	5 %	media	1.100256	1.001633	1.000237	3.0461
			adventitia	1.002218	1.041685	1.001179	
	O 1	10 %	media	1.129065	1.017664	1.009421	3.0728
			adventitia	1.012596	1.012452	1.048481	
	O 1	15 %	media	1.156364	1.013684	1.009008	3.3080
			adventitia	1.110242	1.034600	1.020030	
	O 1	20 %	media	1.181418	1.004397	1.007175	3.5258
			adventitia	1.138317	1.004326	1.014598	
	O 2	5.5436 %	media	1.109837	1.072172	1.011108	3.8326
			adventitia	1.016684	1.073480	1.014855	
	O 3	0/5/10/15 %	media	1.103369	1.001659	1.000556	4.1900
			adventitia	1.017183	1.002098	1.006666	
⊥t⊥t⊥t	O 1	0 %	media	1.063002	1.000143	1.096813	3.7688
			adventitia	1.000527	1.146872	1.177643	
	O 1	5 %	media	1.097586	1.008500	1.250239	3.1010
			adventitia	1.017054	1.076154	1.250675	
	O 1	10 %	media	1.135204	1.017403	1.275691	3.0740
			adventitia	1.055479	1.035081	1.281631	
	O 1	15 %	media	1.155806	1.015865	1.254909	3.3485
			adventitia	1.095275	1.014425	1.244970	
	O 1	20 %	media	1.179229	1.007581	1.252018	3.5962
			adventitia	1.160064	1.010670	1.261282	
	O 2	7.3640 %	media	1.112525	1.011838	1.255431	3.0966
			adventitia	1.050124	1.058388	1.325486	
	O 3	0/5/10/15 %	media	1.099511	1.007861	1.243307	4.2069
			adventitia	1.052146	1.010066	1.246286	
‖ i‖ i‖ i	O 1	0 %	media	1.001498	1.004048	1.145081	3.4019
			adventitia	1.007780	1.001084	1.041764	
	O 1	5 %	media	1.006680	1.057704	1.156961	2.9535
			adventitia	1.043361	1.009862	1.077034	

(continued on next page)

Table B.2: Optimized growth parameters for the two-layered arterial segment defined in Sec. 7.5.2, loaded with an internal pressure of 120 mmHg *(continued)*.

model	mode	ε_z	layer	$\vartheta^+_{(1)}$	$\vartheta^+_{(2)}$	$\vartheta^+_{(3)}$	f_{obj}
	O 1	10 %	media	1.004951	1.121462	1.138915	3.0140
			adventitia	1.015750	1.053113	1.006783	
	O 1	15 %	media	1.000659	1.168972	1.126432	3.3220
			adventitia	1.004177	1.091119	1.023675	
	O 1	20 %	media	1.000137	1.236904	1.118651	3.3640
			adventitia	1.000191	1.138236	1.001972	
	O 2	5.9801 %	media	1.000630	1.065015	1.149039	3.0081
			adventitia	1.009671	1.009708	1.012070	
	O 3	0/5/10/15 %	media	1.008610	1.099673	1.150573	4.1685
			adventitia	1.009568	1.037745	1.044439	
‖ t ‖ t ‖ t	O 1	0 %	media	1.000100	1.499861	1.160124	4.4390
			adventitia	1.198192	1.000100	1.238713	
	O 1	5 %	media	1.000162	1.285151	1.232646	4.0544
			adventitia	1.033127	1.010245	1.207459	
	O 1	10 %	media	1.000133	1.499370	1.204649	4.1499
			adventitia	1.011745	1.068804	1.365664	
	O 1	15 %	media	1.000188	1.395488	1.331821	4.2369
			adventitia	1.013106	1.149565	1.192171	
	O 1	20 %	media	1.000111	1.452285	1.000144	4.3435
			adventitia	1.021892	1.238811	1.047761	
	O 2	2.8518 %	media	1.000691	1.492427	1.289802	4.1002
			adventitia	1.047018	1.001029	1.208955	
	O 3	0/5/10/15 %	media	1.000127	1.415379	1.024145	4.5225
			adventitia	1.003277	1.059353	1.201271	
‖ d‖ d‖ i	O 1	0 %	media	1.000196	1.485517	1.141223	3.1346
			adventitia	1.495836	1.000200	1.001601	
	O 1	5 %	media	1.000837	1.216586	1.140194	2.8151
			adventitia	1.035953	1.005647	1.209417	
	O 1	10 %	media	1.000509	1.238184	1.143858	2.9325
			adventitia	1.002637	1.035718	1.064177	
	O 1	15 %	media	1.001027	1.347476	1.142978	2.9891
			adventitia	1.021548	1.156034	1.040067	
	O 1	20 %	media	1.000100	1.295737	1.147749	3.1411
			adventitia	1.012976	1.184856	1.000107	
	O 2	1.9470 %	media	1.007955	1.279004	1.149536	2.9545
			adventitia	1.093752	1.008462	1.058440	
	O 3	0/5/10/15 %	media	1.005832	1.344140	1.150080	3.3001
			adventitia	1.033279	1.076575	1.085871	

Table B.3: Optimized growth parameters for the substitute model of the patient-specific artery from Sec. 8.1, loaded with a pressure of 120 mmHg.

model	mode	ε_z	$\vartheta^+_{(1)}$	$\vartheta^+_{(2)}$	$\vartheta^+_{(3)}$	f_{obj}
0 0	–	0 %	–	–	–	4.7471
	–	5 %	–	–	–	5.2522
	–	10 %	–	–	–	5.6302
	–	15 %	–	–	–	5.6256
	–	20 %	–	–	–	5.1861
□i	O 1	0 %	1.050943	–	–	2.9623
	O 1	5 %	1.092670	–	–	2.9838
	O 1	10 %	1.147692	–	–	3.0426
	O 1	15 %	1.210160	–	–	3.1778
	O 1	20 %	1.266335	–	–	3.3492
	O 2	0.0056 %	1.050731	–	–	2.9623
	O 3	0/5/10/15 %	1.158989	–	–	3.2493
⊥i⊥i	O 1	0 %	1.045009	1.000290	–	2.4377
	O 1	5 %	1.073529	1.000277	–	1.9922
	O 1	10 %	1.092662	1.000368	–	1.5979
	O 1	15 %	1.120418	1.015627	–	2.4783
	O 1	20 %	1.157810	1.023813	–	3.1798
	O 2	7.8118 %	1.093791	1.011708	–	1.8440
	O 3	0/5/10/15 %	1.118641	1.000559	–	2.2409
⊥d⊥d	O 1	0 %	1.051008	1.000131	–	2.2541
	O 1	5 %	1.097059	1.020886	–	2.2664
	O 1	10 %	1.075818	1.000102	–	1.8807
	O 1	15 %	1.125251	1.000110	–	2.4139
	O 1	20 %	1.165209	1.043964	–	3.1237
	O 2	2.7031 %	1.069257	1.001492	–	2.2480
	O 3	0/5/10/15 %	1.114280	1.000101	–	3.3344
⊥t⊥t	O 1	0 %	1.044388	1.008173	–	2.1361
	O 1	5 %	1.076037	1.002268	–	1.8843
	O 1	10 %	1.094917	1.000115	–	1.6156
	O 1	15 %	1.129806	1.001660	–	2.2620
	O 1	20 %	1.163008	1.039376	–	3.5147
	O 2	10.447 %	1.092923	1.003683	–	1.6063
	O 3	0/5/10/15 %	1.057585	1.475699	–	5.9563
⊥i⊥i⊥i	O 1	0 %	1.047677	1.000406	1.000186	2.4423
	O 1	5 %	1.073139	1.000198	1.000133	1.9963
	O 1	10 %	1.094626	1.000320	1.000109	1.5898
	O 1	15 %	1.124866	1.000522	1.022707	1.7280
	O 1	20 %	1.173522	1.021982	1.045445	2.0177
	O 2	11.618 %	1.103208	1.012973	1.006005	1.6473

(continued on next page)

Table B.3: Optimized growth parameters for the substitute model of the artery from Sec. 8.1, loaded with a pressure of 120 mmHg *(continued)*.

model	mode	ε_z	$\vartheta^+_{(1)}$	$\vartheta^+_{(2)}$	$\vartheta^+_{(3)}$	f_{obj}
	O 3	0/5/10/15 %	1.112381	1.001530	1.013760	2.2023
‖ i ‖ i ‖ i	O 1	0 %	1.000103	1.000104	1.093562	1.7957
	O 1	5 %	1.015151	1.021642	1.131760	1.3734
	O 1	10 %	1.000574	1.095415	1.096356	1.5866
	O 1	15 %	1.008616	1.172282	1.120695	1.7523
	O 1	20 %	1.000249	1.184529	1.097931	1.7986
	O 2	2.5871 %	1.000332	1.003290	1.136242	1.4722
	O 3	0/5/10/15 %	1.000161	1.129204	1.080326	2.1490
‖ d‖ d‖ i	O 1	0 %	1.001638	1.216887	1.134703	1.5305
	O 1	5 %	1.021673	1.023935	1.173092	1.4840
	O 1	10 %	1.000784	1.078904	1.088973	1.7739
	O 1	15 %	1.003023	1.184464	1.099906	1.9515
	O 1	20 %	1.001793	1.257987	1.092355	2.0840
	O 2	2.3720 %	1.024738	1.000152	1.176348	1.4993
	O 3	0/5/10/15 %	1.005779	1.170534	1.083575	2.1692

Bibliography

Ahamed, T., Dorfmann, L. & Ogden, R. W. (2016): "Modelling of residually stressed materials with application to AAA". In: *Journal of the Mechanical Behavior of Biomedical Materials* 61, pp. 221–234.

Akyildiz, A. C., Chai, C.-K., Oomens, C. W. J., van der Lugt, A., Baaijens, F. P. T., Strijkers, G. J. & Gijsen, F. J. H. (2017): "3D Fiber Orientation in Atherosclerotic Carotid Plaques". In: *Journal of Structural Biology* 200 (1), pp. 28–35.

Altenbach, H. (2012): *Kontinuumsmechanik. Einführung in die materialunabhängigen und materialabhängigen Gleichungen.* 2nd edition. Berlin/ Heidelberg: Springer-Verlag. isbn: 978-3-642-24118-5.

Ambrosi, D., Ateshian, G. A., Arruda, E. M., Cowin, S. C., Dumais, J., Goriely, A., Holzapfel, G. A., Humphrey, J. D., Kemkemer, R., Kuhl, E., Olberding, J. E., Taber, L. A. & Garikipati, K. (2011): "Perspectives on biological growth and remodeling". In: *Journal of the Mechanics and Physics of Solids* 59 (4), pp. 863–883.

Ambrosi, D., Ben Amar, M., Cyron, C. J., DeSimone, A., Goriely, A., Humphrey, J. D. & Kuhl, E. (2019): "Growth and remodelling of living tissues: perspectives, challenges and opportunities". In: *Journal of the Royal Society Interface* 16 (157), p. 20190233.

Ares, G. D., Blanco, P. J., Urquiza, S. A. & Feijóo, R. A. (2017): "Identification of residual stresses in multi-layered arterial wall tissues using a variational framework". In: *Computer Methods in Applied Mechanics and Engineering* 319, pp. 287–313.

Ateshian, G. A. & Ricken, T. (2010): "Multigenerational interstitial growth of biological tissues". In: *Biomechanics and Modeling in Mechanobiology* 9, pp. 689–702.

Balzani, D., Böse, D., Brands, D., Erbel, R., Klawonn, A., Rheinbach, O. & Schröder, J. (2012): "Parallel simulation of patient-specific atherosclerotic arteries for the enhancement of intravascular ultrasound diagnostics". In: *Engineering Computations* 29 (8), pp. 888–906.

Balzani, D., Neff, P., Schröder, J. & Holzapfel, G. A. (2006): "A polyconvex framework for soft biological tissues. Adjustment to experimental data". In: *International Journal of Solids and Structures* 43 (20), pp. 6052–6070.

Balzani, D., Schröder, J. & Gross, D. (2007): "Numerical simulation of residual stresses in arterial walls". In: *Computational Materials Science* 39 (1), pp. 117–123.

Balzani, D. & Zahn, A. (2017): "Residual stresses resulting from growth and remodeling in arterial walls". In: *Proceedings of the VII International Conference on Computational Methods for Coupled Problems in Science and Engineering.* Ed. by Papadrakakis, M., Oñate, E. & Schrefler, B. submitted.

Bergel, D. H. (1960): "The visco-elastic properties of the arterial wall". Dissertation. Queen Mary University of London.

Betten, J. & Helisch, W. (1992): "Irreduzible Invarianten eines Tensors vierter Stufe". In: *Zeitschrift für Angewandte Mathematik und Mechanik* 72 (1), pp. 45–57.

Bindel, D. (2011): *MATFEAP – MATLAB interface to FEAP. Version 0.8.* URL: `http://www.cs.cornell.edu/~bindel/sw/matfeap` (visited on Oct. 16, 2020).

Braeu, F. A., Seitz, A., Aydin, R. C. & Cyron, C. J. (2017): "Homogenized constrained mixture models for anisotropic volumetric growth and remodeling". In: *Biomechanics and Modeling in Mechanobiology* 16 (3), pp. 889–906.

Brands, D., Klawonn, A., Rheinbach, O. & Schröder, J. (2008): "Modelling and convergence in arterial wall simulations using a parallel FETI solution strategy". In: *Computer Methods in Biomechanics and Biomedical Engineering* 11 (5), pp. 569–583.

Burton, A. C. (1954): "Relation of Structure to Function of the Tissues of the Wall of Blood Vessels". In: *Physiological Reviews* 34 (4), pp. 619–642.

Carew, T. E., Vaishnav, R. N. & Patel, D. J. (1968): "Compressibility of the Arterial Wall". In: *Circulation Research* 23 (1), pp. 61–68.

Chuong, C. J. & Fung, Y.-C. (1986): "On Residual Stresses in Arteries". In: *Journal of Biomechanical Engineering* 108 (2), pp. 189–192.

Clark, J. M. & Glagov, S. (1985): "Transmural Organization of the Arterial Media. The Lamellar Unit Revisted". In: *Arteriosclerosis, Thrombosis, and Vascular Biology* 5 (1), pp. 19–34.

Comellas, E., Carriero, A., Giorgi, M., Pereira, A. & Shefelbine, S. J. (2018): "Modeling the Influence of Mechanics on Biological Growth". In: *Numerical Methods and Advanced Simulation in Biomechanics and Biological Processes*. Ed. by Cerrolaza, M., Shefelbine, S. J. & Garzón-Alvarado, D. Elsevier. Chap. 2, pp. 17–35. ISBN: 978-0-12-811718-7.

Creane, A., Maher, E., Sultan, S., Hynes, N., Kelly, D. J. & Lally, C. (2011): "Prediction of fibre architecture and adaptation in diseased carotid bifurcations". In: *Biomechanics and Modeling in Mechanobiology* 10 (6), pp. 831–843.

Cyron, C. J., Aydin, R. C. & Humphrey, J. D. (2016): "A homogenized constrained mixture (and mechanical analog) model for growth and remodeling of soft tissue". In: *Biomechanics and Modeling in Mechanobiology* 15 (6), pp. 1389–1403.

Cyron, C. J. & Humphrey, J. D. (2017): "Growth and remodeling of load-bearing biological soft tissues". In: *Meccanica* 52 (3), pp. 645–664.

Driessen, N. J. B., Wilson, W., Bouten, C. V. C. & Baaijens, F. P. T. (2004): "A computational model for collagen fibre remodelling in the arterial wall". In: *Journal of Theoretical Biology* 226, pp. 53–64.

Driessen, N. J. B., Cox, M. A. J., Bouten, C. V. C. & Baaijens, F. P. T. (2008): "Remodelling of the angular collagen fiber distribution in cardiovascular tissues". In: *Biomechanics and Modeling in Mechanobiology* 7 (2), pp. 93–103.

Fausten, S., Balzani, D. & Schröder, J. (2016): "An algorithmic scheme for the automated calculation of fiber orientations in arterial walls". In: *Computational Mechanics* 58 (5), pp. 861–878.

Fung, Y.-C. (1991): "What Are the Residual Stresses Doing in Our Blood Vessels?" In: *Annals of Biomedical Engineering* 19 (3), pp. 237–249.

Fung, Y.-C. & Liu, S. Q. (1989): "Change of residual strains in arteries due to hypertrophy caused by aortic constriction". In: *Circulation Research* 65, pp. 1340–1349.

Genet, M., Rausch, M. K., Lee, L. C., Choy, S., Zhao, X., Kassab, G. S., Kozerke, S., Guccione, J. M. & Kuhl, E. (2015): "Heterogeneous growth-induced prestrain in the heart". In: *Journal of Biomechanics* 48, pp. 2080–2089.

Göktepe, S., Abilez, O. J. & Kuhl, E. (2010): "A generic approach towards finite growth with examples of athlete's heart, cardiac dilation, and cardiac wall thickening". In: *Journal of the Mechanics and Physics of Solids* 58 (10), pp. 1661–1680.

Hai, C.-M. & Murphy, R. A. (1988): "Cross-bridge phosphorylation and regulation of latch state in smooth muscle". In: *American Journal of Physiology* 254, pp. C99–C106.

Han, H.-C. & Fung, Y.-C. (1995): "Longitudinal strain of canine and porcine aortas". In: *Journal of Biomechanics* 28 (5), pp. 637–641.

Han, H.-C., Ku, D. N. & Vito, R. P. (2003): "Arterial Wall Adaptation under Elevated Longitudinal Stretch in Organ Culture". In: *Annals of Biomedical Engineering* 31 (4), pp. 403–411.

Hariton, I., deBotton, G., Gasser, T. C. & Holzapfel, G. A. (2007a): "Stress-driven collagen fiber remodeling in arterial walls". In: *Biomechanics and Modeling in Mechanobiology* 6, pp. 163–175.

Hariton, I., deBotton, G., Gasser, T. C. & Holzapfel, G. A. (2007b): "Stress-modulated collagen fiber remodeling in a human carotid bifurcation". In: *Journal of Theoretical Biology* 248, pp. 460–470.

Himpel, G., Kuhl, E., Menzel, A. & Steinmann, P. (2005): "Computational modelling of isotropic multiplicative growth". In: *Computer Modeling in Engineering & Sciences* 8, pp. 119–134.

Himpel, G. (2007): "Computational Modeling of Biomechanical Phenomena. Remodeling, Growth and Reorientation". Dissertation. Technische Universität Kaiserslautern.

Holzapfel, G. A. (2000): *Nonlinear Solid Mechanics. A Continuum Approach for Engineering.* Chichester: John Wiley & Sons. isbn: 0471823198.

Holzapfel, G. A. (2006): "Determination of material models for arterial walls from uniaxial extension tests and histological structure". In: *Journal of Theoretical Biology* 238, pp. 290–302.

Holzapfel, G. A., Gasser, T. C. & Ogden, R. W. (2000): "A New Constitutive Framework for Arterial Wall Mechanics and a Comparative Study of Material Models". In: *Journal of Elasticity* 61, pp. 1–48.

Holzapfel, G. A., Niestrawska, J. A., Ogden, R. W., Reinisch, A. J. & Schriefl, A. J. (2015): "Modelling non-symmetric collagen fibre dispersion in arterial walls". In: *Journal of the Royal Society Interface* 12, p. 20150188.

Holzapfel, G. A. & Ogden, R. W. (2010): "Modelling the layer-specific three-dimensional residual stresses in arteries, with an application to the human aorta". In: *Journal of the Royal Society Interface* 7 (46), pp. 787–799.

Holzapfel, G. A., Sommer, G., Auer, M., Regitnig, P. & Ogden, R. W. (2007): "Layer-Specific 3D Residual Deformations of Human Aortas with Non-Atherosclerotic Intimal Thickening". In: *Annals of Biomedical Engineering* 35 (4), pp. 530–545.

Holzapfel, G. A., Sommer, G., Gasser, T. C. & Regitnig, P. (2005): "Determination of layer-specific mechanical properties of human coronary arteries with nonatherosclerotic intimal thickening and related constitutive modeling". In: *American Journal of Physiology: Heart and Circulatory Physiology* 289 (5).

Horny, L., Adamek, T., Vesely, J., Chlup, H., Zitny, R. & Konvickova, S. (2012): "Age-related distribution of longitudinal pre-strain in abdominal aorta with emphasis on forensic application". In: *Forensic Science International* 214, pp. 18–22.

Humphrey, J. D., Eberth, J. F., Dye, W. W. & Gleason, R. L. (2009): "Fundamental role of axial stress in compensatory adaptations by arteries". In: *Journal of Biomechanics* 42 (1), pp. 1–8.

Humphrey, J. D. & Rajagopal, K. R. (2002): "A constrained mixture model for growth and remodeling of soft tissues". In: *Mathematical Models and Methods in Applied Sciences* 12 (3), pp. 407–430.

Humphrey, J. D. (2002): *Cardiovascular Solid Mechanics. Cells, Tissues, and Organs*. New York: Springer Science + Business Media. isbn: 978-0-387-21576-1.

Humphrey, J. D. (2008): "Biological Soft Tissues". In: *Springer Handbook of Experimental Solid Mechanics*. Ed. by Sharpe Jr., W. N. New York: Springer Science + Business Media. Chap. 7. isbn: 978-0-387-30877-7.

Imatani, S. & Maugin, G. A. (2002): "A constitutive model for material growth and its application to three-dimensional finite element analysis". In: *Mechanics Research Communications* 29 (6), pp. 477–483.

Jackson, Z. S., Gotlieb, A. I. & Langille, B. L. (2002): "Wall Tissue Remodeling Regulates Longitudinal Tension in Arteries". In: *Circulation Research* 90, pp. 918–925.

Joldes, G. R., Noble, C., Polzer, S., Taylor, Z. A., Wittek, A. & Miller, K. (2018): "A simple method of incorporating the effect of the Uniform Stress Hypothesis in arterial wall stress computations". In: *Acta of Bioengineering and Biomechanics* 20 (3), pp. 59–67.

Kamiya, A. & Togawa, T. (1980): "Adaptive regulation of wall shear stress to flow change in the canine carotid artery". In: *American Journal of Physiology: Heart and Circulatory Physiology* 239 (1), H14–H21.

Krasny, W., Morin, C., Magoariec, H. & Avril, S. (2017): "A comprehensive study of layer-specific morphological changes in the microstructure of carotid arteries under uniaxial load". In: *Acta Biomaterialia* 57, pp. 342–351.

Kuhl, E., Maas, R., Himpel, G. & Menzel, A. (2007): "Computational modeling of arterial wall growth. Attempts towards patient-specific simulations based on computer tomography". In: *Biomechanics and Modeling in Mechanobiology* 6 (5), pp. 321–331.

Kuhl, E. (2014): "Growing matter: A review of growth in living systems". In: *Journal of the Mechanical Behavior of Biomedical Materials* 29, pp. 529–543.

Kuhl, E. & Holzapfel, G. A. (2007): "A continuum model for remodeling in living structures". In: *Journal of Materials Science* 42, pp. 8811–8823.

Langille, B. L. (1993): "Remodeling of Developing and Mature Arteries: Endothelium, Smooth Muscle, and Matrix". In: *Journal of Cardiovascular Pharmacology* 21.

Latorre, M. & Humphrey, J. D. (2018): "A mechanobiologically equilibrated constrained mixture model for growth and remodeling of soft tissues". In: *Zeitschrift für Angewandte Mathematik und Mechanik* 98 (12), pp. 2048–2071.

Lee, L. C., Genet, M., Acevedo-Bolton, G., Ordovas, K., Guccione, J. M. & Kuhl, E. (2015): "A computational model that predicts reverse growth in response to mechanical unloading". In: *Biomechanics and Modeling in Mechanobiology* 14 (2), pp. 217–229.

Leung, D. Y. M., Glagov, S. & Mathews, M. B. (1976): "Cyclic Stretching Stimulates Synthesis of Matrix Components by Arterial Smooth Muscle Cells in vitro". In: *Science* 191 (4226), pp. 475–477.

Levy, B. I. & Tedgui, A. (1999): "Morphologic aspects of the large artery vascular wall". In: *Biology of the arterial wall*. Ed. by Levy, B. I. & Tedgui, A. Dordrecht/Boston/London: Kluwer Academic Publishers. isbn: 0-7923-8458-X.

Liu, H., Zhang, M., Liu, M., Martin, C., Cai, Z. & Sun, W. (2019): "Finite element simulation of three dimensional residual stress in the aortic wall using an anisotropic tissue growth model". In: *Journal of the Mechanical Behavior of Biomedical Materials*.

Lubarda, V. A. & Hoger, A. (2002): "On the mechanics of solids with a growing mass". In: *International Journal of Solids and Structures* 39, pp. 4627–4664.

Lyness, J. N. (1968): "Differentiation Formulas for Analytic Functions". In: *Mathematics of Computation* 22, pp. 352–362.

Lyness, J. N. & Moler, C. B. (1967): "Numerical differentiation of analytic functions". In: *SIAM Journal on Numerical Analysis* 4.2, pp. 202–210.

Maltzahn, W. W. von, Warriyar, R. G. & Keitzer, W. F. (1984): "Experimental measurements of elastic properties of media and adventitia of bovine carotid arteries". In: *Journal of Biomechanics* 17 (11), pp. 839–847.

MathWorks (2014/2018): *MATLAB*. R2014a/R2018b. url: `https://de.mathworks.com/products/matlab.html` (visited on Oct. 18, 2020).

Matsumoto, T. & Hayashi, K. (1996a): "Response of Arterial Wall to Hypertension and Residual Stress". In: *Biomechanics. Functional Adaptation and Remodeling*. Ed. by Hayashi, K., Kamiya, A. & Ono, K. Tokyo: Springer. isbn: 4-431-70173-7.

Matsumoto, T. & Hayashi, K. (1996b): "Stress and Strain Distribution in Hypertensive and Normotensive Rat Aorta Considering Residual Strain". In: *Journal of Biomechanical Engineering* 118 (1), pp. 62–73.

Menzel, A. & Kuhl, E. (2012): "Frontiers in growth and remodeling". In: *Mechanics Research Communications* 42, pp. 1–14.

Murtada, S., Arner, A. & Holzapfel, G. A. (2012): "Experiments and mechanochemical modeling of smooth muscle contraction: Significance of filament overlap". In: *Journal of Theoretical Biology* 297, pp. 176–186.

Murtada, S., Kroon, M. & Holzapfel, G. A. (2010): "A calcium-driven mechanochemical model for prediction of force generation in smooth muscle". In: *Biomechanics and Modeling in Mechanobiology* 9 (6), pp. 749–762.

Niestrawska, J. A., Viertler, C., Regitnig, P., Cohnert, T. U., Sommer, G. & Holzapfel, G. A. (2016): "Microstructure and mechanics of healthy and aneurysmatic abdominal aortas: experimental analysis and modelling". In: *Journal of the Royal Society Interface* 13 (124), p. 20160620.

Nissen, R., Cardinale, G. J. & Udenfriend, S. (1978): "Increased turnover of arterial collagen in hypertensive rats". In: *Proceedings of the National Academy of Sciences of the United States of America* 75, pp. 451–453.

Nolan, D. R. & McGarry, J. P. (2016): "On the compressibility of Arterial Tissue". In: *Annals of Biomedical Engineering* 44 (4), pp. 993–1007.

Ogden, R. W. (2017): "Nonlinear Continuum Mechanics and Modeling the Elasticity of Soft Biological Tissues with a Focus on Artery Walls". In: *Biomechanics: Trends in Modeling and Simulation*. Ed. by Holzapfel, G. A. & Ogden, R. W. Springer International Publishing Switzerland, pp. 83–156. isbn: 978-3-319-41475-1.

Olsson, T. & Klarbring, A. (2008): "Residual stresses in soft tissue as a consequence of growth and remodeling: application to an arterial geometry". In: *European Journal of Mechanics, A/Solids* 27 (6), pp. 959–974.

Ooshima, A., Fuller, G. C., Cardinale, G. J., Spector, S. & Udenfriend, S. (1974): "Increased Collagen Synthesis in Blood Vessels of Hypertensive Rats and Its Reversal by Antihypertensive Agents". In: *Proceedings of the National Academy of Sciences of the United States of America* 71, pp. 3019–3023.

Pierce, D. M., Fastl, T. E., Rodriguez-Vila, B., Verbrugghe, P., Fourneau, I., Maleux, G., Herijgers, P., Gomez, E. J. & Holzapfel, G. A. (2015): "A method for incorporating three-dimensional residual stretches/stresses into patient-specific finite element simulations of arteries". In: *Journal of the Mechanical Behavior of Biomedical Materials* 47, pp. 147–164.

Polzer, S., Bursa, J., Gasser, T. C., Staffa, R. & Vlachovsky, R. (2013): "A Numerical Implementation to Predict Residual Strains from the Homogeneous Stress Hypothesis with Application to Abdominal Aortic Aneurysms". In: *Annals of Biomedical Engineering* 41 (7), pp. 1516–1527.

Rachev, A., Stergiopulos, N. & Meister, J.-J. (1998): "A Model for Geometric and Mechanical Adaptation of Arteries to Sustained Hypertension". In: *Journal of Biomechanical Engineering* 120, pp. 9–17.

Rhodin, J. A. G. (2014): "Architecture of the Vessel Wall". In: *Comprehensive Physiology. Supplement 7: Handbook of Physiology, The Cardiovascular System, Vascular Smooth Muscle*, pp. 1–31. First published in print 1980.

Robertson, A. M. & Watton, P. N. (2013): "Mechanobiology of the Arterial Wall". In: *Transport in Biological Media*. Ed. by Becker, S. M. & Kuznetsov, A. V. 1st edition. Elsevier. Chap. 8, pp. 275–347. isbn: 978-0-12-415824-5.

Rodbard, S. (1975): "Vascular Caliber". In: *Cardiology* 60, pp. 4–49.

Rodriguez, E. K., Hoger, A. & McCulloch, A. D. (1994): "Stress-dependent finite growth in soft elastic tissues". In: *Journal of Biomechanics* 27 (4), pp. 455–467.

Sáez, P., Peña, E., Martínez, M. A. & Kuhl, E. (2014): "Computational modeling of hypertensive growth in the human carotid artery". In: *Computational Mechanics* 53 (6), pp. 1183–1196.

Schriefl, A. J., Wolinski, H., Regitnig, P., Kohlwein, S. D. & Holzapfel, G. A. (2013): "An automated approach for three-dimensional quantification of fibrillar structures in optically cleared soft biological tissues". In: *Journal of the Royal Society Interface* 10 (80), p. 20120760.

Schriefl, A. J., Zeindlinger, G., Pierce, D. M., Regitnig, P. & Holzapfel, G. A. (2012): "Determination of the layer-specific distributed collagen fibre orientations in human thoracic and abdominal aortas and common iliac arteries". In: *Journal of the Royal Society Interface* 9 (71), pp. 1275–1286.

Schröder, J. & Brinkhues, S. (2014): "A novel scheme for the approximation of residual stresses in arterial walls". In: *Archive of Applied Mechanics* 84 (6), pp. 881–898.

Schröder, J. & Neff, P. (2003): "Invariant formulation of hyperelastic transverse isotropy based on polyconvex free energy functions". In: *International Journal of Solids and Structures* 40 (2), pp. 401–445.

Schröder, J. & von Hoegen, M. (2016): "An engineering tool to estimate eigenstresses in three-dimensional patient-specific arteries". In: *Computer Methods in Applied Mechanics and Engineering* 306, pp. 364–381.

Shadwick, R. E. (1999): "Mechanical design in arteries". In: *The Journal of Experimental Biology* 202, pp. 3305–3313.

Sigaeva, T., Sommer, G., Holzapfel, G. A. & Di Martino, E. S. (2019): "Anisotropic residual stresses in arteries". In: *Journal of the Royal Society Interface* 16 (151), p. 20190029.

Simo, J. C., Taylor, R. L. & Wriggers, P. (1991): "A note on finite-element implementation of pressure boundary loading". In: *Communications in Applied Numerical Methods* 7 (7), pp. 513–525.

Skalak, R., Zargaryan, S., Jain, R. K., Netti, P. A. & Hoger, A. (1996): "Compatibility and the genesis of residual stress by volumetric growth". In: *Journal of Mathematical Biology* 34, pp. 889–914.

Slaughter, W. S. (2002): *The Linearized Theory of Elasticity*. Boston: Birkhäuser. isbn: 0-8176-4117-3.

Soleimani, M., Muthyala, N., Marino, M. & Wriggers, P. (2020): "A novel stress-induced anisotropic growth model driven by nutrient diffusion: Theory, FEM implementation and applications in bio-mechanical problems". In: *Journal of the Mechanics and Physics of Solids* 144, p. 104097.

Spencer, A. J. M. & Rivlin, R. S. (1958): "Finite Integrity Bases for Five of Fewer Symmetric 3 x 3 Matrices". In: *Archive for Rational Mechanics and Analysis* 2 (1), pp. 435–446.

Taber, L. A. & Humphrey, J. D. (2001): "Stress-Modulated Growth, Residual Stress, and Vascular Heterogeneity". In: *Journal of Biomechanical Engineering* 123 (6), pp. 528–535.

Takamizawa, K. & Hayashi, K. (1987): "Strain energy density function and uniform strain hypothesis for arterial mechanics". In: *Journal of Biomechanics* 20 (1), pp. 7–17.

Tanaka, M., Fujikawa, M., Balzani, D. & Schröder, J. (2014): "Robust numerical calculation of tangent moduli at finite strains based on complex-step derivative approximation and its application to localization analysis". In: *Computer Methods in Applied Mechanics and Engineering* 269, pp. 454–470.

Tanaka, M., Sasagawa, T., Omote, R., Fujikawa, M., Balzani, D. & Schröder, J. (2015): "A highly accurate 1st- and 2nd-order differentiation scheme for hyperelastic material models based on hyper-dual numbers". In: *Computer Methods in Applied Mechanics and Engineering* 283, pp. 22–45.

Taylor, R. L. (2008): *FEAP – Finite Element Analysis Program. Version 8.2*. University of California. Berkeley. url: `http://projects.ce.berkeley.edu/feap/` (visited on Jan. 27, 2020).

Tower, T. T., Neidert, M. R. & Tranquillo, R. T. (2002): "Fiber Alignment Imaging During Mechanical Testing of Soft Tissues". In: *Annals of Biomedical Engineering* 30 (10), pp. 1221–1233.

Truesdell, C. & Noll, W. (1965/1992): *The Non-Linear Field Theories of Mechanics*. 2nd edition. Corrected reprint of the original edition from 1965. Berlin: Springer. isbn: 3-540-55098-4.

Uhlmann, K., Zahn, A. & Balzani, D. (2021): "Simulation of Arterial Walls: Growth, Fiber Reorientation, and Active Response". In: *Solid (Bio)mechanics: Challenges of the Next Decade*. Ed. by Sommer, G., Li, K., Haspinger, D. & Ogden, R. W. In press. Springer.

Urevc, J., Brumen, M., Flis, V. & Štok, B. (2015): "Applying Thermomechanical Analogy to Predict the Arterial Residual Stress State". In: *Journal of Mechanical Engineering* 61 (1), pp. 5–23.

Urevc, J., Halilovič, M., Brumen, M. & Štok, B. (2016): "An approach to consider the arterial residual stresses in modelling of a patient-specific artery". In: *Advances in Mechanical Engineering* 8 (11), pp. 1–19.

Vaishnav, R. N. & Vossoughi, J. (1987): "Residual stress and strain in aortic segments". In: *Journal of Biomechanics* 20 (3), pp. 235–239.

Valentín, A. & Holzapfel, G. A. (2012): "Constrained mixture models as tools for testing competing hypotheses in arterial biomechanics: A brief survey". In: *Mechanics Research Communications* 42, pp. 126–133.

Valentín, A., Humphrey, J. D. & Holzapfel, G. A. (2013): "A finite element-based constrained mixture implementation for arterial growth, remodeling, and adaptation: Theory and numerical verification". In: *International Journal for Numerical Methods in Biomedical Engineering* 29 (8), pp. 822–849.

Wang, J. H.-C. & Thampatty, B. P. (2006): "An introductory review of cell mechanobiology". In: *Biomechanics and Modeling in Mechanobiology* 5 (1), pp. 1–16.

Wang, R., Brewster, L. P. & Gleason Jr., R. L. (2013): "In-situ characterization of the uncrimping process of arterial collagen fibers using two-photon confocal microscopy and digital image correlation". In: *Journal of Biomechanics* 46 (15), pp. 2726–2729.

Weisbecker, H., Pierce, D. M. & Holzapfel, G. A. (2014): "A generalized prestressing algorithm for finite element simulations of preloaded geometries with application to the aorta". In: *International Journal for Numerical Methods in Biomedical Engineering* 30, pp. 857–872.

Wolinsky, H. (1970): "Response of the Rat Aortic Media to Hypertension". In: *Circulation Research* 26 (4), pp. 507–522.

Wolinsky, H. & Glagov, S. (1967): "A Lamellar Unit of Aortic Medial Structure and Function in Mammals". In: *Circulation Research* 20, pp. 99–111.

Wriggers, P. (2008): *Nonlinear Finite Element Methods*. Berlin/Heidelberg: Springer-Verlag. isbn: 978-3-540-71000-4.

Yosibash, Z., Manor, I., Gilad, I. & Willentz, U. (2014): "Experimental evidence of the compressibility of arteries". In: *Journal of the Mechanical Behavior of Biomedical Materials* 39, pp. 339–354.

Yossef, O. E., Farajian, M., Gilad, I., Willenz, U., Gutman, N. & Yosibash, Z. (2017): "Further experimental evidence of the compressibility of arteries". In: *Journal of the Mechanical Behavior of Biomedical Materials* 65, pp. 177–189.

Zahn, A. & Balzani, D. (2016): "Modeling residual stresses in arterial walls based on anisotropic growth". In: *Proceedings in Applied Mathematics and Mechanics* 16, pp. 115–116.

Zahn, A. & Balzani, D. (2017): "Modeling of anisotropic growth and residual stresses in arterial walls". In: *Acta Polytechnica CTU Proceedings* 7. Ed. by Zlámal, P. & Kytýř, D., pp. 85–90. issn: 2336-5382.

Zahn, A. & Balzani, D. (2018a): "A combined growth and remodeling framework for the approximation of residual stresses in arterial walls". In: *Zeitschrift für Angewandte Mathematik und Mechanik* 98 (12), pp. 2072–2100.

Zahn, A. & Balzani, D. (2018b): "Study of model variants in a combined framework for multiplicative growth and remodeling in arterial walls". In: *Proceedings in Applied Mathematics and Mechanics* 18 (1).

Zahn, A. & Balzani, D. (2019a): "Optimization-based comparison of different anisotropic models for growth and remodeling in arterial walls". In: *Proceedings of the 8th GACM Colloquium on Computational Mechanics for Young Scientists from Academia and Industry*. Ed. by Gleim, T. & Lange, S. ISBN: 978-3-86219-5093-9. kassel university press GmbH, pp. 405–408. isbn: 978-3-7376-5093-9.

Zahn, A. & Balzani, D. (2019b): "Optimization-based comparison of different approaches for the automatized calculation of residual stresses and fiber orientations in arteries". In: *Proceedings of the XV International Conference on Computational Plasticity – Fundamentals and Applications*. Ed. by Oñate, E., Owen, D. R. J., Peric, D., Chiumenti, M. & de Souza Neto, E. ISBN: 978-84-949194-7-3, pp. 170–180.

Zeinali-Davarani, S., Sheidaei, A. & Baek, S. (2011): "A finite element model of stress-mediated vascular adaptation: application to abdominal aortic aneurysms". In: *Computer Methods in Biomechanics and Biomedical Engineering* 14.7–9, pp. 803–817.

Zienkiewicz, O. C. & Taylor, R. L. (2000a): *The Finite Element Method. Volume 1: The Basis*. 5th edition. Oxford: Butterworth-Heinemann. isbn: 0 7506 5049 4.

Zienkiewicz, O. C. & Taylor, R. L. (2000b): *The Finite Element Method. Volume 2: Solid Mechanics*. 5th edition. Oxford: Butterworth-Heinemann. isbn: 0 7506 5055 9.

Zienkiewicz, O. C., Taylor, R. L. & Fox, D. D. (2014): *The Finite Element Method for Solid and Structural Mechanics*. 7th edition. Elsevier Ltd. isbn: 978-1-85617-634-7.

Copyright notices

In the following listing, origin and holder of the copyright of figures from external sources are indicated at full length. Beyond that, changes made to the original figures are declared.

Figure 2.1: Adopted without changes from Rhodin, J. A. G. (2014): "Architecture of the Vessel Wall". In: *Comprehensive Physiology. Supplement 7: Handbook of Physiology, The Cardiovascular System, Vascular Smooth Muscle*, pp. 1–31. First published in print 1980. Copyright © 2010 American Physiological Society.

Figure 2.2: Adopted without changes from Holzapfel, G. A., Sommer, G., Gasser, T. C., et al. (2005): "Determination of layer-specific mechanical properties of human coronary arteries with nonatherosclerotic intimal thickening and related constitutive modeling". In: *American Journal of Physiology: Heart and Circulatory Physiology* 289 (5), Copyright © 2005 American Physiological Society.

Figure 2.3 a) and b): Adopted with formal changes from Holzapfel, G. A., Sommer, G., Auer, M., et al. (2007): "Layer-Specific 3D Residual Deformations of Human Aortas with Non-Atherosclerotic Intimal Thickening". In: *Annals of Biomedical Engineering* 35 (4), pp. 530–545, Copyright © 2007 Biomedical Engineering Society. The original labeling has been replaced for formal reasons.

Figure 2.3 c): Adopted with formal changes from Fung, Y.-C. & Liu, S. Q. (1989): "Change of residual strains in arteries due to hypertrophy caused by aortic constriction". In: *Circulation Research* 65, pp. 1340–1349, Copyright © 1989 American Heart Association. Dispensable labeling and the grayish background have been removed, the contrast has been increased.

Figure 2.4: Drawing extracted from Holzapfel, G. A., Gasser, T. C. & Ogden, R. W. (2000): "A New Constitutive Framework for Arterial Wall Mechanics and a Comparative Study of Material Models". In: *Journal of Elasticity* 61, pp. 1–48, Copyright © 2001 Kluwer Academic Publishers. The original labeling of the individual components on the left has been removed in favor of the bullet points added on the right.

Figure 2.5: Adopted with formal changes from Matsumoto, T. & Hayashi, K. (1996a): "Response of Arterial Wall to Hypertension and Residual Stress". In: *Biomechanics. Functional Adaptation and Remodeling*. Ed. by Hayashi, K., Kamiya, A. & Ono, K. Tokyo: Springer. isbn: 4-431-70173-7, Copyright © 1996 Springer-Verlag Tokyo.

The indicated primary source, where only smaller cutouts of the figures are shown, is Matsumoto, T. & Hayashi, K. (1996b): "Stress and Strain Distribution in Hypertensive and Normotensive Rat Aorta Considering Residual Strain". In: *Journal of Biomechanical Engineering* 118 (1), pp. 62–73, Copyright © 1996 The American Society of Mechanical Engineers.

Figure 6.1: Background figure extracted and adopted (display window, colors) from Schriefl, A. J., Zeindlinger, G., et al. (2012): "Determination of the layer-specific distributed collagen fibre orientations in human thoracic and abdominal aortas and common iliac arteries". In: *Journal of the Royal Society Interface* 9 (71), pp. 1275–1286, Copyright © 2011 The Royal Society.

Figure 6.3: Reused with formal changes (font, colors) from Zahn, A. & Balzani, D. (2018a): "A combined growth and remodeling framework for the approximation of residual stresses in arterial walls". In: *Zeitschrift für Angewandte Mathematik und Mechanik* 98 (12), pp. 2072–2100, Copyright © 2018 WILEY-VCH Verlag GmbH & Co. KGaA, Weinheim.

Figure 6.4: Reused with formal changes (font, colors) from Zahn, A. & Balzani, D. (2018a): "A combined growth and remodeling framework for the approximation of residual stresses in arterial walls". In: *Zeitschrift für Angewandte Mathematik und Mechanik* 98 (12), pp. 2072–2100, Copyright © 2018 WILEY-VCH Verlag GmbH & Co. KGaA, Weinheim.

Figure 6.5: Reused with formal changes (font, colors, denotation of the vectors) from Zahn, A. & Balzani, D. (2018a): "A combined growth and remodeling framework for the approximation of residual stresses in arterial walls". In: *Zeitschrift für Angewandte Mathematik und Mechanik* 98 (12), pp. 2072–2100, Copyright © 2018 WILEY-VCH Verlag GmbH & Co. KGaA, Weinheim.

Educational background

01/2018 – 12/2020	Research associate at the Chair of Continuum Mechanics, Department of Civil and Environmental Engineering, Ruhr-Universität Bochum
09/2014 – 12/2017	Reserach associate at the Institute of Mechanics and Shell Structures, Department of Civil Engineering, Technische Universität Dresden
07/2014 – 08/2014	Research assistant at the Institute of Mechanics and Shell Structures, Department of Civil Engineering, Technische Universität Dresden
10/2007 – 03/2014	Civil engineering studies at Technische Universität Dresden
03/2007	General qualification for university entrance

Mitteilungen aus dem Institut für Mechanik
RUHR-UNIVERSITÄT BOCHUM
Nr. 186

ISBN 978-3-935892-64-3